

Turbulence simulations of the high confinement mode pedestal in tokamak fusion experiments

Leonhard Andrew Leppin

Complete reprint of the dissertation approved by the TUM School of Computation,
Information and Technology of the Technical University of Munich for the award of the
Doktor der Naturwissenschaften (Dr. rer. nat.).

Chair: Prof. Dr. Martin Schulz

Examiners:

1. Hon.-Prof. Dr. Frank Jenko
2. Prof. Dr. Ulrich Stroth

The dissertation was submitted to the Technical University of Munich on 08.11.2023 and
accepted by the TUM School of Computation, Information and Technology on 27.03.2024 .



MAX PLANCK INSTITUTE
FOR PLASMA PHYSICS



PhD Thesis

**Turbulence simulations of the
high confinement mode pedestal in
tokamak fusion experiments**

prepared by

Leonhard Andrew Leppin

from Berlin

at the Max Planck Institute for Plasma Physics

Thesis period: 15th November 2019 until 14th November 2023

First referee: Prof. Dr. Frank Jenko

Second referee: Prof. Dr. Ulrich Stroth

Zusammenfassung

Diese Dissertation behandelt einen zentralen Aspekt der Fusionsforschung: Die Physik des Transportes in magnetisch eingeschlossenen Plasmen. Der Fokus liegt auf der Simulation von Turbulenz im äußeren Bereich des eingeschlossenen Plasmas in Tokamaks. Einer der führenden gyrokinetischen Codes, GENE, wurde verbessert und großskalige Simulationen wurden durchgeführt. Das Verständnis von turbulenter Transport wurde durch die Simulation von Plasmaentladungen der Experimente JET und AUG erweitert.

Das Ziel der Fusionsforschung ist die Stromerzeugung mit Hilfe von kontrollierter Kernfusion. Die entscheidende Herausforderung in der Fusion mittels magnetischem Einschluss ist es ein heißes Plasma aus Wasserstoffisotopen so gut einzuschließen, dass mehr Energie durch Fusionsreaktionen freigesetzt wird, als zur Aufrechterhaltung des heißen Plasmas benötigt wird. Der mögliche Energiegewinn einer Fusionsanlage hängt stark davon ab wie gut der radiale Transport von Energie und Teilchen aus dem Plasma durch das Magnetfeld verhindert werden kann. In vielen Szenarien ist Turbulenz der entscheidende Mechanismus für den Energieverlust. In Tokamak Experimenten kann Turbulenz in einem schmalen Bereich nahe der letzten geschlossenen magnetischen Flussfläche unterdrückt werden. Dies bildet das Pedestal der H-Mode. Die Eigenschaften des Pedestals haben einen wichtigen Einfluss auf die gesamte Einschlussqualität des Plasmas. Da Turbulenz die Eigenschaften des Pedestals entscheidend mitprägt, ist ein umfassendes Verständnis von Pedestalturbulenz ein wichtiger Beitrag für die Entwicklung von verbesserten Plasmaszenarien.

Die entscheidenden turbulenten Transportmechanismen zu bestimmen, ist allerdings eine große wissenschaftliche und numerische Herausforderung. Die starken Gradienten stellen viel Energie für die Turbulenz bereit, weshalb viele physikalische Effekte im Pedestal relevant werden. Diese umfassen global Effekte, elektromagnetische Fluktuationen, Ionenskalen und Elektronenskalen Instabilitäten und Scherströmungen.

In dieser Arbeit werden diese Herausforderungen durch ein Upgrade des gyrokinetischen GENE Codes angegangen. Mit Hilfe des Upgrades wurden die ersten globalen, nichtlinearen, elektromagnetischen Turbulenzsimulationen eines ASDEX Upgrade Pedestals durchgeführt. Neben dem ASDEX Upgrade Szenario (Type-I ELMy H-mode), konnte der weiterentwickelte Code erfolgreich auf ein JET hybrid-Szenario H-moden Pedestal angewandt werden. Die globalen, nichtlinearen Simulationen ermöglichen die Analyse der radialen Struktur von Ionenskalen-Turbulenz im gesamten Pedestal von Pedestal Top bis Fuß. Eine detaillierte Charakterisierung von gyrokinetischen Instabilitäten mit lokalen, linearen Simulationen und nichtlineare Simulationen auf Elektronenskalen, vervollständigen die gyrokinetische Analyse.

In beiden untersuchten Pedestals von AUG und JET hat der Transport eine komplexe radiale Struktur und umfasst viele Skalen und Transportkanäle. Der dominante Elektronentransportkanal im AUG Pedestal wird von Strukturen verschiedener Größe verursacht. Auf dem Pedestal Top sind Ionenskalen TEM (Gefangene Elektronen

Mode)/MTM (Mikro Tearing Mode) Instabilitäten für den Transport verantwortlich, während im Zentrum des Pedestals ETGs (Elektronen Temperatur Gradienten Mode) auf Elektronenskalen den Transport übernehmen. Turbulenter Ionen Wärmefluss ist auf dem Pedestal Top vorhanden, aber stark verringert im Pedestal Zentrum. Magnetische Verscherung führt lokal zu einer Stabilisierung der Instabilitäten und Reduktion des Wärmetransportes. Im JET Pedestal wird Transport auf dem Pedestal Top von ITG (Ionen Temperatur Gradient) Moden getrieben und von ETG Moden im Pedestal Zentrum. In beiden Pedestals ist die $E \times B$ Verscherung wesentlich für eine Reduktion des Wärmeflusses in den globalen, nichtlinearen Simulationen. Des Weiteren wird eine komplexe Struktur der Pedestal-ETG Moden in beiden Szenarien beobachtet. Vergleiche zwischen linearen und nichtlinearen Modenstrukturen offenbaren, dass Ionenskalen-Turbulenz in großen Teilen des Pedestals ausgeprägte quasi-lineare Eigenschaften besitzt.

Zusammenfassend entwickelt diese Dissertation die gyrokinetische Analyse von H-Moden Pedestals weiter und verbessert das Verständnis von Pedestalturbulenz durch hochaufgelöste gyrokinetische Simulationen.

Teile der Ergebnisse, die in den Kapiteln 3, 4, and 5 präsentiert werden, wurden vorab veröffentlicht in Leppin, L., Görler, T., Cavedon, M., Dunne, M., Wolfrum, E., Jenko, F. & the ASDEX Upgrade Team. Complex Structure of Turbulence across the ASDEX Upgrade Pedestal. *Journal of Plasma Physics* **89**, 905890605. doi:10.1017/S0022377823001101 (2023). Teile der Ergebnisse, die in Kapitel 6 präsentiert werden, wurden zur Veröffentlichung eingereicht in Leppin, L., Görler, T., Frassinetti, L., Saarelma, S., Hobirk, J., Jenko, F. & JET Contributors. The JET Hybrid H-mode Scenario from a Pedestal Turbulence Perspective. *Nuclear Fusion* **Submitted** (2024).

Abstract

This thesis deals with a central part of fusion research: The physics of transport processes in magnetically confined plasmas. In particular, it focuses on the simulation of turbulence in the outer confined region of tokamak fusion experiments. For this purpose, one of the leading turbulence codes, GENE, has been upgraded, and large-scale simulations on multiple national supercomputers have been performed. As a result, the code's applicability has been extended to new plasma regimes, and the understanding of turbulent transport has been expanded through high-fidelity simulations of plasma discharges from the JET and AUG tokamak experiments.

Fusion research aims to generate electricity using controlled nuclear fusion. The key challenge in magnetic confinement fusion is to confine a hot plasma of hydrogen isotopes well enough such that more energy is released by nuclear fusion than is required to maintain the plasma at fusion conditions. The energy gain of a fusion reactor critically depends on how well the outward transport of energy and particles can be controlled. In many scenarios, turbulence is the dominant energy loss mechanism. In tokamak experiments, turbulence can be suppressed in a narrow region close to the last closed flux surface, the so-called pedestal of the high confinement mode (H-mode). The properties of the pedestal, with its steep temperature and density profiles, strongly influence the overall confinement. Since turbulence is one of the key ingredients in shaping H-mode pedestals, a detailed understanding of pedestal turbulence is crucial for developing improved plasma scenarios.

Identifying the relevant turbulent transport mechanisms in a pedestal, however, is a great scientific and numerical challenge. The steep gradients provide large amounts of free energy to the development of turbulence. Hence, in pedestal conditions, many physical effects become relevant, including global effects, electromagnetic fluctuations, the presence of ion-scale as well as electron-scale instabilities, and shear flows.

In this thesis, this challenge is addressed by upgrading one of the leading gyrokinetic codes, the GENE code. Using the code upgrade, the first global, nonlinear, electromagnetic turbulence simulations of an ASDEX Upgrade pedestal are performed. Besides the ASDEX Upgrade scenario (Type-I ELMy H-mode), the new code capabilities are successfully applied to a JET hybrid scenario H-mode pedestal. The global, nonlinear simulations enable analyzing the (ion-scale) turbulent heat flux structure in the full pedestal from pedestal top to foot. A detailed characterization of instabilities via local, linear simulations at the pedestal top, center, and foot, as well as dedicated nonlinear electron-scale simulations complete the gyrokinetic analysis.

In both investigated pedestals from AUG and JET, we find turbulent transport to have a complex radial structure that is multi-scale and multi-channel. The dominant electron transport channel in the AUG pedestal is found to transition in scale. At the pedestal top, ion-scale TEM (Trapped Electron Mode)/MTM (Micro Tearing Mode) instabilities fuel electron transport, whereas in the pedestal center, electron-scale ETG-driven (Electron Temperature Gradient mode) transport takes over. Turbulent ion heat flux

is present at the pedestal top and strongly reduces towards the steep gradient region. Magnetic shear is found to locally contribute to the stabilization of microinstabilities and reduction of heat flux. In the JET pedestal, transport due to ITG (Ion Temperature Gradient) modes is found to play an important role on the pedestal top, and ETGs are found in the pedestal center. In both pedestals, $E \times B$ shear is confirmed to strongly reduce heat fluxes in the global, nonlinear simulations. Furthermore, a complex structure of pedestal-ETG modes is identified in both scenarios. Comparisons between linear and nonlinear mode structures reveal a remarkable quasilinear nature of ion-scale turbulence in large parts of the pedestal.

Overall, this thesis pushes the frontiers of the gyrokinetic analysis of H-mode pedestals and improves the understanding of pedestal turbulence by high-fidelity gyrokinetic simulations.

Parts of the results presented in Chapters 3, 4, and 5 have been published in Leppin, L., Görler, T., Cavedon, M., Dunne, M., Wolfrum, E., Jenko, F. & the ASDEX Upgrade Team. Complex Structure of Turbulence across the ASDEX Upgrade Pedestal. *Journal of Plasma Physics* **89**, 905890605. doi:10.1017/S0022377823001101 (2023). Parts of the results presented in Chapter 6 have been submitted for publication in Leppin, L., Görler, T., Frassinetti, L., Saarelma, S., Hobirk, J., Jenko, F. & JET Contributors. The JET Hybrid H-mode Scenario from a Pedestal Turbulence Perspective. *Nuclear Fusion* **Submitted** (2024).

Contents

Zusammenfassung	iii
Abstract	v
1. Introduction	1
1.1. The case for fusion energy	1
1.2. Fusion process	3
1.3. Principles of magnetic confinement: The tokamak	4
1.4. Transport & stability in tokamaks	6
1.5. Plasma turbulence	9
1.6. The High-confinement mode (H-mode)	11
1.7. Figures of merit	12
1.8. Thesis outline	13
1.9. Summary	14
2. Mathematical framework: Gyrokinetics	17
2.1. Particle trajectories in strongly magnetized plasmas	17
2.2. Kinetic framework	21
2.3. Gyrokinetics	22
2.4. Summary	33
3. Numerical implementation: The GENE code	35
3.1. Overview	35
3.2. Coordinates & Numerics	36
3.3. Electromagnetic upgrade	44
3.4. Applicability of the GENE code to the pedestal	53
3.5. MHD limit of global gyrokinetics	56
3.6. Parallel hyperdiffusion	58
3.7. Summary	62
4. The H-mode pedestal and its instabilities	63
4.1. The pedestal from a turbulence perspective	63
4.2. Instability types	68
4.3. Quasilinear models	72
4.4. Distinguishing between modes	74

4.5. (Pedestal) microinstabilities	80
4.6. Dealing with experimental uncertainties	85
4.7. Summary	86
5. AUG pedestal simulations	87
5.1. Experimental scenario	87
5.2. Instability characterization	91
5.3. Nonlinear simulations	99
5.4. Further ELM timepoints	112
5.5. GENE-Tango approach in the pedestal	115
5.6. Summary	120
6. JET pedestal simulations	123
6.1. Experimental scenario	123
6.2. Instability characterization	127
6.3. Nonlinear, global simulations	141
6.4. Summary	146
7. Conclusions & Outlook	149
7.1. Discussion and Outlook	151
A. Appendix	155
A.1. Derivation of additional terms	155
A.2. AUG simulation settings	159
A.3. JET simulation settings	161
A.4. ASDEX Upgrade (AUG) tokamak	162
A.5. Joint European Torus (JET) tokamak	162
A.6. High-performance computing systems	163
Nomenclature	167
List of Figures	171
Bibliography	181
Acknowledgements	197
List of Publications	199

1. Introduction

These are exciting times for fusion research! Multiple scientific performance records have been broken in recent years, the interest of politics and the general public has noticeably increased, and private investments in the field have reached unprecedented levels. This progress and interest are motivated by the foremost goal of fusion research: The generation of electricity by controlled nuclear fusion or - to put it more poetically - building a sun on Earth.

This thesis deals with a central part of fusion research: The physics of transport processes in magnetically confined plasmas. In particular, it focuses on the simulation of turbulence in the outer confined region of tokamak fusion experiments. For this purpose, one of the leading turbulence codes, GENE, has been upgraded (Chapter 3), and large-scale simulations on multiple national supercomputers have been performed (Chapter 5 and 6). As a result, the code's applicability has been extended to new plasma regimes, and the understanding of turbulent transport has been expanded through high-fidelity simulations of plasma discharges from the JET and AUG tokamak experiments.

The first chapter introduces the field of fusion research and contextualizes the main body of my thesis. In the beginning, I outline the case for fusion energy and introduce the fusion process itself and the magnetic confinement of plasma. Then, the role of plasma turbulence for heat and particle transport and its suppression in the high-confinement mode (H-mode) is outlined.

1.1. The case for fusion energy

Humanity faces a global energy challenge. Important aspects of this challenge are illustrated in Fig. 1.1. The left plot shows the CO₂ emissions of selected countries as a function of their gross domestic product (GDP) per capita in the year 2017. The data shows a clear correlation between the wealth of a country and the emission of greenhouse gases. As a consequence, countries can be roughly sorted into two groups. One group is characterized by a lack of usable energy and the other by too high CO₂ emissions. In light of climate change caused by the anthropogenic emission of greenhouse gases [3], the desirable location for most countries in this figure would be the lower right corner, characterized by high wealth at low CO₂ emissions. The right plot adds a time perspective to the discussed challenge. The global primary energy demand

1. Introduction

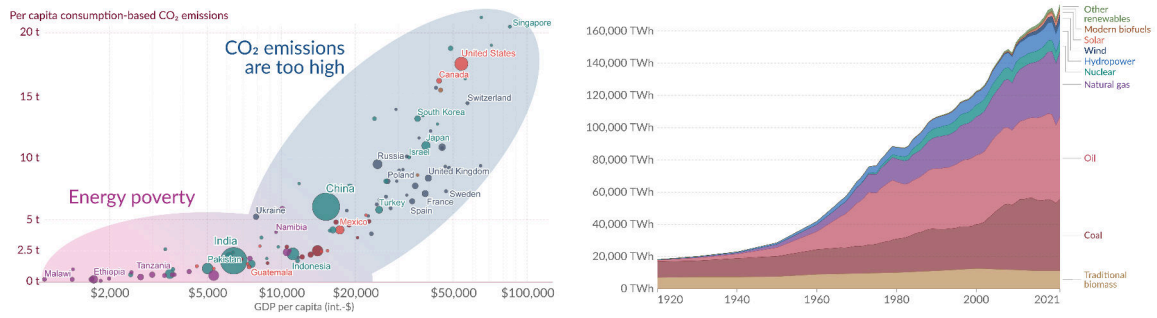


Fig. 1.1.: Illustration of the global energy challenge. Left: CO₂ emissions of countries as a function of GDP (both per capita). Modified from [5]. Right: Global primary energy consumption by source as a function of time. Modified from [4].

has increased more than 8-fold in the past century, and even in 2021, more than 80% of it is provided by fossil fuels [4]. This illustrates the need to develop all possible types of CO₂-neutral electricity generation. Nuclear fusion promises to be one of them. It would have the benefits of being a non-intermittent, baseload-capable method of electricity generation.

Recent performance records demonstrate the growing scientific maturity of fusion research. In December 2021, the Joint European Torus (JET), the world's largest fusion experiment, achieved a new record of 59 megajoules of sustained fusion energy [6]. In the same month, the EAST tokamak in China achieved a world-record pulse length of over 1000 seconds (or more than 17 minutes) [7]. In February 2023, Wendelstein 7-X, the world's largest fusion experiment of the stellarator type, achieved a significant milestone with an energy turnover of 1 gigajoule in an eight-minute-long plasma discharge [8]. And in December 2022, the National Ignition Facility (NIF), a laser-driven inertial confinement experiment, achieved *scientific* energy breakeven [9].

At the same time, public policy worldwide and private investments have increased their support of fusion research. The German government has voiced its support for fusion energy research in a recent position paper and funding program [10, 11]. In the UK, the STEP program aims to develop a prototype fusion power plant in a public-private partnership [12], and the US government is "developing a bold decadal vision for commercial fusion energy" [13]. Fusion start-up companies have received more than 6 billion USD in private and public investments in the past years, the majority of which is concentrated on a few companies [14]. Technological advances like magnets based on high-temperature superconductors developed by Commonwealth Fusion Systems offer promising paths to fusion pilot plants [15]. The number of newly founded companies and the amount of investment they receive may be seen as signs of a forming fusion energy industry that promises to take the science developed in the past decades at

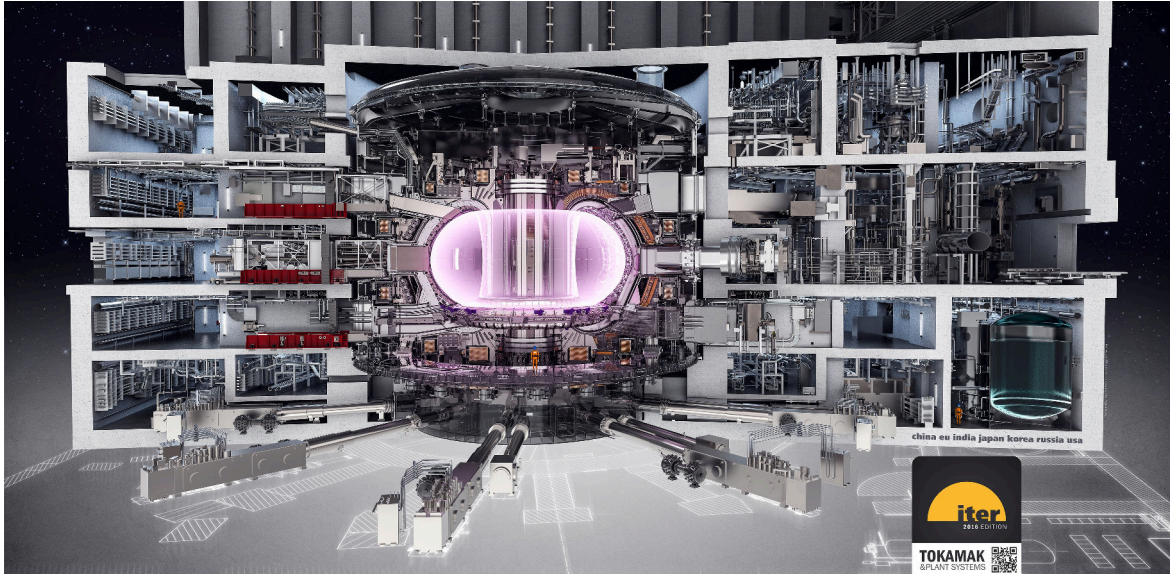


Fig. 1.2.: Rendering of ITER plant. Plasma physics is a crucial but only one part contributing to realizing fusion energy. Credit: ITER Organization, <https://www.iter.org/> .

national labs to application.

While this thesis is concerned with computational plasma physics, specifically plasma turbulence, it is emphasized that many other fields of science, technology, and engineering are indispensable for developing fusion reactors. Plasma-facing wall materials, plasma heating systems, Tritium breeding, and magnet technologies - to name just a few - are all essential areas of active research. This is illustrated by a rendering of ITER (iter.org), the international next-step experiment currently under construction in France, in Fig. 1.2.

1.2. Fusion process

The energy that fusion devices want to utilize is released when two light atomic nuclei fuse. The resulting fusion product is slightly lighter than the sum of the reactants, and the mass difference is released as kinetic energy. Fig. 1.3 shows the process for the hydrogen isotopes Deuterium (1 proton + 1 neutron) and Tritium (1 proton + 2 neutrons). Deuterium and Tritium fuse to form a Helium nuclei or α -particle, which carries about 20% of the released energy, and a neutron, which carries the remaining 80%.

The probability of fusion to occur under atmospheric conditions is negligibly small. High temperatures and densities are required to reach meaningful probabilities for the equally charged atomic nuclei to overcome the Coulomb barrier by quantum tunneling

1. Introduction

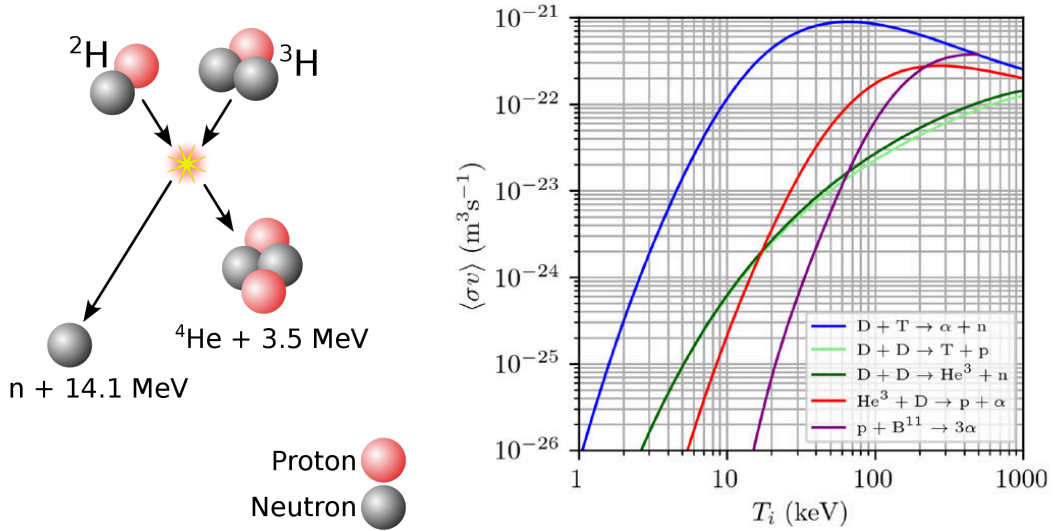


Fig. 1.3.: Left: Fusion of Deuterium $\text{D}=\text{}^2\text{H}$ and Tritium $\text{T}=\text{}^3\text{H}$. Taken from wikipedia.org/wiki/Nuclear_fusion. Right: Fusion reactivity for different fusion reactions. Taken from [16].

and fuse due to the strong nuclear force. Such conditions are most notably present in stars, which are powered by nuclear fusion.

While multiple fusion reactions take place in stars (CNO cycle, p-p cycle), the fuel of choice for most fusion reactor concepts is a Deuterium-Tritium mixture. The reason is the comparatively high reactivity in the achievable temperature range of 10 keV, see Fig. 1.3 on the right. (Via the Boltzmann constant $1\text{ eV} \hat{=} 11605\text{ K}$, so $10\text{ keV} \approx 10^8\text{ K} = 100\text{ million K}$.)

Even though a controlled, self-sustaining fusion reaction is the goal of this research, the fusion process itself will be of no further interest in this thesis. In none of our simulations, fusion is actually simulated. We are only concerned with simulating and optimizing the conditions for fusion to occur in the experiments. The impact of fusion-born fast α -particles on plasma dynamics in burning plasmas, however, is a topic of active research. It is not part of this thesis.

1.3. Principles of magnetic confinement: The tokamak

The fundamental requirement to achieve fusion is to keep atomic nuclei hot enough and dense enough for long enough. There are different routes for achieving this. In the core of the sun, the gravitational force and sheer size are decisive for achieving temperatures of about 15 million K, high densities (150 g/cm^3), and very long confinement times

1.3. Principles of magnetic confinement: The tokamak

[17]. This route is not reproducible on Earth. Instead, one technical option is inertial confinement fusion (ICF) [18], in which small hydrogen pellets are rapidly heated and compressed by powerful lasers, and the inertia of the exploding pellet provides the confinement time. Here, very high densities and high temperatures are reached, but only for fractions of a second, as the pellet is rapidly expanding after its implosion. The more widespread approach is magnetic confinement fusion (MCF), which uses magnetic fields to confine a hot plasma of about 100 million K at low densities of about 10^{-7} g/cm³ at confinement times of several seconds.

In the presence of strong magnetic fields, the charged particles of the plasma are bound to a spiraling motion along magnetic field lines by the electromagnetic Lorentz force. If the magnetic field lines close on themselves (or end losses are minimized, see mirror machines), the plasma is confined. The two dominant magnetic confinement fusion concepts are the tokamak and the stellarator. Both are toroidal devices, but they differ in how the magnetic field is created and the specifics of the magnetic field shape. In stellarators, the magnetic field is entirely created by external coils and can have a complex, non-axisymmetric shape. In tokamaks, on the other hand, an induced current in the plasma creates a component of the magnetic field that is axisymmetric (up to small ripples due to a finite number of coils). Following successes in the late 1960s, most fusion research has been focused on tokamaks, while stellarators are profiting in recent years from improved computational and optimization techniques that allow to exploit the flexibility in stellarator design compared to tokamaks. This thesis deals with tokamak plasmas, in particular with shots from the experiments JET (Joint European Torus), UK and AUG (ASDEX Upgrade), Germany.

Fig. 1.4, top shows the tokamak concept. Toroidal field coils (blue) and plasma current (green arrow) induced by the central solenoid/transformer (green) create a magnetic field with helical field lines (black). The field lines form nested magnetic flux-surfaces with the magnetic axis in the center and the last closed flux-surface (LCFS), also called separatrix, at the boundary to the open field line region or scrape-off layer (SOL) (cf. Fig. 1.4, right). In plasma (MHD) equilibrium, the flux-surfaces are surfaces of constant plasma pressure. The ratio of poloidal to toroidal magnetic field strength, and hence the pitch angle of the field lines, changes in general from flux-surface to flux-surface. The magnetic field strength on a given flux-surface changes, being strongest on the inside and weakest on the outside (see Fig. 1.4, left). The sides are referred to as the high-field/inboard side (HFS) and low-field/outboard side (LFS).

The necessary temperatures for fusion can be generated by multiple heating systems. In the start or ramp-up phase of experiments, the induced current heats the plasma

1. Introduction

due to its resistivity. As the plasma heats up, its resistivity reduces ($\eta_{sp} \propto 1/T_e^{3/2}$) and the resistive heating becomes less effective. To further heat the plasma, microwaves created by gyrotrons (Electron Cyclotron Resonance Heating (ECRH) or Ion Cyclotron Resonance Heating (ICRH)) can be used. Alternatively, fast neutral particles can be injected (neutral beam injection, NBI) that enter the plasma and deposit their energy in the plasma. Typically used heating powers in large tokamak experiments are on the order of 5-30 MW. In future reactors, the plasma is planned to be dominantly self-heated by the fusion-born α particles. Fuelling is done by puffing gas or shooting frozen Deuterium pellets into the plasma. Only a few milligrams of plasma are typically in the vessel at a given point. The most common fuels in current experiments are Hydrogen, Deuterium, or Helium. As of writing this thesis, JET is the only device in operation that is approved to perform experiments with the radioactive Hydrogen isotope Tritium. Plasma discharges, referred to as shots, typically last about 10 s (τ_E is significantly smaller) in machines with copper magnet coils (e.g. JET, AUG, DIII-D) and are limited by the cooling of the magnets. Devices with superconducting coils (W7-X, EAST) can reach longer discharges on the order of tens of minutes.

In steady-state, by definition, the same amount of power that enters the plasma or is generated by fusion leaves it. Three main channels transfer energy out of the plasma: Bremsstrahlung from the gyrating charged particles, neutrons from the fusion reactions, which are uncharged and hence not confined by the magnetic field, and plasma transport by convection/diffusion. The magnetic field in modern tokamaks is designed to direct the transport losses to a specific region in the vessel, the so-called divertor (cf. Fig. 1.4, right). In high-performance discharges with several MW of heating power, the divertor conditions approach the limits of all known materials (cooled tungsten tiles are the leading choice). This is only amplified in reactor scenarios. Designing the exhaust in a way that is simultaneously compatible with high-performance plasmas and the heat load limits of materials is one of the grand challenges of fusion research - for plasma physics as well as for materials science.

1.4. Transport & stability in tokamaks

The difficult part about magnetic confinement fusion is keeping the plasma confined. Behind this rather obvious statement hides a plethora of physics ranging from collisions to collective fluid-like motion, to (gyro-)kinetic turbulence, to large-scale self-organization. All of these phenomena significantly alter the simplistic view of single particles confined by the Lorentz force and mostly degrade plasma confinement. Gener-

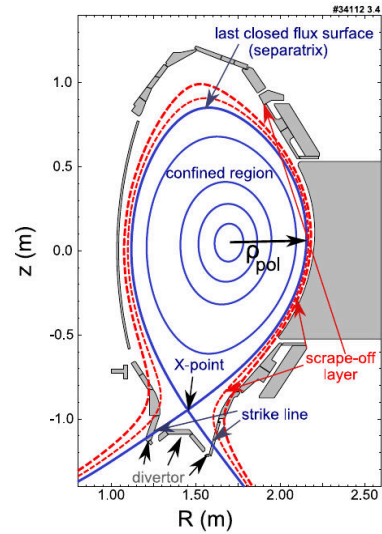
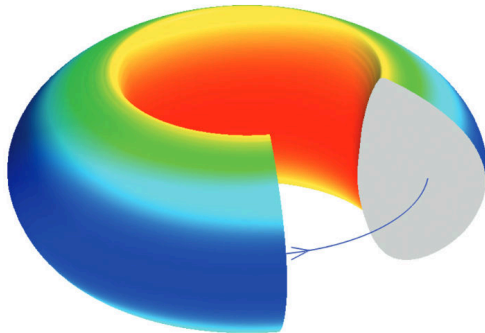
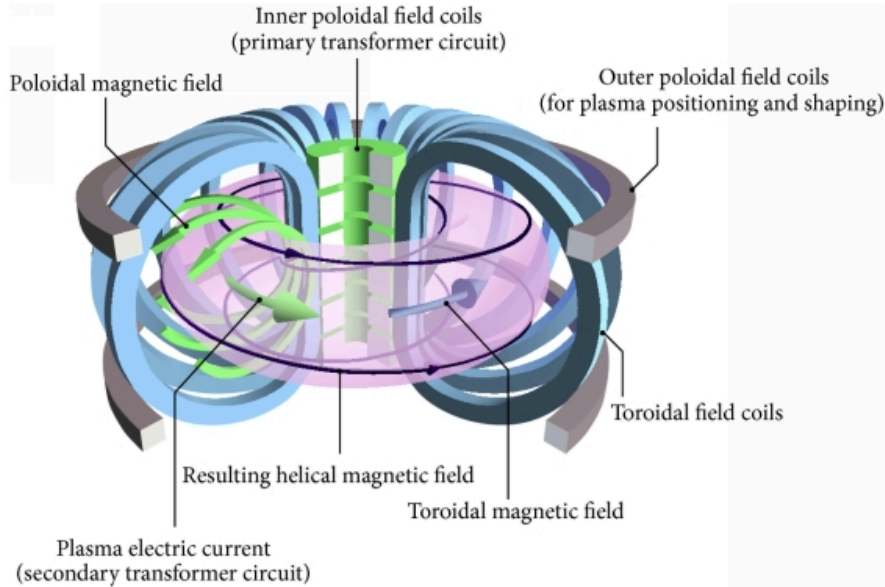


Fig. 1.4.: Top: Tokamak magnet structure. Credit: EUROfusion. Left: Magnetic field strength on a flux-surface in a tokamak. Example from DIII-D experiment. Reprinted from [19], with the permission of AIP publishing. Right: Poloidal cross-section showing nested flux surfaces in the confined region, separatrix, scrape-off layer, and divertor. Taken from [20] with the permission from P. Manz.

1. Introduction

ally, in the confined region, only the radial transport from flux-surface to flux-surface is of interest since energy and particles that stay on a given flux-surface remain confined.

The first challenge is to maintain a plasma that is magneto-hydrodynamically (MHD) stable. Since the plasma is a conducting medium, electric currents are created within it (intentionally and unintentionally), which modify the magnetic field structure and can cause instabilities (kink and tearing)[21]. These instabilities impose limits on the accessible pressure (β limit) and density (Greenwald limit [22]) of the plasma. An uncontrolled violation of these limits can cause disruptions, which are a violent loss of plasma confinement that can damage the experimental device. Disruption avoidance and mitigation are important research areas for the preparation of larger experiments and pilot plants. But even in an MHD stable plasma, confinement is not perfect.

One effect degrading confinement is collisions. Through collisions, particles, and energy can be transferred radially from one flux-surface to the next. Their impact is strongly increased in toroidal geometry due to the presence of additional particle orbits (trapped particles), which leads to the so-called neoclassical transport [23]. Nonetheless, collisional transport is, in most regimes, not the dominant transport channel. Fusion would be significantly easier and cheaper to achieve if collisional transport was the only transport mechanism.

The more critical effect degrading confinement is turbulence. Historically, this has been referred to as anomalous transport since the observed transport in experiments was up to two orders of magnitude higher than the predicted collisional transport. Driven by the large temperature and density differences between the plasma core and edge, the plasma forms coherent structures that extend over several flux surfaces and are very efficient in transporting heat and particles outwards. Turbulent transport is the focus of this thesis.

Besides these convective and diffusive energy loss mechanisms, plasma energy is also lost by radiation. The electrically charged ions and electrons constantly emit bremsstrahlung on their spiraling trajectory along field lines. Some of the radiation is reabsorbed by the plasma, but a substantial part transfers heat out of it.

While good confinement is desirable, the complete suppression of heat and particle transport is not the goal. In particular, for the control of impurities in the plasma, some outward transport is desirable. Even small amounts of heavy (high Z) impurities can otherwise compromise the plasma by radiating away large amounts of energy. Also, for effective fueling by gas puffs from the edge, radial transport is essential. In reactors, the outward transport of the fusion product or "helium ash" also becomes important.

1.5. Plasma turbulence

So far, my introduction has focused on the mission-driven aspect of this research: Control a plasma in a device to generate electricity. Besides this important application, there is also an intrinsic, basic research motivation to study the rich dynamics of plasma turbulence. While natural plasmas are not widespread on Earth (notable exceptions are lightning and auroras), plasma turbulence is the prevalent state (>99%) of ordinary matter in the observable universe. Stars, the interstellar medium, or accretion disks of black holes are all examples of natural plasma turbulence. Historically, the development of high-temperature plasma physics has been shaped by fusion research, and its challenges remain at the forefront of the discipline.

Plasma turbulence shares many phenomenological properties with neutral fluid turbulence. It is a dissipative, non-equilibrium state that requires constant energy input to prevent its decay. The turbulent structures/eddies are multi-scale - they comprise a wide range of sizes, from system scales to electron gyroradius scales. Turbulence is a non-linear, non-local complex system with infinitely many degrees of freedom. This leads to a chaotic and irregular motion that depends highly sensitively on initial conditions. In effect, individual particle or field dynamics become unpredictable and irreproducible, even though the underlying equations of motion are well known. This necessitates a statistical perspective on the physics and renders averages and distributions the important observables.

There are, however, also multiple effects that differentiate plasma turbulence from its neutral fluid counterpart. Most notably, kinetic effects, i.e. effects that depend on the particular velocity distribution of the plasma, become relevant. The interaction of electromagnetic waves and particles gives rise to Landau damping [24], which acts as an additional channel of dissipation besides collisions. This alters the classic fluid turbulence picture of Richardson's energy cascade [25], involving a large-scale energy injection, inertial cascade, and small-scale dissipation. Not only the dissipation range is different, but also the energy injection is more complex, as can be seen by considering the growth rate spectra of plasma instabilities (see later chapters). One typically finds a wide range of unstable modes from reactor scales down to electron scales that all interact in the full turbulent system. Plasma turbulence in a tokamak is not only fuelled at a single scale but by a broad spectrum of modes. Consequently, there is no known universal inertial range for plasmas that would be similar to Kolmogorov's K41 theory [26, 27] for Navier-Stokes turbulence.

The strong magnetic field in a tokamak renders the turbulence quasi-2D, as is visualized

1. Introduction

in Fig. 1.5. Along the magnetic field lines, transport is very fast, which creates strongly elongated eddies that display complex dynamics, mainly in the poloidal cross-section. Therefore, as in fluid 2D turbulence, energy cascades in both directions exist in tokamak plasmas. Energy can be transferred to smaller structures as well as to larger ones. Large zonal flows, for instance, are an established saturation mechanism for turbulence driven by specific instabilities [28].

The free energy driving the turbulence in a tokamak is provided by radial temperature and density gradients. In the edge region of tokamak plasmas - the focus of this thesis - these gradients can become particularly large. The relation of different driving gradients to each other and further physical parameters like collisionality and plasma β determine the character of the turbulent state. More details on that are discussed in the result sections of this thesis.

The study of plasma turbulence greatly profits from direct numerical simulations and high-performance computing. Analytical results derived from first principles are even less feasible for plasma turbulence than for the famously difficult Navier-Stokes equations of neutral fluids. However, since the governing equations of motion are comparatively easy to set up, plasma turbulence is a prime candidate for numerical simulations.

For plasma turbulence, a hierarchy of models has evolved. The highest fidelity models are fully kinetic, taking into account the complete phase space dynamics of the plasma. The next stage is gyrokinetic models, which try to retain most relevant kinetic effects at drastically reduced computationally cost. This is the model of choice in this thesis and is discussed in detail in the following chapter. The next stage is various fluid models (MHD see e.g. JOREK code [29], Braginskii see e.g. GRILLIX code [30]) that do not include kinetic effects but can be very effective in high collisionality regions of tokamak plasmas, like the scrape-off layer. The fastest models with the least fidelity are quasi-linear models that do not directly simulate the nonlinear turbulence but only solve for linear instabilities and apply fixed saturation rules. For traditional core turbulence, these models (e.g. TGLF [31, 32] or QuaLiKiz [33, 34]) are very successful in predicting turbulent fluxes. The success of quasi-linear models demonstrates the strong influence the driving instabilities have on the nonlinear turbulent state. For the edge region and, in particular, the pedestal (see next section), quasi-linear models are just being developed. Edge pedestal turbulence is much less well understood than tokamak core turbulence due to strong gradients and the proximity to the open field line region. This motivates code extensions and turbulence characterization like the ones presented in this thesis.



Fig. 1.5.: 3D rendering of a GENE turbulence simulation of a tokamak. Taken from genecode.org .

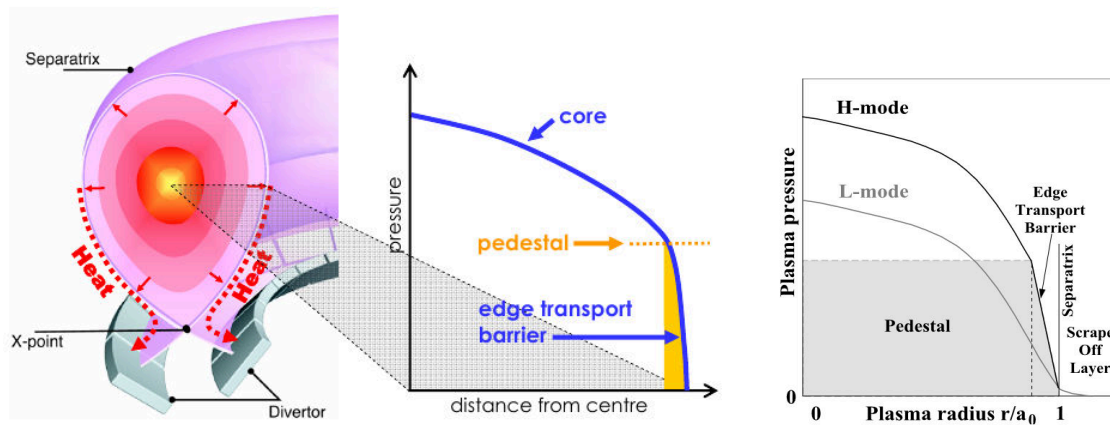


Fig. 1.6.: Left: Illustration of the H-mode pedestal. Reprinted from [35], with the permission of AIP Publishing. Right: Comparison of typical L-mode with H-mode pressure profiles. Reproduced from [36] with permission from IAEA.

1.6. The High-confinement mode (H-mode)

The high-confinement mode (H-mode) is characterized by the presence of an edge transport barrier that lifts the pressure profile, see Fig. 1.6. In this pedestal, turbulent transport is suppressed, and the gradients of temperature and density are increased. The shape of the pressure profile in the core is usually stiff, i.e. an increase in heating power does not significantly alter the profile but causes more turbulent transport at barely changed profiles. Consequently, the plasma core pressure in H-mode is strongly increased in comparison to the low-confinement mode (L-mode), since in H-mode, similar core profile shapes are maintained at increased absolute values (see Fig. 1.6, right). Hence, the H-mode pedestal, which is dominantly a plasma edge effect, influences the whole plasma and improves fusion conditions in the core of the plasma device. In H-mode, the energy confinement time increases by roughly a factor of two compared to

1. Introduction

L-mode [37].

The H-mode was experimentally discovered in 1982 at the ASDEX tokamak [38]. It has since then been reproduced at most large international tokamak experiments, including JET and DIII-D [39]. It is the default high-performance scenario for ITER and many demonstration reactor concepts.

H-mode is accessed by an increase in heating power, which triggers a bifurcation in the plasma dynamics. It is a prime example of a self-organization phenomenon. Experimental and theoretical studies show that a radial electric field and strong shear flows build up that decorrelate turbulent eddies and thereby suppress turbulent transport. The pedestal grows until it reaches large-scale stability limits that trigger modes that flatten the gradients and destroy the pedestal. These Edge Localized Modes (ELMs) have typical frequencies of 10-100 Hz and rapidly expel large amounts of energy and particles (up to 15%) [40] from the plasma, which can damage the divertor. Hence, ELMs have to be avoided in reactors, and a lot of experimental and theoretical research is dedicated to the development of ELM suppression and ELM-free scenarios with H-mode-like properties.

While a basic understanding of the H-mode is established, many open questions on the precise dynamics, causal relationships, and parameter dependencies remain. In particular, no predictive model exists for the threshold power of the L-H transition P_{LH} and many important properties of the pedestal. This means that state-of-the-art predictions for essential properties of H-mode plasmas in future experiments are mainly based on an extrapolation of experimental scaling laws rather than a physics-based model. One approach to improving this situation is a first-principles characterization of pedestal turbulence, as is performed in this thesis.

1.7. Figures of merit

In the last section of this chapter, I want to define more precisely what is meant by good confinement and chart the progress achieved in fusion research towards net energy gain.

The energy confinement time τ_E is defined as the ratio of the plasma energy $W \approx 3VnT$ and the heating power P required to sustain the energy of the confined plasma: $\tau_E = W/P$. If the plasma was perfectly isolated, the confinement time would tend to infinity, and if transport losses increase, the power to sustain the plasma energy has to increase as well, lowering the energy confinement time.

To achieve net energy gain, the goal is for the plasma to heat itself by the fusion born α particles in a self-sustaining reaction. This is called ignition, and the ignited plasma is referred to as a burning plasma. One can derive a condition on the combination of density n , temperature T , and confinement time τ_E for the plasma to reach ignition, the so-called Lawson criterion. The product $nT\tau_E$ is called Lawson parameter, and the product of all three essential quantities $nT\tau_E$ is called triple product.

The energy gain factor Q compares the power generated by fusion to the external heating power: $Q = P_{fus}/P_{ext}$. Breakeven ($Q = 1$) is reached when the fusion reactions create the same amount of power as is externally applied. In a burning plasma, Q reaches infinity since no external heating power is required ($P_{ext} = 0$). There is ambiguity in how to define the external heating power. One can either use only the power that directly heats the plasma or the wall-plug power that is required to run the heating systems, which takes into account their efficiency losses. The first option yields the scientific Q factor Q_{sci} , and the latter the engineering Q factor Q_{eng} . For an electricity-generating fusion device, $Q_{eng} > 1$ is decisive. The record for Q_{sci} in a tokamak is 0.67, set up in 1997 at JET. $Q_{sci} > 1$ has been achieved in an inertial confinement experiment [9], where, however, $Q_{eng} \ll 1$ due to the low efficiency of the driving lasers. The target for ITER is to achieve $Q_{sci} = 10$. Fig. 1.7 shows the progress in the achieved Lawson parameter and Q_{sci} across many different experiments in a log-log plot.

1.8. Thesis outline

This thesis is structured as follows: This first chapter has given a brief overview of the field of fusion research and has provided the broad context for this thesis. Chapter 2 introduces the mathematical framework of gyrokinetics, which is used to describe plasma dynamics throughout this thesis. Chapter 3 contains the first new results: After a short description of the GENE code, a new electromagnetic upgrade, which has been implemented within this thesis, is described. Furthermore, the applicability of the GENE code in pedestal conditions is discussed. In particular, the MHD limit of large modes is studied linearly, and the role of parallel hyperdiffusion is critically examined. Chapter 4 has two purposes: It introduces the machinery used in the following chapters to analyze turbulence simulations and reviews the current understanding of pedestal turbulence. Chapters 5 and 6 then analyze pedestal turbulence in two shots from world-leading fusion experiments, AUG and JET, in a comprehensive gyrokinetic analysis employing the new code upgrade presented in Chapter 3. Finally, in Chapter

1. Introduction

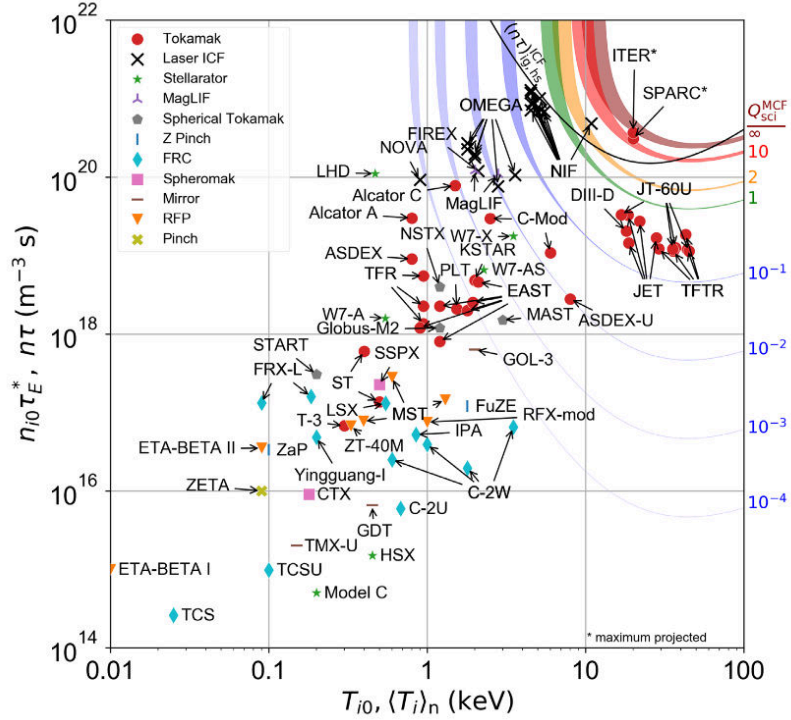


Fig. 1.7.: Lawson parameter achieved in different experiments. Illustrating progress, variety of approaches, and strong impact of tokamak experiments (red dots). Taken from [16].

7, conclusions are drawn, and an outlook is given.

Each chapter begins with a short overview and ends with a brief summary, which includes, for the first chapters some recommended further literature.

The appendix contains more details on the derivation of the electromagnetic upgrade, simulation settings and short introductions to the experiments AUG and JET, as well as the supercomputers used for the simulations presented in this thesis. Symbols and abbreviations are listed in the Nomenclature.

1.9. Summary

This introduction has motivated the study of plasma turbulence in nuclear fusion research. The attractive promise of fusion power plants and the crucial role plasma turbulence takes for plasma confinement, and hence the size and cost of power plants, have been outlined. The academic interest in plasma turbulence as a not well-understood prime example of complex, collective behavior featuring emergent phenomena has been highlighted. Furthermore, the need for high-performance computing to simulate plasma micro-dynamics on relevant scales has been outlined and the importance of an improved

understanding of H-mode pedestal turbulence has been motivated. Before an upgrade of the numerical tools used in this thesis is discussed and applied to experimental scenarios in later chapters, the next chapter introduces the underlying mathematical model: Gyrokinetics.

Recommended further literature

- Energy and economic charts: www.ourworldindata.org/energy and references therein.
- On the history of fusion research: D. Clery, *A Piece of the Sun: The Quest for Fusion Energy*, Overlook Press, 2013.
- Overview of fusion start-ups: www.fusionindustryassociation.org
- Online lecture on the basics of fusion research by Alf Köhn-Seemann from the University of Stuttgart: <https://www.youtube.com/@DerPlasma/>
- Review on the H-mode: Wagner, F. A Quarter-Century of H-mode Studies. *Plasma Physics and Controlled Fusion* **49**, B1–B33. doi:10.1088/0741-3335/49/12B/S01 (12B 2007)
- Turbulence in fluids - well-written background: Davidson, P. A. *Turbulence: An Introduction for Scientists and Engineers* (Oxford University Press, Oxford; New York, 2004)
- Most fusion plasma physics textbooks cover most of the topics introduced in this chapter. E.g. in German: Stroth, U. *Plasmaphysik: Phänomene, Grundlagen und Anwendungen* 2. Auflage (Springer Spektrum, Berlin, 2018) or in English: Stacey, W. M. *Fusion Plasma Physics* (Wiley-VCH ; John Wiley [distributor], Weinheim : Chichester, 2005).

2. Mathematical framework: Gyrokinetics

This chapter introduces the model used for the description of plasma dynamics throughout this thesis. Starting from single-particle dynamics, the kinetic description of plasma dynamics and the gyrokinetic Vlasov-Maxwell system are presented. The derivation of gyrokinetics and its underlying assumptions is outlined, and its validity in the pedestal is examined.

2.1. Particle trajectories in strongly magnetized plasmas

The mathematical description of plasma dynamics starts simple: With the motion of single particles under the forces of external electric and magnetic fields. The principal force acting on the charged particles is the Lorentz force $\mathbf{F} = q(\mathbf{E} + \mathbf{v} \times \mathbf{B})$, where q is the charge of the particle, \mathbf{E} an electric field, \mathbf{v} the velocity of the charged particle and \mathbf{B} a magnetic field. Different kinds of motions are generated depending on the spatial and temporal properties of the electromagnetic fields. Homogenous magnetic fields will induce different motions than magnetic fields that have peaks and valleys, and stationary electric fields will generate less varied trajectories than electric fields that change in time, to name just a few examples. Under a strong anisotropic magnetic field, the dynamics of particles can be sensibly decomposed in two kinds: The one along the magnetic field lines and the one in the plane perpendicular to it. This is the case for a tokamak.

The principal motion of charged particles in a homogeneous magnetic field without electric fields is spiraling around the field line. Along the magnetic field line, the motion is undisturbed and in the perpendicular plane the particle has a circular trajectory with a frequency of $\omega_c = qB/m$, where m is the mass of the particle, called gyrofrequency and a radius $\rho_L = v_\perp/\omega_c = mv_\perp/qB = \sqrt{2mT}/qB$. Associated with the periodic gyromotion as an adiabatic invariant is the magnetic moment $\mu = \rho_L q v_\perp / 2 = \frac{1/2 m v_\perp^2}{B}$. It is conserved under sufficiently slow changes.

2. Mathematical framework: Gyrokinetics

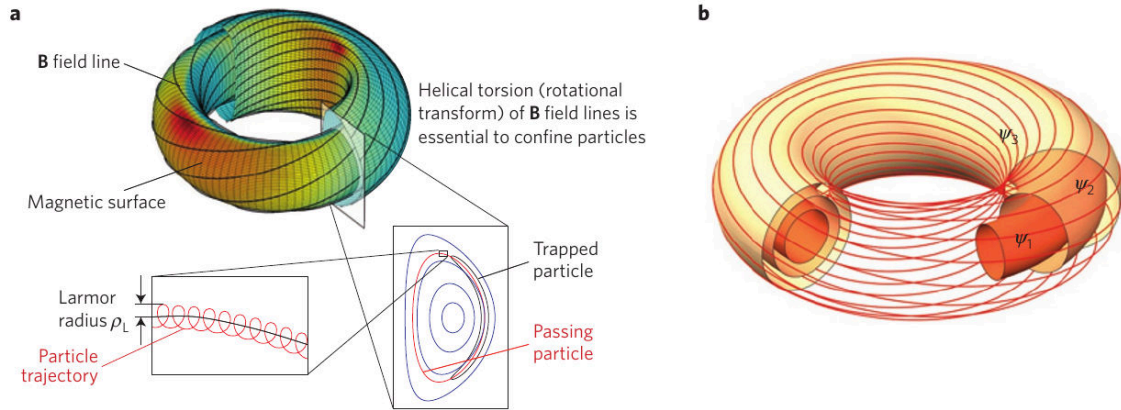


Fig. 2.1.: Illustration of the magnetic field structure and particle orbits in a tokamak. Taken from [43]. Reproduced with permission from Springer Nature.

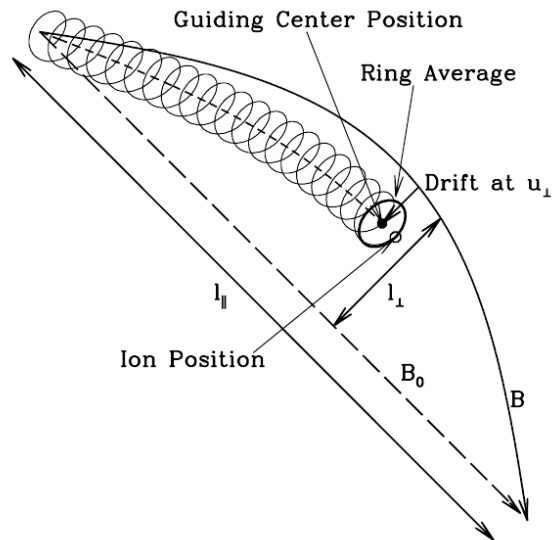


Fig. 2.2.: Illustration of guiding center and drifts in gyrokinetic theory. The full particle motion consists of a gyromotion around the guiding center trajectory. The guiding center trajectory follows the perturbed magnetic field line (solid, labeled B) in contrast to the equilibrium magnetic field (dashed, labeled B_0) and is subject to drifts, e.g. due to electric fields. Reproduced from [44] with permission from G.Howes and AAS.

2.1.1. Parallel motion: Trapped and passing particles

The motion along the field line becomes more complex when the magnetic field strength varies along the magnetic field line. This is the case in a tokamak where $B \propto 1/R$, with the major radius R , i.e. the magnetic field is stronger on the inside than on the outside of the torus. In this case, particles are decelerated towards the increasing magnetic field, and if their initial parallel motion is slow enough, they are turned around. This is also called magnetic mirror effect, as particles are reflected by the increasing magnetic field. Whether a particle gets reflected is determined by the so-called pitch angle between the magnetic field and the particle's velocity: $\tan \alpha = v_{\perp}/v_{\parallel}$. This effect can cause particles to be trapped at the outboard side of the tokamak. One calls these trapped particles and the other passing particles. The orbits of the trapped particles are named after their shape in the poloidal projection "banana orbits". They play an important part in neoclassic transport theory, where they can appear as the step widths. Depending on the reflection point of the particles, one can distinguish between deeply trapped particles and others. The changing magnetic field strength has a noteworthy consequence for the size of the Larmor radius. It is not constant around the torus but is largest at the outboard midplane and gets smallest on the inboard side.

2.1.2. Perpendicular motion: Drifts

The gyromotion of the particle in the perpendicular plane is modified if an additional force is acting. In a strong magnetic field, the resulting motion can be viewed as a superposition of the gyromotion and a drift motion with the velocity $\mathbf{v}_D = \mathbf{F} \times \mathbf{B}/qB^2$. Depending on the force, these drifts have different properties and may, for example, be in equal or opposite directions for ions and electrons. The following subsections introduce the most important drifts.

$\mathbf{E} \times \mathbf{B}$ drift

This drift occurs in the presence of a time-independent electric field. With the force $\mathbf{F} = q\mathbf{E}$, the drift velocity becomes $\mathbf{v}_D = \mathbf{v}_{E \times B} = \mathbf{E} \times \mathbf{B}/B^2$. This is a very important drift for large-scale plasma motion and in the dynamics of plasma microinstabilities. Notice that this drift does neither depend on the mass nor the charge of the particle. So, electrons and heavy ions drift at the same speed in the same direction. Hence, the $\mathbf{E} \times \mathbf{B}$ drift does not create a current.

Polarization drift

This drift occurs in the presence of a time-varying electric field, where the change of the electric field is much slower than the gyrofrequency. The drift velocity is $\mathbf{v}_{\text{pol}} = \frac{m}{qB^2} \frac{\partial \mathbf{E}_{\perp}}{\partial t}$, where \mathbf{E}_{\perp} is the electric field component perpendicular to the magnetic field lines. The drift depends on the charge of the particle, so electrons and ions drift in opposite directions. It depends on the mass, so it is more relevant for ions than for electrons. The polarization drift is not included in standard gyrokinetics.

∇B drift

This drift occurs in the presence of a perpendicular magnetic field strength gradient. With the force $\mathbf{F} = -\frac{1}{2}mv_{\perp}^2 \nabla_{\perp} B/B$ the drift velocity becomes $\mathbf{v}_{\nabla B} = -\frac{mv_{\perp}^2}{2q} \nabla_{\perp} B \times \mathbf{B}/B^3$, where $\nabla_{\perp} B$ is the gradient of the magnetic field strength B in the direction perpendicular to the magnetic field. The drift depends on the charge of the particle, so electrons and ions drift in opposite directions. Furthermore, it depends on the perpendicular energy of the particles.

Curvature drift

This drift occurs in the presence of curved magnetic field lines. With a centrifugal-like force $\mathbf{F} = m \frac{v_{\parallel}^2}{R_c} \frac{\mathbf{R}_c}{R_c}$, where the radius of curvature \mathbf{R}_c can be related to magnetic field derivatives such that the drift velocity becomes $\mathbf{v}_c = \frac{mv_{\parallel}^2}{qB} (\nabla \times \hat{\mathbf{b}})_{\perp}$. The drift depends on the charge of the particle, so electrons and ions drift in opposite directions. Furthermore, it depends on the parallel energy of the particles.

Diamagnetic drift

This drift does not occur in the single particle description because it is a collective phenomenon relying on the concept of pressure p like e.g. in the fluid description. $\mathbf{F} = \nabla p$ then $\mathbf{v}_{\text{dia}} = -\nabla p \times \mathbf{B}/(qnB^2)$, where n is the density. The name of the drift is derived from the diamagnetic current $j_{\text{dia}} = -\nabla p \times \mathbf{B}/B^2$, which reduces the magnetic field strength in the plasma. The diamagnetic drift of ions and electrons points in opposite directions. The diamagnetic drift is not explicitly included in standard gyrokinetics.

2.2. Kinetic framework

Tracking each particle of the plasma individually is not a feasible approach to studying the collective dynamics of the plasma, given plasmas of interest have particle densities of about 10^{20}m^{-3} in volumes of $10 - 100\text{m}^3$. A comprehensive description of plasma dynamics is possible with kinetic theory. The central element of kinetic theory is the distribution function f , which is a probability density in 6-dimensional phase space spanned by 3 space and 3 velocity coordinates. Integrating f over some phase space volume $f dx^3 dv^3$ gives the probability of finding particles with a certain velocity at a certain position. The phase space distribution f replaces individual discrete particles with a continuum description in phase space, akin to the continuum description of fluids in real space. By calculating moments of the distribution function, all important plasma properties can be calculated: densities, velocities, temperatures, etc. Of particular importance is the kinetic description when the plasma is not well thermalized, i.e. the distribution of velocities deviates from a Maxwellian distribution, which is implicitly assumed in an MHD description. In this case, the description becomes more accurate when retaining the full velocity space distribution and not collapsing it to a single scalar, the temperature. There are physical effects that are only revealed by a kinetic treatment, Landau damping being the prime example. The time evolution of the phase space distribution function f for a plasma species is given in the absence of collisions by the Vlasov equation:

$$\frac{df}{dt} = \frac{\partial}{\partial t} f + \frac{\partial \mathbf{x}}{\partial t} \cdot \nabla f + \frac{\partial \mathbf{v}}{\partial t} \cdot \nabla_v f = 0, \quad (2.1)$$

where

$$\frac{\partial \mathbf{v}}{\partial t} = \frac{q}{m} (\mathbf{E} + \mathbf{v} \times \mathbf{B}) \quad (2.2)$$

is given by the Lorentz force. Each particle species (e.g. electrons and ions) is described by its own distribution function. The equation is closed by the Maxwell equations, which determine the \mathbf{E} and \mathbf{B} fields due to the generated current density \mathbf{j} and charge density ρ . Ampère's law:

$$\nabla \times \mathbf{B} = \frac{4\pi}{c} \mathbf{j} + \frac{1}{c} \frac{\partial \mathbf{E}}{\partial t} \quad (2.3)$$

Law of induction:

$$\nabla \times \mathbf{E} = -\frac{1}{c} \frac{\partial \mathbf{B}}{\partial t} \quad (2.4)$$

Gauss's law (takes the form of Poisson's equation, when \mathbf{E} is expressed via its potential ϕ , such that $\mathbf{E} = -\nabla\phi$):

$$\nabla \cdot \mathbf{E} = -\nabla^2 \phi = 4\pi\rho \quad (2.5)$$

2. Mathematical framework: Gyrokinetics

Gauss's law for magnetism:

$$\nabla \cdot \mathbf{B} = 0 \tag{2.6}$$

2.3. Gyrokinetics

The kinetic plasma description introduced in the previous section is a valid and comprehensive description of plasma dynamics. In fact, it is more complete and requires fewer assumptions than the description we will employ, called gyrokinetics. However, while the kinetic description is easy to understand conceptually, it carries a prohibitively high computational cost in many real-world applications. Based on estimates of G. Hammett for the speed-up due to gyrokinetics compared to a brute-force fully kinetic algorithm (about at least 10^8) [45] and the experiences gained in this thesis (simulating 1 ms of an AUG pedestal in a global simulation took about 12 days on 6000 CPU cores), one can conclude that a fully kinetic simulation of a realistic scenario would take years on modern supercomputers. The name of the game is, therefore, to find ways in which the computational cost can be reduced without giving up too much of the relevant physics. The central insight underlying gyrokinetics is the time-scale separation between the fast gyromotion and comparatively slow motions dominating radial transport processes. Consequently, one can afford to ignore details of the gyromotion and still capture plasma turbulence. This is achieved by averaging over the gyromotion and treating particles as charged rings, following a guiding-center (or, more precisely, gyro-center). The reduction in computational cost is realized by a larger time step that does not have to resolve the fast gyromotion and by a reduction of phase space dimensions from the 6D fully kinetic phase space to a 5D gyrokinetic phase space. Deriving the appropriately modified Vlasov-Maxwell system is a formidable mathematical challenge, in particular, if important properties of the system, like energy conservation, should be retained exactly. The critical steps are outlined in the following subsections. As we progress, we will trade in conceptual and mathematical simplicity for reduced computational cost. In the end, we will arrive at a system that exploits many physical properties of the plasma dynamics and can be simulated much faster. The numerical implementation of this system is discussed in the next chapter.

We follow Ref. [46] in the derivation.

2.3.1. Hamiltonian formulation & guiding-center coordinates

The first important step for deriving the gyrokinetic plasma description is reformulating the dynamics in terms of Hamiltonian mechanics. This framework provides the tools for a rigorous elimination of the fast gyromotion. Instead of the forces that were the focus of attention in the Newtonian perspective on drifts in the previous sections, the energetics of the system become central. The Hamiltonian for a particle in electromagnetic fields can be written as:

$$H = \frac{p^2}{2m} + e\phi, \quad (2.7)$$

where $\mathbf{p} = m\mathbf{v}$ is the kinetic momentum, m the mass, e the charge and ϕ the electric potential. The Lagrangian is

$$\Gamma = \left(\frac{e}{c} \mathbf{A} + \mathbf{p} \right) \cdot d\mathbf{x} - H, \quad (2.8)$$

where \mathbf{A} is the magnetic vector potential. From the Hamiltonian, the equations of motion can be derived via Hamilton's equations or, equivalently, via the Euler-Lagrange equations from the Lagrangian,

$$\frac{d}{dt} \left(\frac{\partial \Gamma}{\partial \dot{\mathbf{q}}} \right) - \frac{\partial \Gamma}{\partial \mathbf{q}} = 0, \quad (2.9)$$

where \mathbf{q} are generalized coordinates. This puts the Hamiltonian or Lagrangian as the central object. All necessary manipulations are performed on the Hamiltonian, and then the equations of motion can be derived.

To render the fast gyromotion ignorable, we transform the phase space coordinates. In naive cartesian coordinates, the gyromotion is, in general, part of all coordinate dimensions. To eliminate part of it, it is desirable to construct a coordinate system such that the gyromotion influences only one or a few of the coordinates. A clever coordinate choice for this purpose is to align the velocity coordinates with the principle particle motion, using essentially cylindrical coordinates in velocity space along the magnetic field lines. One dimension is the velocity parallel to the magnetic field lines v_{\parallel} , another dimension is the size of the gyroradius, which encodes the magnitude of the perpendicular velocity v_{\perp} and the third dimension is an angle θ measuring the position on the gyrocircle determining the direction of the perpendicular velocity (gyrophase). Typically, not the gyroradius size but the magnetic moment $\mu = \rho_L q v_{\perp} / 2 = \frac{1/2 m v_{\perp}^2}{B}$ is used as the coordinate. It has the advantage of being an adiabatic invariant of the particle motion, i.e. for slow changes in the magnetic field μ is conserved. Together with

2. Mathematical framework: Gyrokinetics

three spatial coordinates that contain the position of the guiding center, this system is called "guiding center coordinates". This has transformed the part of the motion we are not interested in into a single dimension: The gyrophase angle θ .

The fast gyromotion angle and the magnetic moment μ can be identified as an action-angle coordinate pair. The dependence of the Hamiltonian on θ is eliminated, and μ is conserved. This allows one to derive the following Vlasov equation:

$$\frac{dF}{dt} + \frac{d\mathbf{X}}{dt} \cdot \nabla F + \frac{dv_{\parallel}}{dt} \frac{\partial F}{\partial v_{\parallel}} = 0. \quad (2.10)$$

Compare this equation to the original kinetic Vlasov equation Eq. 2.1. The velocity derivative term is drastically reduced. Only the parallel derivative remains since, for the other two velocity coordinates, one of the factors is zero ($d\mu/dt = 0$ and $dF/d\theta = 0$). For a homogeneous plasma without any fluctuations, we have reached the goal: Eq. 2.10 does not depend on the gyroangle, and the new distribution function F lives in a 5D phase space instead of the 6D kinetic one. However, the plasmas we are interested in are neither homogeneous nor in equilibrium. The challenge is now to retain this structure even though the electric and magnetic fields are, in general, changing in space and time, which distorts the gyromotion, making it not exactly periodic. For arbitrarily large and sudden changes of the electromagnetic fields, this is not possible. If particles are not approximately gyrating, the whole guiding center approach ceases to make sense. In this case, only the full 6D kinetic equation treats the dynamics appropriately. If changes are, however, not too large and fast, there is a chance to salvage the 5D phase space by a perturbative approach. This is done in two steps: The first for small changes of the magnetic field in space, which will result in the guiding-center Hamiltonian, whose equations of motion are the so-called drift-kinetic equations. The second transformation is for small fluctuations of the E and B fields, which will result in the gyro-center Hamiltonian, whose equation of motion is the gyrocenter Vlasov equation. The following section specifies what is meant by small and slow changes.

2.3.2. Assumptions on the perturbations

The gyrokinetic equations are designed to be valid for dynamics in which averaging over the gyroradius instead of fully resolving the gyromotion of particles is a good approximation. This approximation is good if the dynamics fulfill several requirements on their spatio-temporal properties. Here, we introduce them. The assumptions presuppose a decomposition of the distribution function as well as electric and magnetic field into time-independent background parts and time-dependent fluctuating parts,

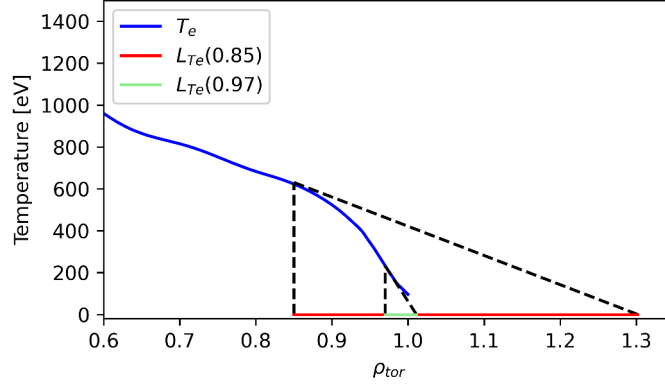


Fig. 2.3.: Illustration of the gradient scale length using a fitted electron temperature profile from a real AUG shot (#31529). Gradient scale lengths at two positions are shown.

e.g. $F = F_0 + f_1$ with the background F_0 and fluctuations f_1 . Mathematically, the assumptions are expressed in terms of small non-dimensional ordering parameters $\epsilon \ll 1$. They also make frequent use of the gradient scale length L_X as a measure for change in space or time. Fig. 2.3 shows the gradient scale length concept. It is frequently used to measure the change of profiles. Its geometric interpretation is the base of the triangle spanned by the slope $\nabla_r X$ of X at r and the height $X(r)$. It is essentially a scaled version of the gradient defined by the relation $\nabla_r X = X(r) / -L_X$. Resulting in $L_X = -X / \nabla_r X = 1 / \nabla_r \ln(X)$. The figure illustrates that a change in the gradient scale length is caused by a change in gradient and absolute value. In the following, L^r refers to spatial gradient scales and $L_X^t = \partial \ln(X) / \partial t$ to temporal gradient scales.

The gyrokinetic ordering assumptions on perturbations employed in the following are:

- Relative fluctuations of the distribution F , the electric field E and the magnetic field B are small: $f_1/F_0 \approx e\delta\phi/T_e \approx \delta B/B \approx \epsilon_\delta \ll 1$
- On the size of a gyroradius, the background magnetic field should not change too much. Mathematically: $\rho_i/L_B^r \approx \epsilon_B \ll 1$.
- During one gyroorbit, the background magnetic field should not change too much. The duration of a gyroorbit is the inverse of the gyrofrequency ω_c . Mathematically: $1/\omega_c 1/L_B^t \approx \epsilon_B^3 \ll 1$.
- On the size of a gyroradius, the background distribution F_0 should not change too much. F_0 contains information about temperature and density profiles. Therefore, this is also a condition on the temperature and density gradients. Mathematically: $\rho_i/L_F^r \approx \epsilon_F \ll 1$.
- During one gyroorbit, the background distribution F_0 should not change too

2. Mathematical framework: Gyrokinetics

much. The duration of a gyroorbit is the inverse of the gyrofrequency ω_c . Mathematically: $1/\omega_c 1/L_F^t \approx \epsilon_F^3 \ll 1$.

- During one gyroorbit, the distribution function, and the electromagnetic fields should not fluctuate too much. Mathematically: $\omega/\omega_c \approx \epsilon_\omega \ll 1$.
- Fluctuations of the distribution function and the electromagnetic fields in the perpendicular direction are on the size of the gyroradius but much larger in the parallel direction. Mathematically: $k_\perp \rho_i \approx \epsilon_\perp \approx 1$ and $k_\perp \gg k_\parallel$.

In summary, small fluctuations should be slow compared to the gyrofrequency, and background changes should be large and slow compared to the gyromotion. These assumptions define what is meant by small changes or small fluctuations in the following. This ordering is the standard ordering inspired by core turbulence and is employed for GENE. It is not unique.

2.3.3. Perturbative transforms to guiding-center and gyro-center phase space

The transformation of phase space to guiding center coordinates has enabled us to derive a Vlasov equation that is independent of the fast gyroangle θ . We want to retain this independence even for small perturbations, in the sense defined in the previous section. Two types of perturbations will be considered: Changes of the magnetic background field and fluctuations of the E and B field. For each perturbation, the Hamiltonian/Lagrangian is transformed by a near-identity Lie transform (a method from differential geometry, see e.g. Refs. [46, 47]) to a new Hamiltonian/Lagrangian that restores the independence with respect to the fast gyromotion. The first transformation dealing with changes of the magnetic background field yields the so-called guiding-center Hamiltonian. It is an expansion in the small, non-dimensional parameter ϵ_B .

$$H_{gc} = \frac{p_\parallel}{2m} + \mu B_0. \quad (2.11)$$

$$\Gamma_{gc} = \frac{1}{\epsilon_B} \frac{e}{c} \left(\mathbf{A}_0 + \epsilon_B \frac{c}{e} p_\parallel \hat{\mathbf{b}}_0 + O(\epsilon_B^2) \right) \cdot d\mathbf{X} + \epsilon_B \frac{mc}{e} \mu d\theta, \quad (2.12)$$

where $\hat{\mathbf{b}}_0 = \frac{\mathbf{B}_0}{B_0}$, e is the charge and m the mass of the particle species. Equations are adapted from Ref. [46].

The second transformation, dealing with small fluctuations of the E and B fields, yields the gyro-center Hamiltonian and Lagrangian. It is an expansion in the small, non-dimensional parameter ϵ_δ . In the following $\langle \cdot \rangle = 1/(2\pi) \int d\theta$ denotes a gyroaverage

and $\{\cdot\}$ a Poisson bracket. The gyrocenter Hamiltonian is:

$$\bar{H}_{gy} = \bar{H}_0 + \epsilon_\delta \bar{H}_1 + \epsilon_\delta^2 \bar{H}_2, \quad (2.13)$$

with

$$\bar{H}_1 = e \langle \delta\psi_{gc} \rangle = e \left\langle \delta\phi_{gc} - \frac{\mathbf{v}_\perp}{c} \cdot \delta\mathbf{A}_{\perp gc} \right\rangle - \frac{ev_\parallel}{c} (1 - \beta) \langle \delta A_{\parallel gc} \rangle, \quad (2.14)$$

$$\begin{aligned} \bar{H}_2 = & -\frac{e^2}{2\omega_0} \left\langle \left\{ \delta\tilde{\Psi}_{gc}, \delta\tilde{\psi}_{gc} \right\}_0 \right\rangle + \frac{e^2}{2mc^2} \left(\langle |\delta\mathbf{A}_{gc}|^2 \rangle \right. \\ & \left. - \beta \langle \delta A_{\parallel gc} \rangle^2 \right) + \alpha \langle \delta\mathbf{A}_{\perp gc} \rangle \cdot \frac{\hat{\mathbf{b}}_0}{B_0} \times \nabla \bar{H}_1, \end{aligned} \quad (2.15)$$

where

$$\delta\tilde{\Psi}_{gc} = \int \delta\tilde{\psi}_{gc} d\theta = \int \delta\psi_{gc} - \langle \delta\psi_{gc} \rangle d\theta, \quad (2.16)$$

and the first-order effective potential $\delta\psi_{gc}$ is defined in the equation for \bar{H}_1 . The gyrocenter Lagrangian is:

$$\Gamma_{gy} = \frac{e}{c} \left(\mathbf{A}_0 + \epsilon_\delta \delta\mathbf{A}_{gy} + \frac{c}{e} \bar{p}_\parallel \hat{\mathbf{b}}_0 \right) \cdot d\bar{\mathbf{X}} + \frac{mc}{e} \bar{\mu} d\bar{\theta}, \quad (2.17)$$

with the gyrocenter magnetic perturbation

$$\delta\mathbf{A}_{gy} = \alpha \langle \delta\mathbf{A}_{\perp gc} \rangle + \beta \langle \delta A_{\parallel gc} \rangle \hat{\mathbf{b}}_0. \quad (2.18)$$

Equations are adapted from Ref. [46]. If $\alpha = \beta = 0$ the model is called Hamiltonian (or p_\parallel) gyrocenter model; if $\alpha = \beta = 1$ the model is called symplectic (or v_\parallel) gyrocenter model. GENE uses a parallel symplectic gyrocenter model ($\alpha = 0, \beta = 1$). It is presented in the next section.

2.3.4. Gyrokinetic Vlasov equation

From the gyrocenter Hamiltonian, finally, the gyrokinetic Vlasov equation can be derived. One arrives at an equation that appears identical to the Vlasov equation Eq. 2.10 we motivated earlier. However, note that F now denotes a different distribution function: It is the distribution of gyrocenters in gyrocenter phase space instead of the unperturbed guiding-center distribution.

$$\frac{\partial F}{\partial t} + \frac{d\mathbf{X}}{dt} \cdot \nabla F + \frac{dv_\parallel}{dt} \frac{\partial F}{\partial v_\parallel} = 0, \quad (2.19)$$

2. Mathematical framework: Gyrokinetics

where the equations of motion for $\frac{d\mathbf{X}}{dt}$ and $\frac{dv_{\parallel}}{dt}$ can be calculated from the gyrocenter Lagrangian or Hamiltonian using the Euler-Lagrange or Hamilton equations, respectively. The parallel velocity and perpendicular drifts are

$$\frac{d\mathbf{X}}{dt} = v_{\parallel} \hat{\mathbf{b}}_0 + \frac{B_0}{B_{0\parallel}^*} (\mathbf{v}_{\bar{\xi}} + \mathbf{v}_{\nabla B} + \mathbf{v}_c), \quad (2.20)$$

with the effective magnetic field $B_{0\parallel}^* = \hat{\mathbf{b}} \cdot \mathbf{B}_0^* = \hat{\mathbf{b}} \nabla \times (\mathbf{A}_0 + \mathbf{B}_0 v_{\parallel} / \omega_c)$. The parallel acceleration is

$$\frac{dv_{\parallel}}{dt} = -\frac{d\mathbf{X}}{dt} \cdot \left(q \nabla \bar{\phi}_1 + \mu \nabla (B_0 + \bar{B}_{1\parallel}) \frac{1}{mv_{\parallel}} \right) - \frac{q}{mc} \frac{\partial \bar{A}_{1\parallel}}{\partial t}. \quad (2.21)$$

In these expression the modified potential

$$\bar{\chi}_1 := \bar{\phi}_1 - \frac{v_{\parallel}}{c} \bar{A}_{1\parallel} + \frac{\mu}{q} \bar{B}_{1\parallel}, \quad (2.22)$$

the generalized $E \times B$ drift

$$\mathbf{v}_{\bar{\chi}} = \frac{c}{B_0^2} \mathbf{B}_0 \times \nabla \bar{\chi}_1, \quad (2.23)$$

the ∇B drift

$$\mathbf{v}_{\nabla B_0} = \frac{\mu c}{q B_0^2} \mathbf{B}_0 \times \nabla B_0, \quad (2.24)$$

and the curvature drift

$$\mathbf{v}_c = \frac{v_{\parallel}^2}{\omega_c} (\nabla \times \hat{\mathbf{b}}_0)_{\perp} \quad (2.25)$$

were used. Equations are adapted from Ref. [48]. Overbars denote gyroaveraged fields, with the gyroaverage operator $\mathcal{G} = \frac{1}{2\pi} \int d\theta$. A crucial part of the dynamics described by this equation is the advection by the generalized $E \times B$ drift $\mathbf{v}_{\bar{\chi}}$, which enters directly the advection term $d\mathbf{X}/dt \cdot \nabla F$ and also the parallel acceleration. It is determined by the self-generated electric and magnetic potentials (see Maxwell's equations in the following subsection) and thereby introduces a nonlinear self-interaction of the plasma that is a prerequisite for the occurrence of turbulent behavior.

The δf splitting

We analyze the gyrokinetic Vlasov equation further by explicitly splitting the distribution function F into a time-independent background F_0 and a small perturbation f_1 . This is referred to as δf splitting and is used in the GENE code. We obtain:

$$\begin{aligned} & \frac{\partial(F_0 + f_1)}{\partial t} - \frac{q}{mc} \frac{\partial \bar{A}_{1\parallel}}{\partial t} \frac{\partial(F_0 + f_1)}{\partial v_{\parallel}} + \left(v_{\parallel} \hat{\mathbf{b}} + \frac{B}{B_{\parallel}^*} (\mathbf{v}_{\nabla B} + \mathbf{v}_{\chi} + \mathbf{v}_c) \right) \\ & \cdot \left(\nabla(F_0 + f_1) - \frac{1}{mv_{\parallel}} (\mu \nabla(B + \bar{B}_{1\parallel}) + q \nabla \bar{\phi}_1) \frac{\partial(F_0 + f_1)}{\partial v_{\parallel}} \right) = 0. \end{aligned} \quad (2.26)$$

We can now identify terms of different order in the expansion parameter ϵ , where we treat the different ϵ_B , ϵ_F , ϵ_{δ} to be of the same order. Due to the strong anisotropy, derivatives of fluctuating quantities with respect to perpendicular directions are assumed to be of order $1/\rho_{\text{ref}}$. In contrast, derivatives of fluctuating quantities in the parallel direction are of order $1/L_{\text{ref}}$. To put it more intuitively: Fluctuating quantities are small ($f_1 \approx O(\epsilon)$), and they also change only little along the field lines ($\partial f_1/\partial z \approx O(\epsilon)$) but perpendicular to the magnetic field they may change so strongly that $\partial f_1/\partial x \approx O(1)$. Derivatives of equilibrium quantities are assumed to be of order $1/L_{\text{ref}}$ in all directions. Furthermore, the drift velocities are in the perpendicular direction, so dot products with the drift velocities select the perpendicular components.

0th-order terms:

$$v_{\parallel} \hat{\mathbf{b}} \cdot \left(\nabla F_0 - \frac{1}{mv_{\parallel}} \mu \nabla B \frac{\partial F_0}{\partial v_{\parallel}} \right) = 0. \quad (2.27)$$

1st-order terms:

$$\begin{aligned} \frac{\partial f_1}{\partial t} &= \frac{q}{mc} \frac{\partial \bar{A}_{1\parallel}}{\partial t} \frac{\partial F_0}{\partial v_{\parallel}} \\ & - \frac{B}{B_{\parallel}^*} (\mathbf{v}_{\nabla B} + \mathbf{v}_{\chi} + \mathbf{v}_c) \cdot \left(\nabla(F_0 + f_1) - \frac{1}{mv_{\parallel}} (\mu \nabla(B + \bar{B}_{1\parallel}) + q \nabla \bar{\phi}_1) \frac{\partial F_0}{\partial v_{\parallel}} \right) \\ & + v_{\parallel} \hat{\mathbf{b}} \cdot \left(\nabla f_1 - \frac{1}{mv_{\parallel}} \left(\mu \nabla B \frac{\partial f_1}{\partial v_{\parallel}} - \nabla(q \bar{\phi}_1 + \mu \bar{B}_{1\parallel}) \frac{\partial F_0}{\partial v_{\parallel}} \right) \right). \end{aligned} \quad (2.28)$$

It has been shown that higher-order terms can be usually neglected [49]. Nonetheless, for completeness, the 2nd order terms:

$$\begin{aligned} & \frac{q}{mc} \frac{\partial \bar{A}_{1\parallel}}{\partial t} \frac{\partial f_1}{\partial v_{\parallel}} - v_{\parallel} \hat{\mathbf{b}}_0 \cdot \frac{1}{mv_{\parallel}} [\mu \nabla \bar{B}_{1\parallel} + q \nabla \bar{\phi}_1] \frac{\partial f_1}{\partial v_{\parallel}} \\ & - \frac{B}{B_{\parallel}^*} (v_{B_0} + v_{\chi} + v_c) \cdot \left(\frac{1}{mv_{\parallel}} [\mu \nabla B + \mu \nabla \bar{B}_{1\parallel} + q \nabla \bar{\phi}_1] \frac{\partial f_1}{\partial v_{\parallel}} \right) = 0. \end{aligned} \quad (2.29)$$

Only 0th- and 1st-order terms are retained in the GENE code. Note that the first-order terms contain linear terms as well as terms that contain products of derivatives

2. Mathematical framework: Gyrokinetics

of fluctuating quantities - in that sense, they are nonlinear, but still of $O(\epsilon)$, due to the perpendicular derivatives.

2.3.5. Gyrokinetic Maxwell equations

We have so far neglected the implications of the phase space transformations for the Maxwell equations. However, they must be appropriately transformed as well, such that they are defined on the same phase space as the Vlasov equation and can close the Vlasov-Maxwell system using the moments of the correct phase space distribution.

Moments calculation

In general, the a-th moment in v_{\parallel} and b-th moment in v_{\perp} is defined as follows:

$$M_{ab}(x) = \int f_{pc}(\mathbf{x}, \mathbf{v}) v_{\parallel}^a v_{\perp}^b d^3v \quad (2.30)$$

This definition uses the particle distribution function f_{pc} . However, since we simulate the evolution of the gyrocenter distribution, we need to express the moments in terms of the gyrocenter distribution. The necessary transform from gyrocenter phase space to particle phase space is done by the so-called pull-back operator (a term from differential geometry) T^* . The inverse transformation (from particle to gyrocenter phase space) is done by the push-forward operator T . The pull-back operator is defined in terms of generating functions G_1 , the details of which can be found e.g. in Ref. [50]:

$$T^* f_1 = f_1 + G_1^X \cdot \nabla F_0 + G_1^{v_{\parallel}} \frac{\partial F_0}{\partial v_{\parallel}} + G_1^{\mu} \frac{\partial F_0}{\partial \mu} \quad (2.31)$$

Under the assumption of a local Maxwellian background distribution and in the limit of small ϵ_B , it takes the form

$$T^* f_1 = f_1 - \left(q\tilde{\phi}_1 - \mu\bar{B}_{1\parallel} \right) \frac{F_0}{T_0} \quad (2.32)$$

The definition of moments becomes

$$M_{ab}(x) = \frac{1}{m} \int \delta(\mathbf{X} - \mathbf{x} + \rho) T^* f_{gy,1}(\mathbf{X}, v_{\parallel}, \mu) B_{\parallel}^* v_{\parallel}^a v_{\perp}^b d^3X dv_{\parallel} d\mu d\theta \quad (2.33)$$

where $f_{gy,1}$ is the gyrocenter distribution function. Based on this relation for the moments, the field equations for the electric and magnetic potential can be formulated.

Poisson equation for electric potential

The Poisson equation for the electric potential becomes

$$-\nabla^2\phi = 4\pi\rho = 4\pi\sum_s q_s n_{1s}(\mathbf{x}) = 4\pi\sum_s q_s M_{00,s}(\mathbf{x}) \quad (2.34)$$

where the sum is over species s .

Two notable natural limits exist for the relation between the electric potential and the particle densities, which allow one to simplify either the electron or ion dynamics. In the limit of small electron mass $m_e/m_i \rightarrow 0$, electrons have vanishing gyroradius and an instantaneous reaction to electrostatic potential fluctuations. The electron distribution function is not evolved in time, and the Poisson equation for the electrons simplifies to a modified Boltzmann relation:

$$\frac{e(\phi_1 - \langle\phi_1\rangle_{FS})}{T_{0e}} = \frac{n_{1e}}{n_{0e}} \quad (2.35)$$

where $\langle\cdot\rangle_{FS}$ denotes a flux surface average. This limit is referred to as adiabatic electrons.

In the limit of short-wavelength fluctuations, gyroaverages over the ion gyroradius vanish. The Poisson equation for the ions simplifies to the Boltzmann relation:

$$-\frac{q_i\phi_1}{T_{0i}} = \frac{n_{1i}}{n_{0i}} \quad (2.36)$$

This limit is referred to as adiabatic ions.

Ampère's law for magnetic potential

Ampère's law can be written as

$$\nabla \times \mathbf{B} = \nabla \times (\nabla \times \mathbf{A}) = -\nabla^2 \mathbf{A} = \frac{4\pi}{c} \mathbf{j} \quad (2.37)$$

where we have used the Coulomb gauge $\nabla \cdot \mathbf{A} = 0$ and have neglected the presence of an equilibrium E field. To formulate field equations, the magnetic vector potential is decomposed into parallel and perpendicular components. The field equation for the parallel component of the vector potential, which expresses fluctuations perpendicular to the magnetic field, is:

$$-\nabla_{\perp}^2 \bar{A}_{1\parallel} = \frac{4\pi}{c} j_{1\parallel} = \frac{4\pi}{c} \sum_s q_s M_{10,s}(\mathbf{x}) \quad (2.38)$$

2. Mathematical framework: Gyrokinetics

The field equation for the perpendicular components of the vector potential, which expresses compressional magnetic fluctuations (B_{\parallel}) along the magnetic field lines, is:

$$(\nabla \times \mathbf{B}_1)_{\perp} = \frac{4\pi}{c} j_{1\perp} = \frac{4\pi}{c} \sum_s q_s M_{01,s}(\mathbf{x}) \quad (2.39)$$

As in most gyrokinetic codes, B_{\parallel} fluctuations are, at the moment, only implemented for local simulations in GENE.

2.3.6. Collisions

So far, our plasma model contains the interaction of charged particles via self-generated electromagnetic fields. This is, however, only part of the full dynamics. There are also direct interactions between two or more particles in the form of collisions. This requires an extension of the collisionless Vlasov equation to a Boltzmann-type equation that includes some kind of collision operator C .

$$\frac{\partial F}{\partial t} + \frac{d\mathbf{X}}{dt} \cdot \nabla F + \frac{dv_{\parallel}}{dt} \frac{\partial F}{\partial v_{\parallel}} = C(F) \quad (2.40)$$

The collisions provide dissipation and can have an important influence on the stability of modes. In general, collision frequencies in a hot plasma are low, but in particular, in tokamak edge plasma, where temperatures decrease, the influence of collisions becomes increasingly important. This can, for example, affect trapped particle modes that are stabilized by the de-trapping of particles due to collisions. Throughout this thesis, I will also refer to the equation with collisions as Vlasov equation.

2.3.7. Validity of gyrokinetics in the pedestal

Gyrokinetics has mainly been built on assumptions derived from experimental measurements of tokamak core turbulence. The validity of gyrokinetics in the pedestal is, therefore, a topic of active research.

One important aspect of the gyrokinetic assumptions is the gyroradius size compared to changes of the background distribution F_0 , which should be small: $\rho_i/L_F \ll 1$. Fig. 2.4 shows this ratio for temperature and density profiles of an AUG pedestal. Over large regions $\rho/L < 0.05$, but in the steepest gradient region, it peaks at around 0.15. This shows that for ion scale turbulence, the limits of gyrokinetics are being tested locally in the pedestal, and it is, to some extent, a matter of debate how well the assumptions

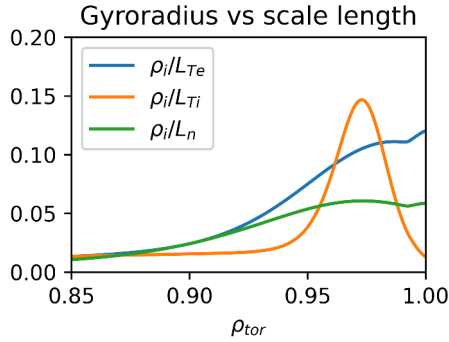


Fig. 2.4.: Ratio of ion gyroradius and temperature/density scale lengths in the pedestal of an ASDEX Upgrade shot (#31529).

still hold. Electron scale dynamics satisfies the limits more easily since the electron gyroradius is a factor $m_e/m_D \approx 1/60$ smaller than the ion gyroradius.

A further gyrokinetic assumption that may be compromised in the pedestal concerns the relative fluctuation amplitudes. In particular, close to the scrape-off layer, large fluctuation amplitudes are being experimentally observed [51–53]. This is discussed in some more detail in the context of δ - f and full- f models in Sec. 3.4.

These gyrokinetic limitations motivate the study of kinetic and hybrid kinetic-gyrokinetic modes. In recent studies, kinetic corrections to ITG modes and the excitation of Ion Bernstein waves have been investigated [54]. So far, these kinetic studies are restricted to electrostatic simulations in slab geometry. It is, therefore, difficult to assess what the role of these additional physics effects might be in real pedestal conditions, where magnetic fluctuations and curvature are an essential part of the dynamics.

Since gyrokinetics is derived perturbatively, it is clear that not all aspects of kinetic dynamics are captured and that kinetic simulations may modify the results of gyrokinetic simulations. The crucial question will be whether, in the full system, these modifications are on the level of higher-order corrections or whether e.g. they introduce additional relevant transport mechanisms. So far, no indications for the latter have been reported. In light of the success of gyrokinetics in many tokamak conditions and the above discussion, the approach for this thesis is to assume that gyrokinetics is able to capture the vast majority of microturbulence in the pedestal.

2.4. Summary

This chapter has presented the mathematical equations used to describe plasma dynamics in this thesis. The derivation of gyrokinetics has been outlined, and the gyrokinetic

2. Mathematical framework: Gyrokinetics

Vlasov-Maxwell system has been shown. Finally, possible limitations of gyrokinetics in the pedestal were discussed. The next chapter will discuss the implementation of these equations in the GENE code. Emphasis is put on an electromagnetic upgrade and the challenges of applying GENE under pedestal conditions.

Recommended further literature

- Good introduction: Krommes, J. A. The Gyrokinetic Description of Microturbulence in Magnetized Plasmas. *Annual Review of Fluid Mechanics* **44**, 175–201. doi:10.1146/annurev-fluid-120710-101223 (2012)
- The review paper: Brizard, A. J. & Hahm, T. S. Foundations of Nonlinear Gyrokinetic Theory. *Reviews of Modern Physics* **79**, 421–468. doi:10.1103/RevModPhys.79.421 (2007)
- From a GENE perspective: Goerler, T. *Multiscale Effects in Plasma Microturbulence* (Universität Ulm, Ulm, 2009) or Told, D. *Gyrokinetic Microturbulence in Transport Barriers* PhD thesis (Universität Ulm, Ulm, 2012) or another PhD thesis. They are all available on www.genecode.org.
- The derivation of gyrokinetics is heavily based on Hamiltonian and Lagrangian mechanics as well as differential geometry. Any textbook on these topics can be helpful. As a concise reminder, e.g. Stone, M. & Goldbart, P. *Mathematics for Physics: A Guided Tour for Graduate Students* doi:10.1017/CB09780511627040 (Cambridge University Press, Cambridge, 2009).

3. Numerical implementation: The GENE code

This chapter introduces the code used for all simulations presented in this thesis: GENE, the Gyrokinetic Electromagnetic Numerical Experiment. The chapter begins with a brief overview of GENE and its capabilities. The central part of this chapter is an upgrade to the global, nonlinear, electromagnetic version of GENE, which has been implemented within this thesis based on the proof-of-principle in [56]. Furthermore, the bounds of applicability of GENE in the pedestal are highlighted. Linear, global growth rates in the MHD limit are discussed, and the role of hyperdiffusion is critically examined.

3.1. Overview

GENE is an efficient and versatile code for the simulation of plasma microturbulence and analysis of gyrokinetic instabilities. It has a development history of more than 20 years [57], has been advanced in more than 15 PhD projects, comprises about 200,000 lines of code, and is used at a large number of research institutions worldwide. GENE regularly runs on many of the largest supercomputers and is currently being ported to GPUs to exploit the latest exascale HPC systems [58]. Together with a few other codes like (C)GYRO, XGC, GTC, GKW, GEM, GYSELA, or ORB5, it is considered to be one of the leading plasma microturbulence codes in the world.

Most parts of the code are written in object-oriented Fortran 2008, with extensive diagnostic tools for post-processing written in IDL and Python. Development is coordinated in a git repository, and CI/CD (continuous integration/continuous delivery) practices are employed. For example, about 20 automated regression tests have to be passed by each new pull request before it is merged into the master branch of the development version. The extended development team comprises PhD students, postdocs, and permanent staff at several different research institutes, with the core development team based at IPP Garching. An official release version of the GENE code is freely available upon request. Two other variants of the GENE code exist, which are not further discussed or used within this thesis but mentioned for completeness: GENE-3D [59, 60], the stellarator version of the GENE code, which is designed for non-axisymmetric (3D) magnetic field geometries and GENE-X [61, 62], which is

3. Numerical implementation: The GENE code

designed for studies of edge turbulence, including the scrape-off layer. Both are under active development, and their most recent advances are documented in PhD theses by Felix Wilms (GENE-3D) and Philipp Uibl (GENE-X).

GENE provides many options for the numerical calculation of the time evolution of the gyrokinetic Vlasov-Maxwell system introduced in the previous chapter. GENE assumes δf splitting of the distribution function into an equilibrium and a fluctuating part. Local Maxwellian and non-Maxwellian background distributions [63] can be used. The algorithms are grid-based (Eulerian), in contrast to particle-based (Lagrangian) Particle-In-Cell (PIC)-codes. GENE can solve the linearized and the full nonlinear system of equations for an arbitrary number of plasma species. Linear simulations can be performed as initial value simulations to identify the fastest-growing instabilities and by an eigenvalue solver that solves for subdominant modes as well. Simulations can be performed in radially local flux-tube geometry as well as in global simulation domains [64]. In local simulations, background plasma densities and temperatures and their gradients are radially constant across the simulation domain, whereas in global simulations, they change. Simulations can be performed with fluctuations of only the electric potential (electrostatic) and also with magnetic fluctuations (electromagnetic). Also, neoclassic simulations can be conducted. Not all combinations of local/global, linear/nonlinear, and electrostatic/electromagnetic can be used. In local flux-tube geometry, all other combinations are possible. In global simulations, however, electromagnetic fluctuations are more difficult. In this thesis, an upgrade for perpendicular magnetic fluctuations ($\bar{A}_{1\parallel}$) in global, nonlinear simulations is presented. The implementation of parallel, compressional magnetic fluctuations ($\bar{B}_{1\parallel}$) in global simulations is currently under development. Multiple collision operators are available, ranging from pitch-angle approximations to Sugama [56] and exact Landau-Boltzmann collision operators [65]. Multiple magnetic geometries are available, including interfaces to g-eqdk (efit) for experimental geometries [50].

3.2. Coordinates & Numerics

3.2.1. Field aligned coordinates

The coordinates for the velocity space have been introduced in the previous chapter: v_{\parallel} and μ . The real space coordinates remain to be fixed. To make use of the structure of the plasma dynamics imposed by the background magnetic field, the real space coordinates are chosen to be aligned with magnetic field lines. This is an efficient use for the closed field line region but has a strong limitation for the simulation of the edge

region of the plasma: At the separatrix and X-point, the field-aligned coordinates are ill-defined, excluding this physically important part of the plasma from the simulation. This drawback is addressed in the GENE-X code, which is based on the FCI (Flux-Coordinate Independent) approach [66, 67]. In GENE, however, the simulation domain remains restricted to the closed field line region.

The GENE coordinates are based on straight-field-line coordinates, with a radial coordinate ρ that labels flux-surfaces, a modified poloidal angle (straight field-line angle) θ and the unmodified toroidal angle ϕ . GENE uses the COCOS coordinate convention index 12 [68]. The GENE coordinates are defined as:

$$x = \rho \quad (3.1)$$

$$y = C_y[\sigma_{I_p}q(\rho)\theta - \phi] \quad (3.2)$$

$$z = \theta \quad (3.3)$$

where x is the radial coordinate, y the binormal coordinate or field-line label, z the parallel coordinate. In the definition of y appear σ_{I_p} , the sign of the plasma current, and C_y . For most geometry interfaces $C_y = \frac{\rho_0}{q_0}\sigma_{B_t}$, where σ_{B_t} is the sign of the toroidal magnetic field. The specific choice for the flux-surface label ρ depends on the geometry interface used. In GENE typically the normalized toroidal magnetic flux $\rho_{\text{tor}} = \sqrt{(\Psi_{\text{tor}} - \Psi_{\text{tor}}(\text{axis})) / (\Psi_{\text{tor}}(\text{separatrix}) - \Psi_{\text{tor}}(\text{axis}))}$ is used, with the toroidal magnetic flux Ψ_{tor} . The safety factor $q = d\Psi_{\text{tor}}/d\Psi_{\text{pol}} = d\phi/d\theta \approx$ toroidal turns/poloidal turns is the magnetic field line pitch or angle. Note that the field line pitch, in general, changes from flux-surface to flux-surface, making the safety factor a function of the radial coordinate and giving rise to the definition of the magnetic shear $\hat{s} = x_0/q_0 dq/dx$. Subscripts 0 refer to the value at the reference position.

These coordinates are based on a representation of the background magnetic field as $B_0 = C\nabla x \times \nabla y$. The corresponding Jacobian is $J^{-1} = (\nabla x \times \nabla y) \cdot \nabla z = \frac{B_0 \cdot \nabla z}{C}$.

Note that the coordinates x, y, z do not form a cartesian but a curvilinear, non-orthogonal coordinate system. This often renders interpretations of projections and coordinates unintuitive since a direct identification of poloidal and toroidal directions in the torus with the chosen coordinates is not possible. Fig. 3.1 illustrated the windedness of a field line taken from the edge region of an ASDEX Upgrade discharge. Additionally, the mapping is a function of the field line pitch, which, in general, is different for each flux surface. The standard reference for field-aligned coordinates is D'haeseleer, W. D., Hitchon, W. N. G., Callen, J. D. & Shohet, J. L. *Flux Coordinates and Magnetic Field Structure: A Guide to a Fundamental Tool of Plasma Theory*

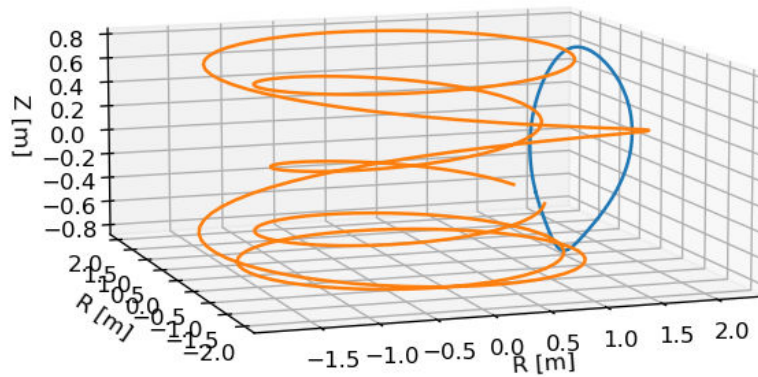


Fig. 3.1.: One poloidal turn of a field line (coordinate line of z) in orange and the corresponding contour of a poloidal cross-section ($x = \text{const.}$) in the edge of an ASDEX Upgrade H-mode shot.

(Springer Berlin Heidelberg, Berlin, Heidelberg, 1991).

3.2.2. Velocity space grid

The velocity grid for each species is typically set up as follows: The parallel velocity v_{\parallel} is discretized with 32 equidistant grid points in the domain $[-3\sqrt{2T_0/m}, 3\sqrt{2T_0/m}]$. The magnetic moment μ is discretized with 16 grid points distributed following Gauss-Laguerre in the domain $[0, 9T_0/B_{ref}]$. Box sizes and resolutions can be adapted for each case. A difficulty arises in global simulations when the background temperatures strongly change radially within the simulation domain. One has the option to either use conventional velocity space resolutions, which then strongly under-resolve the velocity space of the low-temperature region, or to use much higher resolutions, which would not be necessary in the high-temperature region and cause a strongly increased computational cost. In particular, in the edge pedestal region, where temperatures may drop by a factor of ten from core to scrape-off layer temperatures in a few cm, this challenge arises. A solution to this problem is to set up the velocity space non-uniformly, i.e. differently in the low and high-temperature regions. One approach to achieve this is a block-structured grid, where the number of velocity space grid points is equal in each block, but the maximum and minimum values are modified in the different regions/blocks, effectively adapting the resolution. This solution has been implemented within the PhD thesis of Denis Jarema [70, 71] and is illustrated in Fig. 3.2. In particular, the handling of gyroaverages across block boundaries is non-trivial.

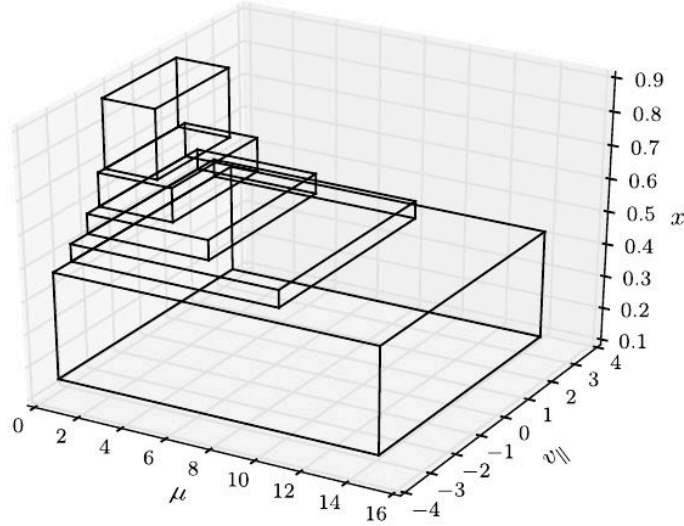


Fig. 3.2.: Illustration of block-structured velocity grids. Reprinted from [71] with permission from Elsevier.

3.2.3. Boundary conditions

Radial direction

In local simulations, the radial boundary condition is periodic. This is possible because, in local simulations, the background profiles of temperature and density are radially constant. The radial coordinate is represented in Fourier space with $k_x = jk_{x,min} = j\frac{2\pi}{L_x}$, utilizing the periodic boundary.

In global simulations, the radial boundary condition typically is a Dirichlet condition, i.e. the perturbed distribution function is assumed to be zero outside the simulation domain. To smooth the transition to the Dirichlet condition, Krook-buffer zones are used, covering a few percent of the radial domain, which dampen the fluctuations and/or drive close to the boundary. Their specific shape and width can be adjusted for each simulation. The finite width of the buffer zones, in combination with the field-aligned coordinates, imposes a limitation on how close to the separatrix global GENE simulations can yield physical results. In global simulations, the radial coordinate is represented in real space.

Binormal direction

In the binormal direction, periodicity is imposed based on the toroidal symmetry.

$$f(x, y, z) = f(x, y - L_y, z) \quad (3.4)$$

3. Numerical implementation: The GENE code

with $L_y = \frac{2\pi C_y}{n_0}$, where n_0 is the lowest toroidal wave number. The binormal direction is represented in Fourier space, with

$$k_y = j k_{y,min} = j \frac{2\pi}{L_y}. \quad (3.5)$$

Parallel direction

The parallel boundary condition is the most delicate one. Due to the appearance of the straight field line angle θ in both the y and z coordinates, they get coupled. The boundary condition for the global code is:

$$f(x, k_y, z) = f(x, k_y, z + 2\pi) e^{i2\pi j n_0 q(x)}. \quad (3.6)$$

In local simulations, additionally, consistency with the radial boundary condition has to be achieved. The consequence is a coupling of binormal and radial wavenumber. The parallel boundary condition in the local code is:

$$f(k_x, k_y, z) = f(k_x + 2\pi \hat{s} k_y, k_y, z + 2\pi) e^{i2\pi k_y \hat{s} r_0} \quad (3.7)$$

This imposes a condition on the box sizes $N = 2\pi \hat{s} L_x / L_y$, where N has to be an integer.

3.2.4. Background distribution

The standard choice for the background distribution function of each species in GENE is a local Maxwellian. This means each flux surface has a Maxwellian background adapted to the background temperature and density of the species on the flux surface. It is defined as:

$$F_0(x, v_{\parallel}, \mu) = \frac{n_0(x)}{\pi^{3/2} v_T^3(x)} e^{-\frac{mv_{\parallel}^2/2 + \mu B_0(x)}{T_0(x)}} \quad (3.8)$$

with $v_T = \sqrt{2T_0/m}$. Alternative choices for the background distribution can be found in Ref. [63].

3.2.5. Sheared equilibrium flows

As introduced in previous chapters, the presence of an electric field causes an $E \times B$ drift $v_E = E \times B / B^2$. For E fields caused by the self-generated fluctuating electric potential, these drifts are self-consistently included within the gyrokinetic GENE simulation. The

effect of equilibrium background E-fields, however, has to be modeled explicitly. In the pedestal, a radial electric field E_r is considered to be of particular importance for the regulation of turbulence. The exact physical mechanism for creating E_r is a topic of ongoing research, but it is established that neoclassic and turbulent effects contribute to it. GENE is a gradient-driven, δf code, and neoclassic terms are often not included in standard GENE simulations. The impact of the neoclassic terms has been studied in Ref. [72, 73]. Therefore, the influence of the v_{E_r} has to be explicitly modeled to be included in the simulations. An essential property of the radial electric field is that it changes radially, and hence, the v_{E_r} introduces a shear to the plasma.

The effect of sheared equilibrium flows is modeled as follows in GENE simulations. Different implementations for radially constant shearing rates exist for the local and global code versions. They are based on the Hammet $E \times B$ shear model and documented in [50] and updated in [74]. Here, I focus on the implementation of a radially changing shearing rate in global simulations, as this has been primarily used in the simulations performed for this thesis.

Let us assume a purely toroidal rotation with an angular toroidal velocity $\Omega_\phi = \dot{\phi}$. Based on the definition of GENE's coordinates, this corresponds to a velocity in the binormal direction $y = C_y[q(\rho)\theta - \phi]$:

$$\dot{y} = -C_y\Omega_\phi \quad (3.9)$$

This background velocity is included as an additional term in the Vlasov equation:

$$\frac{\partial f}{\partial t} = -\dot{y}\frac{\partial f}{\partial y} + \dots \quad (3.10)$$

and an implicit solution is constructed using a Fourier Ansatz. One finds that any distribution function of the form

$$f = Ae^{-iC_y\Omega_\phi k_y t} \quad (3.11)$$

solves this additional part of the Vlasov equation, where A is an arbitrary prefactor. Hence, in GENE, the appropriately normalized exponent $-iC_y\Omega_\phi k_y t$ is calculated from an input profile of Ω_ϕ , and the distribution function is multiplied by the exponential. The current implementation is restricted to a purely toroidal rotation and does not include the effect of the velocity shear on the background distribution F_0 itself. Thereby, the so-called parallel flow shear instability [50] is not included in the global code unless a shifted Maxwellian is currently being implemented in [T. Jitsuk et al., to be

submitted].

3.2.6. Collision operator

Several collision operators are implemented in GENE. For the simulations shown in this thesis, a linearized Landau-Boltzmann collision operator ("landau" in GENE terminology) has been the standard choice. It models binary (two-particle) collisions and has the form

$$C(F_i, F_j) = \nabla_v \cdot (D \cdot \nabla_v - R)F_j \quad (3.12)$$

for collisions of species i with species j where D is a diffusion tensor and R a friction coefficient, see [75]. Besides the linearized Landau-Boltzmann collision operator, these collision operators are available (listed in increasing order of fidelity): Pitch angle, Landau-Boltzmann [75], Sugama, which satisfies conservation properties [56], and an exact linearized Landau operator, including full finite Larmor radius (FLR) effects [65].

3.2.7. Sources and sinks

In global simulations, artificial sources and sinks for energy and particles are necessary to keep temperature and density profiles constant on average. This avoids a flattening of gradients and eventual violation of the δf approach by too strong profile variations. They are implemented by Krook-type operators and defined in [64]. These Krook-type source and sink terms are distinct from the Krook-buffer zones used at the boundaries of global simulations mentioned previously.

3.2.8. Numerical schemes

The overall discretization scheme used by GENE is the method of lines. All space and velocity derivatives and integrations are discretized first before a time-stepping scheme integrates the resulting ordinary differential equation. The time integration is typically done with a fourth-order Runge-Kutta method. Differentiation for directions with a Fourier representation is a simple product. Derivatives of directions in real space are implemented via fourth-order centered finite differences. Higher-order derivatives are available. The parallel space and velocity derivatives are implemented with a second-order Arakawa scheme [76]. The nonlinearity in the local code version is calculated by differentiation in Fourier space and multiplication in real space. Thanks to FFT algorithms, the Fourier transformation is computationally cheaper than evaluating the product by a convolution in Fourier space. In the global code version, an

Arakawa scheme [76] is used to discretize the nonlinearity. The gyroaverage operator is implemented by a finite element method. Velocity space integration is implemented via Gaussian quadrature.

A variety of averages like heat flux and fields are evaluated at regular timestep intervals and written out as diagnostics for analysis of the simulation. The full distribution function is usually only written out to checkpoints for the continuation of the simulation. This drastically reduces the disk storage required, which still can easily reach tens to hundreds of GB per Simulation.

GENE is heavily MPI parallelized and runs routinely on several hundred compute nodes comprising, in total, several thousand CPUs. A GPU-version of GENE based on the purpose-built library GTENSOR is also in development and has already demonstrated good utilization of GPUs [58].

3.2.9. Verification and Validation

The aim of performing simulations is generally to gain insights into the properties and dynamics of a (physical) system. Two questions have to be confirmed to be able to make statements about the physical system based on the simulation output: 1) Are we solving the equations correctly? and 2) Are we solving the correct equations? The first question can be answered by *verification*, i.e. by assuring that the numerical implementation actually solves the analytical equations we want to solve. Verification can be done by numerical tests, like e.g. code benchmarks, regression tests, comparisons with analytic results in simplified setups, or the method of manufactured solutions. The second question can be answered by *validation*, i.e. by confirming that the equations we are solving are actually describing the system we are interested in. Validation can be done by a detailed comparison of simulation results to experimental measurements.

For core turbulence simulations, GENE has been extensively tested and validated against other gyrokinetic codes and experimental results. See for example Refs. [64, 77–79]. For pedestal scenarios, the validation of gyrokinetic codes is a topic of active research. This thesis contributes to this topic by a detailed heat flux comparison in this challenging environment and enables a more comprehensive validation of GENE in future studies.

3.3. Electromagnetic upgrade

This section presents an upgrade to the global electromagnetic code version. It addresses a challenge with global, nonlinear, electromagnetic GENE simulations, which tended to be numerically unstable. Previously, the only viable option was to reduce the strength of magnetic fluctuations by artificially reducing the plasma beta used in the simulation. With the new upgrade, this is no longer necessary, and global, nonlinear, electromagnetic GENE simulations at experimental β values have been observed to be stable. This enables more realistic turbulence simulations of various tokamak plasma scenarios, particularly of the edge pedestal. It has also already been successfully employed for studying electromagnetic modes in the core [80].

First, I present how magnetic fluctuations used to be treated in the GENE code by introducing a modified distribution function. Then, the influence of possibly relevant analytical differences on higher-order terms is investigated. This investigation finds that analytical differences are not responsible for the observed instability of electromagnetic fluctuations. Then, the solution for the instabilities, involving a change of the main distribution function, which leads to an additional field equation and an additional nonlinear term, is presented. It is based on previous work by [81], and a proof-of-principle implemented in [56]. Finally, a few technical explanations are provided on the code changes that the new implementation involves. The solution has now been implemented in the refactored, object-oriented version of the GENE code and is compatible with most of its functionalities, in particular the use of block-structured velocity grids. This renders global, nonlinear, electromagnetic turbulence simulations of the pedestal stable and computationally feasible.

Parts of this section have been published in Leppin, L., Görler, T., Cavedon, M., Dunne, M., Wolfrum, E., Jenko, F. & Team, A. U. Complex Structure of Turbulence across the ASDEX Upgrade Pedestal. *Journal of Plasma Physics* **Accepted** (2023).

3.3.1. Vlasov equation in GENE

Section 2.3.4 has shown the gyrokinetic Vlasov equation in a general form. As it is presented there, it is not yet ready for a numerical implementation. Several steps have to be taken first, for which different choices are possible and that may differ from code to code. The first step was already shown: A δf splitting of the distribution function. Furthermore, a coordinate system for the real space part of the phase space has to be chosen. As discussed earlier (see Sec. 3.2.1), in GENE, a field-aligned coordinate system is used. Next, the background distribution F_0 has to be chosen. In GENE, it

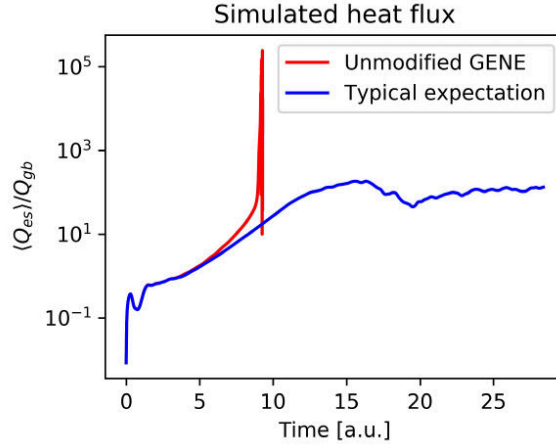


Fig. 3.3.: Electrostatic heat flux of a global, nonlinear, electromagnetic simulations with unmodified GENE compared to a saturating heat flux as it would be expected in a stable simulation.

is typically a local Maxwellian. Finally, all quantities should be normalized to obtain dimensionless quantities of similar magnitude for the numerical algorithms. In GENE notation, reference temperature, mass, and length are, for example, denoted by T_{ref} , m_{ref} , L_{ref} , and the non-dimensional quantities by a $\hat{\cdot}$ such that e.g. $m_i = \hat{m}_i m_{\text{ref}}$. All the steps mentioned here can be found in detail in Ref. [48]. One obtains the following GENE Vlasov equation (cf. Eq. (2.60) in Ref. [48]):

$$\begin{aligned}
 \frac{\partial \hat{g}_{1\sigma}}{\partial \hat{t}} = & -\frac{1}{\hat{\mathcal{C}}} \frac{\hat{B}_0}{\hat{B}_{0\parallel}^*} \left[\hat{\omega}_{n\sigma} + \hat{\omega}_{T\sigma} \left(\frac{\hat{v}_{\parallel}^2 + \hat{\mu} \hat{B}_0}{\hat{T}_{p\sigma}} - \frac{3}{2} \right) \right] \hat{F}_{0\sigma} \partial_{\hat{y}} \hat{\chi}_1 \\
 & - \frac{\hat{B}_0}{\hat{B}_{0\parallel}^*} \frac{\hat{T}_{0\sigma}(x_0)}{\hat{q}_{\sigma}} \frac{\hat{\mu} \hat{B}_0 + 2\hat{v}_{\parallel}^2}{\hat{B}_0} \hat{K}_x \hat{\Gamma}_{\sigma,x} \\
 & - \frac{\hat{B}_0}{\hat{B}_{0\parallel}^*} \left[\frac{\hat{T}_{0\sigma}(x_0)}{\hat{q}_{\sigma}} \frac{\hat{\mu} \hat{B}_0 + 2\hat{v}_{\parallel}^2}{\hat{B}_0} \hat{K}_y - \frac{\hat{T}_{0\sigma}(x_0)}{\hat{q}_{\sigma} \hat{B}_0} \frac{\hat{v}_{\parallel}^2}{\hat{\mathcal{C}}} \beta_{\text{ref}} \frac{\hat{p}_0}{\hat{B}_0} \hat{\omega}_{p\sigma} \right] \hat{\Gamma}_{\sigma,y} \\
 & - \frac{\hat{B}_0}{\hat{B}_{0\parallel}^*} \frac{1}{\hat{\mathcal{C}}} \left(\partial_{\hat{x}} \hat{\chi}_1 \hat{\Gamma}_{\sigma,y} - \partial_{\hat{y}} \hat{\chi}_1 \hat{\Gamma}_{\sigma,x} \right) \\
 & - \hat{v}_{T\sigma}(x_0) \frac{\hat{\mathcal{C}}}{\hat{J} \hat{B}_0} \hat{v}_{\parallel} \hat{\Gamma}_{\sigma,z} + \frac{\hat{v}_{T\sigma}(x_0)}{2} \frac{\hat{\mathcal{C}}}{\hat{J} \hat{B}_0} \hat{\mu} \partial_z \hat{B}_0 \frac{\partial \hat{F}_{1\sigma}}{\partial \hat{v}_{\parallel}} \\
 & + \frac{\hat{B}_0}{\hat{B}_{0\parallel}^*} \frac{\hat{T}_{0\sigma}(x_0)}{\hat{q}_{\sigma}} \frac{\hat{\mu} \hat{B}_0 + 2\hat{v}_{\parallel}^2}{\hat{B}_0} \hat{K}_x \left[\hat{\omega}_{n\sigma} + \hat{\omega}_{T\sigma} \left(\frac{\hat{v}_{\parallel}^2 + \hat{\mu} \hat{B}_0}{\hat{T}_{p\sigma}} - \frac{3}{2} \right) \right] \hat{F}_{0\sigma}
 \end{aligned} \tag{3.13}$$

where the $\hat{\omega}_{X\sigma}$ denote inverse background gradient scale lengths and \hat{K}_x , \hat{K}_y , $\hat{\mathcal{C}}$, \hat{J} are

3. Numerical implementation: The GENE code

geometry related constants. As an example, the density gradient scale length:

$$\hat{\omega}_{n\sigma} = \frac{1}{L_n} = -\frac{L_{\text{ref}}}{n_{0\sigma}(x)} \frac{\partial n_{0\sigma}(x)}{\partial x}. \quad (3.14)$$

The subscript σ is a species index. The effective magnetic field $\hat{B}_{0\parallel}^*$ is defined as

$$\hat{B}_{0\parallel}^* = \hat{\mathbf{b}} \cdot \hat{\mathbf{B}}_0^* = \hat{\mathbf{b}} \cdot \nabla \times \mathbf{A}_0^* = \hat{\mathbf{b}} \cdot \nabla \times (\mathbf{A}_0 + \mathbf{B}_0 v_{\parallel} / \omega_c) \quad (3.15)$$

and the abbreviation Γ has been introduced:

$$\Gamma_i = \frac{\partial g_1}{\partial x_i} - \frac{q}{m v_{\parallel}} \frac{\partial F_0}{\partial v_{\parallel}} \frac{\partial \bar{\chi}_1}{\partial x_i}. \quad (3.16)$$

In the above equations, the modified potential

$$\bar{\chi}_1 := \bar{\phi}_1 - \frac{v_{\parallel}}{c} \bar{A}_{1\parallel} + \frac{\mu}{q} \bar{B}_{1\parallel} \quad (3.17)$$

has been used. In Ref. [48], the modified potential is denoted by the Greek letter ξ . It denotes the same quantity. $\chi = \xi$.

Note that the GENE Vlasov equation does not contain the distribution function f_1 . It has been replaced by the new redefined distribution function

$$g_1 = f_{1\sigma} - \frac{q_{\sigma}}{m_{\sigma} c} \bar{A}_{1\parallel} \frac{\partial F_{0\sigma}}{\partial v_{\parallel}}. \quad (3.18)$$

The motivation for the redefinition is the time derivative of the gyroaveraged parallel magnetic vector potential $\bar{A}_{1\parallel}$, which appears as part of the parallel acceleration in Eq. 2.21 and is a 1st-order term, see Eq. 2.28. It is the only remaining time derivative in the Vlasov equation, except for the partial time derivative of the distribution function itself. For the use of an explicit time scheme, the time derivatives must not appear on both sides of the equation. Hence, the usual ansatz of GENE has been to combine all terms with a time derivative into the new distribution function g . This implementation works well in many cases but tends to be unstable in global, nonlinear, electromagnetic simulations.

3.3.2. Role of higher-order terms

Before the working solution is presented, it is worthwhile to investigate whether analytical differences caused by the use of the modified distribution function g and associated

approximations are the cause for the numerical instabilities. From a computational standpoint, this would be preferable: Fixing the analytical differences might be computationally less expensive and would require fewer code changes.

For this purpose, the 1st-order terms identified in Eq. 2.28 are analyzed and sorted by the power of fluctuating quantities.

The terms that are independent of fluctuating quantities:

$$0 = \frac{B}{B_{\parallel}^*} (\mathbf{v}_{\nabla B} + \mathbf{v}_c) \cdot \left(\nabla F_0 - \frac{1}{mv_{\parallel}} (\mu \nabla B) \frac{\partial F_0}{\partial v_{\parallel}} \right). \quad (3.19)$$

The terms that are linear in the fluctuating quantities:

$$\begin{aligned} \underbrace{\frac{\partial f_1}{\partial t} - \frac{q}{mc} \frac{\partial \bar{A}_{1\parallel}}{\partial t} \frac{\partial F_0}{\partial v_{\parallel}}}_{\partial g_1 / \partial t} &= - \frac{B}{B_{\parallel}^*} (\mathbf{v}_{\nabla B} + \mathbf{v}_c) \cdot \left(\nabla f_1 - \frac{1}{mv_{\parallel}} (\mu \nabla \bar{B}_{1\parallel} + q \nabla \bar{\phi}_1) \frac{\partial F_0}{\partial v_{\parallel}} \right) \\ &\quad - \frac{B}{B_{\parallel}^*} \mathbf{v}_{\chi} \cdot \left(\nabla F_0 - \frac{1}{mv_{\parallel}} (\mu \nabla B) \frac{\partial F_0}{\partial v_{\parallel}} \right) \\ &\quad + v_{\parallel} \hat{\mathbf{b}} \cdot \left(\nabla f_1 - \frac{1}{mv_{\parallel}} \left(\mu \nabla B \frac{\partial f_1}{\partial v_{\parallel}} + \nabla (q \bar{\phi}_1 + \mu \bar{B}_{1\parallel}) \frac{\partial F_0}{\partial v_{\parallel}} \right) \right). \end{aligned} \quad (3.20)$$

The terms that are quadratic in the fluctuating quantities:

$$\begin{aligned} 0 &= \frac{B}{B_{\parallel}^*} \mathbf{v}_{\chi} \cdot \left(\nabla f_1 - \frac{1}{mv_{\parallel}} (\mu \nabla \bar{B}_{1\parallel} + q \nabla \bar{\phi}_1) \frac{\partial F_0}{\partial v_{\parallel}} \right) \\ &= \frac{c}{B_{\parallel}^*} \hat{\mathbf{b}}_0 \times \nabla \underbrace{\left(\bar{\phi}_1 - \frac{v_{\parallel}}{c} \bar{A}_{1\parallel} + \frac{\mu}{q} \bar{B}_{1\parallel} \right)}_{\chi} \cdot \underbrace{\left(\nabla f_1 - \frac{1}{mv_{\parallel}} (\mu \nabla \bar{B}_{1\parallel} + q \nabla \bar{\phi}_1) \frac{\partial F_0}{\partial v_{\parallel}} \right)}_{\Gamma}. \end{aligned} \quad (3.21)$$

Of these terms, the non-linear (quadratic) terms are the numerically most expensive. The analysis demonstrates the origin of the terms χ and Γ in the nonlinearity.

One can express Γ through g_1 instead of f_1 :

$$\begin{aligned} \Gamma_i &= \frac{\partial f_1}{\partial x_i} - \frac{1}{mv_{\parallel}} \frac{\partial F_0}{\partial v_{\parallel}} \frac{\partial}{\partial x_i} (q \bar{\phi}_1 + \mu \bar{B}_{1\parallel}) \\ &= \frac{\partial g_1}{\partial x_i} - \frac{q}{mv_{\parallel}} \frac{\partial F_0}{\partial v_{\parallel}} \frac{\partial \bar{\chi}_1}{\partial x_i} + \frac{q}{mc} \bar{A}_{1\parallel} \frac{\partial}{\partial x_i} \left(\frac{\partial F_0}{\partial v_{\parallel}} \right) \end{aligned} \quad (3.22)$$

Currently, the last term of this equation is neglected because it is of higher order than the other terms (it directly depends on a fluctuating quantity and not only on

3. Numerical implementation: The GENE code

derivatives thereof; cf. [48], p. 131). The order of $\epsilon = \rho_{\text{ref}}/L_{\text{ref}}$ of the terms is explicitly investigated in the following, comparing Γ expressed through f_1 and g_1 .

Start with Γ in terms of f_1 :

$$\begin{aligned} \left[\frac{\partial f_1}{\partial x_i} \right] &= \frac{\rho_{\text{ref}}}{L_{\text{ref}}} \frac{1}{\rho_{\text{ref}}} = \frac{1}{L_{\text{ref}}} \\ \left[\frac{1}{mv_{\parallel}} \frac{\partial F_0}{\partial v_{\parallel}} \right] &= \frac{1}{m_{\text{ref}} c_{\text{ref}}} \frac{1}{c_{\text{ref}}} \\ \left[\frac{\partial}{\partial x_i} q \bar{\phi}_1 \right] &= \frac{1}{\rho_{\text{ref}}} e \frac{T_{\text{ref}}}{e} \frac{\rho_{\text{ref}}}{L_{\text{ref}}} = \frac{T_{\text{ref}}}{L_{\text{ref}}} \\ \left[\frac{\partial}{\partial x_i} \mu \bar{B}_{1\parallel} \right] &= \frac{1}{\rho_{\text{ref}}} \frac{T_{\text{ref}}}{B_{\text{ref}}} B_{\text{ref}} \frac{\rho_{\text{ref}}}{L_{\text{ref}}} = \frac{T_{\text{ref}}}{L_{\text{ref}}} \end{aligned} \quad (3.23)$$

where $x_i = x, y$. So with $T_{\text{ref}} = m_{\text{ref}} c_{\text{ref}}^2$, the total dimension is $1/L_{\text{ref}}$.

Now consider Γ in terms of g_1 :

$$\left[\frac{\partial g_1}{\partial x_i} \right] = \left[\frac{\partial f_1}{\partial x_i} - \frac{q}{mc} \frac{\partial \bar{A}_{1\parallel}}{\partial x_i} \frac{\partial F_0}{\partial v_{\parallel}} - \frac{q}{mc} \bar{A}_{1\parallel} \frac{\partial}{\partial x_i} \frac{\partial F_0}{\partial v_{\parallel}} \right] \quad (3.24)$$

with

$$\begin{aligned} \left[\frac{\partial f_1}{\partial x_i} \right] &= \frac{1}{L_{\text{ref}}} \\ \left[\frac{q}{mc} \frac{\partial \bar{A}_{1\parallel}}{\partial x_i} \frac{\partial F_0}{\partial v_{\parallel}} \right] &= \frac{e}{m_{\text{ref}} c} \rho_{\text{ref}} B_{\text{ref}} \frac{\rho_{\text{ref}}}{L_{\text{ref}}} \frac{1}{\rho_{\text{ref}}} \frac{1}{c_{\text{ref}}} = \frac{\Omega_{\text{ref}}}{c_{\text{ref}}} \frac{\rho_{\text{ref}}}{L_{\text{ref}}} = \frac{1}{L_{\text{ref}}} \\ \left[\frac{q}{mc} \bar{A}_{1\parallel} \frac{\partial}{\partial x_i} \frac{\partial F_0}{\partial v_{\parallel}} \right] &= \frac{e}{m_{\text{ref}} c} \rho_{\text{ref}} B_{\text{ref}} \frac{\rho_{\text{ref}}}{L_{\text{ref}}} \frac{1}{L_{\text{ref}}} \frac{1}{c_{\text{ref}}} = \frac{\Omega_{\text{ref}}}{c_{\text{ref}}} \frac{\rho_{\text{ref}}^2}{L_{\text{ref}}^2} = \frac{\rho_{\text{ref}}}{L_{\text{ref}}} \frac{1}{L_{\text{ref}}} \end{aligned} \quad (3.25)$$

One finds that $\partial_{x_i} g_1$ contains terms of zeroth order and 1st order in $\epsilon = \rho_{\text{ref}}/L_{\text{ref}}$. The first order term is exactly canceled by the last term in Eq. 3.22 so that the order of Γ_i remains unaffected by the change from f to g as it should be. However, in the current implementation of GENE, the last term in Eq. 3.22 is omitted. This has two consequences: First, the order of truncation is not consistent anymore (due to the order ϵ term implicitly contained in $\partial_{x_i} g_1$) and second, Γ_i retains an $\bar{A}_{1\parallel}$ dependence through $\partial_{x_i} g_1$, which was not present before. To investigate if this analytical difference is responsible for the observed instabilities, the neglected last term of Γ and associated terms have been implemented in GENE. In the appendix A.1.1, the exact terms that had to be added are derived. The result of the investigation is that the inclusion of all terms in Γ does not resolve the numerical instabilities, as is shown in Fig. 3.5, left. Both GENE versions, with and without the additional $\bar{A}_{1\parallel}$ term, diverge within a short time

for the same scenario. Therefore, I now turn to the successful change: A redefinition of the main distribution function used in GENE.

3.3.3. Redefining the main GENE distribution function: The f-version

As explained in a previous section, GENE uses the distribution function $g_1 := f_1 - \frac{q}{mc} \bar{A}_{1\parallel} \frac{\partial F_0}{\partial v_{\parallel}}$ as the main distribution function to make the Vlasov equation solvable by an explicit time stepping scheme. There is, however, another way to achieve this, which retains f_1 as the main distribution function. This solution is based on work in [81] and has been derived for GENE in the Ph.D. thesis of Paul Crandall [56]. Here, the analytical idea of the solution is presented, followed by an outline of the new implementation of the f-version in the object-oriented production branch of GENE, which has been implemented within this thesis. Importantly, the new implementation is integrated with the block-structured velocity grids. The same electromagnetic model has recently also been implemented in GENE-3D [60], the stellarator version of the GENE code. Related approaches are also being followed in gyrokinetic particle-in-cell (PIC) codes [83].

The numerical instabilities can be avoided by solving for $\bar{A}_{1\parallel}$ with an additional field equation derived from Ampère's law $\nabla_{\perp}^2 A_{1\parallel} = (-4\pi/c)j$. By applying a time derivative to Ampère's law, using

$$E_{\parallel}^{\text{ind}} = -\frac{1}{c} \frac{\partial A_{1\parallel}}{\partial t} \quad (3.26)$$

and writing the time derivative of f_1 as

$$\frac{\partial F_1}{\partial t} = \frac{q}{m} \bar{E}_{\parallel}^{\text{ind}} \frac{\partial F_0}{\partial v_{\parallel}} + R, \quad (3.27)$$

where R denotes all remaining terms, one finds:

$$\nabla_{\perp}^2 E_{\parallel}^{\text{ind}} = \frac{4\pi}{c^2} \sum_i q_i \int d^3 v v_{\parallel} \mathcal{G}^{\dagger} \left\{ \frac{q_i}{m_i} \bar{E}_{\parallel}^{\text{ind}} \frac{\partial F_{0,i}}{\partial v_{\parallel}} + R_i \right\}, \quad (3.28)$$

where the current j has been expressed as a velocity space integral over the gyrocenter distribution function F_1 , and the sum goes over all species i . Collecting all terms containing $E_{\parallel}^{\text{ind}}$ on one side of the equation, the final field equation becomes (cf. Eq. (5.8) in Ref. [56]):

$$\left(\nabla_{\perp}^2 + \frac{4\pi}{c^2} \sum_i \frac{q_i^2}{m_i} \int d^3 v \mathcal{G}^{\dagger} v_{\parallel} \frac{\partial F_{0,i}}{\partial v_{\parallel}} \mathcal{G} \right) E_{\parallel}^{\text{ind}} = \frac{4\pi}{c^2} \sum_i q_i \int d^3 v \mathcal{G}^{\dagger} v_{\parallel} R_i, \quad (3.29)$$

3. Numerical implementation: The GENE code

which is solved numerically. The operator \mathcal{G} denotes the gyroaverage operator, and \mathcal{G}^\dagger denotes a backwards gyroaverage, as discussed in Ref. [50].

Effectively, $E_{\parallel}^{\text{ind}} = (-1/c)\partial A_{1\parallel}/\partial t$ is treated as an additional independent field that is calculated from the distribution function f_1 each time step. Next, the necessary code changes are outlined.

3.3.4. Implementation details

This subsection has been part of an internal report distributed to GENE users. The differences between the Vlasov equation underlying standard GENE and the new f-version are highlighted. Furthermore, the most important code changes are summarized.

In standard GENE the $\Gamma_{\sigma,i}$ appearing in the Vlasov Eq. 3.13 are expressed through $g_{1\sigma}$ and only terms in lowest order of $\epsilon = \frac{\rho_{\text{ref}}}{L_{\text{ref}}}$ are retained. By plugging in the resulting $\Gamma_{\sigma,i}$ in Eq. 3.13, one obtains the Vlasov equation as implemented in standard GENE (cf. Ref. [48], p. 132, Eq. (A.1)).

For the f-version, we plug in the $\Gamma_{\sigma,i}$ expressed through $f_{1\sigma}$. In addition, we plug in $g_{1\sigma} = f_{1\sigma} - \frac{q_{\sigma}}{m_{\sigma}c} \bar{A}_{1\parallel} \frac{\partial F_{0\sigma}}{\partial v_{\parallel}}$ on the left-hand side and rearrange, so that we have $\frac{\partial f_{1\sigma}}{\partial t} = \dots$. We obtain an equation that is very similar to the Vlasov equation as implemented in standard GENE (cf. Ref. [48], p. 132, Eq. (A.1)). The differences are highlighted in the following equation:

$$\begin{aligned}
 \frac{\partial \hat{f}_{1\sigma}}{\partial \hat{t}} = & \frac{1}{\hat{C}} \frac{\hat{B}_0}{\hat{B}_{0\parallel}^*} \left[\hat{\omega}_{n\sigma} + \hat{\omega}_{T\sigma} \left(\frac{\hat{v}_{\parallel}^2 + \hat{\mu}\hat{B}_0}{\hat{T}_{0\sigma}/\hat{T}_{0\sigma}(x_0)} - \frac{3}{2} \right) \right] \hat{F}_{0\sigma} \hat{v}_{T\sigma}(x_0) \hat{v}_{\parallel} \partial_{\hat{y}} \hat{A}_{1\parallel} \\
 & - \left\{ \frac{1}{\hat{C}} \frac{\hat{B}_0}{\hat{B}_{0\parallel}^*} \left[\hat{\omega}_{n\sigma} + \hat{\omega}_{T\sigma} \left(\frac{\hat{v}_{\parallel}^2 + \hat{\mu}\hat{B}_0}{\hat{T}_{0\sigma}/\hat{T}_{0\sigma}(x_0)} - \frac{3}{2} \right) \right] \hat{F}_{0\sigma} \right. \\
 & \quad \left. + \frac{\hat{B}_0}{\hat{B}_{0\parallel}^*} \frac{\hat{T}_{0\sigma}(x_0)}{\hat{T}_{0\sigma}} \frac{\hat{\mu}\hat{B}_0 + 2\hat{v}_{\parallel}^2}{\hat{B}_0} \hat{K}_y \hat{F}_{0\sigma} + \frac{\hat{B}_0}{\hat{B}_{0\parallel}^*} \frac{\hat{T}_{0\sigma}(x_0)}{\hat{T}_{0\sigma}} \frac{\hat{v}_{\parallel}^2}{\hat{C}} \beta_{\text{ref}} \frac{\hat{p}_0}{\hat{B}_0^2} \hat{\omega}_p \hat{F}_{0\sigma} \right\} \partial_{\hat{y}} \hat{\phi}_1 \\
 & - \frac{\hat{B}_0}{\hat{B}_{0\parallel}^*} \frac{\hat{T}_{0\sigma}(x_0)}{\hat{T}_{0\sigma}} \frac{\hat{\mu}\hat{B}_0 + 2\hat{v}_{\parallel}^2}{\hat{B}_0} \hat{K}_x \hat{F}_{0\sigma} \partial_{\hat{x}} \hat{\phi}_1 \\
 & - \frac{\hat{B}_0}{\hat{B}_{0\parallel}^*} \frac{\hat{T}_{0\sigma}(x_0)}{\hat{q}_\sigma} \frac{\hat{\mu}\hat{B}_0 + 2\hat{v}_{\parallel}^2}{\hat{B}_0} \hat{K}_x \partial_{\hat{x}} \hat{f}_{1\sigma} \\
 & - \left\{ \frac{\hat{B}_0}{\hat{B}_{0\parallel}^*} \frac{\hat{T}_{0\sigma}(x_0)}{\hat{q}_\sigma} \frac{\hat{\mu}\hat{B}_0 + 2\hat{v}_{\parallel}^2}{\hat{B}_0} \hat{K}_y + \frac{\hat{B}_0}{\hat{B}_{0\parallel}^*} \frac{\hat{T}_{0\sigma}(x_0)}{\hat{q}_\sigma} \frac{\hat{v}_{\parallel}^2}{\hat{C}} \beta_{\text{ref}} \frac{\hat{p}_0}{\hat{B}_0^2} \hat{\omega}_p \right\} \partial_{\hat{y}} \hat{f}_{1\sigma} \\
 & - \hat{v}_{T\sigma}(x_0) \frac{\hat{C}}{J\hat{B}_0} \hat{v}_{\parallel} \left(\partial_z \hat{F}_{0\sigma} + \frac{\hat{q}_\sigma}{\hat{T}_{0\sigma}} \hat{F}_{0\sigma} \partial_z \hat{\phi}_1 + \frac{\hat{T}_{0\sigma}(x_0)}{\hat{T}_{0\sigma}} \hat{F}_{0\sigma} \hat{\mu} \partial_z \hat{B}_{1\parallel} \right) \\
 & + \frac{\hat{v}_{T\sigma}(x_0)}{2} \frac{\hat{C}}{J\hat{B}_0} \partial_z \hat{B}_0 \frac{\partial \hat{F}_{1\sigma}}{\partial \hat{v}_{\parallel}} + \frac{\hat{B}_0}{\hat{B}_{0\parallel}^*} \frac{1}{\hat{C}} \left(-\partial_{\hat{x}} \hat{\chi}_1 \partial_{\hat{y}} \hat{f}_{1\sigma} + \partial_{\hat{y}} \hat{\chi}_1 \partial_{\hat{x}} \hat{f}_{1\sigma} \right) \\
 & + \frac{\hat{q}_\sigma}{\hat{T}_{0\sigma}} \frac{\hat{F}_{0\sigma}}{\hat{T}_{0\sigma}} \left(-\partial_{\hat{x}} \hat{\chi}_1 \partial_{\hat{y}} \hat{\phi}_1 + \partial_{\hat{y}} \hat{\chi}_1 \partial_{\hat{x}} \hat{\phi}_1 \right) \\
 & + \frac{\hat{B}_0}{\hat{B}_{0\parallel}^*} \frac{\hat{F}_{0\sigma}}{\hat{q}_\sigma} \frac{\hat{T}_{0\sigma}(x_0)}{\hat{T}_{0\sigma}} \frac{\hat{\mu}\hat{B}_0 + 2\hat{v}_{\parallel}^2}{\hat{B}_0} \hat{K}_x \left[\hat{\omega}_{n\sigma} + \hat{\omega}_{T\sigma} \left(\frac{\hat{v}_{\parallel}^2 + \hat{\mu}\hat{B}_0}{\hat{T}_{0\sigma}/\hat{T}_{0\sigma}(x_0)} - \frac{3}{2} \right) \right] \\
 & + \frac{\hat{q}_\sigma}{\hat{T}_{0\sigma}} \hat{v}_{\parallel} \hat{F}_{0\sigma} \bar{E}_{\text{ind}\parallel}
 \end{aligned} \tag{3.30}$$

The changes are:

- $\hat{g}_{1\sigma}$ is replaced by $\hat{f}_{1\sigma}$.
- $\hat{\chi}_1$'s stemming from $\Gamma_{\sigma,i}$'s are replaced by $\hat{\phi}_1$. To retain all parts of $\hat{\chi}_1$ from the first term of Eq. 3.13 the $\bar{A}_{1\parallel}$ term is explicitly added (first line of Eq. 3.30). (The $\bar{B}_{1\parallel}$ terms are neglected since, at the time of this derivation, they were not implemented for global simulations.)
- A second nonlinear term. (Third line from the bottom.) Further details on the additional nonlinear term are documented in the Appendix A.1.2.

3. Numerical implementation: The GENE code

- An additional term containing the parallel induced E field $E_{\text{ind}\parallel} = \frac{1}{c} \frac{\partial A_{\parallel}}{\partial t}$. The normalized field equation to calculate this parallel induced E-field or plasma induction is given in Eq. 3.29.

These modifications of the underlying equations cause the following code changes:

- A new boolean input parameter is introduced in the general namelist to differentiate between standard GENE (`f_version=F`) and the new f-version (`f_version=T`).
- The distribution function $\hat{g}_{1\sigma}$ is never calculated. Instead `dist_func_g` contains $\hat{f}_{1\sigma}$. Therefore the computation of f in `compute_f.F90` changes to $f = g$ in the `f_version`. This solution is not optimal (same data stored twice) but avoids larger code changes.
- In `emfields_base.F90` and `emfields_i_global.F90` `bar_phi_block`, `bar_dphidij_block`, `bar_dphidij_block` arrays and associated subroutines are introduced in the same way as their `chi` counterparts.
- In `dchidxy_terms.F90` the new type `dphidxy_df_t` and the corresponding subroutines are introduced. The common parent type of the `dchidxy` types and the `dphidxy` type is renamed to `dfielddxy_term_t`.
- A new nonlinear type `df_arakawa_nonlinear_term_fversion_t` is introduced as an extension of `df_arakawa_nonlinear_term_t` in `df_arakawa_nonlinear_term.F90`. The corresponding `add` subroutine adds both nonlinearities.
- A new module and type for the plasma induction term is added: `plasma_induction.F90`. Its `add` subroutine is called in `calc_rhs.F90`.
- In `fieldsolver_df.F90` new subroutines `calc_induced_efield`, `solve_for_E_par_induced` are introduced for the calculation of $E_{\text{ind}\parallel}$.
- Ampere's law changes when one uses $\hat{f}_{1\sigma}$ instead of $\hat{g}_{1\sigma}$ to calculate A_{\parallel} . Compare Eq. (2.95), p.30 and Eq. (2.97), p.30 in [48] and note the additional term on the left-hand side in Eq. (2.97). This is accounted for by an `if(.not.f_version)` block in `fieldsolver_df.F90`.

Next to the additional field equation for the plasma induction, this approach requires an additional nonlinear term between the fields. In total, these changes increase the computational time per time step by approximately 30%. The new electromagnetic model is furthermore compatible with the use of block-structured velocity grids [71]. The f-version is only implemented for global simulations since, in local simulations, the

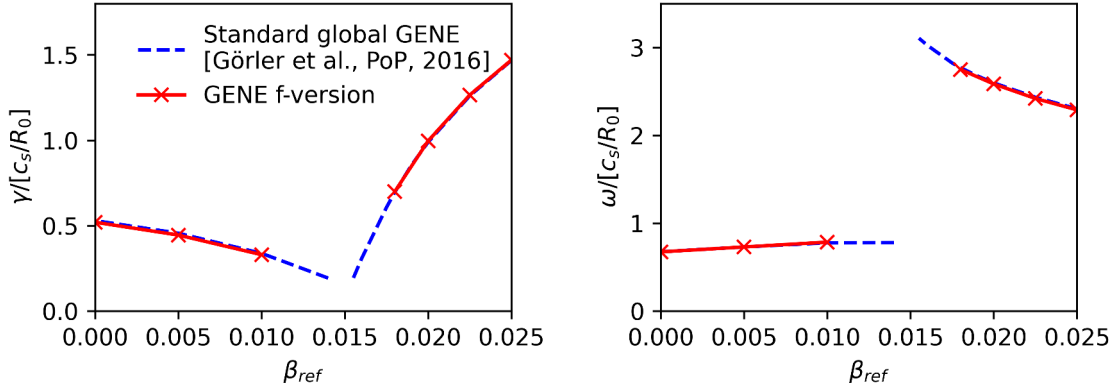
Global, linear β -scan


Fig. 3.4.: Growth rate (left) and frequency (right) comparison between unmodified global GENE and the new f-version in a scan over plasma β . Standard GENE data from Ref. [77].

existing implementation had no stability problems. The f-version can be easily used by setting the flag `f_version=T` in the `&general` namelist of the GENE input parameter file.

The implementation has been tested in global, linear simulations against an existing benchmark of GENE global and the ORB5 code. Excellent agreement for growth rates and frequencies in the investigated range of plasma β values has been found, see Fig. 3.4.

It has been confirmed that the new implementation indeed solves the numerical instabilities in global, nonlinear, electromagnetic GENE simulations by running the same scenario with and without the new implementation. Fig. 3.5 shows the electrostatic heat flux as a proxy for the stability of the simulations for two scenarios simulated with unmodified GENE and the new f-version. Only the f-version is stable in these cases. The only difference in the input parameter files between the simulations shown is the flag `f_version=T` or `f_version=F`. The stability of the f-version has been confirmed in additional cases, e.g. the JET case shown in Chapter 6. For all global, nonlinear simulations presented in this thesis, the new f-version has been used.

3.4. Applicability of the GENE code to the pedestal

The GENE code was initially developed for the study of tokamak core turbulence. Therefore, it had not been designed to adequately deal with all of the challenging physics effects that influence pedestal physics. Nonetheless, it has been extended in

3. Numerical implementation: The GENE code

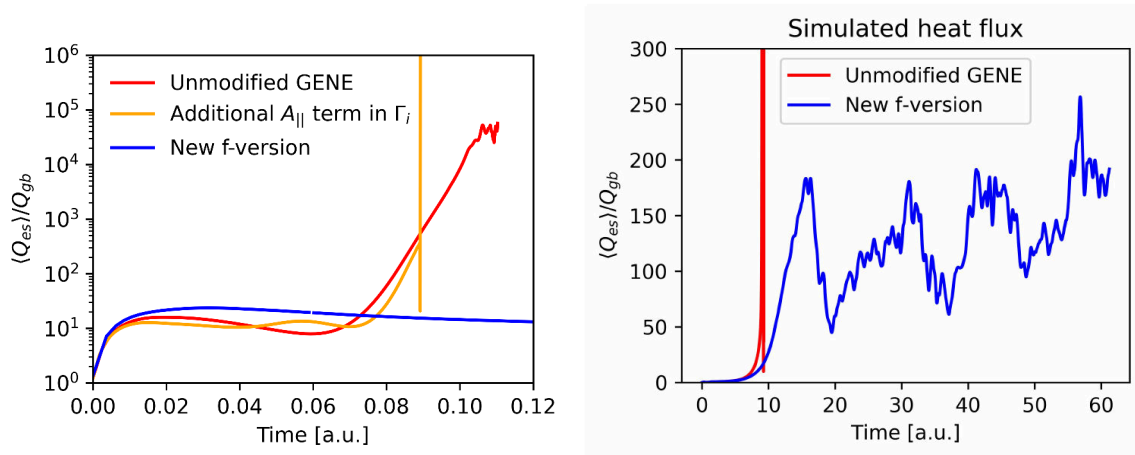


Fig. 3.5.: Electrostatic heat fluxes as a proxy for the stability of the simulations. Unmodified GENE and the version with the additional $\bar{A}_{1\parallel}$ term in Γ_i are both unstable. The new f-version is stable for the same parameters. Left: NSTX-derived scenario. Right: ASDEX Upgrade pedestal of shot #31529.

recent years and PhD projects to improve its applicability to pedestal scenarios. Some of the upgrades and limitations have already been mentioned throughout this chapter, but they are compiled here for reference. Most design choices described below have in common that they significantly reduce the computational cost of gyrokinetic simulations while having a negligible impact on the fidelity of core turbulence simulations. For pedestal parameters, however, their impact can become significant.

In section 2.3.7, possible bounds of the validity of gyrokinetics in the pedestal have been discussed. These apply to all codes that are based on similarly derived models. In addition to these, code-specific implementation choices can influence its readiness for edge and pedestal simulations.

For the GENE code, one of the important choices is the field-aligned coordinate system. While it is computationally very well suited for the closed field line region, it principally excludes the separatrix from the simulation domain and limits the study of the open field line region, though slab-like simulations have been performed [84]. In combination with the radial buffer zones required in global simulations for the Dirichlet boundary condition, this places the outer limit of the region accessible to physics studies a few mm inside of the separatrix.

A further important decision is the explicit splitting of the distribution function in the δf scheme. This limits the relative fluctuation amplitudes that the model can capture. In the scrape-off layer, relative fluctuation amplitudes have been experimentally and in full-f codes observed to approach 100% in the form of blobs [51–53, 85, 86]. In particular, close to the separatrix at the pedestal foot, large fluctuation amplitudes

could hence be expected. This aspect amplifies the limitations discussed with respect to field-aligned coordinates, that GENE is not well suited to study the region very close to the separatrix ($\rho_{tor} > 0.99$).

A related aspect is the gradient-driven approach, which fixes the density and temperature profiles and gradients on average. This is a double-edged feature: On the one side, it allows a direct simulation of turbulence in experimentally measured scenarios. No extra work is required to recreate the experimental scenario since geometry and profiles are direct inputs to the simulation setup. On the other side, this approach does not allow for a self-consistent evolution of the profiles, in contrast to flux-driven simulations. Artificial sources and sinks always compensate the effect of the simulated turbulent heat fluxes on the profiles. The GENE-Tango framework (see Refs. [80, 87] and Chapter 5 aims to bridge this gap by coupling GENE to a transport solver.

Furthermore, while GENE simulations can include an arbitrary number of gyrokinetic charged particle species, the effects of neutral particles are not included. In particular, as a particle source and in determining particle fluxes, their dynamics can become significant. Generally, the study of neutrals and turbulence interaction is just starting.

Nonetheless, within the discussed limits, the GENE code is well suited for studying pedestal turbulence. In particular, the full range of fluctuation scales from ion to electron gyroradius scale can be covered in GENE simulations. As will be discussed in more detail, the ability to simulate electron scale fluctuations becomes especially important for capturing turbulence in the pedestal center. Typically, the resolution of electron scale dynamics is not possible for flux-driven codes. Furthermore, the ability to perform linear and nonlinear simulations in local and global domains with the same code enables a detailed and comprehensive analysis of turbulence and its underlying instabilities. Also, the limitations of local simulation domains can be easily tested. Several upgrades have improved the efficacy of GENE in pedestal scenarios: Block-structured velocity grids [70] have made global simulations with large temperature gradients computationally more feasible, improved collision operators [56] have further increased the ability to assess the accuracy of simulations, and the upgrade of the electromagnetic model, presented in this thesis, has improved the stability of global, nonlinear simulations. From a practical standpoint, these upgrades aim to bring the knowledge and extensive experience encoded in the GENE project to the pedestal region.

In parallel to the extension of established gyrokinetic codes like GENE, many of the outlined limitations are approached by the community with a new generation of codes like XGC, Gysela-X, and GENE-X, that feature complementary design choices to core

3. Numerical implementation: The GENE code

gyrokinetic codes: They are flux-driven, full-f codes, and use coordinate systems that are not limited by the separatrix. Such codes promise to enable very valuable studies of pedestal physics. However, one of the factors making pedestal studies so challenging is that, very likely, the most suitable code for the pedestal top is not simultaneously the most suitable code for the pedestal foot when taking into account model complexity and computational cost. This is rooted in the substantial difference in important physics mechanisms between the pedestal top and foot. Presumably, only a combination of simulation codes will be able to provide a comprehensive explanation of pedestal turbulence.

3.5. MHD limit of global gyrokinetics

This section expands on a specific aspect of the validity of gyrokinetics in the pedestal: The ability of global gyrokinetic simulations to capture large-scale MHD modes. Important elements of pedestal dynamics, like edge localized mode cycles, can be captured by magnetohydrodynamic simulations [40], and MHD modes are an essential constituent in reduced predictive pedestal models (EPED [88, 89]). These are strong indications that system-scale modes with low toroidal wave numbers n are a crucial ingredient of pedestal stability and dynamics. In the derivation of gyrokinetics, however, the size of perpendicular fluctuations is assumed to be small compared to the system scale (high n). This has motivated a recent study comparing growth rates of large-scale electromagnetic modes between the MHD code MISHKA and gyrokinetic code ORB5 [90]. Here, we add global GENE simulations to this comparison.

Fig. 3.6 shows growth rates obtained with MISHKA, ORB5, and global GENE for a scenario designed for the presence of kinetic ballooning modes. GENE simulations were performed with the same geometry and temperature profiles as shown in [90]. ORB5 and GENE simulations were performed at different values of $\rho^* = \rho_i/a$, where a is the minor radius and ρ_i the ion gyroradius. This modifies the size of background profile variations in relation to the gyroradius size in global simulations. Effectively, as $\rho^* \rightarrow 0$, a fixed number of gyroradii see a smaller and smaller fraction of the full profile. The limit of $\rho^* \rightarrow 0$ is also called the local limit since, in local gyrokinetic simulations, profiles and gradients are constant across the simulation domain. At low n ORB5 and global GENE show a good agreement and similar deviations w.r.t to the MHD code MISHKA. Gyrokinetic low- n growth rates are systematically lower than the MHD growth rates. The reduction of growth rates at high n in the gyrokinetic codes compared to MISHKA is expected [91]. It is caused by the effective averaging

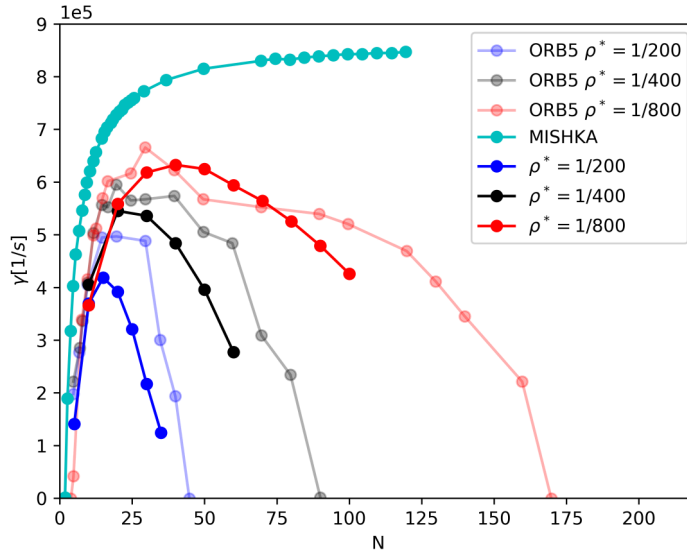


Fig. 3.6.: Growth rate spectrum of (Kinetic) Ballooning modes for different ρ^* calculated with ORB5, MISHKA, and global GENE. ORB5 and MISHKA data from Collar et al., PPCF, 2020 [90].

of fluctuations due to the fast gyromotion of particles, which takes a central role in gyrokinetics but is not included in MHD fluid descriptions of the plasma. Often, this is referred to as Finite Larmor Radius (FLR) effects.

Fig. 3.7 adds local GENE simulations at the steepest gradient position to the growth rate comparison. Local GENE simulations were performed with different magnetic fluctuations. One scan was performed with A_{\parallel} and B_{\parallel} fluctuations, and one scan only with A_{\parallel} fluctuations, but a modification to the ∇B -drift compensating for the missing B_{\parallel} fluctuations. The latter is the same model employed in the global simulations, which currently can not include B_{\parallel} fluctuations. The comparison of the two local scans allows a first estimate of the possible influence of the missing B_{\parallel} fluctuations in global simulations. In the given scenario, at low n , the difference is small. However, local and global growth rates deviate more strongly at the lowest n . This is likely due to a mode transition caused by the stronger drive in the local simulation, which only sees the steepest gradient, whereas, in global simulations, the effective drive is an average of higher and lower gradient areas. Frequencies in global and local simulations agree well.

Further extensions for improved consistency of MHD and gyrokinetics are being investigated in the community. For example, the generalization of the background distribution function to a shifted Maxwellian, which includes the effect of background currents, would e.g. enable tearing mode studies and promise a more realistic gyrokinetic descrip-

3. Numerical implementation: The GENE code

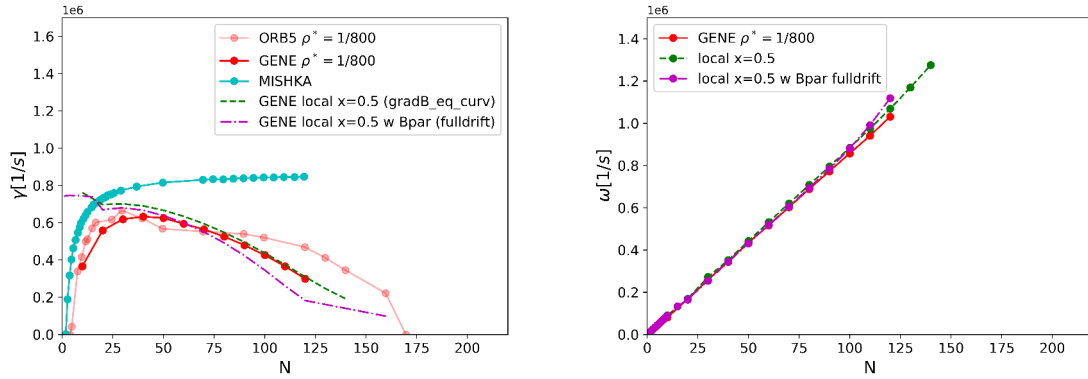


Fig. 3.7.: Growth rate (left) and frequency (right) spectra of (Kinetic) Ballooning modes for global GENE compared to local results. ORB5 and MISHKA data from Collar et al., PPCF, 2020 [90].

tion. Such a distribution function is currently being implemented in GENE [T. Jitsuk et al., to be submitted]. Furthermore, higher-order corrections to gyrokinetic theory are being studied [92, 93]. For the purposes of this thesis, it is acknowledged that discrepancies to MHD for system-scale modes exist, but no attempts to mitigate them are pursued.

3.6. Parallel hyperdiffusion

The last section of this chapter considers a numerical issue that has been found to require renewed attention under pedestal conditions. The central finite difference scheme, which is used in GENE to calculate parallel derivatives, produces high k_{\parallel} aliases on the grid scale, which need to be damped. This is achieved by introducing a parallel hyperdiffusion term, which provides a numerical dissipation designed to dampen the alias modes [50, 94]. The growth rate of the alias modes depends on the growth rate of the original mode. Hence, the strength of parallel hyperdiffusion hyp_z can be controlled by an input parameter, which should be adjusted to match the growth rates. Since hyperdiffusion is a non-physical term designed to compensate numerical artifacts of the differentiation scheme, it should not influence the simulation results. For sufficiently strong hyp_z e.g. heat fluxes of the simulations should converge for some range of hyp_z values. For very large damping amplitudes, the parallel hyperdiffusion, of course, modifies the dynamics. In this thesis, pedestal scenarios were found in which convergence was unexpectedly challenging to achieve in local nonlinear electron scale simulations. Hence, here, the basics of parallel hyperdiffusion and its implementation in GENE are discussed.

The parallel hyperdiffusion term in GENE is defined as [94]:

$$D_n(f_1) = \text{hyp_z} \left(\frac{\Delta z}{2} \right)^n \frac{\partial^n f_1}{\partial z^n} \quad (3.31)$$

It is constructed such that the damping amplitude of the alias modes is independent of the parallel resolution. The alias modes always appear at the highest k_{\parallel} available in the system. This means as the parallel resolution increases the highest k_{\parallel} increases and its damping increases with k_{\parallel}^n , due $\frac{\partial^n f_1}{\partial z^n}$. This is compensated by the term $\left(\frac{\Delta z}{2}\right)^n$, which reduces the damping as the grid spacing Δz gets smaller. As a result, the highest k_{\parallel} modes in the system are damped with the same amplitude for all resolutions, while a fixed k_{\parallel} mode is damped less as the resolution is increased. Standard choice in GENE is a 4th order operator $n = 4$, following the default 4th order finite-difference scheme.

It is emphasized that the occurrence of alias modes is an intrinsic property of the central finite difference scheme. Therefore, a finite hyperdiffusion is necessary, regardless of how high the parallel resolution is. The use of the Arakawa scheme for the parallel derivative (also an option in GENE) prevents an energy accumulation on the highest k_{\parallel} but does not get rid of the aliasing problem itself, see Fig. 3.8.

A few aspects of setting the parallel hyperdiffusion in GENE are pointed out:

- As implemented, the hyperdiffusion operator does not have a mass dependence. Other parts of the Vlasov equation have it. As a consequence, the chosen hyperdiffusion amplitude has to take into account the mass normalization chosen for the simulation. E.g. if the simulation is normalized to the electron mass m_e `hyp_z` has to be set $\sqrt{m_e/m_D} \approx 1/60$ smaller than for a simulation normalized to the deuterium mass m_D , see Fig. 3.9. For two species simulations, this presents a challenge since, typically, the growth rates of electron scales are an order of magnitude larger than ion-scale growth rates hence, either one of the species will be overdamped or underdamped. A partial solution to that is using an additional prefactor (see below), which, however, currently introduces a v_{\parallel} dependence as well.
- For easier comparison with dissipative upwind finite difference schemes, the hyperdiffusion operator can be modified to mimic the dissipation of an upwind stencil. This is achieved by including the additional factor $4/(3\Delta z)$ in the diffusion operator. Note that this changes the dependence of the hyperdiffusion on the resolution (or grid spacing): The highest k_{\parallel} modes are no longer damped with the same amplitude for all resolutions, and the reduction in damping for a fixed k_{\parallel} is reduced compared to the original operator. The modified operator can

3. Numerical implementation: The GENE code

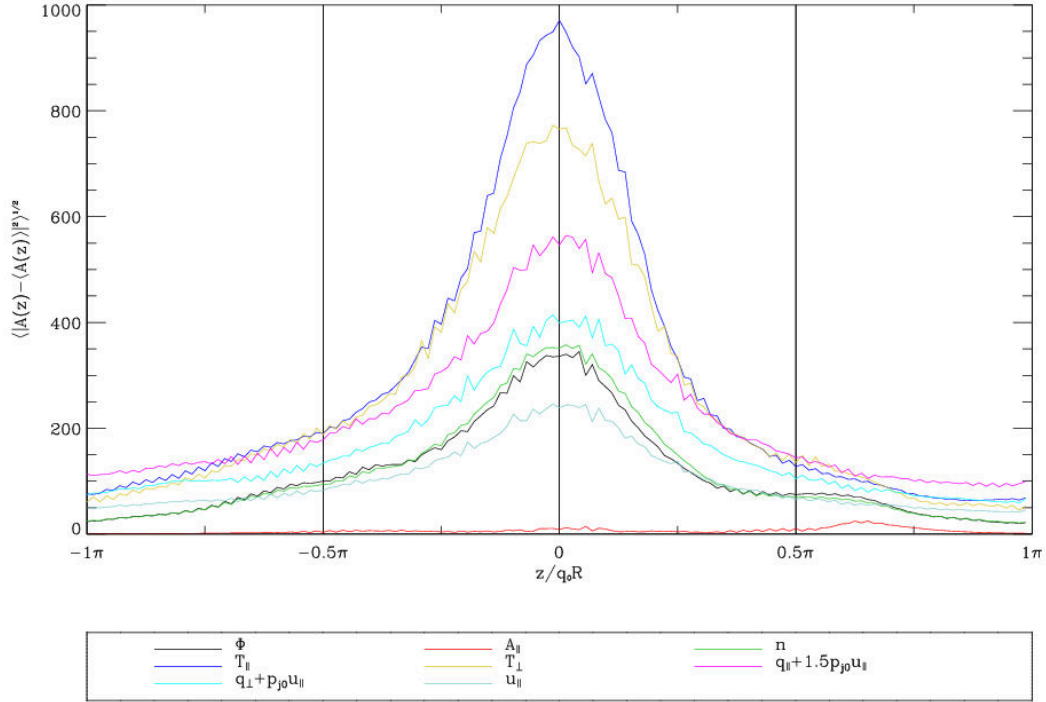


Fig. 3.8.: Fluctuation amplitudes of multiple quantities as a function of the parallel coordinate. From a nonlinear, local, electron-scale simulation with `hyp_z=0` and Arakawa scheme for the parallel derivative. Demonstrates grid scale oscillations in the absence of parallel hyperdiffusion.

be selected by specifying negative `hyp_z` values in the input parameter file. In my opinion, this option is only a good choice if a comparison to upwind schemes is being investigated, e.g. for a direct comparison with codes that use an upwind scheme.

- To achieve full equivalence with upwind schemes, one has to include a v_{\parallel} dependence in the hyperdiffusion operator. This can be added with setting `hypz_with_dz_prefactor=T`. This includes the factor $\sqrt{2\hat{T}_{0\sigma}/\hat{m}_{\sigma}\hat{C}/J\hat{B}_0\hat{v}_{\parallel}}$ in the hyperdiffusion operator. Note that the v_{\parallel} dependence changes the effective amplitude of the hyperdiffusion, depending on the velocity space distribution of f_1 . Hence, `hyp_z` values of simulations with and without this prefactor are not directly comparable, see Fig. 3.10.

In conclusion, a good strategy for setting the parallel hyperdiffusion is as follows: Set a positive `hyp_z` value close to a typical growth rate of modes in the simulation. If necessary, adjust `hyp_z` accounting for the mass normalization of the simulation. Check if the parallel amplitude structure is free of grid-scale oscillations. If not, increase `hyp_z`. Check convergence in the parallel resolution with fixed `hyp_z`. If still in doubt, vary `hyp_z` by some 10% and assess impact.

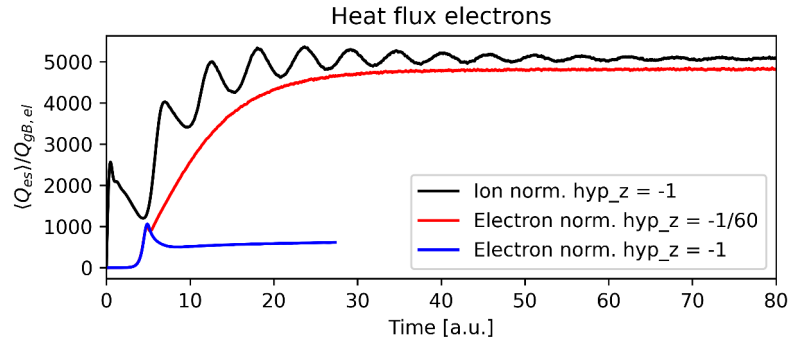


Fig. 3.9.: Demonstration of the influence of the mass normalization on hyperdiffusion. From a nonlinear, local, electron scale pedestal simulation.

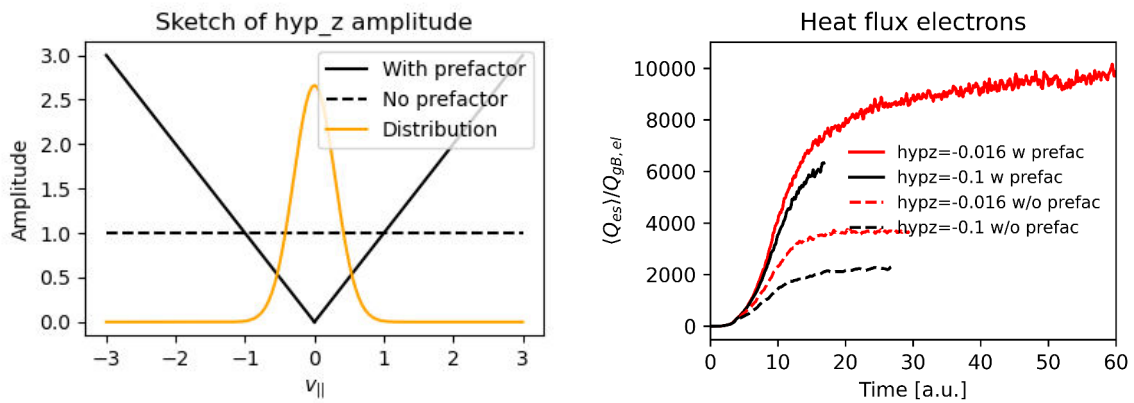


Fig. 3.10.: Left: Sketch of hyp_z amplitude with and without $v_{||}$ dependence through prefactor. For a distribution peaking at $v_{||} = 0$, the hyperdiffusion is effectively lowered. Right: Heat fluxes for different hyp_z settings with and without prefactor. With prefactor, the damping is reduced and the heat flux is increased. The simulations are based on the AUG scenario discussed in Chapter 5

3.7. Summary

This chapter has introduced the GENE code, which is used for all simulation results presented in the following chapters. Emphasis has been put on the electromagnetic upgrade implemented within this thesis based on the proof-of-principle in [56]. The numerical challenges of applying the code to pedestal scenarios have been discussed, particularly the limit of large ballooning modes and the sensitivity of local nonlinear simulations to hyperdiffusion.

Recommended further literature

- Global GENE code version: Görler, T., Lapillonne, X., Brunner, S., Dannert, T., Jenko, F., Merz, F. & Told, D. The Global Version of the Gyrokinetic Turbulence Code GENE. *Journal of Computational Physics* **230**, 7053–7071. doi:10.1016/j.jcp.2011.05.034 (2011)
- Website with all GENE PhD theses: www.genecode.org
- The reference for field-aligned coordinates: D’haeseleer, W. D., Hitchon, W. N. G., Callen, J. D. & Shohet, J. L. *Flux Coordinates and Magnetic Field Structure: A Guide to a Fundamental Tool of Plasma Theory* (Springer Berlin Heidelberg, Berlin, Heidelberg, 1991)
- First derivation of f-version for GENE: Crandall, P. C. *Collisional and Electromagnetic Physics in Gyrokinetic Models* (University of California Los Angeles, 2019)
- Original GENE-hyperdiffusion paper: Pueschel, M., Dannert, T. & Jenko, F. On the Role of Numerical Dissipation in Gyrokinetic Vlasov Simulations of Plasma Microturbulence. *Computer Physics Communications* **181**, 1428–1437. doi:10.1016/j.cpc.2010.04.010 (2010). Previous discussion in ETG context: Told, D. *Gyrokinetic Microturbulence in Transport Barriers* PhD thesis (Universität Ulm, Ulm, 2012).

4. The H-mode pedestal and its instabilities

This chapter serves as a primer for the following two simulation result chapters. First, the properties and challenges of the edge pedestal are analyzed. The analysis focuses on common aspects of pedestals that apply to the gyrokinetic study of pedestals in general. It may be viewed as a summary of lessons learned during the gyrokinetic analysis presented in the following chapters. Then, stability analysis, common types of instabilities, and quasilinear models are introduced. Next, the criteria to characterize turbulence and distinguish instabilities are introduced using examples of the result chapters. Finally, pedestal microinstabilities are summarized.

4.1. The pedestal from a turbulence perspective

"Pedestal" refers to the shape of the temperature and density profiles in the outermost few centimeters (roughly $\rho_{tor} = 0.85 - 1$ or $\rho_{pol} = 0.94 - 1$) of the closed field line region in high confinement mode (H-mode) shots. This region is characterized by profiles that are much steeper than core profiles (cf. Fig. 1.6 and Fig. 4.1). Hence, gradients are much larger, and normalized gradient scale lengths reach values of approx. 20 - 30 instead of 2 - 3 in core conditions.

But not only temperature and density vary substantially inside the pedestal. Many other important plasma parameters change as well. This includes directly depending parameters like the plasma β (decreases), the gyroradius (decreases), or the collisionality (increases), but also magnetic field properties like the magnetic shear, safety factor, and also a radial electric field with an associated velocity shear. See Fig. 5.4 and 6.2

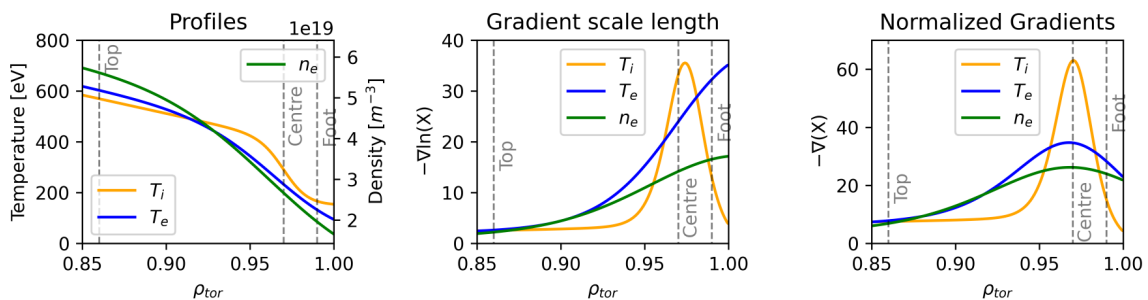


Fig. 4.1.: Temperature and density pedestal profiles from an AUG H-mode.

4. The H-mode pedestal and its instabilities

for examples from AUG and JET. Hence, the overall physical conditions differ substantially between the pedestal top and foot. This has significant consequences for instabilities and dynamics in the different pedestal regions, which will be analyzed in this and the following chapters.

It is helpful to define some nomenclature to distinguish between different regions of the pedestal. I will use the terms pedestal top, pedestal center, and pedestal foot (see dashed vertical lines in Fig. 4.1). Pedestal top or pedestal shoulder refers to the innermost part of the pedestal. Some authors use a modified hyperbolic tangent (mtanh) function to fit pedestal profiles and use the fit parameters to define the pedestal top position [95]. With this convention, the pedestal top typically coincides with the inner knee of the profile, where gradients have already begun to increase. From a gyrokinetic instability perspective, it is more natural to use a position where gradients are still flat just before the onset of strongly increasing gradients. This region between outer core and the mtanh pedestal knee has no established name. I will refer to it by pedestal top as well. The pedestal center is easier to define: It is the steepest gradient region. However, I want to emphasize that the steepest gradient region does not necessarily coincide with the region of strongest instability drive. The gyrokinetic instabilities are driven by the ratio of gradient and absolute value, the gradient scale length. Since the absolute densities and temperatures decrease rapidly, the peak of the gradient scale lengths is typically shifted outwards towards the separatrix (cf. Fig. 4.1). The pedestal foot or pedestal bottom is the outermost region of the pedestal. It is very close to or at the separatrix. The discussion above implies the existence of *the* pedestal. While it is possible to define one pressure pedestal, a closer look at experimental measurements shows that density pedestal and temperature pedestals can exhibit slight differences in the position of the pedestal top, center, or foot. In general, for exact comparisons across different shots and studies, it is worthwhile to directly compare profiles instead of relying on the terminology presented in this paragraph.

The extraordinary property of the L-H transition is that an increase in heating power achieves steeper gradients in temperature and density profiles in the pedestal. In contrast, in typical core scenarios, profiles are stiff, i.e. an increase in heating power does not significantly steepen gradients but causes more turbulent transport at barely changed profiles. It is instructive to consider this aspect from a power balance perspective. In quasi-steady state, the total (turbulent+ neoclassic+ radiation) heat and particle transport through each flux surface is radially constant. If it were not, e.g. temperatures would change in regions with higher heat influx than outflux, and the state would not be quasi-steady by definition. For simplicity, it is assumed in the following that changes in radiation losses are small compared to the turbulent heat flux. While

the full turbulent transport mechanism is a complex interplay of diffusive, convective, and other contributions that are encoded in the Vlasov-Maxwell system, it is a typical choice to derive an effective diffusivity χ from the turbulent heat fluxes Q . In its simplest form (ignoring particle diffusivity): $\chi \propto Q/\nabla T$. This implies that for a radially constant Q and increasing ∇T , the effective diffusivity has to reduce in the edge. In other words, the pedestal is enabled by an edge transport barrier. Having in mind that the majority of transport is typically caused by turbulence, which is driven by temperature and density gradients, this yields an almost paradoxical situation. In the region with increased turbulence drive, the turbulent diffusivity is reduced. At the same time, only due to the small diffusivity could the profiles steepen, and the turbulent drive could become so strong. Hence, an additional mechanism is required that suppresses turbulent transport and is thereby able to establish and sustain the pedestal against the turbulent drive. In the pedestal, shear flows driven by a radial electric field play a crucial role in this suppression [96–98].

Microinstabilities can change their character and relevance in pedestal conditions compared to core conditions. Multiple aspects of pedestal physics contribute to that. An obvious difference is the strongly increased drive in the pedestal center and foot. The concurrently strong drive for modes driven by electron temperature, ion temperature, and density gradients can lead to hybrid modes that share properties of different mode types, as also observed in core turbulence [99]. Additionally, the steep gradients lower the critical threshold β_{crit} for electromagnetic fluctuations [100, 101], that can trigger new types of modes (KBM, MTM, see sections below) and also influence the saturation of predominantly electrostatic modes [102]. Besides the gradients also, the magnetic field geometry influences the microinstabilities. This can affect the instability mechanism, the poloidal position of the mode, and its orientation relative to the magnetic field. This will be discussed in more detail, particularly for electron temperature gradient modes, in later sections and chapters. Furthermore, due to the strong changes in the pedestal, even modes with a small radial extent may experience different drives across their widths. Additionally, the increasing collisionality may reduce the number of trapped particles and thereby lower the impact of trapped particle modes like TEMs. Finally, the suppression of turbulence by shear flows in the pedestal alters the relative importance of modes. While core turbulence is traditionally dominated by so-called ITG and TEM modes (see next section), they are prone to shear flow suppression. The current understanding in the community is that dominantly ETG and MTM modes can prevail in pedestal conditions. This has been summarized and established with the fingerprint concept by Kotschenreuther et al. [103]. In summary, the pedestal conditions create a complex and multi-faceted turbulent state that changes on a length

4. The H-mode pedestal and its instabilities

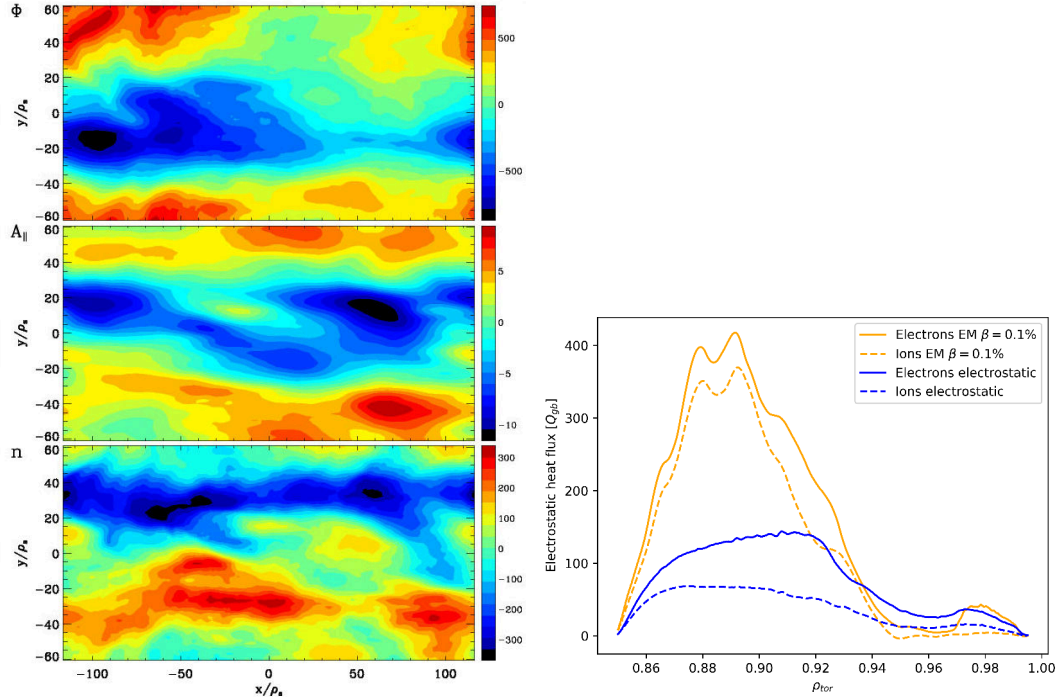


Fig. 4.2.: Left: Contour plots of a nonlinear, local, ion-scale simulation in the steep gradient region of an ASDEX Upgrade pedestal. Top: Electric potential, middle: parallel magnetic potential, bottom: density. Eddies short-circuit around the periodic radial boundary condition (horizontal axis) even with a width of $256\rho_i$. Right: Radial profile of electrostatic heat fluxes of a nonlinear, global pedestal simulation (AUG) with (orange) and without (blue) electromagnetic fluctuations for electrons (solid) and ions (dashed).

scale of just a few mm. I will put an emphasis on this radial structure of the pedestal in the analysis performed in the following two chapters.

The pedestal conditions and their implications for instabilities and turbulence put high demands on gyrokinetic simulations. First, the modeling of $E \times B$ shear in the simulations is unavoidable for realistic turbulent saturation levels and heat fluxes (see Fig. 5.14). The same is true for electromagnetic fluctuations. Even the electrostatic heat flux is strongly influenced by the inclusion of electromagnetic fluctuations (see Fig. 4.2). Furthermore, nonlinear local simulations on ion scales become more difficult. The strong drive causes large eddies, which require wide simulation domains to prevent the eddy from short-circuiting across the radial periodic boundary condition, which would yield unphysically large heat fluxes (see Fig. 4.2). Since the gradients are assumed to be constant in the local approach, the total drive of the system in the local simulation ends up much higher (maximum drive in the whole simulation domain possibly hundreds of gyroradii wide) compared to the very localized steep gradient region (\sim ten gyroradii) and may prevent convergence at all. Resolution demands are also increased in the pedestal. A high radial resolution is required due to the strong

changes in kinetic profiles and magnetic geometry, and a high parallel resolution can become decisive, particularly for electron scale modes (see [104, 105] and next chapter). Additionally, instability spectra show unstable modes over a wide range of scales (see Fig. 5.7), which generally interact in the turbulent system. A comprehensive analysis of transport has, hence to take into account a wide range of scales. In core conditions, ion and electron instabilities are often well separated in size, such that they can be simulated separately to good approximation. In pedestal conditions, however, instability spectra can become continuous in scale, which might increase scale interactions and render a separate simulation of electron and ion scales more difficult. In particularly challenging cases, multi-scale simulations can become unavoidable.

Pedestal properties and dynamics are not only shaped by gyrokinetic turbulence but also by large-scale MHD and neoclassics. A standard H-mode pedestal does not remain stable for long. The pedestal soon hits MHD stability boundaries (peeling-ballooning, see EPED model by Snyder et al. [88, 89]), which cause the pedestal to quickly relax. These edge localized modes (ELMs) expel large amounts of particles and energy (about 10%) from the plasma. An ELM cycle lasts only a few ten ms, such that ELMs may have a repetition rate of 50 - 100 Hz. There also exist other, smaller types of ELMs, depending on the experimental conditions, called Type-II or Type-III ELMs in contrast to the large, bursty Type-I ELMs. It has recently been shown that an ELM cycle can be qualitatively modeled within extended MHD [40].

The shear flows that suppress turbulence in the pedestal are dominantly $E \times B$ flows caused by a radial electric field E_r [97]. The radial electric field can be related to the pressure gradient and currents via a force balance equation derived from the MHD momentum equation. For a single fluid, the MHD momentum equation is:

$$\rho \left(\frac{\partial u}{\partial t} + u \cdot \nabla u \right) = \rho_q E - \nabla \cdot P + J \times B, \quad (4.1)$$

with the mass density ρ , velocity u , charge density ρ_q , electric field E , pressure P , current density J , and magnetic field B . In steady state without flows, this can be written as

$$E = 1/\rho_q (\nabla \cdot P - J \times B) \quad (4.2)$$

and the radial component of this is

$$E_r = 1/\rho_q (\partial_r P - J_\phi B_\theta + J_\theta B_\phi) \quad (4.3)$$

In the pedestal, the radial electric field is mainly balanced by the pressure gradient.

4. The H-mode pedestal and its instabilities

While this force balance is known and extensions to include turbulent effects are being investigated [106], a clear, dynamic understanding of the E_r generation during the L-H transition has not yet been developed.

4.2. Instability types

I have used the term instability several times in the previous sections and chapters, assuming an intuitive understanding of the term without giving a precise technical definition. This is rectified in this section. I will explain this central part of the gyrokinetic analysis in more detail, in particular highlighting what is unstable with respect to what and introducing three instability mechanisms.

The basic idea of stability analysis is the following: Consider a small perturbation of an equilibrium state. In the case of a plasma, this might be a temperature or density perturbation or perturbation of the electric or magnetic field. The question is, what happens to the initial perturbation if the system evolves? Does the perturbation decay, and does the system return to equilibrium? Does the perturbation remain unchanged? Or does the perturbation grow? The first case is called stable, the second marginally stable, and the third unstable. For a plasma, this is a very important consideration since the probability for the plasma to be in a perfect equilibrium is negligibly small. The plasma is, in general, constantly being perturbed on micro- and macroscales, and the crucial question is whether these perturbations remain small and stable or if there are mechanisms of self-amplification that cause them to grow. The short answer is - unfortunately for fusion - that there are many unstable kinds of plasma perturbations on many scales.

The technical stability analysis starts with the underlying equations of motion. The stability of perturbations is part of the dynamics encoded by the equations of motion, like the Vlasov-Maxwell system or MHD equations. Unfortunately, the stability of a perturbation cannot be directly decided from the full nonlinear differential equations. For a linearized system, however, this is possible. The linearization enables one to use an exponential wave ansatz for the perturbation, which is known to solve the linear differential equation. Such a general ansatz does not exist for nonlinear differential equations. The resulting complex dispersion relation then allows one to decide on the stability of different modes. More generally, one could also solve for the full eigenvalue spectrum of the linear operator, which is, however, usually computationally unfeasible. The modes are characterized by their wavenumber k and a complex frequency ω that consists of a real frequency and the growth rate γ . In the numerical solution of the

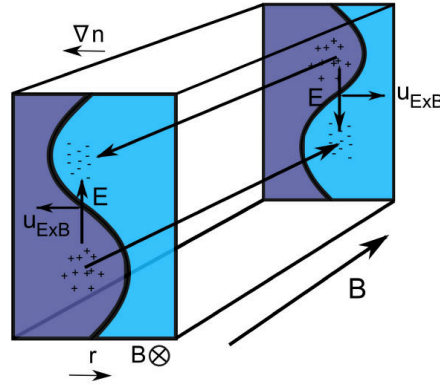


Fig. 4.3.: Illustration of drift wave instability. Taken from [20] with permission from P. Manz, based on [41].

linearized system, unstable modes show exponential growth. Such simulations are performed for the linear growth rate scans shown in the following chapters. The linear ansatz neglects all complex, non-linear dynamics of the system, but it importantly allows one to make statements on stability. In the full system, nonlinear interactions eventually impede the exponential growth of instabilities and cause them to saturate on a certain level. It should be noted that the instabilities of the linear system may not be equivalent to the instabilities of the full system. Additional instabilities may arise, or fast-growing modes may have very low saturation amplitudes, diminishing their relevance, or vice versa. The nonlinear saturation level can typically only be determined by a numerical solution of the nonlinear system. These are the nonlinear turbulence simulations presented in the following chapters. In many plasma physics textbooks, the instability analysis is explained in more detail for the example of MHD instabilities. The general mathematical foundation of stability analysis is developed in the field of dynamical systems.

In the following subsections, three instability mechanisms relevant to gyrokinetic turbulence are presented.

4.2.1. Drift wave instability

The drift wave instability is common in tokamak plasmas. It is caused by the destabilization of a drift wave. The drift wave mechanism is explained first. Consider the situation depicted in Fig. 4.3—a plasma with a density gradient in a uniform magnetic field. The darker blue region has a higher density, and the light blue region has a lower density. A perturbation is applied, which alters the radial gradient and has a finite parallel wavelength. Note that the perturbations in the two snapshots along the magnetic field lines are out of phase. Now, the different inertia of ions and electrons

4. The H-mode pedestal and its instabilities

are crucial. The electrons react much faster to the density gradient and stream from the high-density to the low-density region, creating a surplus of electrons in the low-density region. This creates in the perpendicular plane an electric field from high- to low-density region. And in the presence of an electric field, the $E \times B$ drift transports the whole plasma. Suppose the potential and density perturbation are in phase, as shown in the illustration. In that case, the $E \times B$ drift shifts the density such that the density perturbation effectively drifts downwards in the illustration. The amplitude is constant. The drift wave is marginally stable. A delay of the electron response to the density perturbation destabilizes the drift wave. Then density and potential perturbation are out of phase, and the $E \times B$ drift might act such that the perturbation is amplified. This is a typical situation. Different effects like collisions and Landau damping delay the electron response. While we have used a density gradient and perturbation in the example, the mechanism also applies to temperature or, more generally, to pressure gradients and perturbations.

In summary, the drift wave mechanism: A pressure perturbation creates a potential perturbation (by the species-dependent parallel response) creates $E \times B$ drift creates an effective drift of the perturbation. It is destabilized by a delayed electron response. The drift wave mechanism does not depend on specifics of the magnetic geometry, i.e. it is not curvature-driven. A drift wave has a finite parallel wavenumber k_{\parallel} .

Examples of drift waves are slab-ETG and slab-ITG.

4.2.2. Interchange instability

The interchange instability is common in tokamak plasmas. It requires a magnetic field with finite curvature. All dynamics take place in the perpendicular plane. Consider the situation depicted in Fig. 4.4 — a plasma with a pressure gradient in a curved magnetic field. The relative orientation of pressure gradient and curvature is crucial for the stability of the perturbation. Therefore, two situations are depicted: Right on the outboard side and left on the inboard side of the tokamak. The curvature at both sides points in the same direction. However, the pressure gradient points in opposite directions since the pressure peaks in the center of the plasma. A radial perturbation is applied to the pressure gradient. The curvature drift moves electrons and ions from the high-density region in opposite directions. In the illustration, ions are moved up, and electrons are moved down. This charge separation by the curvature drift creates an electric field, which causes an $E \times B$ drift of the whole plasma. On the inboard side (left), the good curvature region, $E \times B$ drift, and pressure perturbation align such that the perturbation is damped. On the outboard side (right), the bad curvature region,

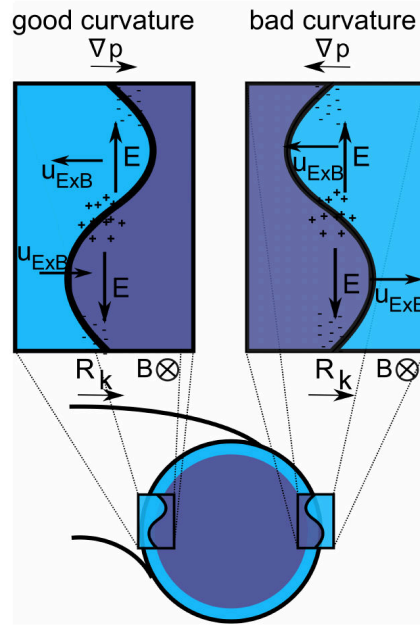


Fig. 4.4.: Illustration of interchange instability. Taken from [20] with permission from P. Manz, based on [41].

$E \times B$ drift, and pressure perturbation align such that the perturbation is amplified.

In summary, the interchange instability: A pressure perturbation creates a potential perturbation (by the species-dependent curvature drift) creates an $E \times B$ drift, which dampens or amplifies the perturbation.

Modes that are driven by the interchange instability have a ballooning structure. They have large fluctuation amplitudes on the outboard side and small fluctuation amplitudes on the inboard side. Or, in different terms: They are unstable on the low field side but stable on the high field side.

Examples of interchange instabilities are toroidal ITG and toroidal ETG. While the exact instability mechanisms differ from a pure interchange mode, TEMs (involving trapped electrons) and KBMs (involving electromagnetic fluctuations) also possess a ballooning structure [20].

4.2.3. Tearing instability

The tearing instability is an instability of the magnetic field. A perturbation in the parallel current locally changes the magnetic field topology and creates a magnetic island, see Fig. 4.5. This is particularly likely to happen at low-order rational surfaces, where the safety factor has rational values, e.g., $q=2/1, 4/3, 5/2$, such that the magnetic

4. The H-mode pedestal and its instabilities

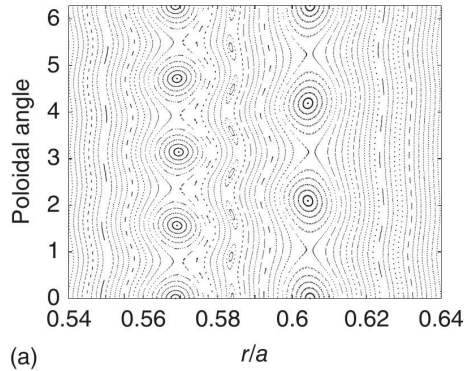


Fig. 4.5.: Illustration of a magnetic island chain by a Poincaré plot of field lines. Reprinted from [107], with the permission of AIP Publishing.

field lines close on themselves after only a few turns around the torus. The magnetic island has its own magnetic X-points and flux surfaces. Since transport is fast on flux surfaces, the island radially connects areas that would have been separated by several flux surfaces without the island's presence. This flattens the pressure gradient across the island. The flattened pressure gradient further reduces the parallel current via the MHD force balance. Hence, the magnetic island is amplified and can grow. For large islands in so-called Neoclassic Tearing Modes, this can have a strong impact on plasma stability and transport and can lead to disruptions.

On smaller scales, at higher wave numbers, Micro-Tearing Modes (MTMs) are driven by a similar mechanism and contribute to turbulent transport.

4.3. Quasilinear models

Quasilinear models aim to circumvent nonlinear simulations by deducing the nonlinear, saturated state from the results of linear simulations. In the previous section, the difference between linear and nonlinear simulations has been explained. While the linearized system allows an analysis of instabilities, only the nonlinear system can reveal fluctuation amplitudes in the developed, turbulent state. By using ad-hoc saturation rules or fits to databases of nonlinear simulations, quasilinear models sidestep the need for expensive nonlinear simulations. The most established quasilinear codes in the plasma turbulence community are TGLF [31, 32] and QuaLiKiz [33, 34]. These codes do not use the full linearized gyrokinetic equation but use further reduced models to calculate the growth rate spectrum to further speed up the model. More recent approaches use Neural Network predictions based on large linear simulation databases of fully gyrokinetic simulations as an alternative option [108].

A simple dimensional estimate for the heat flux is the mixing length model. It is based on a random walk diffusivity $\chi = (\Delta r)^2/\Delta t$, with a characteristic step size Δr and a characteristic time between steps Δt . The step size is assumed to be the ion gyroradius ρ_i , and the time between steps is estimated from the drift frequency ω , yielding: $\chi_i = \rho_i^2 \omega$. The drift frequency can be estimated as $\omega = \frac{v_{th}^2}{\Omega} \frac{k_{\perp}}{L_{\perp}}$ [48]. With the thermal velocity $v_{th} = \sqrt{T_0/m_0}$, perpendicular mode number k_{\perp} and the gradient scale length L_{\perp} . This yields:

$$\chi_{gB} = \frac{k_{\perp} \rho_i^2 v_{th}^2}{L_{\perp} \Omega} = \frac{\rho_i}{a} \frac{T}{qB} \quad (4.4)$$

This is called gyro-Bohm diffusivity [23, 48]. In the last step, $k_{\perp} = 1/\rho_i$ and the assumption that the gradient scale length is given by the minor radius $L_{\perp} = a$ was used. The latter is a reasonable estimate for core profiles in L-mode; however, for pedestal profiles and turbulence, this is not a justified assumption. Therefore, alternative definitions using the actual pedestal gradient have recently received increased attention [104, 109]. From the gyro-Bohm diffusivity, a gyro-Bohm heat flux can be derived:

$$Q_{gB} = \chi_{gB} n_0 \nabla T = \frac{\rho_i}{a} \frac{T}{qB} n_0 \frac{T_0}{a} = \frac{\rho_i^2}{a^2} n_0 T_0 v_{th} \quad (4.5)$$

It is worthwhile to note the dependencies of Q_{gB} on temperature: $Q_{gB} \propto T^{5/2}$. Q_{gB} is a very common normalization for gyrokinetic heat fluxes. It allows one to compare heat fluxes of different scenarios based on how much they deviate from the mixing length expectation. This is well suited for local simulations to which one can assign a single value of Q_{gB} . In global pedestal simulations, the Q_{gB} normalization has to be used with care since Q_{gB} itself varies strongly across the pedestal. Therefore, it partly loses its interpretive value and is best used if scalings are explicitly studied as done in e.g. [104, 109].

A standard quasilinear estimate for the heat flux in units of Q_{gB} is [110, 111]:

$$Q_{QL} = \frac{a}{L_T} \max_{ky} \left(\frac{\gamma}{\langle k_{\perp}^2 \rangle} \right) \quad (4.6)$$

with the growth rate γ and the eigenmode-averaged perpendicular wavenumber $\langle k_{\perp}^2 \rangle$. Here, the mode characteristics γ and $\langle k_{\perp}^2 \rangle$ have been used in a mixing length ansatz as Δt and Δr , respectively.

4. The H-mode pedestal and its instabilities

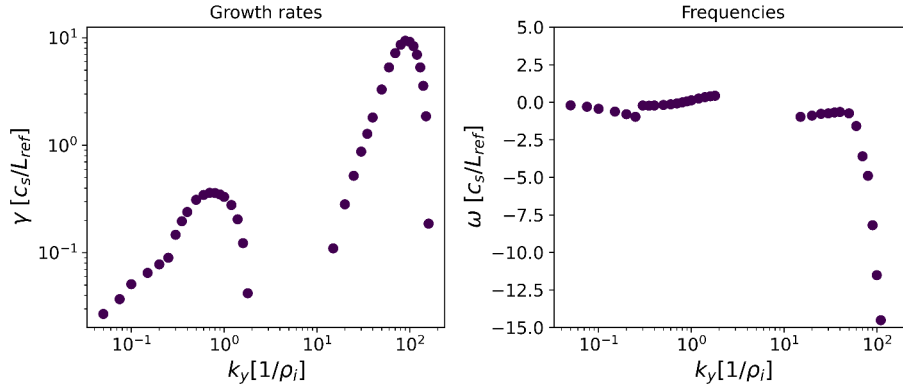


Fig. 4.6.: Example of a growth rate and frequency spectrum of the most unstable mode. The scenario is an ASDEX Upgrade H-mode at $\rho_{tor} = 0.86$ (detailed discussion in Chapter 5).

4.4. Distinguishing between modes

There exists a host of criteria to categorize different microinstabilities. Here, a selection of important criteria is presented. Many of them are applicable to linear simulations. In the next section, they are used to characterize important gyrokinetic instabilities.

4.4.1. Size or wavenumber

The first criterion is the size or wavenumber of the mode. Typically, the binormal wavenumber k_y is considered. A distinction can be made between modes with wavelengths comparable to or larger than the ion gyroradius, which could be driven by either ion or electron dynamics, and modes with wavelengths much smaller than the ion gyroradius, which can only be excited by electron dynamics. Modes much larger than the ion gyroradius border on magnetohydrodynamic modes and the accurate reproduction of such modes within gyrokinetics is a topic of ongoing research, see Sec. 3.5.

4.4.2. Frequency and drift direction

The second criterion is the frequency of the mode and the associated drift direction. Modes may propagate either in the ion or the electron diamagnetic direction, determined by the diamagnetic drift velocity. In GENE conventions, a positive frequency corresponds to the ion diamagnetic drift direction, and a negative frequency to the electron diamagnetic direction. The propagation velocity, i.e. frequency amplitude, can also contain valuable information. Typically, sudden jumps in the frequency spectrum of the dominant mode can reveal mode transitions that are not as visible in the

corresponding growth rate spectrum. See e.g. Fig. 4.6 as an example for a growth rate and frequency spectrum and notice the frequency jump around $k_y = 0.3/\rho_i$.

The frequency is useful for comparing linear simulations with nonlinear simulations and experimental measurements. For comparisons of local with global simulations and measurements, a precise knowledge of underlying large-scale flows, e.g. $E \times B$, and plasma rotation, which shift the apparent mode frequency, is important.

4.4.3. Diffusivity ratios

Another helpful criterion is the ratios of ion and electron diffusivities or heat and particle diffusivities. Since only ratios are considered, this criterion remains applicable to linear simulations, in which the absolute diffusivity values grow without bounds and are hence meaningless. This criterion can also be applied to experimental measurements, allowing a relatively easy comparison of theoretical predictions with experiments. This ansatz and specific values have been formalized recently under the name of fingerprints in [103].

4.4.4. Parallel structure

The parallel structure of the mode contains further important information. Due to the helical shape of the field lines, the parallel structure is tightly linked with the poloidal structure of the mode. The parallel structure can be elongated, with a low k_{\parallel} , peaking at the outboard midplane as is typical for interchange instabilities. It can also have a strong structure with high k_{\parallel} , which is observed in some pedestal ETG modes. Of particular interest is the parity of the mode. It describes the symmetry of the electric and magnetic potential fluctuation amplitudes (real and imaginary parts) with respect to the outboard midplane along the magnetic field line. Most modes have a ballooning parity with a mirror-symmetric electric potential and a point-symmetric magnetic potential. Tearing modes have a tearing parity with a point-symmetric electric potential and a mirror-symmetric magnetic potential. See Fig. 4.7 for an example of the different parities. One can also define a parity factor [112].

4.4.5. Ballooning angle/ tilt at the outboard midplane

Another characteristic of the mode is its radial wavenumber at the outboard midplane, corresponding to the tilt of the mode in the poloidal cross-section or a finite ballooning angle in the ballooning representation. The ballooning angle θ_0 is an angle-like

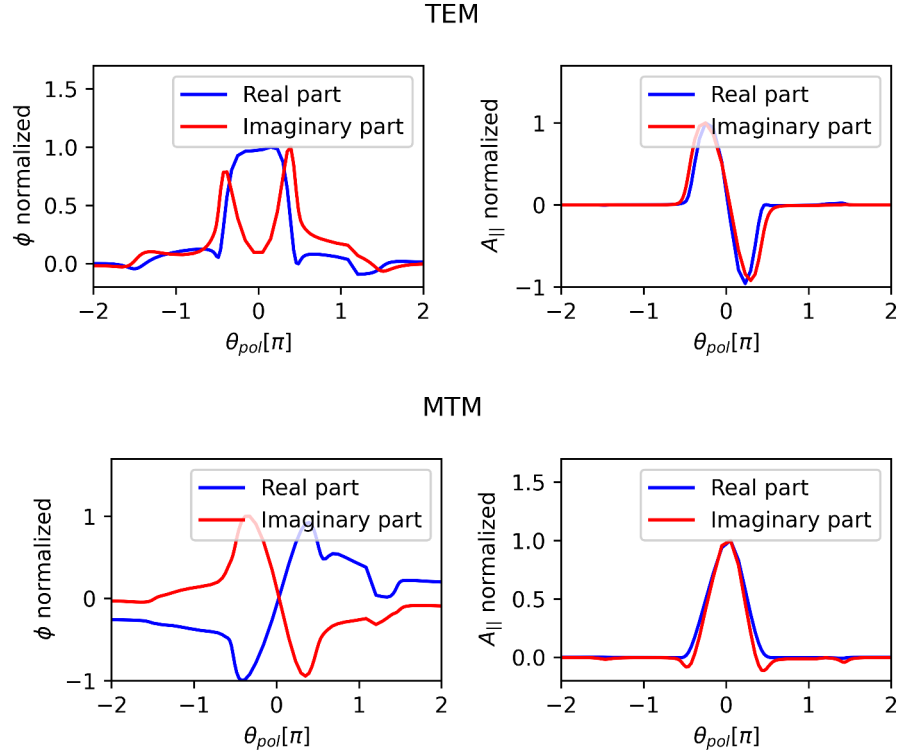


Fig. 4.7.: Example of a ballooning (top) and tearing (bottom) parity. The scenario is an ASDEX Upgrade H-mode at $\rho_{tor} = 0.86$ (detailed discussion in Chapter 5).

coordinate for the parallel direction [113]. It is used to analyze the amplitude of fluctuations along a field line and may extend beyond $[-\pi, \pi]$ for modes with large parallel correlation lengths, wrapping around the torus more than once. The number of parallel connections of a mode n_c resolved in a given flux-tube simulation depends on the binormal wavenumber of the mode k_y , the radial size of the simulation box L_x , the number of radial grid points $nx0$ and the magnetic shear \hat{s} : $n_c = nx0 / (L_x |C_y q_0 / x_0| \hat{s} k_y)$. In GENE simulations, $\theta_0 = 0$ corresponds to the outboard midplane. The ballooning angle is related to the radial wavenumber at the outboard midplane $k_{x,center}$ by $\theta_0 = k_{x,center} / (\hat{s} k_y)$. It is instructive to consider the dependence of this relation on k_y . As k_y increases, $k_{x,center}$ has to increase as well to keep the ballooning angle constant. A consequence is that growth rate scans in k_y with a fixed $k_{x,center}$ probe quite different modes than scans with a fixed ballooning angle. This is illustrated in Fig. 4.8 and 4.9.

4.4.6. Velocity space structure

Of further relevance can be the velocity space structure, see Fig. 4.10. In principle, trapped and passing particles can be distinguished due to the relation of parallel and perpendicular velocity. Hence, their relative contribution to the heat flux can be iden-

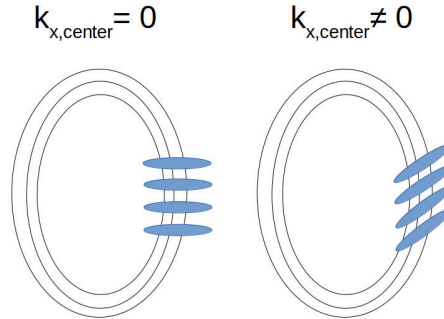


Fig. 4.8.: Illustration of an untilted (left) and tilted (right) mode at the outboard midplane. The tilted mode has a finite radial wave number at the outboard midplane.

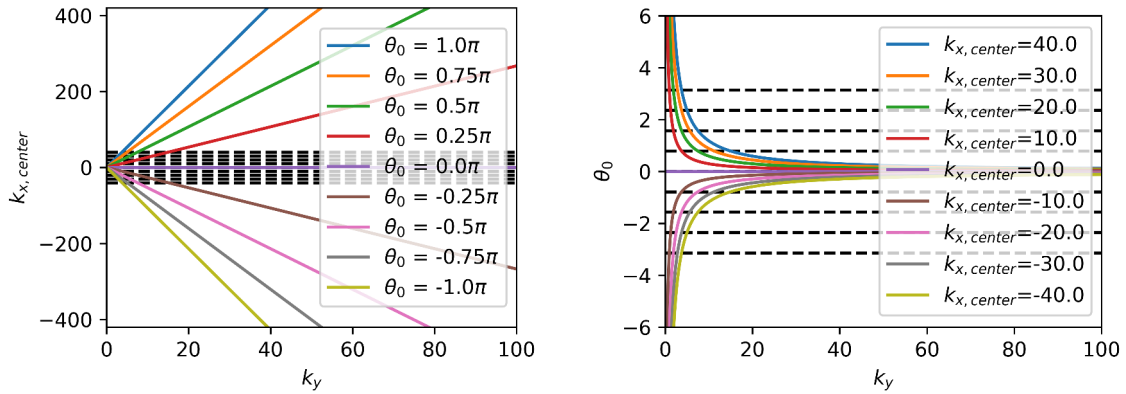


Fig. 4.9.: Illustration of the relation between ballooning angle θ_0 and radial wavenumber $k_{x,center}$ at the outboard midplane as a function of the binormal wavenumber k_y . Left: Lines of constant θ_0 in a $k_{x,center}$ - k_y plot. Right: Lines of constant $k_{x,center}$ in a θ_0 - k_y plot.

4. The H-mode pedestal and its instabilities

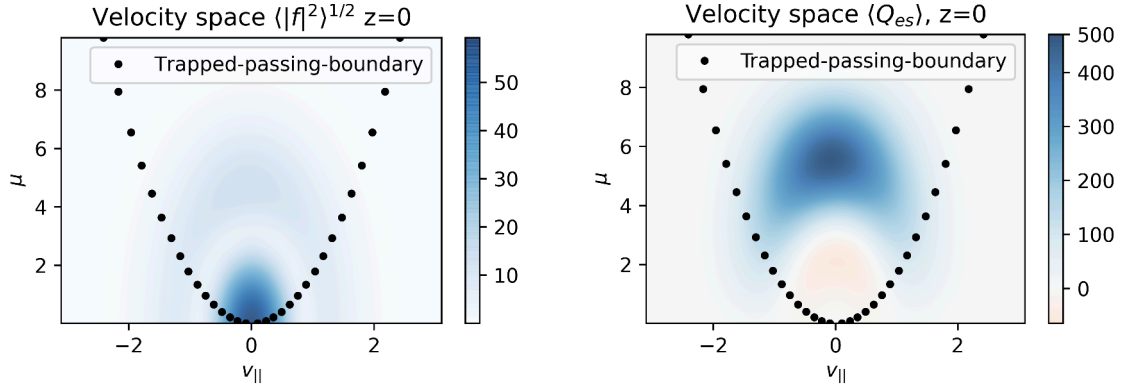


Fig. 4.10.: Example of a velocity space structure. Absolute value of the distribution (left) and heat flux (right). The scenario is a TEM in an ASDEX Upgrade H-mode at $\rho_{tor} = 0.86$ (detailed discussion in Chapter 5).

tified. In practice, it rarely allows for drawing clear conclusions, but it can be helpful as an additional indicator.

4.4.7. Cross phases

Another criterion is the phase difference between different fluctuating fields. Typically, phase differences between electric potential fluctuations and density fluctuations or temperature fluctuations are considered. Phase differences between the magnetic fields ($\bar{A}_{1||}$, $\bar{B}_{1||}$) and density/temperature fluctuations can also be considered for a complete analysis of transport fluxes. The transport is most effective at a phase difference of $\pi/2$ and vanishes at 0. This can be motivated by the instability mechanisms described previously or by the definition of the fluxes, which are calculated from a correlation of T , n fluctuations and the generalized $E \times B$ velocity, see e.g. Ref. [48]. The cross phases are useful for comparing linear and nonlinear simulations and for validation against experimental measurements. Fig. 4.11 shows an example of cross phases from a nonlinear simulation (blue background) and linear simulations (orange circles). A detailed discussion of these simulations is done in the next chapter.

4.4.8. Parameter dependencies

While the previous criteria have been passive in the sense that they can be performed on a given simulation, now a collection of sensitivity studies is described, which require additional simulations. This approach exploits that typically modes are driven by one of the gradients, e.g. the electron temperature gradient, and stabilized by another

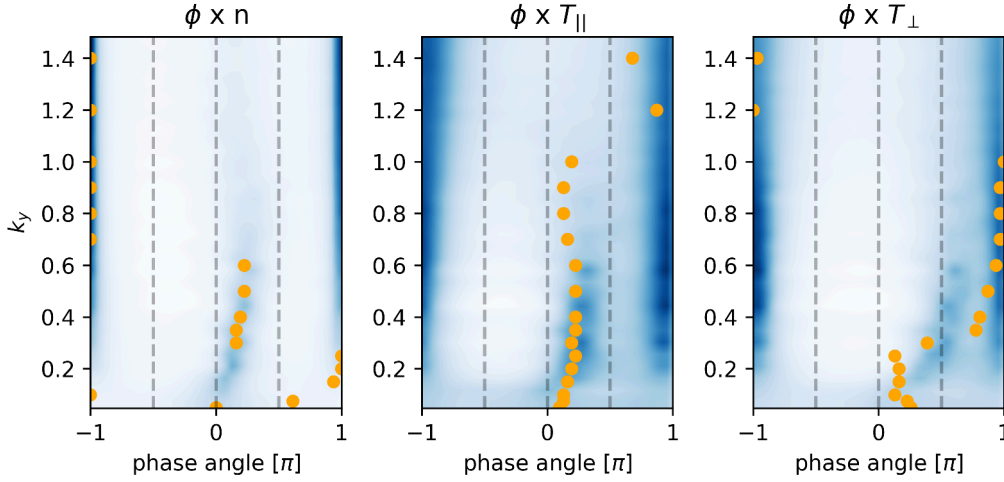


Fig. 4.11.: Example of cross phases. Left: Electric potential ϕ and density n . Middle: Electric potential and parallel temperature. Right: Electric potential and perpendicular temperature. Blue background: Nonlinear simulation. Orange circles: Linear simulations. The scenario is an ASDEX Upgrade H-mode at $\rho_{tor} = 0.86$ (detailed discussion in Chapter 5).

gradient, e.g. the density gradient. By performing additional simulations at artificially changed gradients (e.g. $\pm 30\%$) and comparing resulting growth rates, one can identify the driving gradients. Such scans have been performed for the cases shown in the following two chapters. Similarly, modes may depend on other parameters, like e.g. the plasma β or collisionality. By performing scans in these parameters and comparing growth rates, these can be identified.

A typical property of gyrokinetic instabilities is a nonlinear dependence of the growth rate on the driving gradients. Often, growth rates remain low until a *critical gradient* is reached, after which growth rates strongly increase as a function of the gradient. Famous examples of this behavior include ETG modes [114] and ITG modes [115, 116]. In nonlinear simulations, the critical gradient for the heat flux may be shifted to higher gradient values compared to the critical gradient for growth rates. For ITG turbulence this is referred to as Dimits shift [117, 118].

A principal challenge for such parameter scans is that one risks transitioning to a different mode instead of probing the dependence of one mode at nominal parameters. A good indication of such transitions is the mode frequency. If the frequency changes smoothly with parameter changes, chances are high that just details of a given mode are changed. If, however, sudden jumps in the frequency can be observed, most likely, the dominant mode has changed under the new parameters. This problem can also be circumvented by eigenvalue simulations, which solve for more unstable modes than the

4. The H-mode pedestal and its instabilities

fastest-growing one.

Results of parameter scans are shown and discussed in the following chapters, see e.g. Fig. 5.10 or Fig. 6.14.

4.5. (Pedestal) microinstabilities

This section introduces important gyrokinetic instabilities and their characteristics. Emphasis is on modes that are most likely relevant for transport in the pedestal (ETG, MTM, KBM), but other modes (ITG, TEM) are also described. A short profile/fact sheet summarizes the properties of each instability. Further important questions regarding the instabilities are: What drives them? How do they saturate? How much transport can they cause? Could they be suppressed in specific conditions? What makes them unique/how can they be identified?

4.5.1. Electron Temperature Gradient (ETG) mode

Profile

- Size: Usually much smaller than the ion gyroradius. $k_y \rho_i \approx 10 - 200$. Can extend down to ion scales in pedestal conditions.
- Frequency: Electron diamagnetic drift direction, high frequency.
- Drive: Destabilized by electron temperature gradient $1/L_{Te}$ stabilized by the density gradient $1/L_n$. Hence, has a critical $\eta_e = L_n/L_{Te}$.
- Parity: Ballooning
- electrostatic
- Two branches: Toroidal (interchange drive) and slab (drift wave drive) ETG
- Alternative name: η_e -mode

Based on the gyro-Bohm estimates (see Sec. 4.3), only low levels of electron heat transport are expected since $Q_{gB} \propto \rho_{\text{species}}$ and $\rho_i \approx 42\rho_e$, see Ref. [48]. However, experiments and gyrokinetic simulations show that electrons can carry significant heat transport [119, 120]. One of the essential driving mechanisms for this transport is ETG modes. The significant contribution of ETG modes to electron transport was shown in the early 2000s by Jenko et al. [57, 121]. A critical gradient formula was developed

that estimates the onset of ETG instabilities as a function of gradients and magnetic geometry [114].

Recently, ETGs have received a lot of attention as a driving mechanism of electron transport in the H-mode pedestal [78, 104, 109, 122, 123]. Changes in the structure of ETG modes in pedestal conditions have been analyzed [105, 124, 125] and a quasilinear model for ETG transport in pedestals has been developed [126]. A further important research question concerns the possible impact of cross-scale interactions between electron and ion scale modes [127–129].

ETGs are unique as modes in the gyrokinetic framework that can be unstable on scales much smaller than the ion gyroradius. Two branches of ETGs exist with distinct characteristics: The slab branch produces modes with an isotropic morphology, i.e. $k_x \approx k_y$, and has a high k_{\parallel} . The toroidal branch produces radially elongated streamers $k_x < k_y$ and has a low k_{\parallel} . The two branches have been observed to dominantly occur in different regions of k_y in the pedestal, with toroidal ETGs at lower $k_y \rho_i \approx 1 - 10$ and slab ETGs at higher $k_y \rho_i \approx 50 - 150$ [104, 105].

A principal challenge in the validation of ETG physics against experiments is that ETG mode dynamics are faster and smaller than can be resolved by most available diagnostics [130]. Usually, only effective quantities like the resulting heat flux can be compared.

ETG transport plays a crucial role in the structure of pedestal turbulence investigated in this thesis (cf. following two chapters).

4.5.2. Micro Tearing Modes (MTM)

Profile

- Size: Typically larger than the ion gyroradius. $k_y \rho_i \approx 0.1 - 1$.
- Frequency: Electron diamagnetic drift direction.
- Drive: Destabilized by electron temperature gradient $1/L_{T_e}$ and parallel current perturbations.
- Parity: Tearing
- Electromagnetic
- Located at rational surfaces.

4. The H-mode pedestal and its instabilities

Micro tearing modes have been identified as one of the prime candidates for causing electron transport in the pedestal [103]. They have been found to be relevant in pedestals of DIII-D [131, 132] and JET [133, 134]. The first GENE simulations of microtearing turbulence were performed in [135].

The MTM is unique as a microinstability with tearing parity. It can be distinguished from KBMs, which also cause electromagnetic transport on large scales, by the drift direction and parity.

4.5.3. Kinetic Ballooning Mode (KBM)

Profile

- Size: Ion gyroradius and larger. $k_y \rho_i \approx 0.1 - 1$.
- Frequency: Ion diamagnetic drift direction, high frequencies
- Drive: Destabilized by pressure gradient and plasma β .
- Parity: Ballooning
- Electromagnetic
- Can be excited by higher plasma β in an ITG scenario (see ITG-KBM transition e.g. in Ref. [101]).
- Alternative name: drift-Alfven mode

KBMs are employed as one of the constraints in the EPED model for limiting the pedestal height and width [89]. While linear KBM simulations are established [77, 100], the nonlinear saturation of KBMs, particularly in global simulations, is a topic of active research [136, 137].

4.5.4. Resistive Ballooning Mode (RBM)

Profile

- Size: Ion gyroradius and larger. $k_y \rho_i \approx 0.1 - 1$.
- Frequency: Electron diamagnetic drift direction
- Drive: Destabilized by collisionality
- Parity: Ballooning

RBM s have been proposed to be important in L-H transition dynamics at the edge of tokamak plasmas [138, 139]. They have mainly been studied with fluid-type codes [139, 140], but some linear gyrokinetic studies for L-mode scenarios have been performed [141].

4.5.5. Trapped Electron Mode (TEM)

Profile

- Size: Ion gyroradius $k_y \rho_i \approx 0.5 - 1.5$.
- Frequency: Electron diamagnetic drift direction.
- Drive: Destabilized by electron pressure gradient. Can be driven by an electron temperature and/or density gradient. Stabilized by high collisionality due to de-trapping of particles. Suppressed by $E \times B$ shear.
- Parity: Ballooning
- Electrostatic
- Related to the ubiquitous mode [142, 143].

The TEM is one of the classic core turbulence modes [110]. Since TEMs require trapped particles - a kinetic effect - they are typically not captured by codes based on fluid closures. A TEM can be distinguished from an ITG mode, which causes electrostatic transport on similar k_y ranges by the drift direction, the stabilization by collisionality, and independence from the ion temperature gradient. Furthermore, most of its transport is caused by trapped particles (see velocity space distribution). In the steep gradient region of the pedestal, it is usually suppressed by $E \times B$ shear.

4.5.6. Ion Temperature Gradient (ITG) mode

Profile

- Size: Slightly larger than the ion gyroradius $k_y \rho_i \approx 0.1 - 1$.
- Frequency: Ion diamagnetic drift direction.
- Drive: Destabilized by ion temperature gradient. Stabilized by density gradient. Hence, critical $\eta_i = L_n/L_{T_i}$ Stabilized by plasma β before transition to KBM. Suppressed by $E \times B$ shear.
- Parity: Ballooning

4. The H-mode pedestal and its instabilities

- Electrostatic
- Saturation mainly via zonal flows [144, 145].
- Two branches: Toroidal (interchange drive) and slab (drift wave drive) ITG
- In idealized conditions, it is linearly isomorphic to ETG with reversed roles of ions and electrons. The saturation mechanisms differ.
- Alternative name: η_i mode

The ITG mode is considered one of the classic core turbulence modes [115, 146]. In the steep gradient region of the pedestal, it is usually suppressed by $E \times B$ shear, even though for some JET pedestals, ITGs have been found to be important [133].

4.5.7. Synopsis

A host of different microinstabilities have been introduced. In real-world pedestals, these modes do not appear as clear as the description of the prototypes might suggest. Hybrids may form that have some characteristics of one mode and some of another. Drift directions may be altered, and the dominant drive may subtly change across the spectrum, for example, from TEM to ETG modes. Gradual changes may also be observed radially as one drive weakens and another strengthens, and the geometric properties of the magnetic field change. So, while these modes are useful to identify driving mechanisms of transport channels, no real pedestal is in a pure state of, e.g. ETG-turbulence or MTM-turbulence.

In recent years the following picture of pedestal microinstabilities and transport has emerged: ETG and MTM have been identified to be strong candidates for the most relevant instabilities in the steep gradient region of the pedestal [103–105, 131–134]. In ASDEX Upgrade also, TEMs and KBMs are relevant [147] and in JET-ILW (ITER-like Wall) ITG has been found to be present [148, 149]. In simulations with drift-kinetic electrons, KBMs and Kinetic Peeling-Ballooning modes (KPBM) have been found to be important for pedestal stability [137]. Most of these studies are based on local/linear, local/nonlinear, global/linear, or reduced β simulations. However, to study which turbulent mechanisms drive transport under real pedestal conditions, global/nonlinear simulations at experimental β values are indispensable. Such simulations are presented in this thesis.

4.6. Dealing with experimental uncertainties

The character of instabilities and how much heat flux they drive depends sensitively on the driving temperature and density gradients. In the pedestal, measurement uncertainties of gradients can typically reach values of $\pm 30\%$, see e.g. Fig. 5.2. Hence, an appreciation of these inherent experimental uncertainties is essential for the setup and interpretation of gyrokinetic studies.

Experimental uncertainties do not affect all quantities equally. While electron temperature measurements are possible with different diagnostics simultaneously, ion temperature measurements are notoriously more difficult. They are not always directly accessible but may be inferred from temperature measurements on impurities, which adds additional uncertainties concerning the relation between main ion and impurity temperatures. The measurement uncertainties also apply to the relative position of profiles to each other and the reconstructed magnetic field. Since electron temperature and density can be measured simultaneously with Thomson scattering, there is no uncertainty on their relative position. The ion profile position, however, is more uncertain. It is typically set such that the steepest gradient of T_e and T_i coincide. The relative position to the magnetic field has an uncertainty of a few mm. It is usually fixed by imposing realistic separatrix temperature values.

In local, linear instability analyses, the strategy to deal with experimental uncertainties is straightforward. By varying the input gradients, the sensitivity of a spectrum or individual wavenumbers can be mapped out. For local, linear simulations, this is computationally affordable but can become challenging, such that the use of dedicated uncertainty quantification methods becomes advantageous [150]. In local, nonlinear simulations, the same approach for determining the sensitivity of heat fluxes can be followed. For the comparison to experimental transport measurements, the use of transport fingerprints (diffusivity ratios and mode frequency) as described in [103] can augment this ansatz.

For global, nonlinear simulations, the sensitivity analysis is more complicated. Since a changing profile with changing gradients drives the instabilities in global simulations instead of one single gradient value in local simulations, no straightforward gradient scan is possible. A systematic approach to changing the profiles to match experimental power balance in global simulations is the GENE-Tango framework, discussed in Sec. 5.5. This is a flux-driven approach and hence relies on an accurate knowledge of sources and sinks instead of temperature and density profiles. An alternative approach is to shift the focus on trends and dependencies of physical effects. With this

4. The H-mode pedestal and its instabilities

perspective, the absolute heat flux is mainly a sanity check to see if the simulations are consistent with the experiment. Even factors of three or four difference in heat flux may be acceptable, as typically slightly different profiles would show very good agreement with the experiment. Of primary interest is then how heat fluxes react to different physical effects like flow shear, gradients, or impurities.

4.7. Summary

This chapter has prepared the simulation results presented in the following chapters. Pedestal physics has been analyzed from a turbulence perspective, emphasizing the strong changes in many parameters and shear flow suppression of turbulence. Furthermore, the basic concept of stability analysis, the difference between linear and nonlinear simulations, and relevant instability mechanisms have been outlined. Finally, the most important microinstabilities and criteria to identify these modes were discussed. The current understanding of pedestal turbulence has been summarized, and its boundaries have been highlighted. With this, the stage is set for the following chapters, in which the presented machinery will be applied to two experimental pedestals. By combining the new electromagnetic code upgrade with comprehensive linear studies, the understanding of pedestal turbulence is advanced.

Recommended further literature

- The fingerprint concept for gyrokinetic modes: Kotschenreuther, M., Liu, X., Hatch, D., Mahajan, S., Zheng, L., Diallo, A., Groebner, R., the DIII-D TEAM, Hillesheim, J., Maggi, C., Giroud, C., Koechl, F., Parail, V., Saarelma, S., Solano, E., Chankin, A. & JET Contributors. Gyrokinetic Analysis and Simulation of Pedestals to Identify the Culprits for Energy Losses Using ‘Fingerprints’. *Nuclear Fusion* **59**, 096001. doi:10.1088/1741-4326/ab1fa2 (2019)
- Background literature on stability analysis and nonlinear dynamics: Strogatz, S. H. (2001). *Nonlinear Dynamics and Chaos: with Applications to Physics, Biology and Chemistry*. Perseus.

5. AUG pedestal simulations

This is the first of two simulation result chapters. The presented analysis aims to identify the dominant turbulent transport mechanism in the H-mode pedestal of a real experimental plasma discharge. The shot we investigate in this chapter is a type-I ELMy ASDEX Upgrade discharge. The main focus is on the time point 6ms after the ELM crash, where the profiles show a well-developed pedestal. First, the experimental scenario is presented. Next, linear instabilities in different regions of the pedestal are characterized. Then, nonlinear, global, ion-scale simulations, as well as nonlinear, local, electron-scale simulations, are presented. Preliminary results on the behavior of instabilities and fluxes at different times of the ELM cycle are also discussed. Finally, an outlook on quasi-flux-driven simulations of the pedestal by coupling GENE with the transport code Tango is given.

Parts of this chapter have been published in Leppin, L., Görler, T., Cavedon, M., Dunne, M., Wolfrum, E., Jenko, F. & the ASDEX Upgrade Team. Complex Structure of Turbulence across the ASDEX Upgrade Pedestal. *Journal of Plasma Physics* **89**, 905890605. doi:10.1017/S0022377823001101 (2023).

5.1. Experimental scenario

We investigate the particularly well-diagnosed and studied shot AUG #31529 [151, 152]. Edge density, temperatures of electrons and ions, and flows have been measured in this discharge with advanced edge diagnostics, achieving very high time ($65 \mu\text{s}$) and spatial resolution during an ELM cycle [151]. These measurements and their analysis provide well-resolved temperature and density profiles at different time points of the ELM cycle for the gyrokinetic analysis.

The AUG #31529 shot has NBI (Neutral Beam Injection) and ECRH (Electron Cyclotron Resonance Heating) heating, with a total heating power of $P_{tot} = 8.7 \text{ MW}$, an on-axis B-field of -2.5 T and a plasma current of 0.8 MA . From this shot, we employ ELM-synchronised temperature and density profiles from [151] and pressure-constrained magnetic equilibria, see Fig. 5.1. We focus on the time point 6 ms after the ELM crash, where the pedestal is mostly recovered, and profiles are almost pre-ELM, with a slightly ($\approx 7\%$) reduced electron temperature at the pedestal top.

Fig. 5.2 shows the profiles and corresponding gradient scale lengths used in this study.

5. AUG pedestal simulations

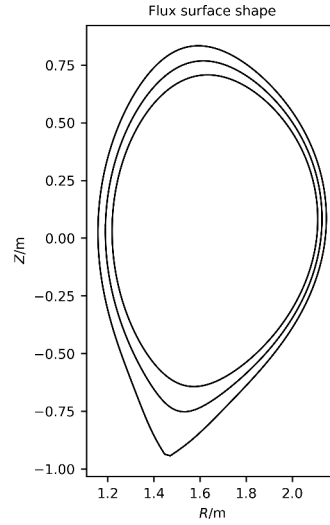


Fig. 5.1.: Poloidal shape of several flux surfaces in the pedestal region of AUG #31529. Generated from the experimental magnetic equilibria.

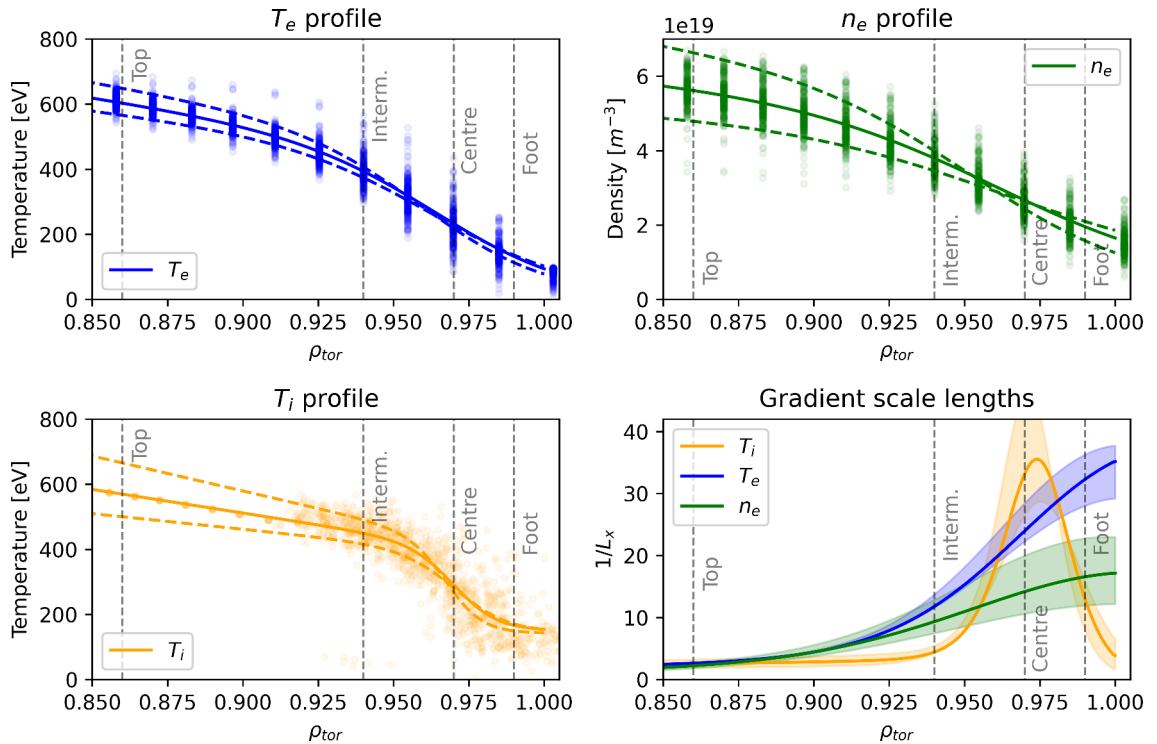


Fig. 5.2.: Profiles and gradient scale length $1/L_X = -X^{-1}\partial X/\partial\rho_{\text{tor}}$ of ion temperature (orange), electron temperature (blue) and density (green) of AUG #31529 6ms after the ELM crash. It is assumed that $n_e = n_i$. Data points show experimental measurements (see main text for details), solid lines show the best mtanh fit, and dashed lines illustrate alternative mtanh fits within the statistical uncertainty of fit parameters. Grey vertical lines indicate positions where instabilities have been characterized in detail (see Sec. 5.2).

Data points are from experimental measurements; lines are modified hyperbolic tangent (mtanh) fits. The T_e and n_e data points show results of the integrated data analysis algorithm (IDA) [153] combining measurements from lithium beam emission (Li-BES) spectroscopy and electron cyclotron emission (ECE) radiometry. The T_i data points show measurements of the edge charge exchange recombination spectroscopy (CXRS) and averaged values of the core-CXRS. For more details, see Ref. [151].

As input for the gyrokinetic simulations, the pedestal profiles were fitted with mtanh functions as defined in [95] in the radial domain $\rho_{tor} = [0.8, 1]$. $\text{mtanh}(z) = a((1 + \alpha z)e^z - e^{-z})/(e^z + e^{-z}) + b$, where $z = (r_{sym} - r)/h_{wid}$. The uncertainty of the fits has been estimated by varying the fit parameters within a 3σ interval of the best fit, where the standard deviation σ was determined from the least squares fit. Fit parameters were varied such that profiles with maximal and minimal average gradients were achieved. For the high gradient case we choose the parameters $[a + 3\sigma_a, b + 3\sigma_b, r_{sym} - 3\sigma_r, h_{wid} - 3\sigma_h, \alpha + 3\sigma_\alpha]$ and for the low gradient case $[a - 3\sigma_a, b - 3\sigma_b, r_{sym} + 3\sigma_r, h_{wid} + 3\sigma_h, \alpha - 3\sigma_\alpha]$. The range of gradients spanned by these fits is shown by the shaded areas in the gradient scale lengths plot (lower right panel of Fig. 5.2). Note that this uncertainty is just a statistical uncertainty of the mtanh fit, which takes into account the variance of experimental data, but does not account for systematic errors in e.g. the relative position of ion and electron temperature profiles or the separatrix position. Hence, it illustrates only part of the total measurement uncertainty, which might be considerably larger.

The vertical, grey, dashed lines in Fig. 5.2 and Fig. 5.3 indicate representative positions for pedestal top/shoulder, an intermediate region, pedestal center, and pedestal foot, where linear, local instability scans have been performed (see Sec. 5.2). With pedestal top/shoulder, I refer to the radial position ($\rho_{tor} = 0.86$) just before the increase of temperature and density gradients, where the growth rate spectrum is still clearly distinct from the pedestal center, as explained in more detail in the previous chapter. Fig. 5.3 contextualizes the pedestal profiles by showing fits to the complete profiles in the range $\rho_{tor} = [0, 1]$ (left) and $\rho_{tor} = [0.5, 1]$ (right).

In Fig. 5.4, the radial profiles of further quantities determining edge physics and microinstabilities are shown: plasma β (strongly falls off from pedestal top to foot), collisionality (strongly increases), the gyroradius (decreases), and the safety factor q (increases but exhibits an intermediate flat region). The flat region in the q profile is caused by the bootstrap current and will be shown to have a stabilizing effect on ion-scale instabilities.

Fig. 5.5 shows the $E \times B$ velocity due to the radial electric field E_r and the corresponding

5. AUG pedestal simulations

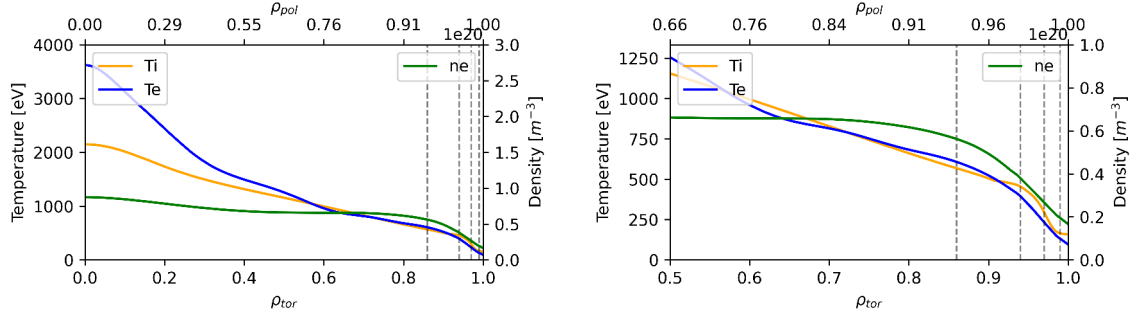


Fig. 5.3.: Fits to complete temperature and density profiles from core to edge of AUG #31529. Left from $\rho_{\text{tor}} = 0$, right from half-radius $\rho_{\text{tor}} = 0.5$. The upper coordinate axis shows the radial position in units of ρ_{pol} . Vertical dashed lines mark the same positions as in Fig. 5.2.

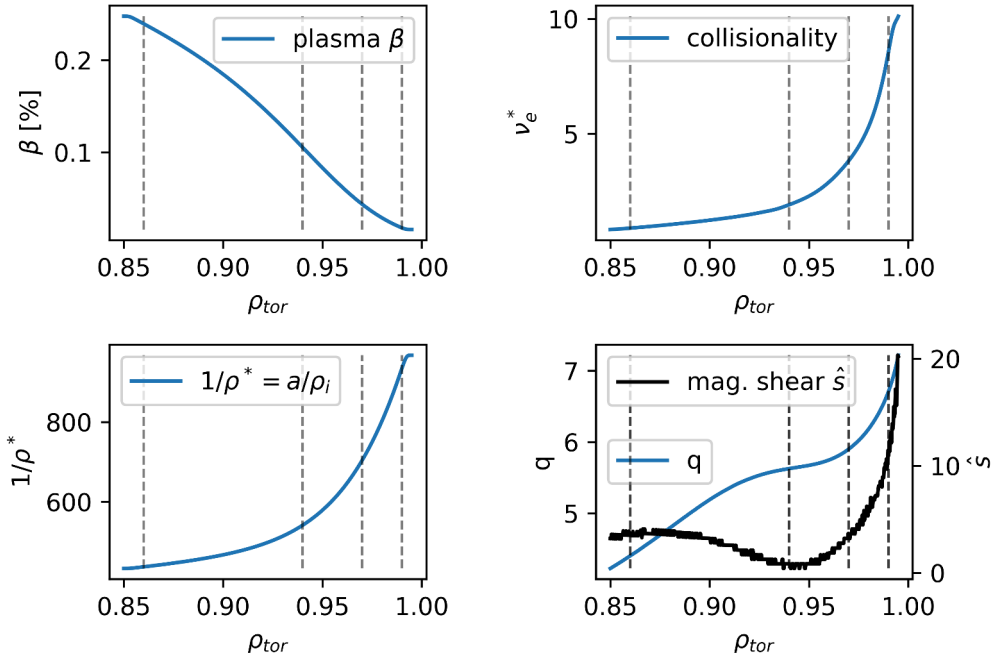


Fig. 5.4.: Profiles of further relevant quantities influencing microinstabilities and edge turbulence: Plasma β (top left), collisionality (top right), ρ^* (bottom left) and safety factor q combined with magnetic shear \hat{s} (bottom right).

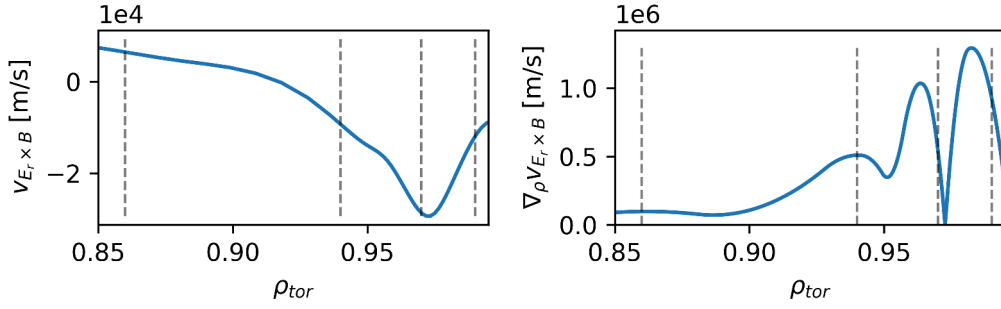


Fig. 5.5.: $E \times B$ velocity $v_{E_r \times B} = E_r \times B/B^2$ (left) and corresponding shear (right) caused by the edge radial electric field E_r .

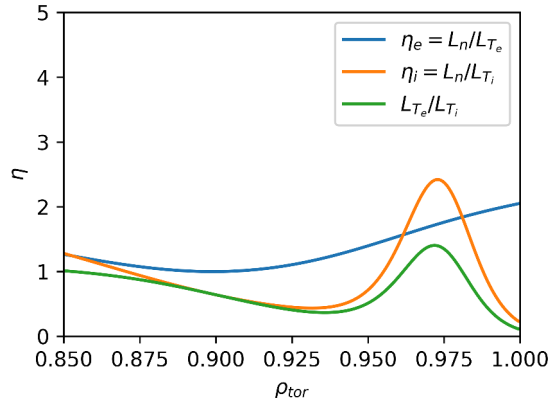


Fig. 5.6.: Relative strength of instability drive: η_i , η_e and L_{T_e}/L_{T_i} .

shear. The $E \times B$ velocity has the highest amplitude in the pedestal center. The resulting $E \times B$ shear in the regions adjacent to the pedestal center is important in suppressing turbulent heat flux.

Fig. 5.6 shows the relative drive of instabilities in the investigated pedestal. η_i peaks in the steep gradient region, whereas η_e increases monotonically from $\rho_{\text{tor}} = 0.9$, indicating a growing ETG drive towards the pedestal foot.

In the next section, I continue with an instability characterization in this scenario with local, linear simulations.

5.2. Instability characterization

To characterize the instabilities present in the given pedestal, we have performed scans with linear local simulations in the binormal wavenumber k_y from $0.05\rho_i^{-1}$ to $350\rho_i^{-1}$ (corresponding to toroidal mode numbers of e.g. $n = [4, 29954]$ at $\rho_{\text{tor}}=0.86$ or $n =$

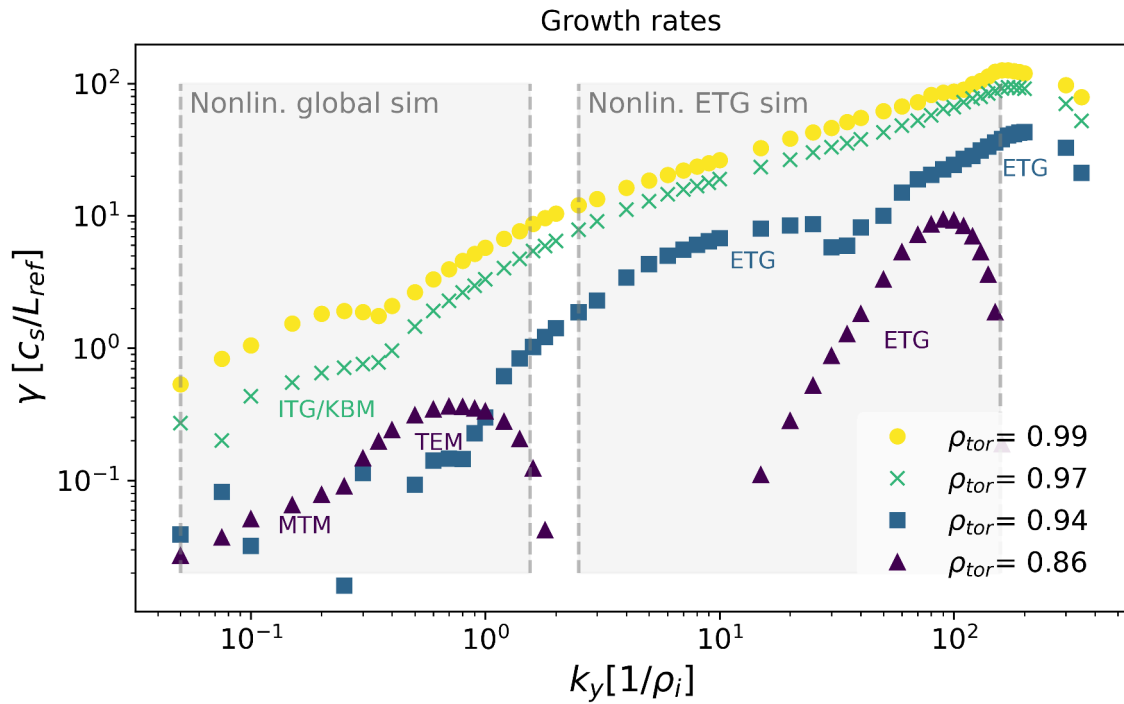


Fig. 5.7.: Growth rate spectra of the dominant mode for four radial positions maximized over ballooning angle. $c_s = \sqrt{T_e/m_i}$ and ρ_i are local normalisations evaluated at each radial position. $L_{ref} = 0.65$ m. Shaded regions indicate the wavenumber ranges used in nonlinear heat flux simulations.

[7, 48365] at $\rho_{\text{tor}}=0.99$), the radial wavenumber at the outboard midplane $k_{x,\text{center}}$ from $-40\rho_i^{-1}$ to $40\rho_i^{-1}$ (connected to the ballooning angle $\theta_0 = k_{x,\text{center}}/(\hat{s}k_y)$) and the radial position ρ_{tor} from 0.85 to 1. Fig. 5.7 shows the growth rate spectra at four positions (pedestal top, intermediate, pedestal center, and pedestal foot) maximized for each ρ_{tor} and k_y over the ballooning angle. At selected wavenumbers, ballooning angles, and radial positions, we have additionally performed scans in temperature and density gradients ($\pm 30\%$), collisionality (0 - $18\nu_e^*$), and plasma β (0% - 1%). In total, about 7000 simulations were performed to characterize linear instabilities. Simulation settings are detailed in the Appendix Sec. A.2.

Following the mode characteristics presented in the previous chapter, I use the following criteria to distinguish between the different instabilities: Parity of the parallel mode structure in ballooning representation (tearing or ballooning), size (ion or electron gyroradius), drift direction (ion or electron diamagnetic), sensitivity on gradients (T_e , T_i , n), dependence on collisionality and plasma β as well as diffusivity and heat flux ratios following the fingerprint approach [103]. An alternative way to identify tearing modes is the tearing or parity factor, see [112], which has been used to verify the identifications. An electromagnetic mode on scales $> \rho_i$ with tearing parity is called MTM. An electromagnetic mode on scales $> \rho_i$ with ballooning parity and drift in ion diamagnetic direction is called KBM. An electrostatic mode on scales $\approx \rho_i$, which is stabilized by collisionality and is not destabilized by ∇T_i , is called TEM. An electrostatic mode on scales $\approx \rho_i$, which is destabilized by ∇T_i and propagates in ion diamagnetic direction, is called ITG. An electrostatic mode on scales $\lesssim \rho_i$ that is destabilized by ∇T_e is called ETG. However, it should be emphasized that precisely categorizing modes on ion scales in the region of very strong drive close to the separatrix is particularly challenging. Different drive mechanisms interact and excite instabilities with characteristics that do not fall neatly in the mode prototypes developed in the study of core turbulence.

At the pedestal shoulder ($\rho_{\text{tor}} = 0.86$, violet triangles in Fig. 5.7), we find MTMs on the largest scales, TEMs at ion scales, a region of stable wavenumbers and then ETGs on electron scales. In agreement with [103], the linear TEMs produce significant outward particle transport ($D_e/(\chi_i + \chi_e) \approx 0.15$, with particle diffusivity D , heat diffusivity χ) compared to MTMs. At the intermediate position ($\rho_{\text{tor}} = 0.94$, blue squares in Fig. 5.7), where the magnetic shear has a minimum, a growth rate gap without any clear mode on ion scales exists. On intermediate scales, more ETG modes occur that were not present at the pedestal shoulder. In the steep gradient region ($\rho_{\text{tor}} = 0.97$, green crosses in Fig. 5.7) on ion scales, we find ITG modes that are close to a KBM transition, as discussed later in Fig. 5.10. At smaller scales, ETG-driven modes are present,

5. AUG pedestal simulations

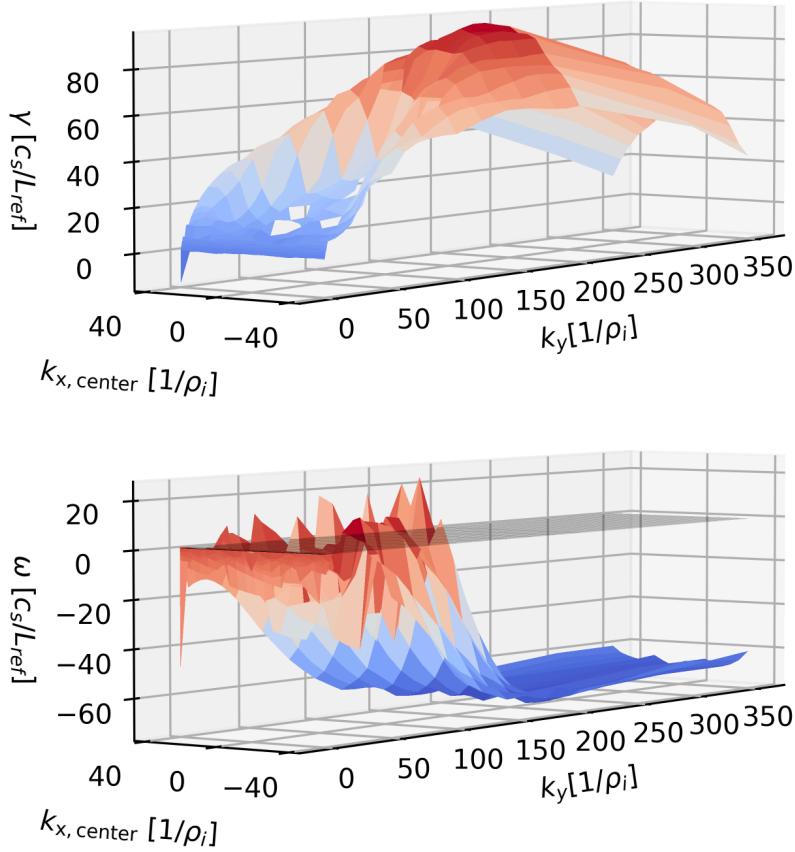


Fig. 5.8.: Growth rate (top) and frequency spectrum (bottom) at $\rho_{tor}=0.97$ in a 3D surface visualization with k_y and $k_{x,center}$ as axes. The color bar corresponds to growth rate and frequency, respectively.

which extend to larger scales towards the pedestal center and foot. At the pedestal foot ($\rho_{tor} = 0.99$, yellow circles in Fig. 5.7) on ion scales modes show an ETG/TEM character but tend to be destabilized with increasing collision frequency. The ETG modes at pedestal center and foot tend to peak increasingly at finite ballooning angle, indicating the presence of toroidal ETG modes [105, 124]. While the fastest growing ETG modes we find tend to be toroidal-ETGs, subdominant slab-ETGs turn out to play an important role in the nonlinear simulations (see Sec. 5.3). Overall growth rates increase from pedestal top to foot.

It is insightful to visualize the results of the growth rate scan differently. I select just one position, the pedestal center, but show the entire k_y - $k_{x,center}$ surface. Fig. 5.8 shows this dependence of growth rates (top) and frequencies (bottom) on k_y and $k_{x,center}$. Notice the trough in growth rates at $k_{x,center} = 0$ up to $k_y \rho_i = 100 - 150$. Until then, finite $k_{x,center}$ have larger growth rates than $k_{x,center} = 0$. The frequency (lower plot) regularly peaks above the $\omega = 0$ surface, showing that, in particular, at finite $k_{x,center}$

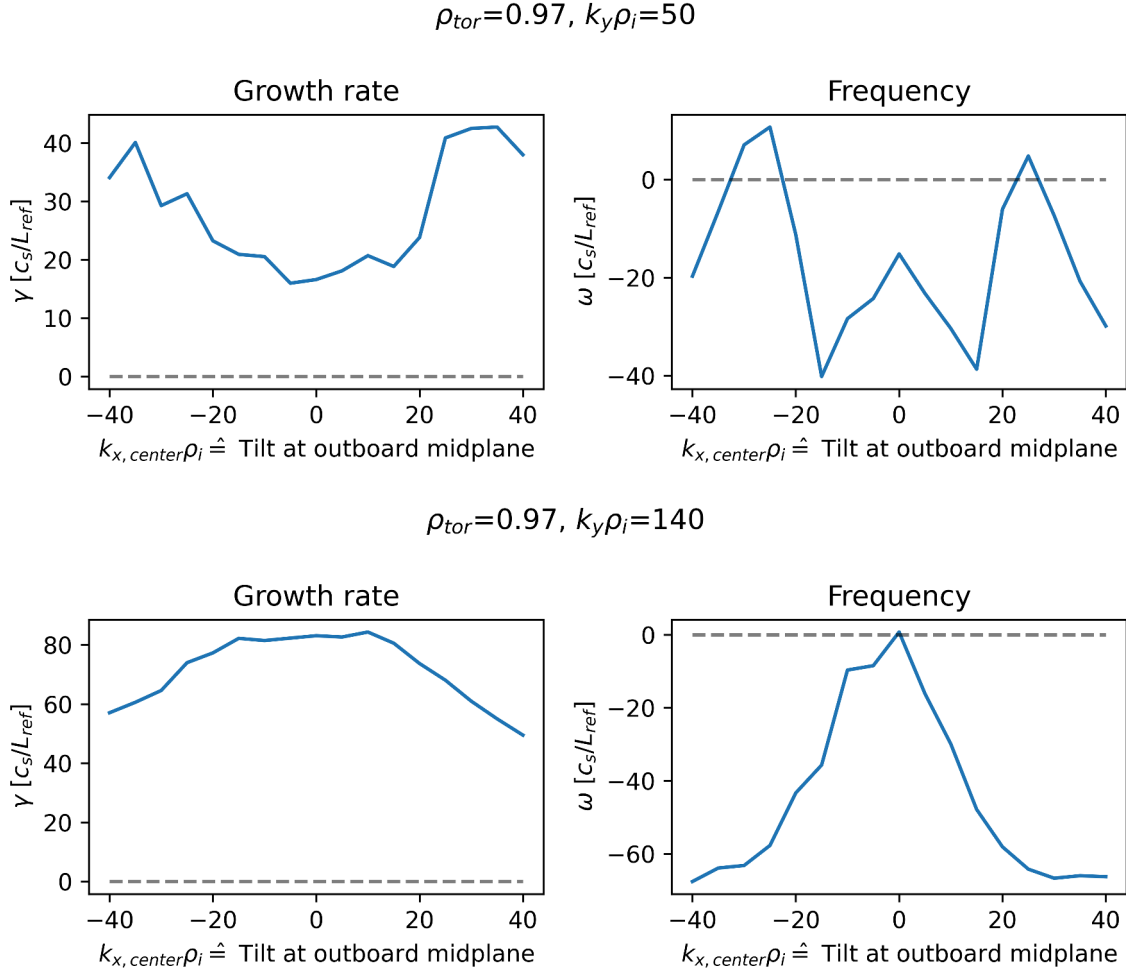


Fig. 5.9.: Growth rates and frequencies as a function of $k_{x,center}$ in the pedestal center $\rho_{tor} = 0.97$ at an intermediate ETG wavenumber $k_y\rho_i = 50$ (top) and a high ETG wavenumber $k_y\rho_i = 140$.

modes with positive frequencies are present at k_y ranges that are ETG dominated. This indicates that under certain conditions, ETGs can have an ion diamagnetic drift direction. Similar observations have recently been reported in [122].

The analysis of the 3D growth rate representation is corroborated by 2D cuts through the instability landscape at $k_y\rho_i = 50$ and $k_y\rho_i = 140$ (see Fig. 5.9). At $k_y\rho_i = 50$ growth rates peak off- $k_{x,center} = 0$ with positive frequencies. At $k_y\rho_i = 140$, however, growth rates peak at $k_{x,center} = 0$. This shows that for pedestal ETGs, the radial wavenumber at the outboard midplane can have a significant influence on growth rates. The $k_{x,center}$ changes correspond to only minimal ballooning angles at high k_y . Nonetheless, they cause noticeable changes in growth rates. For a complete instability characterization, a fine scan of radial wavenumbers with $k_{x,center}$ almost as well resolved as the binormal wavenumber k_y seems necessary. A further investigation is left

5. AUG pedestal simulations

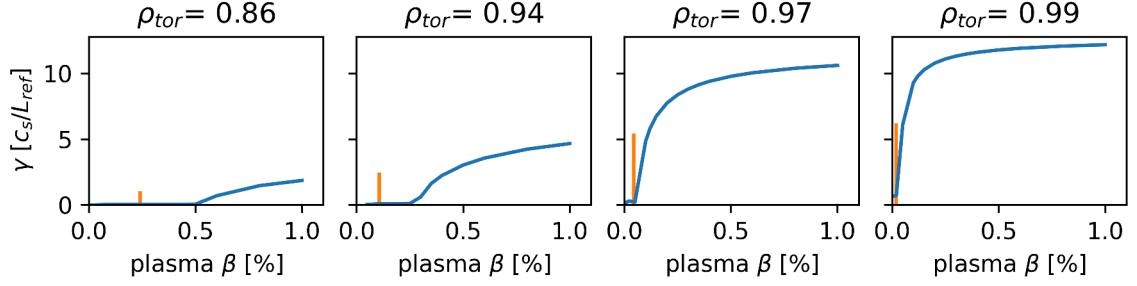


Fig. 5.10.: Growth rates as a function of plasma β at different radial positions. The vertical orange lines indicate the nominal plasma β value at the respective position.

for future work.

Scans over plasma β at different radial positions show that the pedestal in these linear local simulations sits close to a KBM threshold - being closer at the pedestal foot than at the pedestal top (cf. Fig. 5.10). The closeness to the KBM threshold in the pedestal center resembles the use of a KBM constraint in the EPED model [88] for the prediction of the pedestal width. It has, however, been reported that the radial structure of KBMs may not be compatible with the narrow pedestal region [133, 149], suggesting that the local approximation may skew the details of the KBM threshold.

Fig. 5.11 shows a collisionality scan at pedestal top and center for two wavenumbers. On the pedestal top (upper two panels), the TEM presence is visible as the mode stabilizes with increasing collisionality. The reason for the stabilization is a de-trapping of trapped particles as the collision frequency increases. At $k_y \rho_i = 0.5$, a mode transition occurs where a further increase in collisionality increases the growth rate again. In the pedestal center (lower two panels), the dependence on collisionality is less severe. The TEM is no longer present (or at least dominant). Note the slight destabilization with collisionality. This suggests a partly RBM-like character of these modes.

Fig. 5.12 shows the growth rate spectrum for different parallel resolutions. Only small differences are observed between $n_z = 36$ and higher resolutions. The resolution $n_z = 72$ is sufficient for convergence, as all other resolutions up to $n_z = 288$ show the same results. This is in contrast to the JET case (see next chapter) in which resolutions of $n_z = 360$ are necessary for convergence of the fastest growth rates. This indicates that in AUG, most of the fastest growing ETG modes have toroidal character, which have a coarser parallel structure compared to slab-ETG modes. It should be emphasized that this finding applies only to the linearly most unstable mode. Subdominant modes with slab character may exist that require a higher resolution. This will become important for nonlinear simulations in which dominant and subdominant modes interact and may

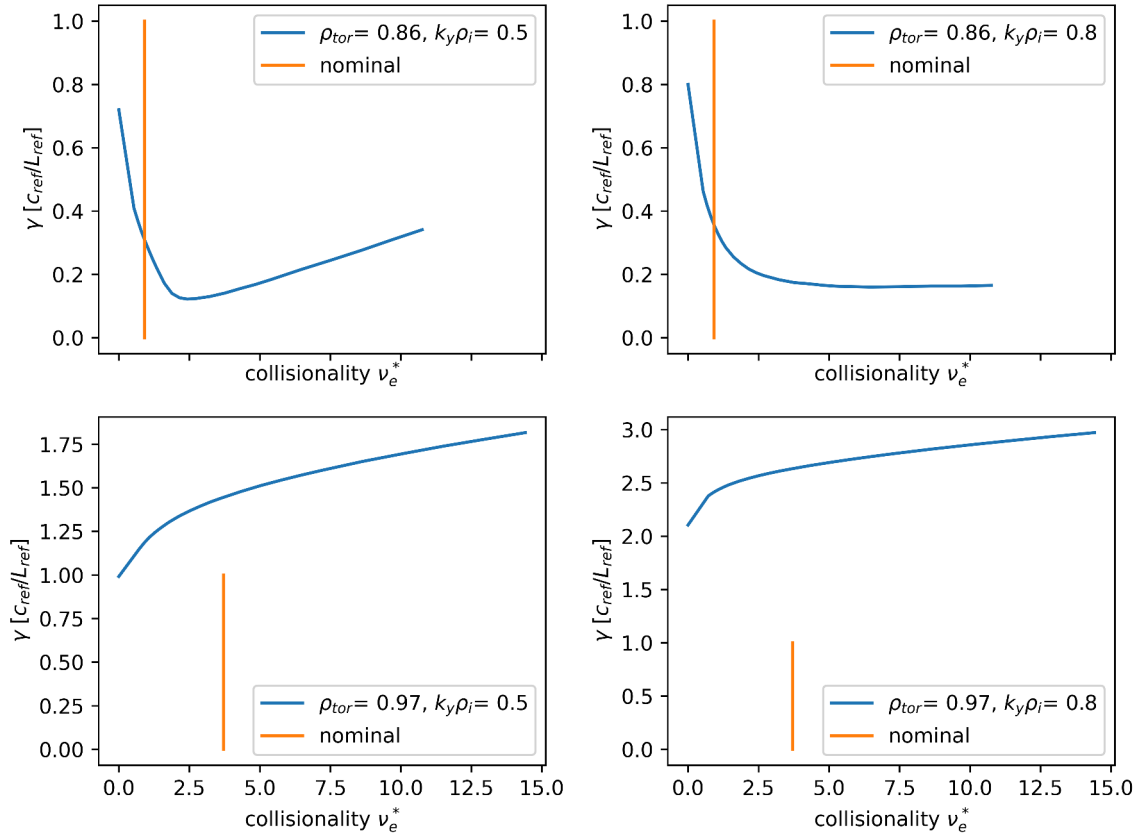


Fig. 5.11.: Growth rates as a function of collisionality at pedestal top ($\rho_{tor} = 0.86$, top) and center ($\rho_{tor} = 0.97$, bottom) and two ion scale wavenumbers $k_y \rho_i = 0.5$ (left) and $k_y \rho_i = 0.8$ (right). Nominal collisionality in orange. The collisionality as defined in Eq. (6.87) of [154] is $\nu_e^* = \sqrt{2} a B_0 / (B_{p0} v_{T,e} \epsilon^{3/2} \tau_e)$, with the minor radius a , thermal velocity $v_{T,e} = \sqrt{2T_e/m_e}$, inverse aspect ratio $\epsilon = a/R$ and the electron collision time τ_e .

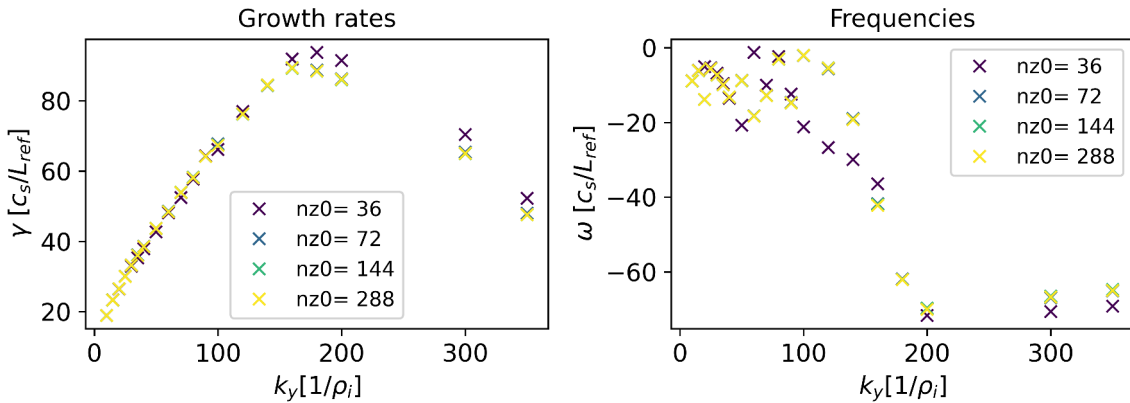


Fig. 5.12.: Growth rate and frequency spectrum at $\rho_{tor} = 0.97$ for different parallel resolutions $nz0$.

5. AUG pedestal simulations

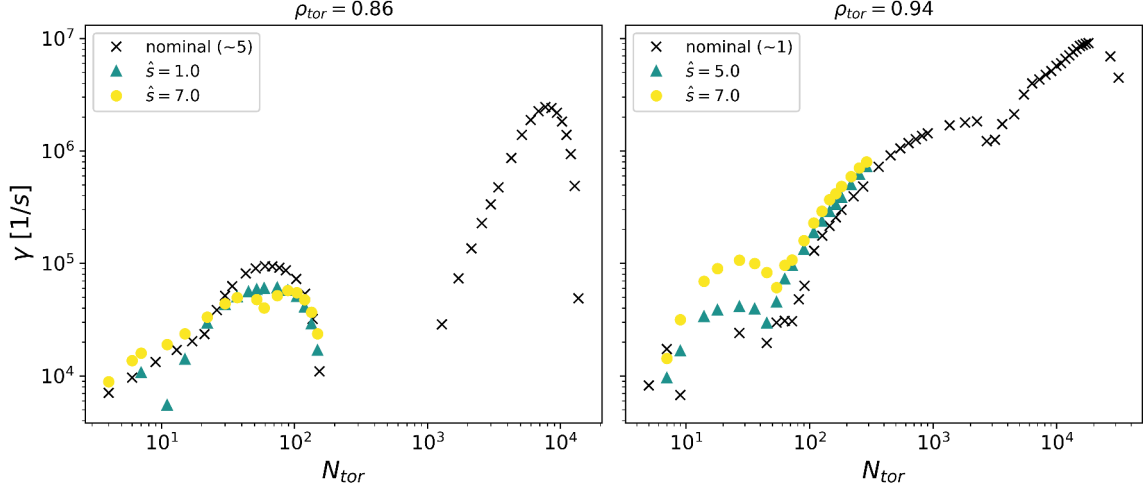


Fig. 5.13.: Linear, local growth rates as a function of the toroidal mode number N_{tor} for three magnetic shear (\hat{s}) values at two different radial positions. Left: pedestal shoulder $\rho_{\text{tor}} = 0.86$. Right: low shear region $\rho_{\text{tor}} = 0.94$. Black crosses are nominal growth rates.

have relevant contributions to the heat flux. So even though $n_z = 72$ is sufficient to capture the maximum linear growth rate accurately, one can not deduce that $n_z = 72$ is sufficient for nonlinear simulations. Indeed, as we will show later in this chapter, it is not.

5.2.1. Pressure and magnetic shear effect: 2nd stability region

The low growth rates on ion scales in the intermediate region ($\rho_{\text{tor}} = 0.94$) between pedestal top and steep gradient are caused by the interplay of low magnetic shear and already increased pressure gradient. Their interplay locally stabilizes ballooning modes (2nd stability region). This can be shown by a scan over the magnetic shear at this position (see Fig. 5.13, right plot). At nominal parameters (black crosses), no clear ion scale mode is present, but with increasing magnetic shear \hat{s} (green triangles and yellow circles), the system leaves the 2nd stability region, and an ion scale mode becomes unstable. At the pedestal shoulder, where a lot of transport is driven on ion scales, lowering the magnetic shear, unfortunately, does not decrease growth rates significantly since the pressure gradient is too low to access the 2nd stability region (Fig. 5.13, left plot green triangles). In contrast, a high magnetic shear lets the pedestal shoulder enter the 1st stability region, where TEMs are suppressed (yellow circles). The influence of the 2nd stability region on microinstabilities has previously, for example, been observed for Internal Transport Barriers [155, 156]. Further scans with e.g. modified profiles are not within the scope of this thesis, but these results illustrate the potential of reducing

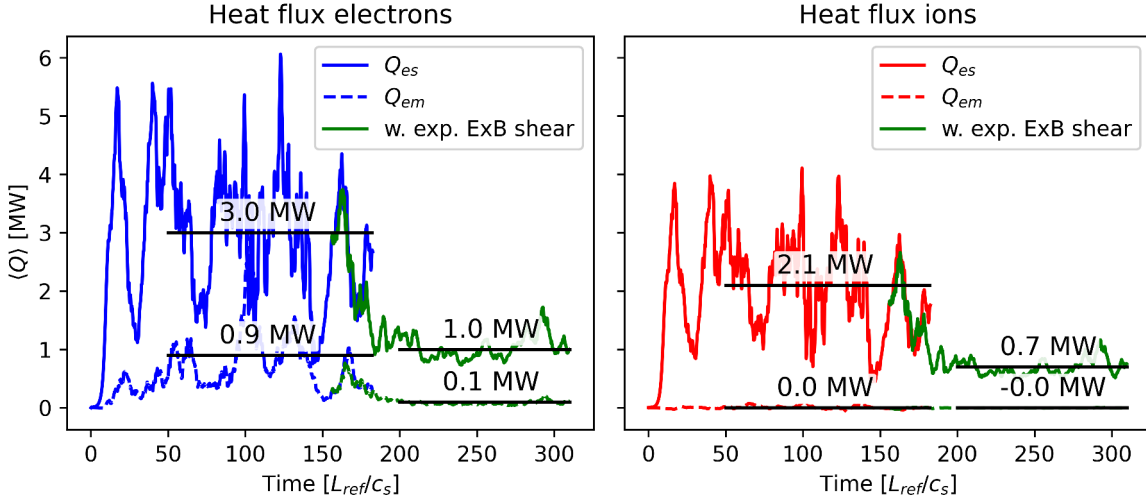


Fig. 5.14.: Volume-averaged heat fluxes (electrostatic Q_{es} and electromagnetic Q_{em}) for electrons (blue, left) and ions (red, right) as a function of time in MW. The green continuations include an external background velocity shear corresponding to experimentally measured $E \times B$ shear.

microturbulence instabilities through careful tailoring of safety factor and pressure profiles.

5.3. Nonlinear simulations

To calculate heat fluxes, we have performed nonlinear, global simulations on ion scales and nonlinear, local simulations on electron scales. This separation is motivated by a strongly reduced computational cost compared to a global multi-scale simulation that resolves all scales in a single simulation. I begin the discussion with the ion-scale simulations.

These are gradient-driven, global, nonlinear, electromagnetic simulations at experimental β values, enabled by the code upgrade presented in Chapter 3. These simulations cover $\rho_{\text{tor}} = 0.85 - 0.995$ in radius (almost the full width shown in Fig. 5.2) and $k_y \rho_i = 0.05 - 1.6$ in binormal wavenumber (corresponding to a toroidal wavenumber $N_{\text{tor}} \approx 4 - 124$), indicated by the left shaded region in Fig. 5.7. They are two species simulations (Deuterium and electrons) with correct mass ratio ($m_e/m_D = 1/3670$), collisions (Landau collision operator), perpendicular magnetic fluctuations $\bar{A}_{1\parallel}$, but without compressional magnetic perturbations $B_{1\parallel}$. When indicated, the simulations include the effect of $E \times B$ rotation due to the radial electric field E_r (cf. Fig. 5.5). For numerical reasons, the background flow in GENE is restricted to the toroidal direction (cf. 3.2.5). To approximate the $E \times B$ shear effect, we retain the magnitude of $v_{E \times B}$

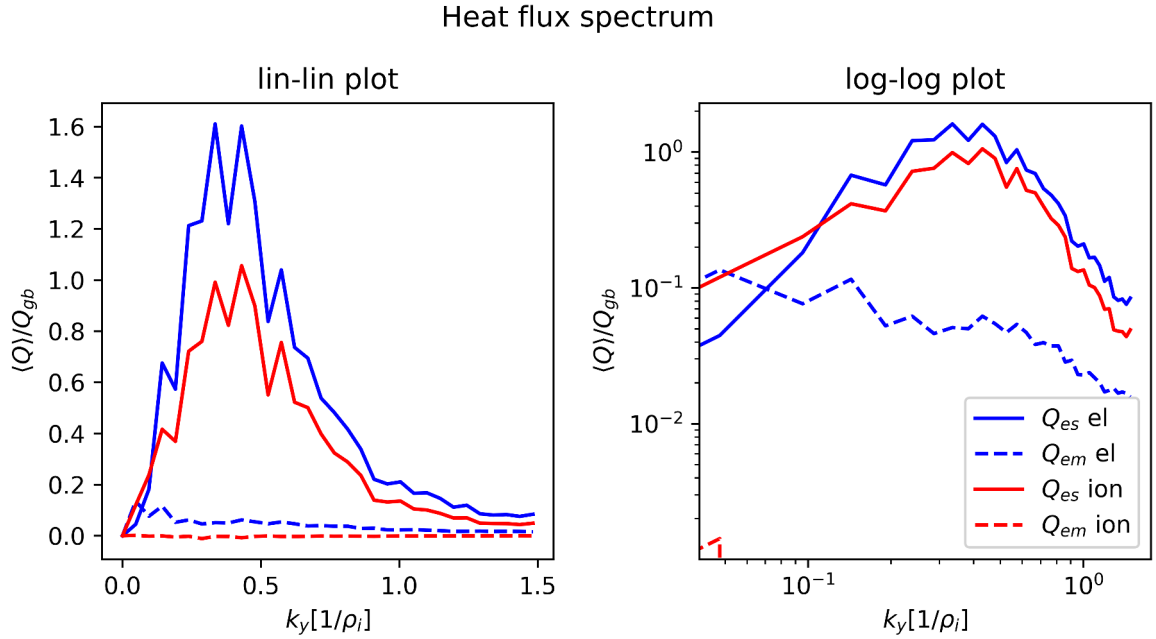


Fig. 5.15.: Heat flux spectra (electrostatic Q_{es} (solid) and electromagnetic Q_{em} (dashed)) of electrons (blue) and ions (red) for the global nonlinear simulation with $E \times B$ shear.

but rotate it to be purely toroidal. In total, the nonlinear global simulations required about 2.5×10^6 CPUh. More details on e.g. grids are specified in the appendix A.2.

The obtained heat fluxes are shown in Fig. 5.14 as a function of time, averaged over real space (flux surface and radius, including the radial buffer zones (see appendix)). In both, the ion and electron channel, the electrostatic heat flux dominates. But while the ions show vanishing electromagnetic heat flux, the electron heat flux is about 1/4 electromagnetic. When including $E \times B$ shear in the simulations, the heat flux is strongly damped in all channels. The electrostatic heat flux is damped by a factor of three, and the electromagnetic heat flux is damped even stronger.

Fig. 5.15 shows the binormal (k_y) heat flux spectrum of the simulation with $E \times B$ shear, analyzed in the time window [200,309] (black bar in Fig. 5.14). Electrostatic transport peaks around $k_y \rho_i = 0.4$, i.e. in the TEM region. The peak of electromagnetic transport is shifted to slightly larger k_y 's, in agreement with the linear MTM presence. At the highest k_y resolved in the simulation, the heat flux is strongly reduced, justifying the cut-off at this scale.

The analysis of the radial heat flux profile is performed in its own subsection, see Sec. 5.3.3. Convergence tests are presented in subsection 5.3.4.

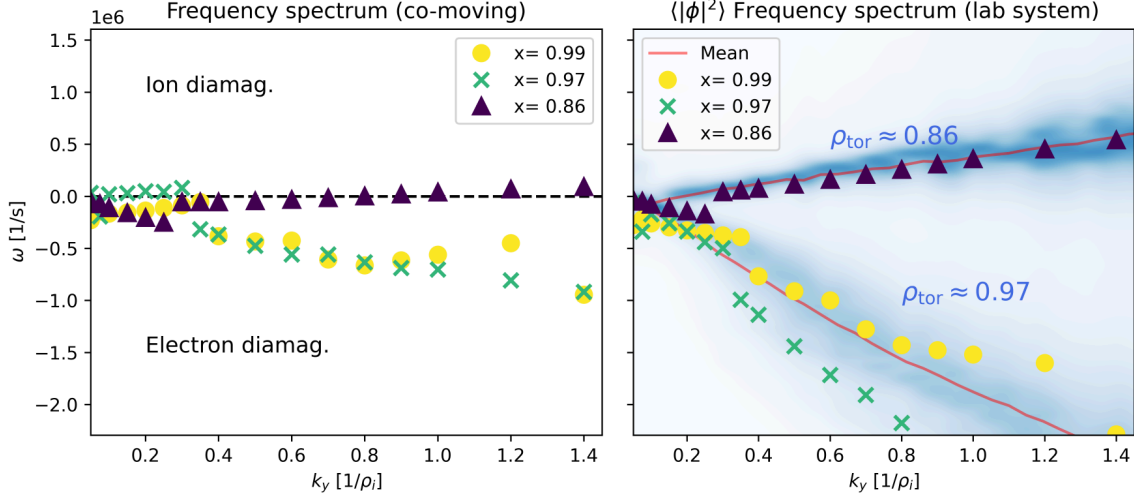


Fig. 5.16.: Comparison of frequencies of global ion scale simulations with linear simulations at two radial positions. Left: Frequency spectra at three radial positions from the linear simulations in a co-moving frame with the plasma. Right: Superposition of the frequency distribution from two positions of the global simulation (blue). Overlaid are the linear frequencies shifted to the lab frame. See main text for details.

5.3.1. Connecting linear and nonlinear results: Frequencies and cross phases

To identify the dominant turbulent transport mechanisms, results from linear and nonlinear simulations have to be connected to test if linear features remain visible and, hence, relevant in the nonlinear saturated state. This can, for instance, be achieved by comparing frequencies and cross phases.

Fig. 5.16 shows the mode frequencies of the linear and nonlinear simulations. The left plot shows the frequency spectrum of the local, linear simulations for three radial positions (pedestal shoulder at $\rho_{\text{tor}} = 0.86$, center at $\rho_{\text{tor}} = 0.97$ and foot at $\rho_{\text{tor}} = 0.99$) in the co-moving frame of reference. In the pedestal shoulder spectrum (violet triangles), the transition from MTM to TEM is visible, and at the pedestal center (yellow circles), the transition from ITG to TEM/ETG. The right plot shows the frequency spectrum of the global, nonlinear simulation analyzed at two positions (pedestal shoulder and center) overlaid by the local, linear spectra. Usually, frequencies from local simulations are specified in a frame co-moving with the $E \times B$ rotation. Since the $E \times B$ rotation depends on the radial position, frequencies of global simulations are specified in the lab frame. For the comparison of both, we transform the local frequencies also to the lab frame, using:

$$\omega_{\text{lab}} = \omega_{\text{co-mov.}} - \Omega_{\text{tor}} C_y \frac{L_{\text{ref}}}{\rho_{\text{ref}}} \frac{L_{\text{ref}}}{c_{\text{ref}}} k_y \quad (5.1)$$

5. AUG pedestal simulations

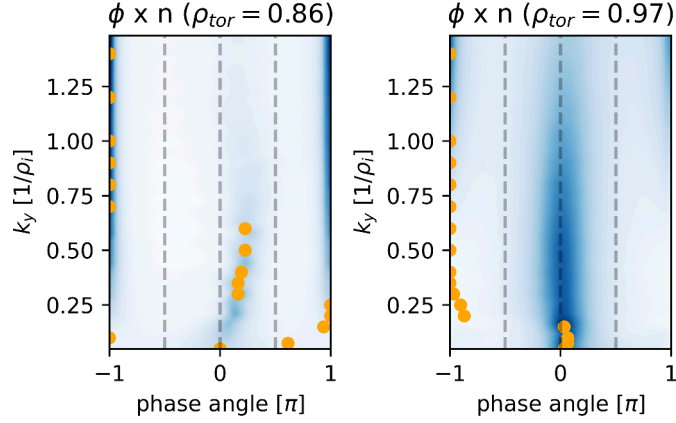


Fig. 5.17.: Cross-phases of electric potential ϕ and electron density fluctuations n from nonlinear simulations (blue background) and linear simulations (orange circles).

with the angular toroidal velocity Ω_{tor} . The sign of Ω_{tor} has to be carefully determined in the chosen coordinate system and conventions on the direction of I_p and B_t . The sign of Ω_{tor} may change with radius, as E_r changes sign.

The comparison shows that at the pedestal shoulder and even center, the linear frequencies persist in the nonlinear simulations. This indicates that the linearly fastest growing modes remain important in the saturated turbulent state. However, one crucial difference appears: At the pedestal shoulder ($\rho_{tor} = 0.86$) and $k_y \rho_i \approx 0.3$ the nonlinear simulation (right plot, upper red line) does not show the mode transition that linear, local simulations present (right plot, violet triangles). This suggests that MTMs are suppressed or at least restricted to the very largest scales in global, nonlinear simulations compared to the local, linear ones. Neither the global nor the local simulations included $\bar{B}_{1\parallel}$ fluctuations. These might impact the presence of MTMs.

The cross-phases of electric potential and electron density fluctuations (see Fig. 5.17) support this picture: Linear mode structures survive in the nonlinear simulations, but on largest scales at the pedestal top differences are visible (left plot), corroborating the suppression of MTM in global, nonlinear simulations observed in the frequency comparison. In the pedestal center (right plot), linear and nonlinear simulations show a cross-phase of $\phi \times n = \pi \equiv 0$ for most of the analyzed k_y s, indicating vanishing turbulent particle transport.

Overall, the remarkable agreement in the frequency and cross-phase comparison between local/linear and global/nonlinear simulations at pedestal shoulder and center encourages the extension of quasilinear models to the pedestal region.

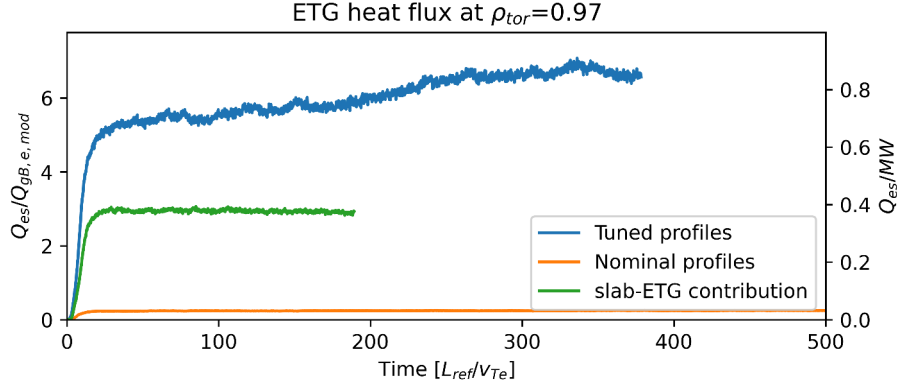


Fig. 5.18.: Heat flux due to ETGs at $\rho_{tor} = 0.97$ as a function of time. $L_{ref} = 0.65$ m, $v_{Te} = \sqrt{2T_e/m_e}$. Left axis in units of modified electron gyroBohm units $Q_{gB,e,mod} = Q_{gB,e} \times 1/L_{Te}^2$ following [104], right axis in units of MW. $Q_{gB,e,mod}$ is evaluated at $\rho_{tor} = 0.97$ for the tuned profiles.

5.3.2. Local, electron scale simulations

Local, nonlinear electron scale simulations have been performed at multiple radial positions between pedestal top and foot. They complement the global, nonlinear simulations, which only cover ion scales up to $k_y \rho_i = 1.6$ at the reference flux-surface. The dedicated ETG simulations cover $k_y \rho_i = 2.5 - 157.5$, i.e. $k_y \rho_e = 0.04 - 2.6$, as indicated by the right shaded region in Fig. 5.7. The simulations use adiabatic ions. Resolutions and further simulation settings are given in the appendix. Fig. 5.18 shows the ETG heat flux obtained in the steep gradient region ($\rho_{tor} = 0.97$) with nominal profiles and tuned profiles that are designed to increase ETG drive but remain within experimental uncertainties at all locations, see Fig. 5.22. At $\rho_{tor} = 0.97$, the tuned profiles have approx. 30% increased $1/L_{Te}$ and 30% decreased $1/L_{ne}$, resulting in a change of $\eta_e = L_{ne}/L_{Te}$ from approx. 1.5 to 3. To make a connection to recent ETG transport scalings for JET and DIII-D [104, 109, 123] heat fluxes are shown in modified electron gyroBohm units (see figure caption) and MW. At nominal parameters, the ETG heat flux is very small, whereas with tuned profiles, ETGs drive substantial transport of about 0.9 MW. This indicates a strong stiffness of ETG transport in the pedestal center. By artificially neglecting magnetic drifts in the simulation, we can selectively turn off the drive of the toroidal ETG branch to assess the relative importance of slab and toroidal ETG for heat transport. The pure slab-ETG simulation produces less than half of the original transport. This shows that nonlinearly, both, slab and toroidal branches contribute substantially to the ETG heat transport in this scenario.

Fig. 5.19 shows the heat flux spectrum of the nonlinear ETG simulations with and

5. AUG pedestal simulations

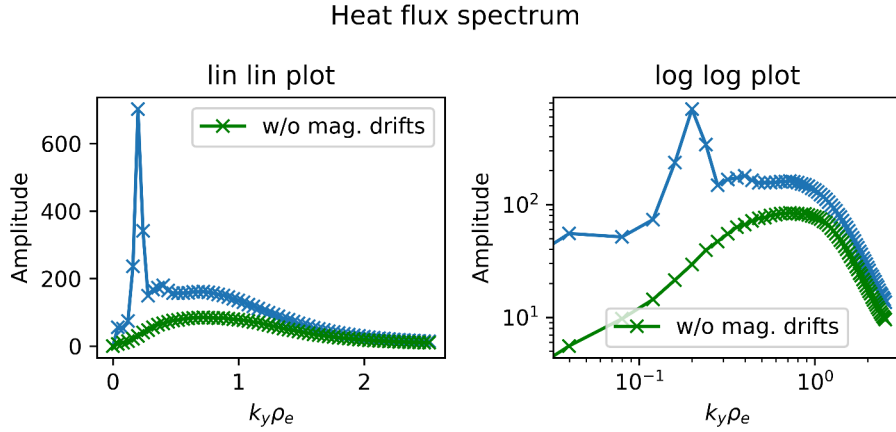


Fig. 5.19.: Heat flux spectra of the nonlinear ETG simulation with and without magnetic drifts.

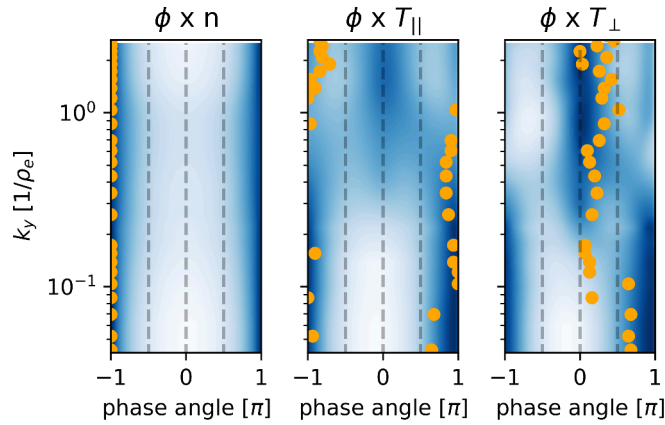


Fig. 5.20.: Cross-phases of electric potential ϕ and electron density fluctuations n (left), parallel temperature component (middle), and perpendicular temperature component (right) from nonlinear simulations (blue background) and linear simulations (orange circles).

without magnetic drifts. Without magnetic drifts the toroidal mode at $k_y \approx 0.2\rho_e^{-1} \approx 12\rho_i^{-1}$ is not present. Towards high k_y , the heat flux strongly reduces, justifying the cut-off of the simulation at this scale.

Fig. 5.20 establishes a connection between the linear and nonlinear ETG simulations by comparing different cross-phases. As expected, ETGs do not contribute to particle transport and $\phi \times n = \pi$ linearly and nonlinearly. In the potential-temperature cross-phases $\phi \times T$, linear and nonlinear simulations show some resemblance but no clear agreement.

Fig. 5.21 shows scans in the parallel hyperdiffusion and resolution performed for the nonlinear ETG simulations. For different parallel resolutions ($n_z = 144, 288, 576$),

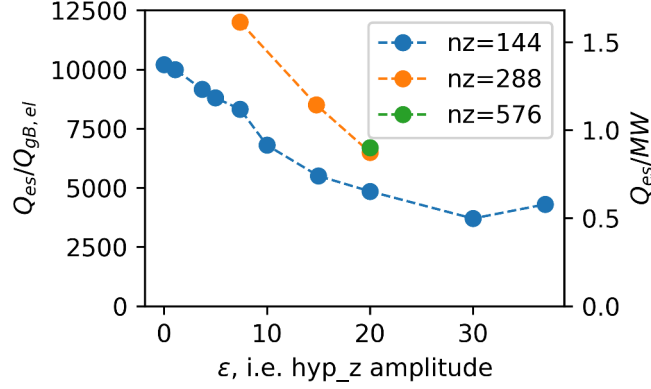


Fig. 5.21.: Dependence of heat flux on parallel hyperdiffusion and resolution.

the influence of the hyperdiffusion amplitude was scanned. The hyperdiffusion values given here correspond to simulations with the following settings: Ion mass normalization ($\hat{m}_i = 1$), `hypz_with_dz_prefactor=F`, `arakawa_zv=T`, `edge_opt=0` and positive `hyp_z` values. As discussed in Sec. 3.6, for `hyp_z=0`, artificial grid-scale oscillations are present. As the hyperdiffusion amplitude is increased, these oscillations are damped, and the heat flux converges (see blue line). An increase in the parallel resolution shifts the damping of the hyperdiffusion to modes with higher k_{\parallel} as explained in Sec. 3.6. This allows a wider range of physical k_{\parallel} modes to exist in the system. The resolution increase to $n_z = 288$ (orange) shows that these modes contribute to the total heat flux. A further resolution increase to $n_z = 576$ (green) shows no further increase in the total heat flux, i.e. convergence. For $hyp_z = 20$, the heat flux converged at a parallel resolution of $n_z = 288$.

5.3.3. Heat flux profile

To study how turbulent transport changes across the pedestal, we consider the heat flux averaged over time and flux surface as a function of the radius. Fig. 5.23 shows essential aspects of the turbulent heat flux profile in the studied ASDEX Upgrade pedestal. Particular care has to be taken with regard to the normalization of the heat flux. Due to the substantial temperature changes across the pedestal, the commonly used gyro-Bohm heat flux based on mixing-length estimates $Q_{gB} = c_s p_i \rho^{*2} = (T_i/m_i)^{1/2} n_i T_i \rho^{*2}$ changes by two orders of magnitude across the pedestal (top left plot). A modified gyro-Bohm heat flux $Q_{gb,mod} = Q_{gb} \times \max(a/L_{Ti}, a/L_{Te})^2$, in which the gradient length replaces the minor radius as the macroscopic length scale, exhibits strong variations across the pedestal as well. We will, therefore, focus the analysis on the heat flux in SI units.

5. AUG pedestal simulations

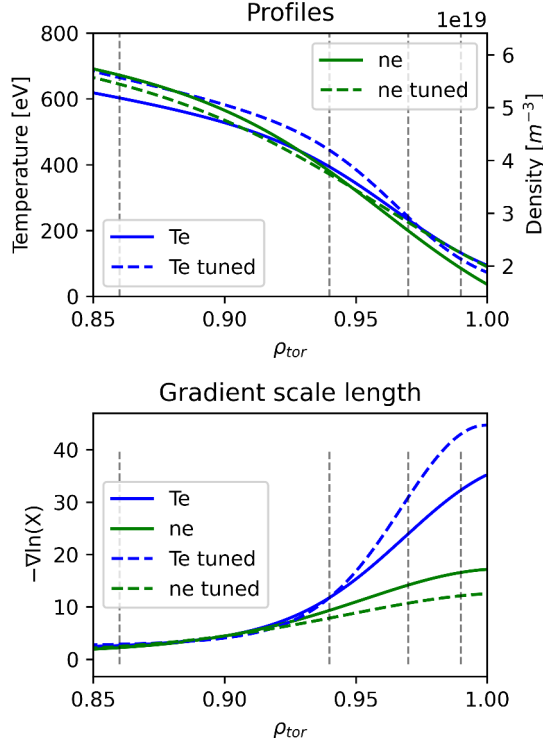


Fig. 5.22.: Tuned electron temperature and density profiles (dashed) used to test the sensitivity of ETG heat flux in comparison to nominal profiles (solid).

Fig. 5.23 (top right) shows the profiles of the different heat flux components (electrostatic, electromagnetic, electron, ion). The dominant component over most of the pedestal is electrostatic electron heat flux (blue solid line), with the exception of $\rho_{tor} \approx 0.97$, where the electrostatic ion heat flux has a local peak. This peak corresponds to the ITG/KBM mode identified in the linear analysis, which occurs at the peak of the ion temperature gradient. Interestingly, the turbulent ion scale heat flux is strongly reduced in all channels from pedestal top to pedestal center and foot - even without $E \times B$ shear. The onset of this reduction coincides with the region of linear stabilization, discussed in Sec. 5.2.1.

Fig. 5.23 (bottom left) illustrates the influence of $E \times B$ shear on the heat flux profiles: It reduces the ion scale heat flux strongly and widens the region of almost vanishing turbulent heat flux. The responsible $E \times B$ shear profile is shown in Fig. 5.5. The shear is non-zero in the whole simulation domain, increasing noticeably starting from $\rho_{tor}=0.9$ and having local peaks at $\rho_{tor}=0.94, 0.96$, and 0.98 . This corresponds well to the almost complete suppression of ion-scale heat flux from $\rho_{tor} \approx 0.92$. The small ion heat flux peak in the pedestal center $\rho_{tor} = 0.97$ corresponds to the minimum of the $E \times B$ velocity, where the shear vanishes.

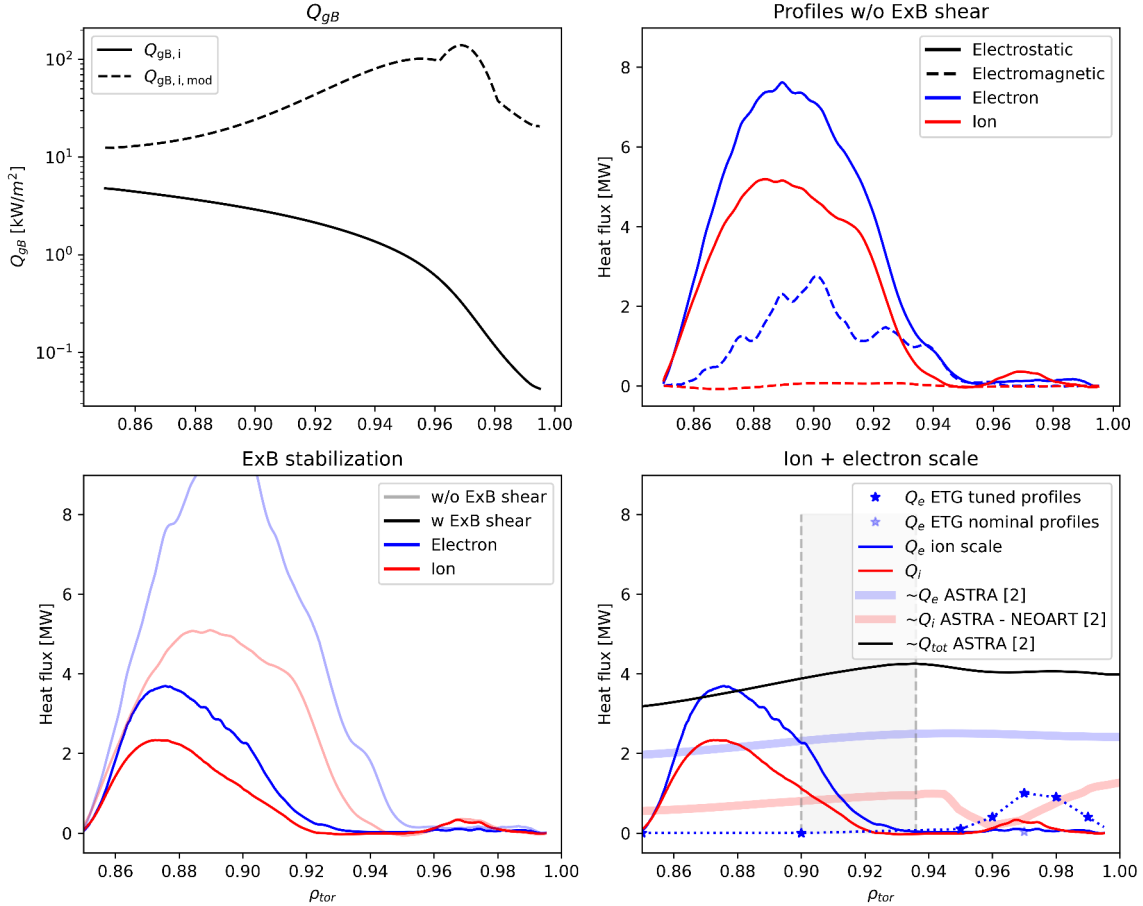


Fig. 5.23.: Turbulent heat flux profile in an ASDEX Upgrade pedestal from pedestal top to foot. Top left: Gyro-Bohm heat flux profile. Top right: Components of the ion scale heat flux profile without $E \times B$ shear. Bottom left: Total heat flux ($Q_{es} + Q_{em}$) due to ion scale turbulence with and without $E \times B$ shear. Bottom right: Total heat flux due to ion scale turbulence from global simulations (red and blue solid line) as well as ETG heat fluxes from local simulations at nominal values (light blue stars) and increased electron temperature gradient (dark blue stars) compared with power balance calculations (broad lines). Region of increased measurement uncertainty in grey.

5. AUG pedestal simulations

Fig. 5.23 (bottom right) shows that the turbulent heat flux on electron scales behaves oppositely across the pedestal compared to the ion scale turbulent heat flux: It vanishes at the pedestal top and strongly increases down the pedestal (stars).

A comparison to power balance and neoclassical calculations shows qualitative agreement in heat flux structure and trends (bottom right plot). The electron channel is dominant throughout the pedestal. Our gyrokinetic simulations reveal that the electron heat flux transitions in scale. At the pedestal top/shoulder, it is driven by ion scale TEM/MTM turbulence, while at the pedestal center and foot, it is driven by small-scale ETG turbulence. While power balance considerations suggest a roughly constant electron heat flux across the pedestal, our gyrokinetic simulations find a reduction towards the pedestal center. The discrepancy might, e.g. be due to T_i and T_e profile uncertainties influencing simulations as well as the implicit uncertainties of the interpreted power balance results.

The region around $\rho_{\text{tor}} = 0.92$ where the total gyrokinetic electron heat flux reaches a minimum likely indicates a limitation of our separate scale ansatz. At this location, heat flux is likely driven by scales that are neither resolved in our global simulations nor the electron scale simulations (cf. Fig. 5.7) and would require multi-scale simulations to be adequately resolved. The ion channel contributes substantially to the total heat flux at the pedestal top/shoulder and reduces to neoclassic values towards the pedestal center. At the pedestal foot, our gyrokinetic simulations do not show the increase of ion heat flux suggested by power balance. The differences in the grey-shaded region are possibly due to increased measurement uncertainties in the ion profile that affect both power balance (see [152]) and gyrokinetic simulations.

For the power balance comparison, the turbulent ion heat flux component was estimated by subtracting neoclassic heat flux calculated with NEOART from the ASTRA result (both from [152]). The total ion heat flux due to power balance is constant [152], and the minimum in the turbulent heat flux is compensated by an increased neoclassical heat flux, which has a roughly constant diffusivity across the pedestal so that its heat flux follows the increasing ion temperature gradient.

The following picture emerges for the investigated scenario: Turbulent heat flux at the pedestal top is dominated by electrostatic TEMs with electromagnetic MTM contributions. The interplay of low magnetic shear and increasing pressure gradient stabilizes modes locally before the steep gradient region ($\rho_{\text{tor}} \approx 0.94$) and reduces turbulent heat flux. $E \times B$ shear suppresses turbulent heat flux strongly in all channels and widens the region of vanishing turbulent ion scale heat flux. Turbulent electron heat flux changes scale across the pedestal, and turbulent ion heat flux strongly reduces towards the

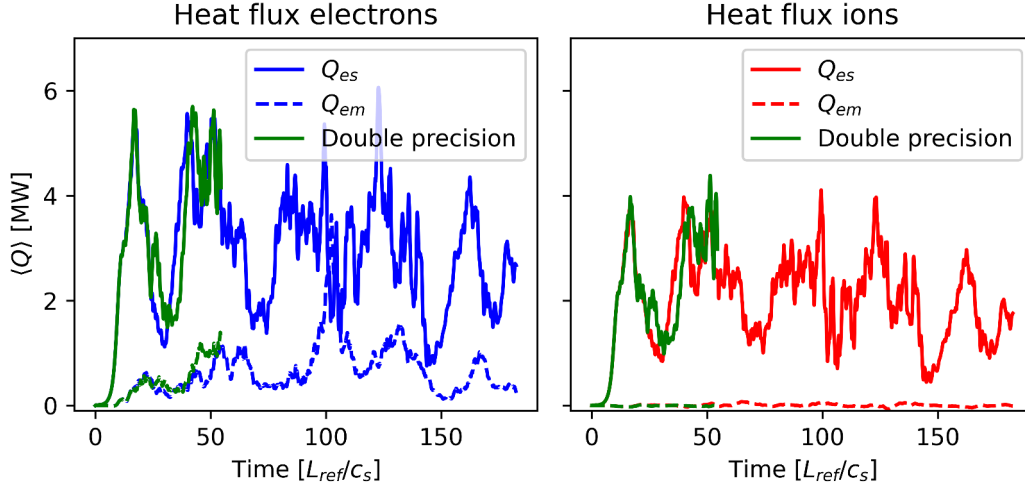


Fig. 5.24.: Convergence test: Double precision.

pedestal center.

5.3.4. Convergence tests

Convergence tests for linear simulations and local, nonlinear ETG simulations have been shown in previous sections. Parallel resolution and parallel hyperdiffusion were discussed. In this section, several convergence tests for the global, nonlinear simulations are discussed.

A principal challenge for convergence tests of the global, nonlinear simulations is the high computational cost of these simulations. Any further increase of the resolution increases this cost even more. Additionally, the high number of degrees of freedom in setting up the simulation (resolution of all five phase space dimensions, time step size, source, sink and boundary settings, hyperdiffusion amplitudes, collision operator settings, and further discretization settings (block-structured grids setup, edge_opt)) renders exhaustive convergence tests unfeasible. A pragmatic compromise has to be found between computational cost and the verification of results. Here, a few convergence tests are discussed on the basis of the resulting heat flux.

Fig. 5.24 compares simulations run with single-precision floating-point format and double-precision floating-point format. They show good statistical agreement, such that most global, nonlinear production runs were performed in single precision. The use of single precision speeds up the simulations almost by a factor of two. Within a collaboration with MPCDF the use of half-precision floating-point format in GENE simulations is currently being evaluated, which promises additional speed-up in partic-

5. AUG pedestal simulations

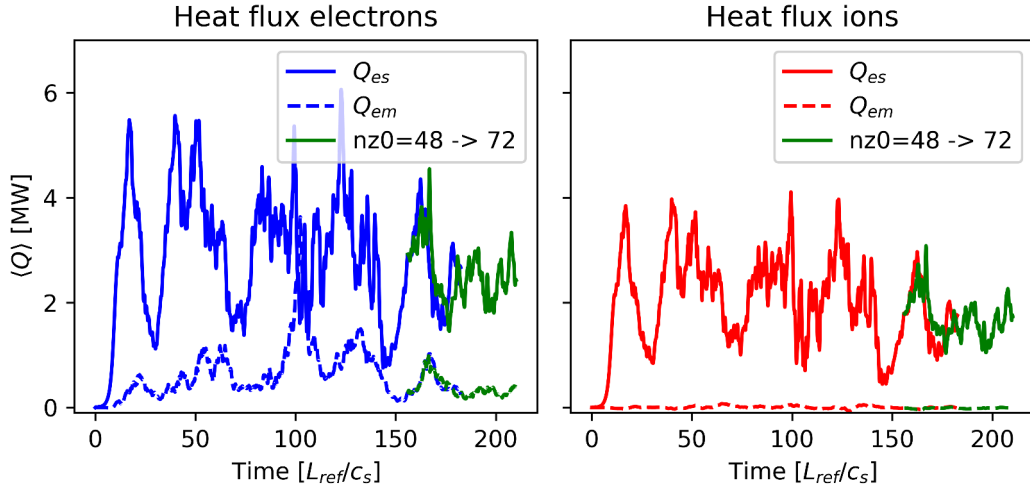


Fig. 5.25.: Convergence test: Parallel resolution

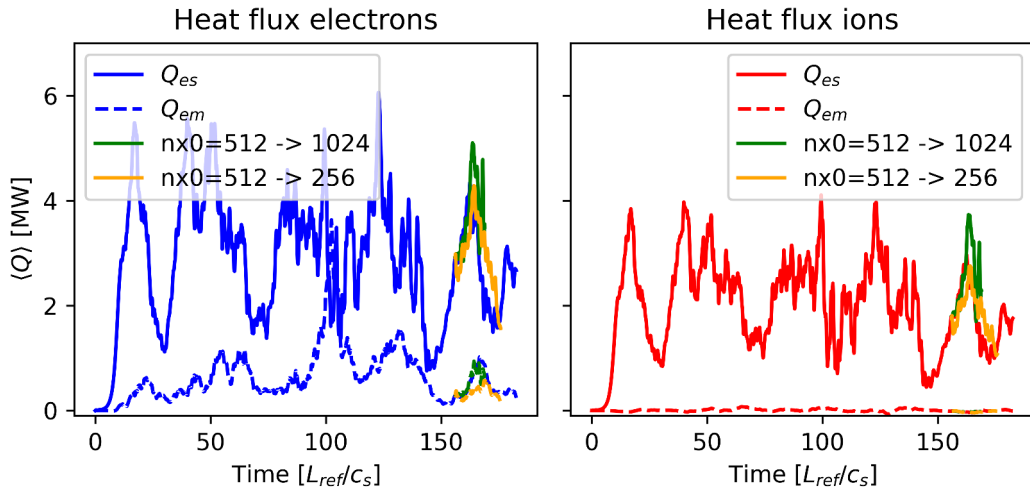


Fig. 5.26.: Convergence test: Radial resolution.

ular in combination with the use of GPUs.

Fig. 5.25 shows a continuation of a global, nonlinear simulation with increased parallel resolution, $n_z = 72$ instead of $n_z = 48$. No strong change in the average heat flux level is observed.

Fig. 5.26 shows a continuation of a global, nonlinear simulation with increased and decreased radial resolution. No strong sudden changes are observed, and a good overlap of time traces between different resolutions is observed. To assess the impact on the average heat flux values, the test simulations are not yet long enough.

Fig. 5.27 shows a continuation of a global, nonlinear simulation with decreased radial hyperdiffusion. No strong changes are observed in the simulated time window.

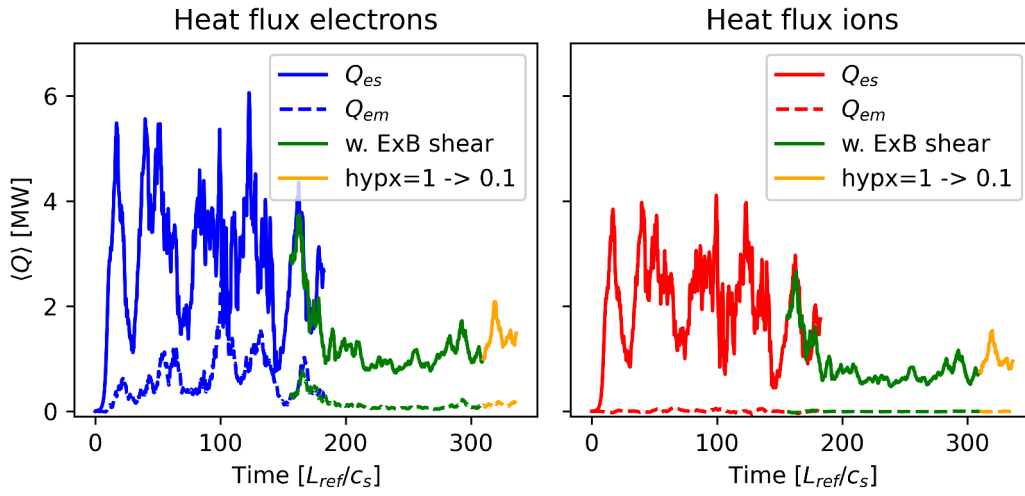


Fig. 5.27.: Convergence test: Radial hyperdiffusion hyp_x .

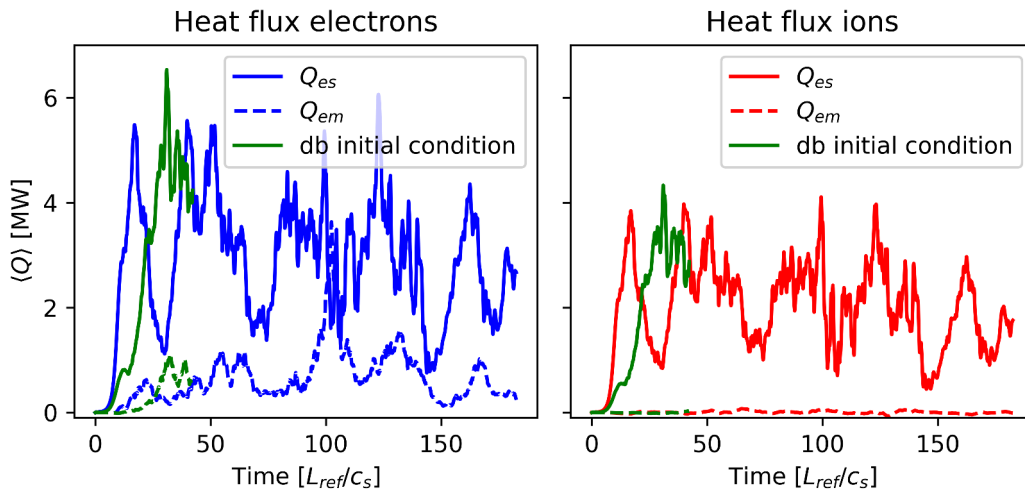


Fig. 5.28.: Convergence test: Initial condition.

5. AUG pedestal simulations

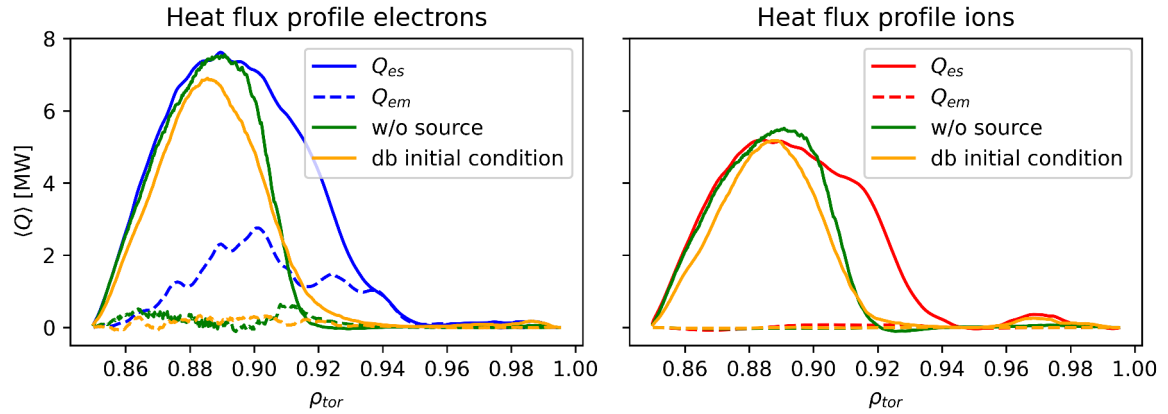


Fig. 5.29.: Convergence test: Heat flux profile without sources and a different initial condition.

Fig. 5.28 shows a test of the influence of the initial condition on the heat flux. While the initial linear phase develops differently, as expected, the saturation occurs on the same heat flux level, independent of the initial condition. Initial conditions "density blob" (a Gaussian in x , k_y and z) and "ppjrn" (a power law in k_x , k_y with random phases and powers of the Jacobian in z) are compared.

Fig. 5.29 investigates the possible influence of sources and initial conditions on the heat flux profile. This is done to confirm that the heat flux structure obtained in the global, nonlinear simulations is not an artifact of a specific initial condition or settings in the energy and particle sources. In the simulation without Krook-type heat and particle sources, the kinetic profiles are not maintained, so only a short time interval just after the initial linear phase is investigated. Radial buffers for the boundary conditions were kept. The comparison shows that the heat flux structure with vanishing heat flux in the steep gradient region is also obtained with changes to the initial condition and sources.

5.4. Further ELM timepoints

The previous three sections have analyzed one timepoint of the ELM cycle (6ms after the ELM crash) in detail. It is also interesting to investigate how turbulence changes during an ELM cycle, considering how strongly an ELM crash changes the temperature and density profiles. This section presents the beginning of such a study. Profiles, growth rates, and heat fluxes at the time points +2ms and +4ms are compared with the +6ms time point.

Fig. 5.30 shows the profiles and gradient scale lengths at the time points +2ms (top),

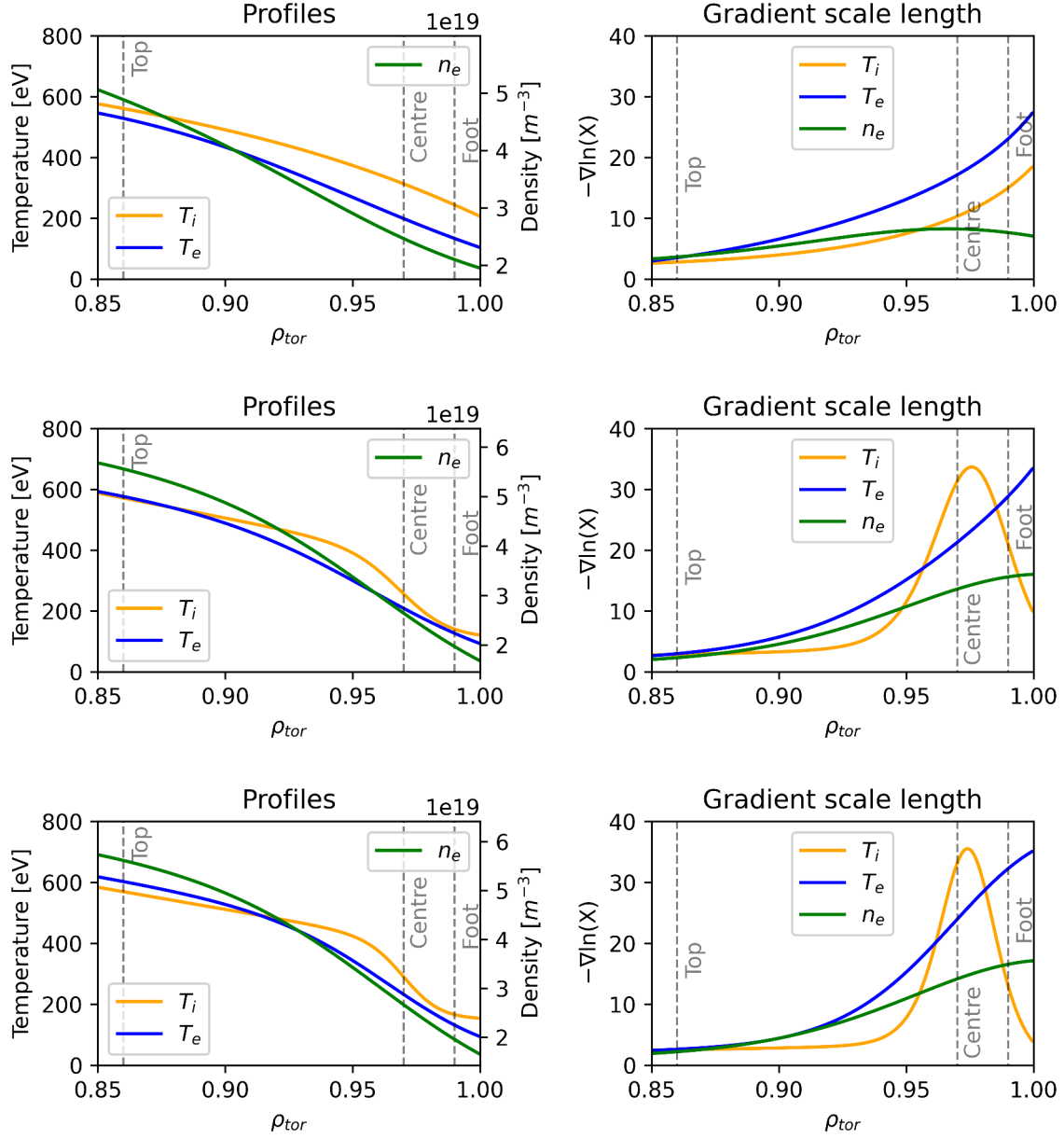


Fig. 5.30.: Profile and gradient comparison for other time points in ELM cycle. From top to bottom: +2ms, +4ms, +6ms. The case +6ms has been investigated in detail in the previous sections.

5. AUG pedestal simulations

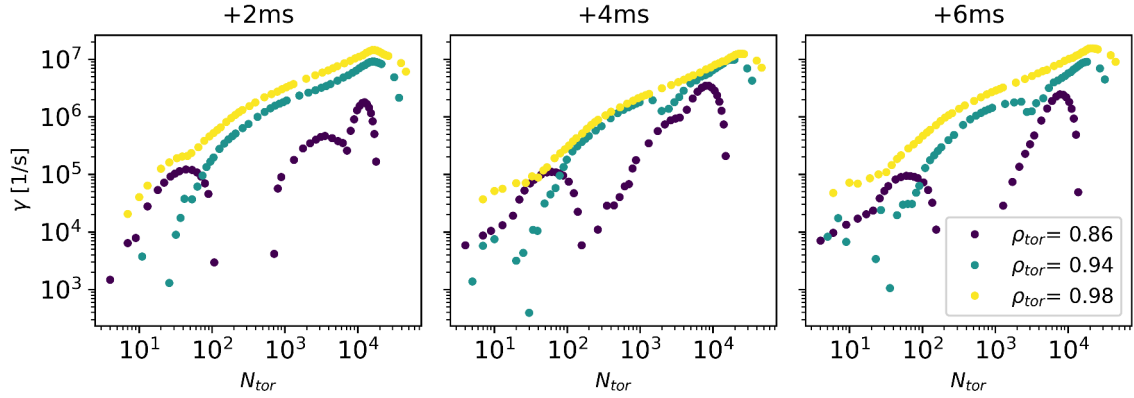


Fig. 5.31.: Growth rate spectra comparison. From left to right: +2ms, +4ms, +6ms. The case +6ms has been investigated in detail in the previous sections.

+4ms (middle), and +6ms (bottom). Shortly after the ELM crash (+2ms) the pedestal has not yet recovered, and gradients are comparatively flat. At +4ms, the pedestal has already partly recovered, in particular, ion temperature and density pedestal have formed. At +6ms, the electron and ion temperature gradients have further increased to conditions very close to the pre-ELM state. During the ELM cycle also, the radial electric field E_r changes, collapsing to L-mode levels at the ELM crash and recovering on time scales of the ion temperature gradient [151]. Hence, the shear flow in the pedestal region changes as well.

The delayed recovery of the electron temperature pedestal in comparison to the density and ion temperature pedestal has been described in Ref. [151]. This has been recently attributed to transport dynamics dominated by heat flux from the core in contrast to local turbulent transport effects in Ref. [152]. Their analysis suggests that the difference in the recovery time is rooted in the different depletion of ion and electron temperatures in the outer core by the ELM. The electron temperature is more strongly reduced in the outer core; hence, it takes longer until the T_e -pedestal is reestablished.

Fig. 5.31 shows growth rate spectra obtained with linear, local simulations for the three time points (left to right) at three positions (colors). For a better direct comparison of growth rates, the x and y axes use units that do not depend on temperature or density normalizations: The toroidal wavenumber N_{tor} instead of $k_y \rho_i$ and $1/s$ instead of c_s/L_{ref} . Scans were performed in the same setup as the +6ms simulations described above, and results are maximized over the ballooning angle. At $\rho_{tor} = 0.86$ on ion scales, a very similar TEM peak is visible during all time points. On electron scales, a second peak exists at +2ms and +4ms. At $\rho_{tor} = 0.94$, the stabilization on ion scales seems present at all time points, showing no clear mode at this position. At $\rho_{tor} = 0.98$

(yellow), an ion-scale peak is present, which is not as prominent in the other time points.

Fig. 5.32 shows a comparison of heat fluxes obtained with global, nonlinear simulations for the three time points. Top: +2ms, Middle: +4ms, Bottom: +6ms. The simulation setup is identical for all three cases. The simulations have been performed without $E \times B$ shear. Hence, they do not include the fact that the shear flows change during an ELM cycle, which influences the turbulent heat fluxes. At all three time points, electrostatic heat transport is dominant, with slightly higher electron heat flux and a non-negligible electromagnetic component in the electron channel. The radially averaged heat fluxes exhibit large fluctuations at all time points. Average turbulent heat fluxes are higher at +2ms and +4ms compared to the +6ms case. Fig. 5.33 reveals that most of the transport visible in these time traces is pedestal top transport. This corroborates the results of the linear comparison that TEM and MTM at the pedestal top are present throughout the ELM cycle. Fig. 5.33 shows that shortly after the ELM crash (top panel), relatively more turbulent heat flux is present at $\rho_{\text{tor}} = 0.97$ compared to the later time points.

The time-resolved power balance analysis of [152] finds a strongly reduced electron heat diffusivity directly after the ELM crash and an electron heat flux lower than the ion heat flux at +4ms in the ELM cycle. This is not observed in the turbulent ion-scale heat fluxes calculated here. Pedestal top turbulent transport at all time points seems to be dominated by TEM/MTM turbulence with slightly more electron than ion heat flux. In the pedestal center, turbulent transport is suppressed, with the highest non-vanishing flux at the time point +2ms.

Further analysis of these simulations is left for future work. Global simulations with $E \times B$ shear and dedicated nonlinear, electron-scale simulations would be natural next steps in this study of turbulent transport at the different inter-ELM time points.

5.5. GENE-Tango approach in the pedestal

The nonlinear simulations presented in the previous sections are all gradient-driven. They rely on given profiles and calculate the resulting heat fluxes. Matching power balance results with gradient-driven simulations typically requires scans in the input gradients. This is straightforward to do for local simulations that are driven by a single constant gradient but is more complicated to do systematically for global simulations. The coupling of gradient-driven GENE simulations with the transport solver Tango [80, 87] offers an automated way of adjusting the input profiles for GENE simulations

5. AUG pedestal simulations

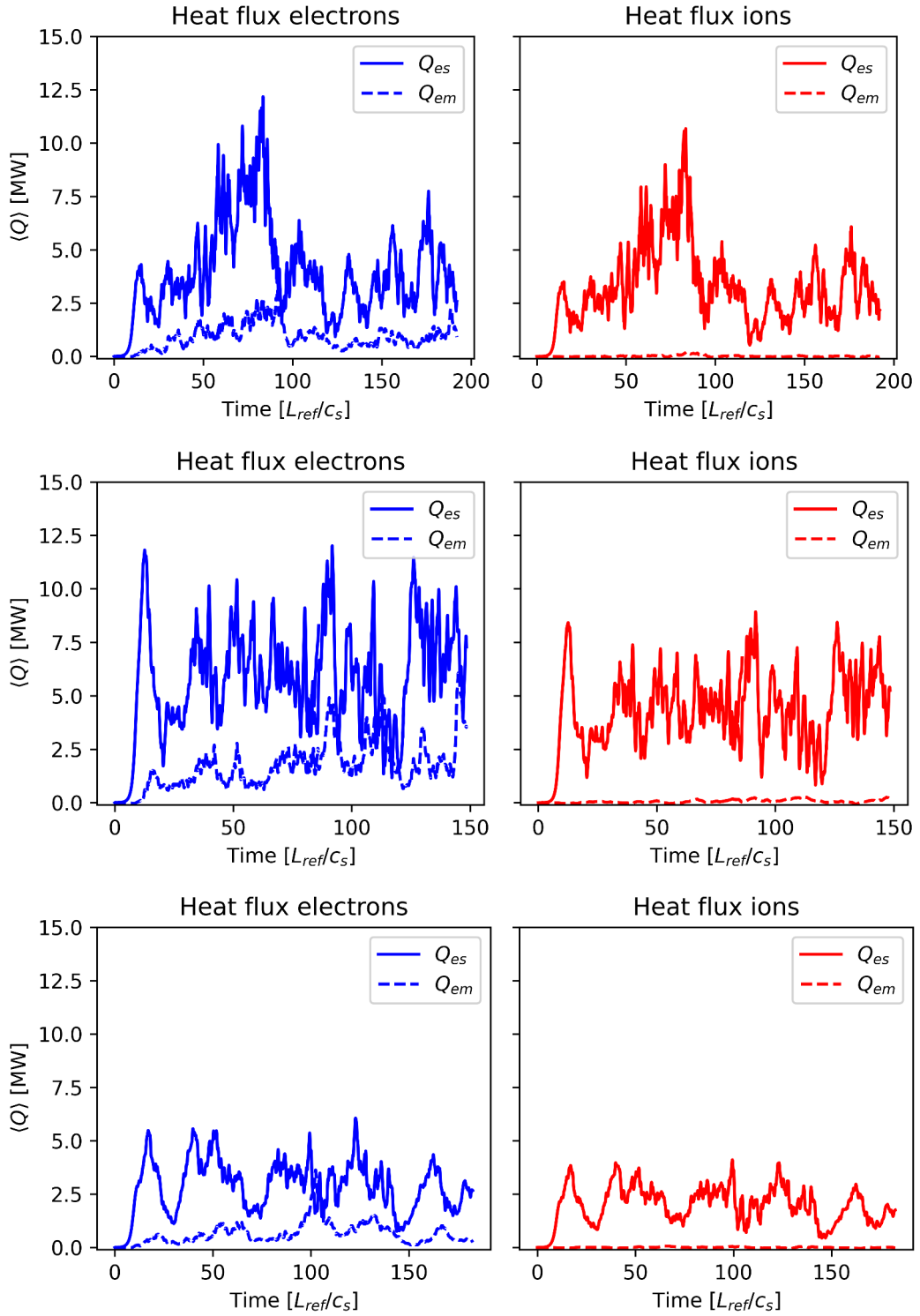


Fig. 5.32.: Heat flux comparisons (radially averaged), without $E \times B$ shear. From top to bottom: +2ms, +4ms, +6ms. The case +6ms has been investigated in detail in the previous sections.

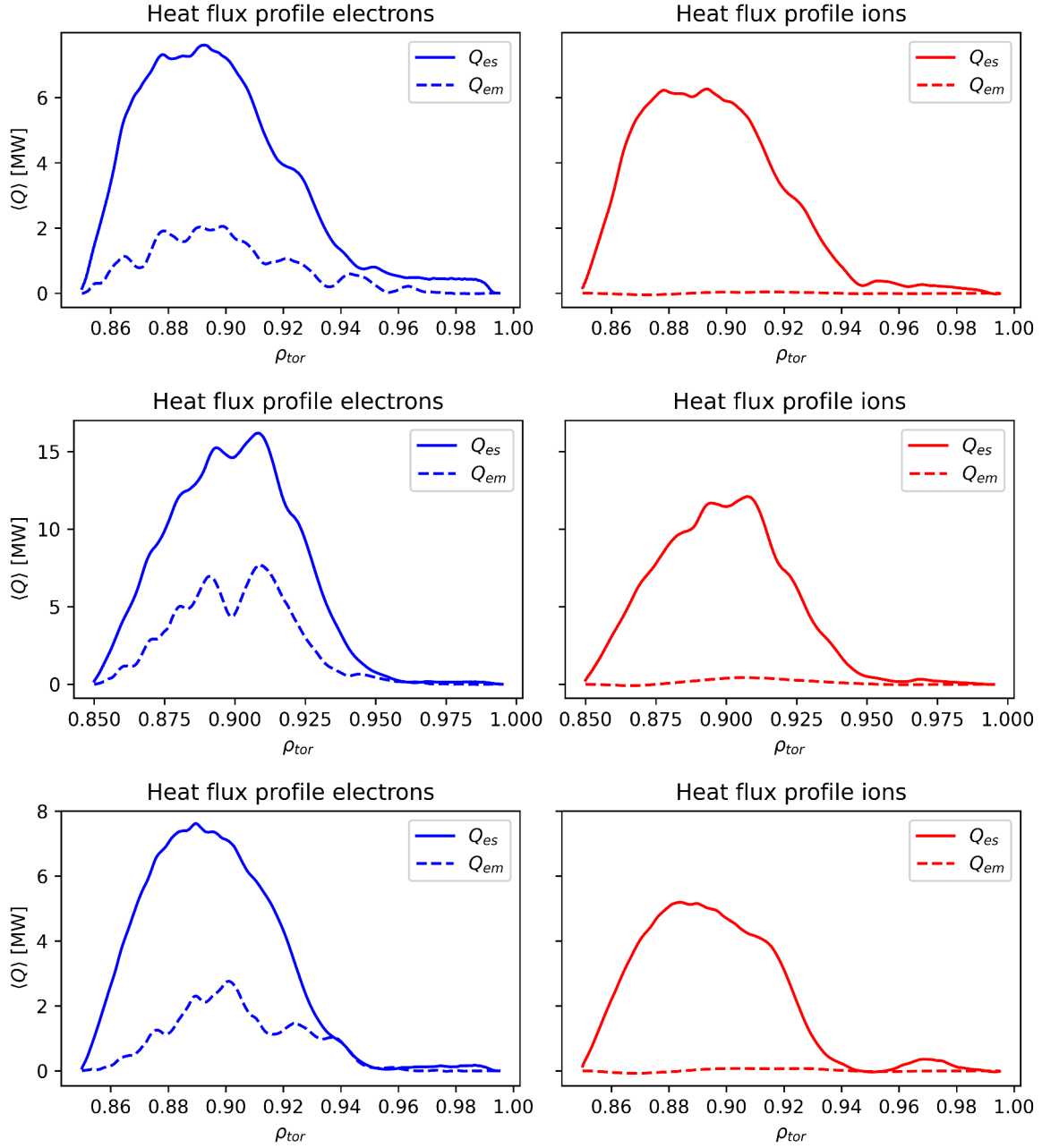


Fig. 5.33.: Heat flux profiles without $E \times B$ shear corresponding to the time traces shown in Fig. 5.32. From top to bottom: +2ms, +4ms, +6ms. The case +6ms has been investigated in detail in the previous sections.

5. AUG pedestal simulations

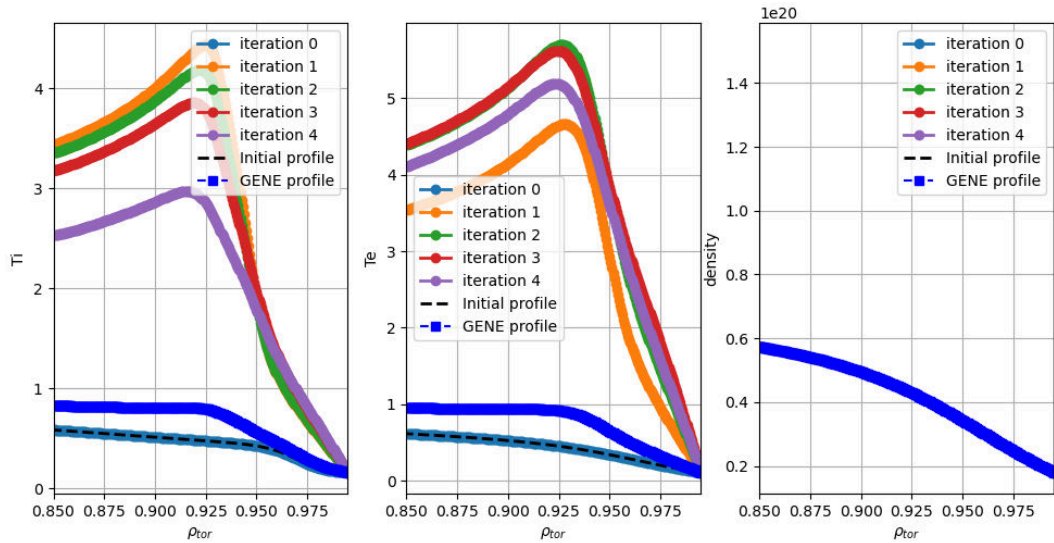


Fig. 5.34.: Profiles of ion temperature (left), electron temperature (center), and density (right) in the simulation domain. Initial experimental profile (dashed), Tango results for five iterations, and the final profiles used in GENE.

to iteratively fit power balance.

The GENE-Tango approach reverses the usual gradient-driven heat flux calculation approach. Instead of using profiles as input and comparing the resulting heat fluxes to power balance, this approach takes the power balance heat flux as input and adjusts the profiles via iterations of transport solver and GENE to find the profiles that produce the defined flux. Then, these GENE-Tango profiles can be compared to experimentally measured profiles. If they are close, this confirms that the model captures all relevant transport phenomena. If substantial differences remain, it indicates that essential parts of transport are not yet included in the model. This could, for example, be neoclassical transport if just turbulent heat flux from GENE simulations is used in the loop.

Here, we build on the successful application of the GENE-Tango approach in core simulations [80] and investigate its application to pedestal scenarios. The GENE-Tango simulations and their analysis have been performed in collaboration with Alessandro di Siena.

Some code development was initially necessary to make the full numerical capabilities of the GENE code usable within the GENE-Tango framework. In particular, block-structured velocity grids, which are required to keep the realistic pedestal scenario computationally tractable and ensure efficient use of computational resources, were employed for the first time in this framework. In the end, we could successfully couple

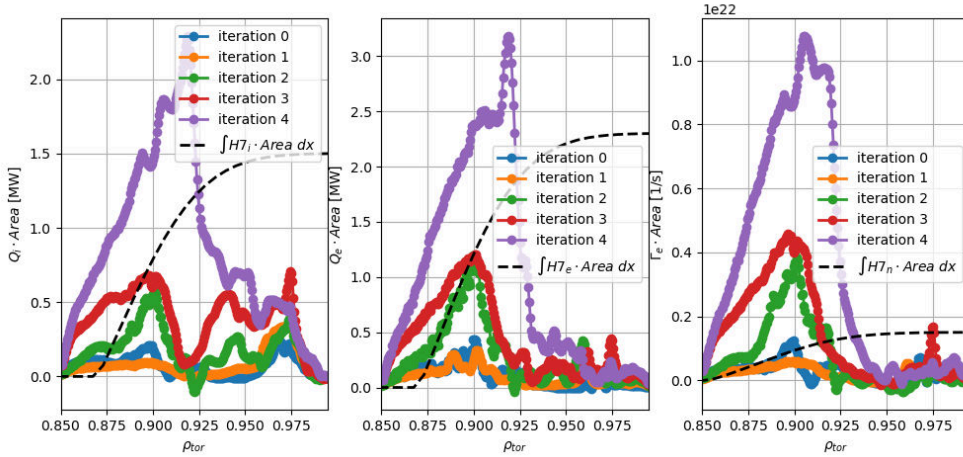


Fig. 5.35.: Evolution of the ion heat flux (left), electron heat flux (middle), and particle flux (right) with the updated profiles in comparison to the power balance model (dashed).

global, nonlinear, electromagnetic gyrokinetic GENE simulations of a realistic pedestal to the transport solver Tango. GENE simulations were performed with $E \times B$ shear. Neoclassic transport and changes to the magnetic equilibrium were not included in the Tango iterations.

The first iterations in the GENE-Tango loop yield strong changes in the electron and ion temperature profiles (see Fig. 5.34) due to the initial distance of the heat fluxes to power balance (see Fig. 5.35). We have kept the density profiles constant due to the high uncertainties of particle sources in the plasma edge and to facilitate convergence. At the pedestal top ($\rho_{tor} = 0.88$), the GENE-Tango loop finds profiles that show an improved match with power balance within just a few iterations. In the steep gradient region ($\rho_{tor} = 0.97$), however, even strongly increased gradients are not sufficient to produce transport that is as high as power balance demands. This finding underlines the crucial importance of transport processes other than ion scale turbulence in the pedestal. It supports previous studies on the steep gradient region showing that ion transport approaches neoclassic levels [152] and our GENE stand-alone simulations showing that electron transport is dominated by small, electron-scale fluctuations (see previous sections). The results obtained with these GENE-Tango calculations corroborate that these findings are robust against uncertainties in the profiles. They also highlight the need to include further physics like neoclassical transport and electron scale transport for accurate profile predictions in the pedestal.

Given the computational cost of these nonlinear pedestal simulations and the needed number of GENE-Tango iterations, this approach has not been investigated beyond the proof-of-principle within this thesis.

5.6. Summary

In this chapter, the gyrokinetic analysis of an ASDEX Upgrade ELMy H-mode pedestal has been presented. The most unstable microinstabilities from just inside the pedestal top to foot were characterized with extensive linear, local scans. At the pedestal top/shoulder, MTM, TEM, and ETG modes were found. In the intermediate region, before the pedestal center modes on ion scales are stabilized by the interplay of magnetic shear and pressure gradient, while on intermediate electron scales, additional ETG modes become unstable. In the pedestal center, ITG modes close to the threshold to KBMs were observed, and at the pedestal foot, modes with TEM/ETG character, which are destabilized with increasing collision frequency, are present. With nonlinear, global, electromagnetic ion scale simulations and nonlinear, local ETG simulations, we have analyzed the heat flux in the pedestal - resolved in radius and scale. The ion scale simulations are enabled by an upgrade of the GENE code (cf. Chapter. 3). We find TEM-driven turbulence with electromagnetic components due to MTMs to be dominant at the pedestal top/shoulder. A combination of linear stabilization and $E \times B$ shear suppresses ion scale turbulence towards the steep gradient region. While the turbulent electron heat flux is picked up by small-scale ETG modes, the ion channel reduces to neoclassic heat flux levels.

The global electromagnetic simulations presented in this study are among the most realistic pedestal turbulence simulations performed to date. Together with dedicated local ETG simulations and the extensive linear instability characterization, they help to confirm the important role of $E \times B$ shear stabilization for pedestal turbulence and demonstrate the transition in scale of electron turbulence from ion scales at pedestal top to electron scales in the steep gradient region.

The investigation of other time points in the ELM cycle has found a similar instability and heat flux structure as in the pre-ELM time point. TEMs and MTMs at the pedestal top cause most of the transport visible in these simulations. Shortly after the ELM crash, more turbulent electron transport in the steep gradient region is observed, and overall, the turbulent heat flux is higher than in the +6ms time point.

Furthermore, a proof-of-principle of quasi-flux-driven global pedestal simulations with the GENE-Tango approach was demonstrated. The first iterations of this ansatz underline the importance of electron scale and neoclassic contributions for the total heat flux in the pedestal. Global ion-scale simulations alone are not sufficient to capture pedestal transport.

The presented study, including the high-fidelity global simulations, confirms, refines,

and extends the current picture of pedestal turbulence. We find a similar mixture of relevant gyrokinetic modes (TEM, MTM, ETG) in the pedestal as identified in previous flux-tube studies of the AUG pedestal and confirm the linear closeness of the pedestal to the KBM threshold [147]. Our global, nonlinear simulations and their detailed comparison to linear results reveal the persistence of TEM/MTM turbulence at the pedestal top in the fully developed turbulent state, including global effects. In agreement with interpretative modeling [152, 157], the turbulent ion heat flux in the pedestal center is found to strongly reduce, such that the total ion heat flux approaches neoclassic levels. Our simulations suggest that already a linear stabilization mechanism contributes to this suppression, which is strengthened by $E \times B$ shear. Consistent with the fingerprint analysis of Ref. [103], we do not find significant contributions of ITGs or TEMs to the heat flux in the pedestal center. Our simulations show a transition of electron heat flux from TEM-driven transport at the pedestal top to ETG-driven transport in the pedestal center. In contrast to gyrokinetic studies on JET [133, 134] and DIII-D [131, 132], we do not find significant electromagnetic transport due to MTMs in the pedestal center. MTMs are present linearly and in the global simulations on the pedestal top but not the pedestal center. Hence, turbulent transport in the pedestal center is dominated by ETG transport in our analysis. Particularly in the nonlinear simulations, we find a complex ETG mode structure, as has been recently also described for JET pedestals [104, 105, 125].

In the next chapter, a similar study for a pedestal of the JET tokamak will be presented.

6. JET pedestal simulations

This is the second of two simulation result chapters. It presents the gyrokinetic analysis of an ELMy H-mode pedestal from the JET tokamak. The structure is very similar to the previous chapter: It begins with the physical scenario, followed by an analysis of instabilities and heat flux calculations.

The aim of this study is the characterization of turbulence in the pedestal of a type-I ELMy hybrid H-mode JET discharge. The successful characterization is the basis of possible next steps investigating particle/impurity transport or the influence of the main isotope on pedestal turbulence in this scenario. From a code testing perspective, the hybrid scenario is attractive because its elevated plasma β increases electromagnetic fluctuations, which the new code upgrade is designed to handle. This is the first study investigating ion-scale turbulence in a JET hybrid H-mode pedestal.

Parts of this chapter have been submitted for publication in Leppin, L., Görler, T., Frassinetti, L., Saarelma, S., Hobirk, J., Jenko, F. & JET Contributors. The JET Hybrid H-mode Scenario from a Pedestal Turbulence Perspective. *Nuclear Fusion* Submitted (2024).

6.1. Experimental scenario

A main difference compared to the previous chapter is the experimental device. In the current chapter, a pedestal of the Joint European Torus (JET) located in Culham, UK, is being analyzed. JET is the largest tokamak fusion experiment that has been operated to date and holds the world record for the highest sustained fusion energy produced in a discharge with 59 MJ [6, 158]. In linear dimensions, JET is two times larger than AUG (major plasma radius 2.96m vs 1.6m). Hence, heating power and temperatures are considerably larger than in AUG.

We are considering a pre-ELM H-mode pedestal from a JET hybrid scenario, shot #97781. This is a Deuterium discharge with NBI and ICRH heating with a total heating power of $P_{tot} = 33$ MW, an on-axis B-field of 3.45 T, a plasma current of 2.3 MA and 12 MW bulk radiation [159]. The discharge has improved confinement of $H_{98,y2} \approx 1.2 - 1.4$. It has been used as a Deuterium reference discharge in the scenario development of the record-breaking JET D-T experiments [158, 159].

The hybrid scenario, also called high- β route or improved H-mode, features improved

6. JET pedestal simulations

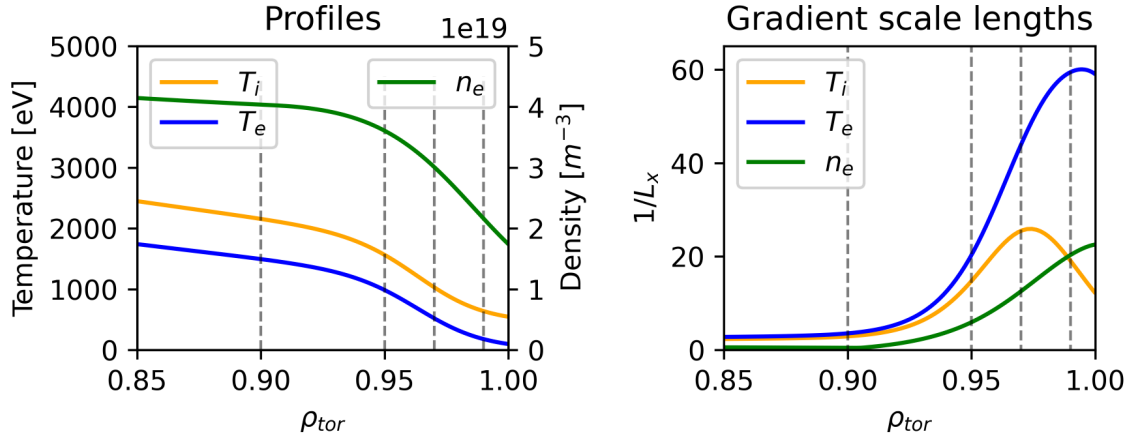


Fig. 6.1.: Left: Temperature and density profiles of the JET #97781 pedestal. Right: The corresponding gradient scale lengths.

confinement properties compared to the $H_{98,y2}$ confinement scaling and is, therefore, an attractive candidate for ITER operation [160–162]. The hybrid scenario derives its name from being a hybrid of the standard tokamak scenario and the advanced tokamak scenario. In the standard scenario, the plasma current, which is required for the poloidal magnetic field, is generated by induction via the central solenoid. The standard scenario is, therefore, inherently pulsed. The advanced tokamak scenario aims to drive the current by self-generated bootstrap currents and external current drive mechanisms, such that this scenario is steady-state capable. The hybrid scenario has a larger bootstrap current fraction and a higher plasma β compared to standard H-modes.

The improved confinement in the hybrid scenario on JET is observed to be due to a combination of reduced core transport and increased pedestal pressure [162]. In core turbulence studies of the hybrid H-mode, electromagnetic stabilization, and fast particle effects have been identified to contribute to reduced core transport [163–165].

The experimental density and temperature profiles, as well as geometry files, were generated through fits to experimental data by the JET Team, in particular Lorenzo Frassinetti and Samuli Saarelma, within the JET pedestal task T17-05.

Fig. 6.1 shows the temperature and density profiles for the pedestal region of JET #97781 pre-ELM. For the presented profiles, particular care was put on fitting the steep gradient region at $\rho_{tor} = 0.97$ well. Grey, dashed, vertical lines indicate positions at which linear stability has been investigated. The position $\rho_{tor} = 0.9$ for the pedestal top, $\rho_{tor} = 0.95$ for the local magnetic shear minimum, $\rho_{tor} = 0.97$ for the pedestal center, and $\rho_{tor} = 0.99$ for the pedestal foot. While best fits to experimental data

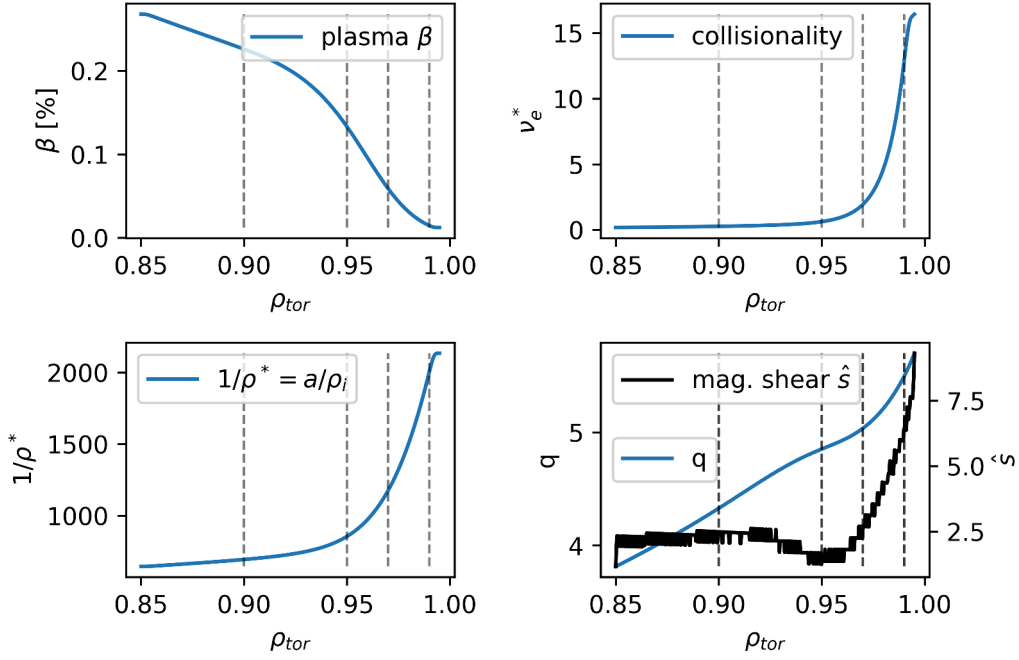


Fig. 6.2.: Radial profiles of plasma β , collisionality, ρ^* , safety factor q and magnetic shear \hat{s} .

are shown in the figure, the ion temperature measurements have comparatively large uncertainties. For instance, $T_i = T_e$ lies within the uncertainties and will be investigated in the instability characterization and heat flux calculation.

Fig. 6.2 shows additional important plasma profiles. Similarly to the AUG case, the local plasma β strongly reduces from pedestal top to bottom, the collisionality increases, the gyroradius decreases, and the safety factor increases. The magnetic shear also exhibits a local minimum between pedestal top and center, but it is less pronounced than in the AUG case.

Fig. 6.3 shows the $E \times B$ velocity (left) and the associated shear used in the simulations. Since no E_r measurements are available for this shot, we use a neoclassic estimate for E_r and calculate from that the corresponding rotation velocity. The script to calculate E_r was originally written by David Hatch based on derivations in [166]. We will test the sensitivity of heat fluxes on the $E \times B$ shear level by using a 50% larger rotation velocity, as shown in orange.

Fig. 6.4 shows density profiles for different assumed effective ion charges. If impurities are present, one may identify an effective ion charge by the density-weighted average of the individual species $Z_{\text{eff}} = \sum_i n_i Z_i^2 / n_e$. The solid lines are the resulting main ion densities, and the dashed lines are the impurity densities. The range of possible

6. JET pedestal simulations

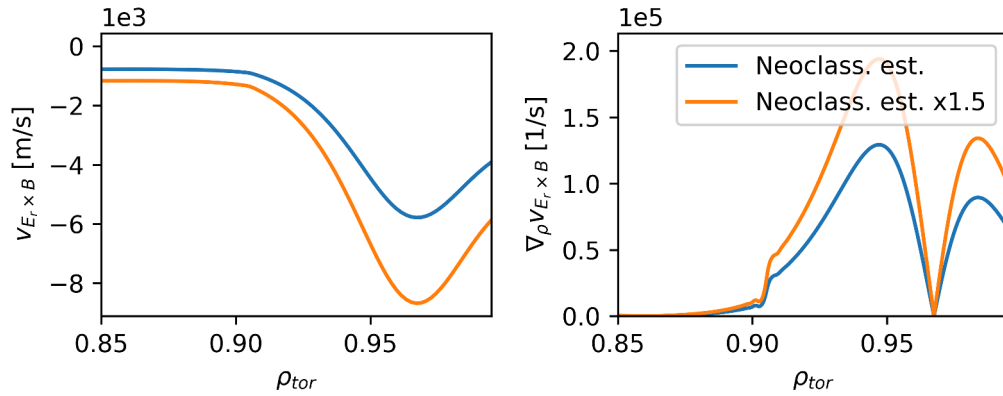


Fig. 6.3.: $E \times B$ velocity $v_{E_r \times B} = E_r \times B/B^2$ (left) and corresponding shear (right) due to a neoclassic radial electric field E_r . For comparison, the $E \times B$ velocity increased by 50% in orange.

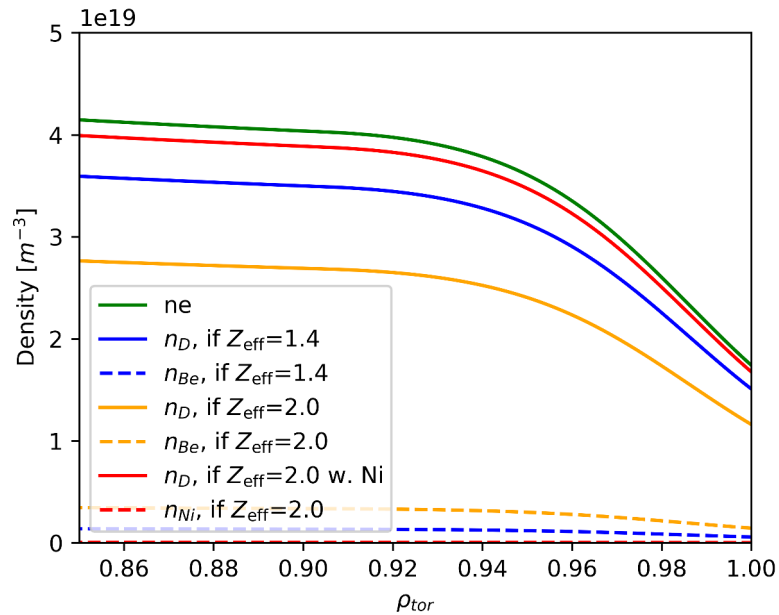


Fig. 6.4.: Density profiles for different assumed effective ion charges Z_{eff} and assumed main impurities.

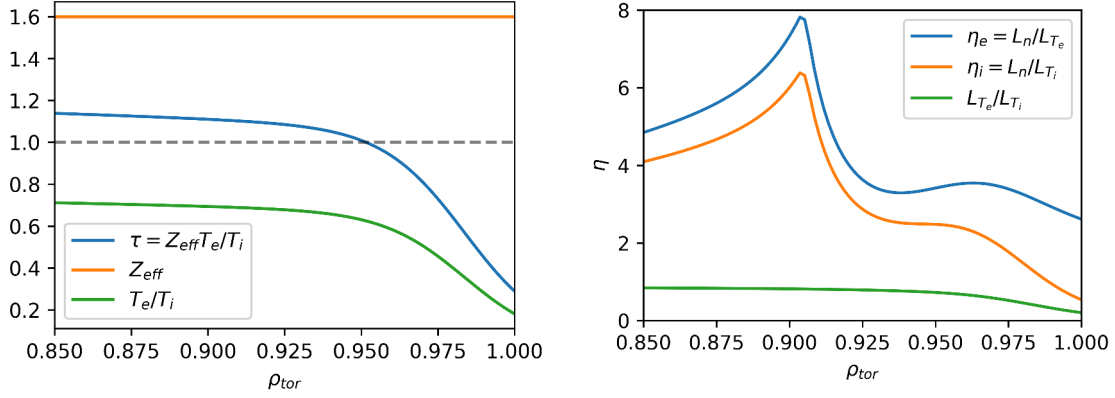


Fig. 6.5.: Left: The ratio of electron to ion temperature, assumed effective ion charge $Z_{eff} = 1.6$, and resulting τ . Right: Ratios of density and temperature gradients.

Z_{eff} is based on experimental analysis [M. Sertoli et al., private communication, 2020] using methods from Ref. [167]. For the modeling, we have focussed on Beryllium as an impurity because among possible candidates, due to its small charge number ($Z=4$), it causes the strongest dilution of the main ion species for a given Z_{eff} and is hence expected to have the most significant effect. Nickel, for example, has a charge number of $Z=28$. So, Beryllium is well suited to examine the upper bound of impurity influence.

Fig. 6.5 (left) shows the ratio of electron to ion temperature and the related quantity τ . The ratio influences stability properties and can become important in adiabatic ion simulations, correcting the effect of the collision operator. Fig. 6.5 (right) shows the ratio of density and temperature gradients. The gradient ratios η_e and η_i peak at comparatively large values at the pedestal top, around $\rho_{tor} = 0.9$. This indicates a strong instability drive at this position.

6.2. Instability characterization

To characterize instabilities, I have performed scans with linear, local simulations in k_y , $k_{x,center}$, and ρ_{tor} . Scans have been performed in the same setup as the characterization of the AUG case, detailed in the previous chapter. The presentation is purposefully comprehensive to illustrate important aspects of a linear gyrokinetic analysis and document findings for future reference. Growth rate spectra at nominal parameters in different visualizations are shown, and several sensitivity scans and convergence tests are discussed.

6. JET pedestal simulations

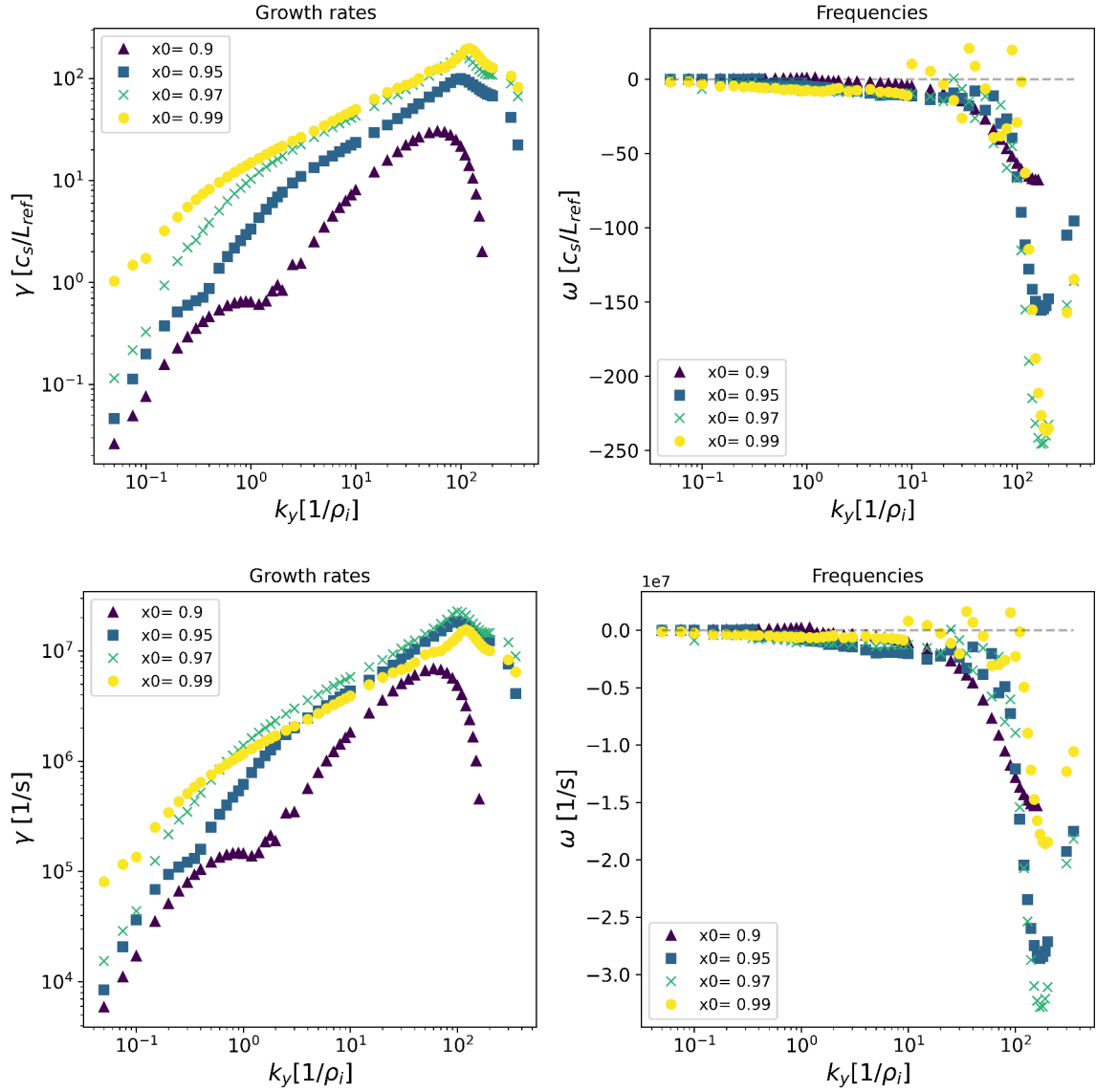


Fig. 6.6.: Top: Growth rate and frequency spectra of the dominant mode at different radial positions from pedestal top to pedestal bottom in a local flux-surface normalization c_s/L_{ref} . Bottom: The same data in SI units 1/s.

6.2.1. Nominal parameters

The instability characterization starts with linear, local scans at nominal parameters. Fig. 6.6 shows growth rate (left) and frequency (right) spectra in two normalizations: In a local flux-surface normalization depending on the local temperature at the investigated position (top) and in SI units (bottom). Growth rates are maximized over $k_{x,\text{center}}\rho_i = [-40, 40]$. Following the mode characterization introduced in the previous two chapters, these modes are identified: The pedestal top on ion-scales is dominated by an ITG mode, followed by an ETG peak on electron scales. In contrast to AUG, already the pedestal top growth rate spectrum shows no stable region at intermediate k_y . Also, at $\rho_{\text{tor}} = 0.95$ in the magnetic shear minimum, no clear growth rate gap on ion-scales is apparent. In the pedestal center, large parts of the spectrum have ETG character down to ion-scales. The bottom plot in SI units reveals that while the growth rates at the pedestal bottom are large compared to the reduced temperatures, they are lower than in the pedestal center in absolute units.

Fig. 6.7 shows the same growth rate and frequency spectra as in Fig. 6.6 emphasizing different aspects of the instability spectrum. The top panels show the data in a lin-lin plot, revealing more details of the smallest electron scales and demonstrating the difference in growth rates between the different radial positions, which is usually skewed in the logarithmic visualization. The bottom panels highlight the ion-scale instabilities that are responsible for substantial parts of heat transport, particularly at the pedestal top. Specifically, the zoomed-in frequency plot (bottom right panel) allows one to identify mode transitions. The pedestal top $\rho_{\text{tor}} = 0.9$ (violet triangles) is ITG dominated (positive frequency branch) up to $k_y\rho_i \approx 1$ before an ETG branch takes over. At $\rho_{\text{tor}} = 0.95$ (blue squares), the transition happens earlier ($k_y\rho_i \approx 0.4$), and at the pedestal center $\rho_{\text{tor}} = 0.97$ (green crosses) even earlier ($k_y\rho_i \approx 0.08$). At the pedestal foot (yellow circles), no positive ITG frequencies are visible.

The previous figures have provided an analysis of the spectra of the most unstable mode at different positions within the pedestal. These spectra have maximized over $k_{x,\text{center}}$. Particularly for pedestal ETG modes, however, the $k_{x,\text{center}}$ structure is non-trivial. Fig. 6.8 shows the full growth rate structure in k_y - $k_{x,\text{center}}$ space at the pedestal center. It is not well suited to show precise values, but it gives an intuitive understanding of the dependencies in the plane. Notice the two approaching flanks at $k_y\rho_i = 10 - 90$ where γ peaks at finite $k_{x,\text{center}}$. This is a signature of the complex ETG structure present in the pedestal. Both toroidal and slab ETG modes are present at a given k_y but at different radial wavenumbers/ballooning angles, as will be discussed in the following. Notice also that the frequencies (bottom plot) sometimes cross the $\omega = 0$ -plane and

6. JET pedestal simulations

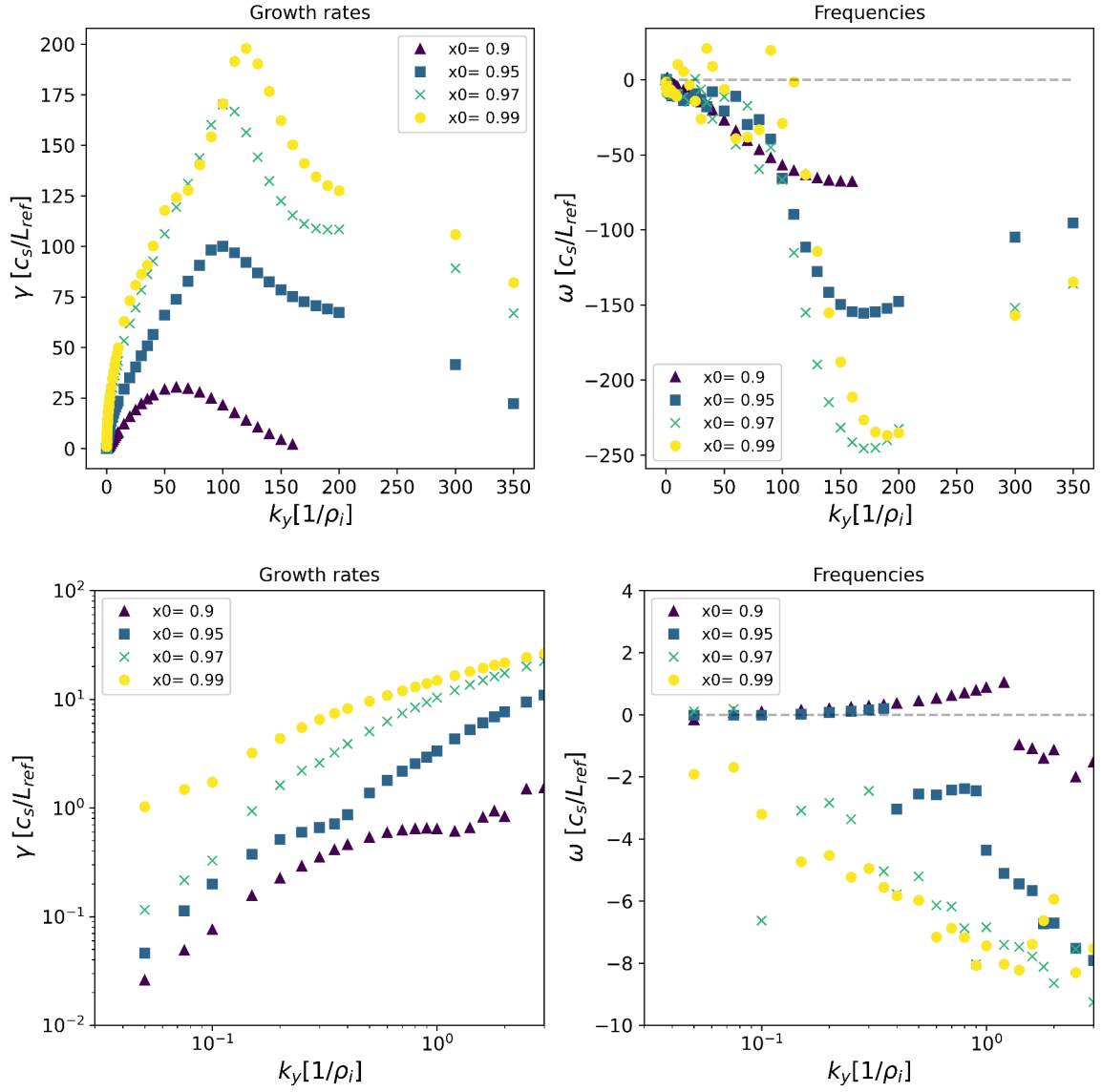


Fig. 6.7.: Top: Growth rate and frequency spectra of the dominant mode at different radial positions in a lin-lin plot. Bottom: Zoom to the ion-scale range in a log-log plot.

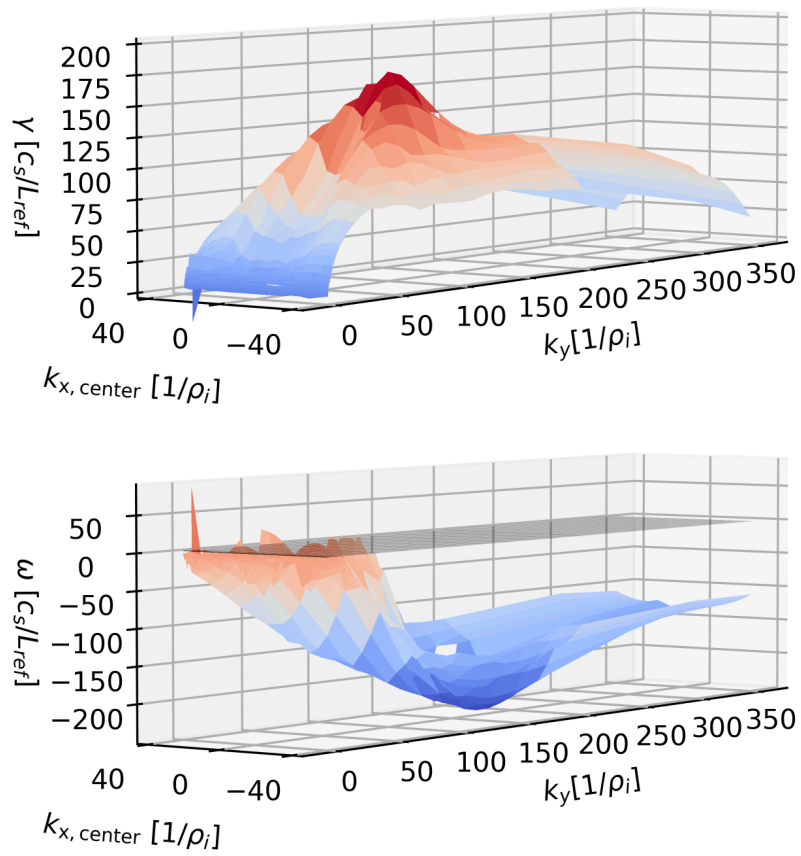


Fig. 6.8.: Growth rate (top) and frequency (bottom) surface of the dominant mode in a k_y - $k_{x, \text{center}}$ plane at $\rho_{\text{tor}} = 0.97$.

6. JET pedestal simulations

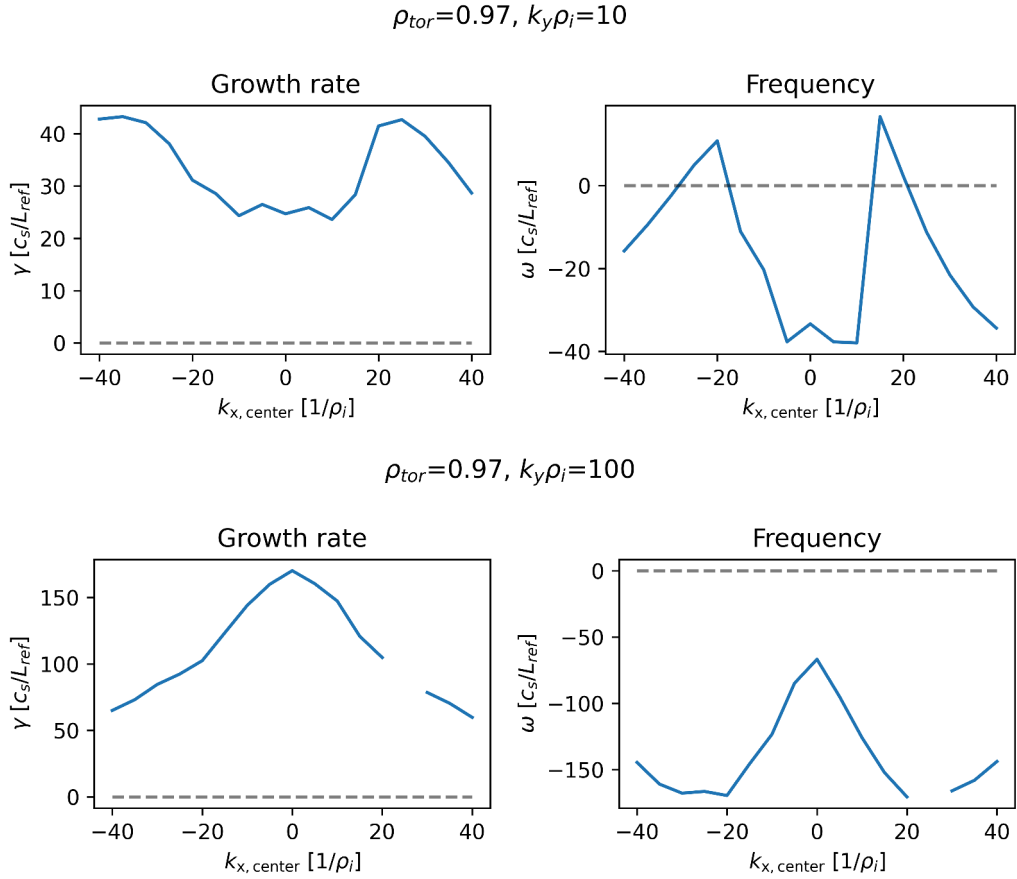


Fig. 6.9.: Growth rates and frequencies of the dominant mode at $\rho_{\text{tor}} = 0.97$ for two k_y s as a function of $k_{x,\text{center}}$.

become positive. This is even better illustrated when considering a cut along $k_{x,\text{center}}$ for a given k_y as done in Fig. 6.9. The overall picture is similar to the linear ETG observations in the AUG case.

The findings deduced from the full k_y - $k_{x,\text{center}}$ -plane can be corroborated by cuts along the $k_{x,\text{center}}$ -dimension at a fixed binormal wavenumber k_y . Fig. 6.9 shows a cut along $k_{x,\text{center}}$ at $\rho_{\text{tor}} = 0.97$ and $k_y\rho_i = 10$ (left) and $k_y\rho_i = 100$. At $k_y\rho_i = 10$, toroidal ETG modes at finite $k_{x,\text{center}}$ values have the highest growth rate. They show positive frequencies. At $k_y\rho_i = 100$ however $k_{x,\text{center}}\rho_i = 0$ dominates. The slab-ETG branch has become more relevant at this wavenumber (see Fig. 6.10).

An indicator for the different ETG branches is the parallel structure of the modes. Fig. 6.10 shows the parallel structure from a high parallel resolution run ($n_z = 360$). At $k_{x,\text{center}}\rho_i = 0$, the mode has an intricate parallel structure indicating a slab-like character. At $k_{x,\text{center}}\rho_i = 20$, the parallel structure is much simpler, indicating the toroidal branch.

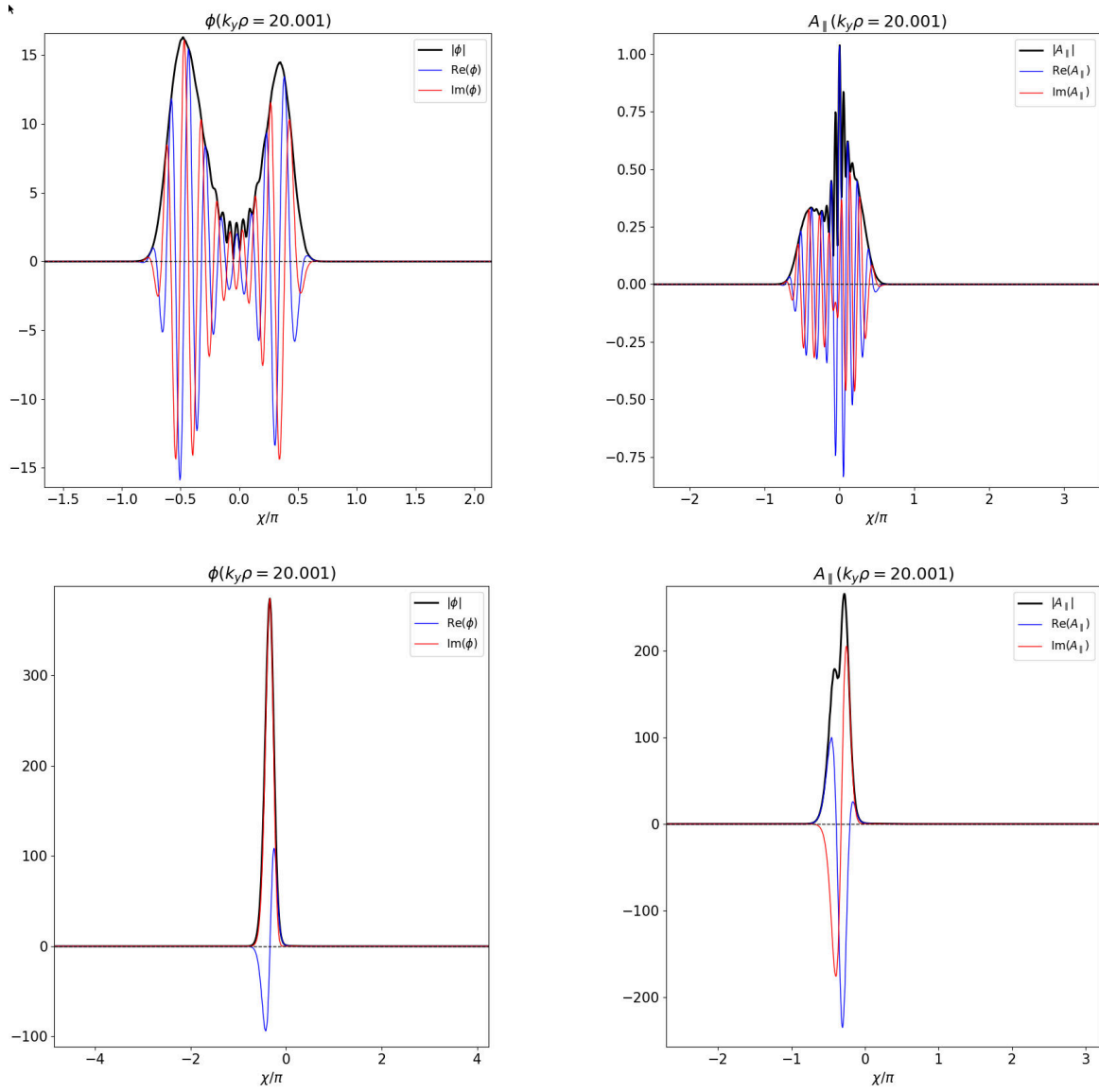


Fig. 6.10.: Parallel structure of the $k_y\rho_i = 20$ mode in the pedestal center. Top: $k_{x,\text{center}}\rho_i = 0$, bottom: $k_{x,\text{center}}\rho_i = 20$.

6. JET pedestal simulations

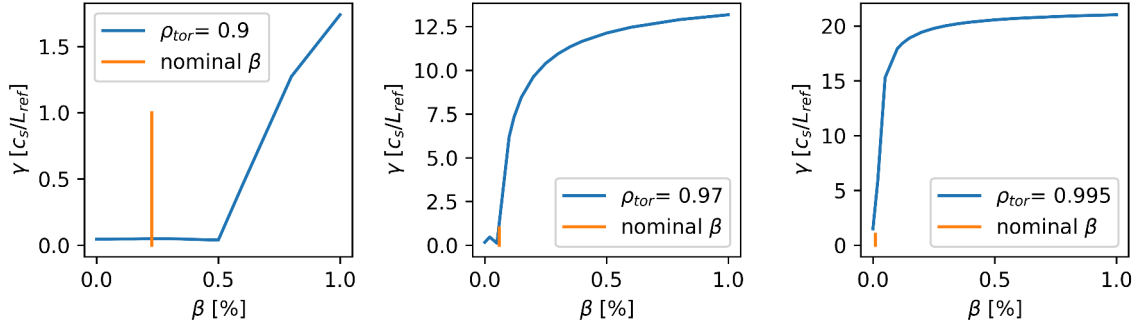


Fig. 6.11.: Linear, local plasma β scan at $k_y \rho_i = 0.075$: Growth rates at different radial positions (left to right: pedestal top, center, foot) as a function of β . The orange bar indicates the nominal β value at the respective position and acts as a yardstick across the plots, always ranging from 0 to 1.

This concludes the analysis of instabilities at nominal parameters. The following subsection investigates the robustness of selected modes against variations of several physical parameters.

6.2.2. Sensitivity scans

This subsection studies the sensitivity of instabilities against changes in plasma β , impurity content, temperature and density gradients, and ion temperature.

Fig. 6.11 shows the closeness to the KBM transition at large-scale modes $k_y \rho_i = 0.075$. As in the AUG case, pedestal center (middle plot) and foot (right plot) are very close to the KBM threshold at nominal parameters in local, linear simulations. This indicates a limitation of the pedestal due to KBM modes.

Fig. 6.12 shows growth rate spectra at the pedestal top (purple) and center (yellow) with changing impurity content of $Z_{eff} = 1.4$ and $Z_{eff} = 2.0$. As the impurity content increases and the main ion species is increasingly diluted, growth rates are reduced. The mode type, however, seems robust and is not changed by the additional impurities. Simulations were performed with three kinetic species, using densities as illustrated in Fig. 6.4.

The inherent uncertainties in the measured density and temperature profiles motivate growth rate scans in the driving gradients. These scans reveal how robust a specific mode is against small changes in the kinetic profiles. I show such scans for three selected modes: The ITG mode at the pedestal top, the ETG/TEM mode on ion scales at the pedestal center, and, for reference, the pure ETG mode at smaller scales at the pedestal center. For each mode 3D scans in the inverse gradient scale lengths

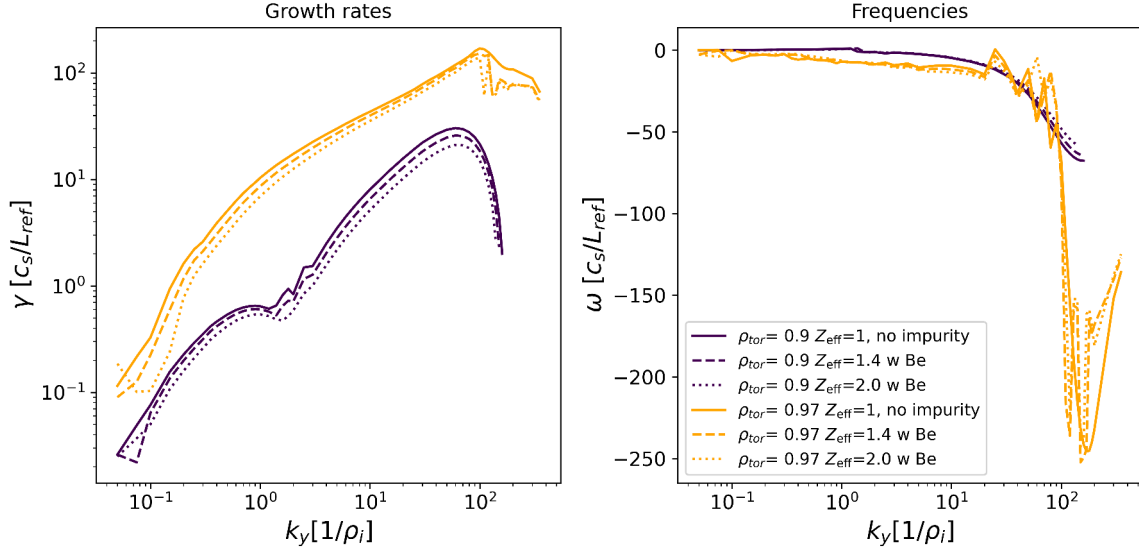


Fig. 6.12.: Growth rate and frequency spectra at pedestal top and center with changing impurity content.

ω_{Ti} , ω_{Te} , ω_n have been performed. Each gradient has been varied by [-30%, -20%, -10%, 0, 10%, 20%, 30%]. The individual plots show cuts through these 3D scans. In each panel, one of the gradients is kept at its nominal value, and the axes correspond to the other two gradients. Growth rates and frequencies are color-coded. The normalization of the color bars changes from panel to panel.

The robustness of the pedestal top ITG mode is investigated in Fig. 6.13. The left column shows growth rates and the right column shows the corresponding frequencies. The dependence on the ion temperature gradient is visible in the top and middle plots of the right column. An additional dependence on the electron temperature gradient is visible as well. The frequency plots show that in the range of scanned gradients, the frequency remains positive and is not strongly changing. In conclusion, the pedestal ITG mode appears robust under the tested gradient changes.

I now turn to the sensitivity of pedestal center modes. Fig. 6.14 shows gradient scans in the pedestal center ($\rho_{tor} = 0.97$) at two wavenumbers, $k_y = 0.2/\rho_i$ (left) and $k_y = 10/\rho_i$. The right column ($k_y = 10/\rho_i$) shows a clear ETG dependence: Growth rates are independent of ω_{Ti} , but increase with ω_{Te} (top plot) and decrease with ω_n . At $k_y = 0.2/\rho_i$ (left column), the ω_{Te} dependence is strong as well, and no ω_{Ti} dependence is visible. However, the ω_n dependence is more complicated (middle panel). This would indicate an ETG/TEM mixture since TEMs possess a more complex dependence on ω_n . Fig. 6.15 shows the corresponding frequencies. Frequencies remain dominantly in the electron diamagnetic direction (negative) in the scanned gradient ranges. The

6. JET pedestal simulations

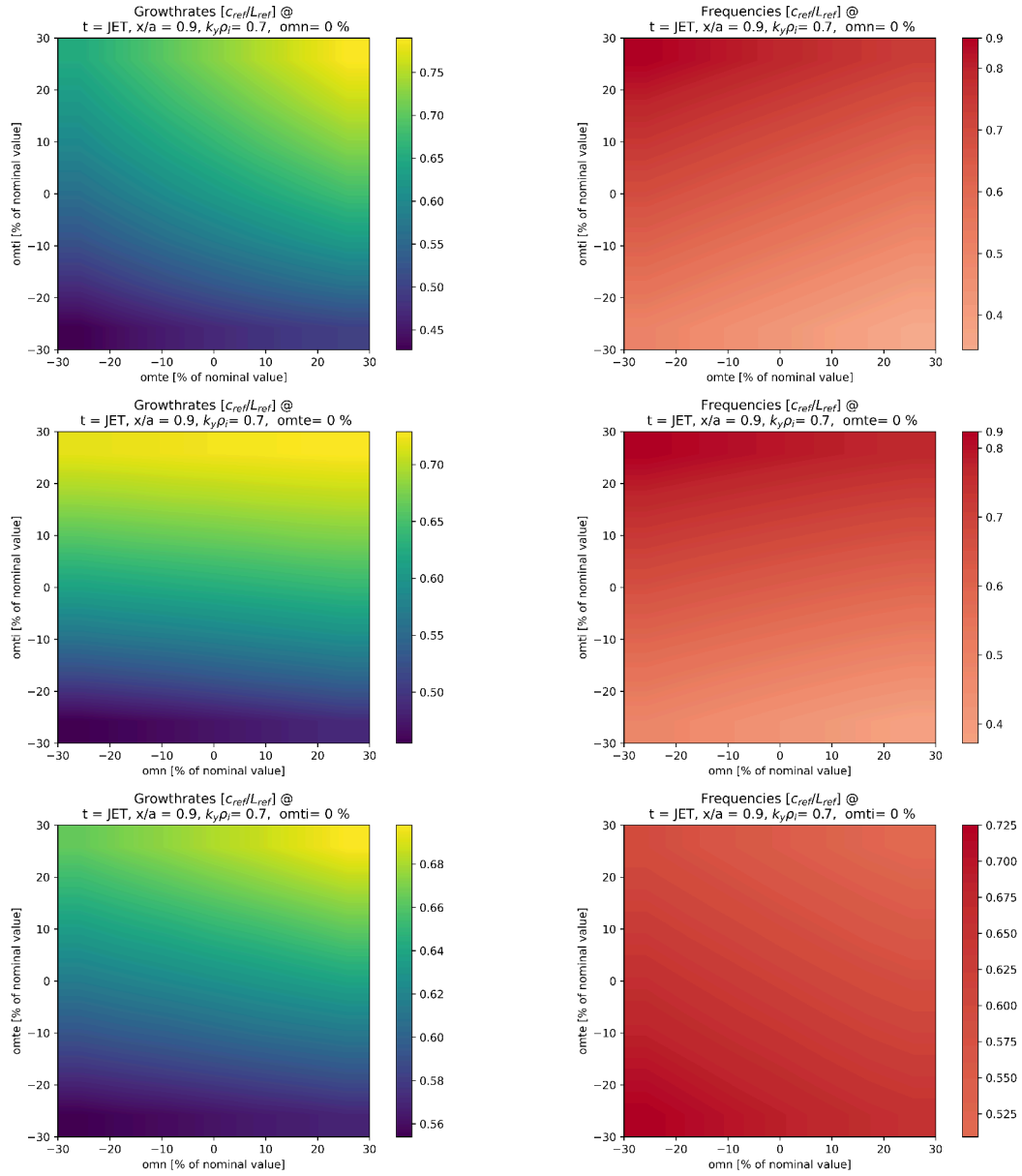


Fig. 6.13.: Growth rates (left) and frequencies (right) scanned over the driving inverse gradient scale lengths ω_{Ti} , ω_{Te} , ω_n at the pedestal top at $k_y \rho_i = 0.7$. Axes of each subplot are variations of the gradient scale lengths from -30% to +30%. Colors show the growth rate/frequency in c_s/L_{ref} . Normalizations are different from panel to panel. Top: ω_{Ti} vs ω_{Te} , Middle: ω_{Ti} vs ω_n , Bottom: ω_{Te} vs ω_n

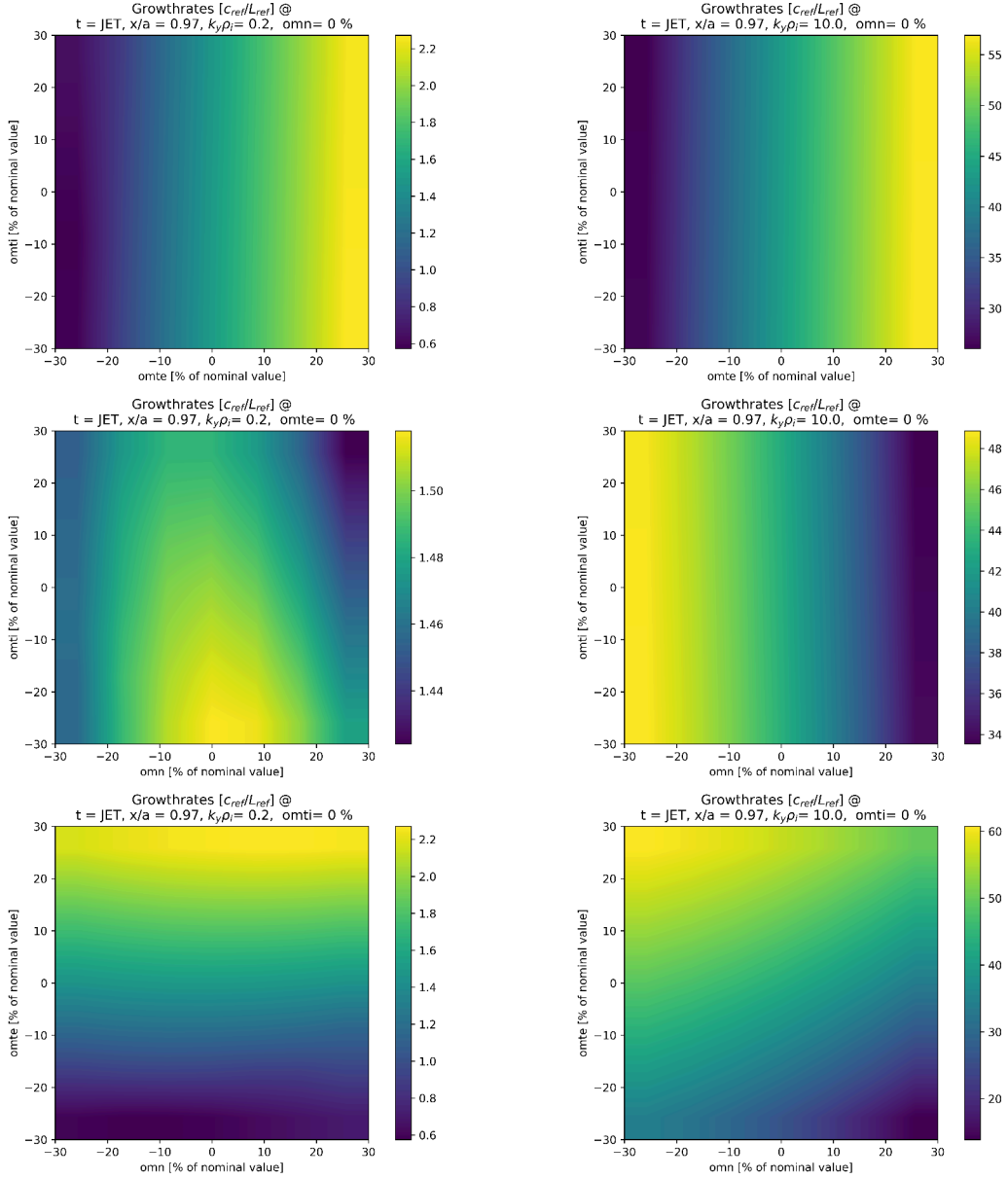


Fig. 6.14.: Growth rates scanned over the driving gradient scale lengths ω_{Ti} , ω_{Te} , ω_n at the pedestal center. Axes of each subplot are variations of the gradient scale lengths from -30% to +30%. Colors show the growth rate in c_s/L_{ref} . Normalizations are different from panel to panel. Left: $k_y = 0.2/\rho_i$, right: $k_y = 10.0/\rho_i$. Top: ω_{Ti} vs ω_{Te} , Middle: ω_{Ti} vs ω_n , Bottom: ω_{Te} vs ω_n

6. JET pedestal simulations

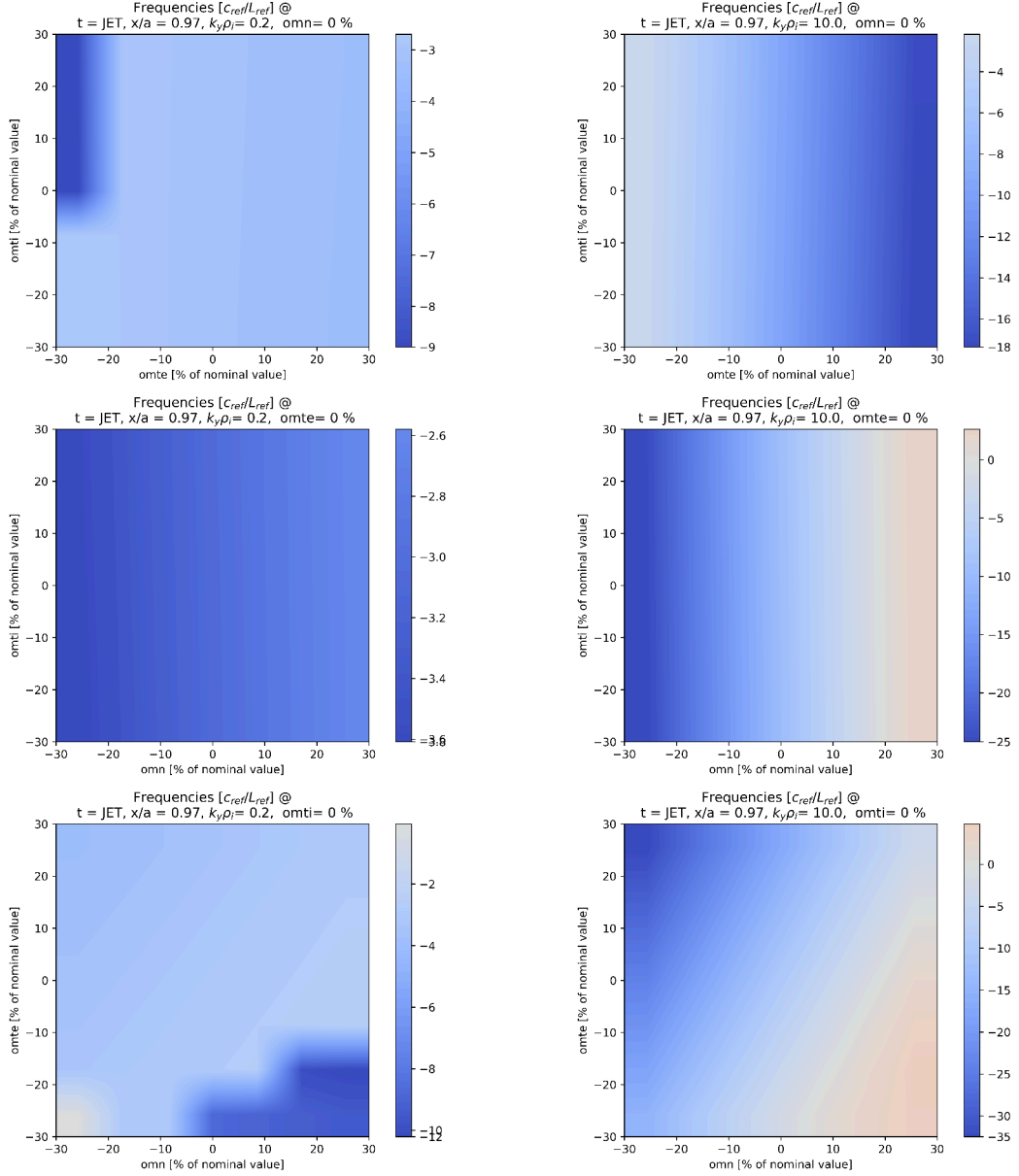


Fig. 6.15.: Frequencies in the gradient scan at the pedestal center corresponding to Fig. 6.14. Axes of each subplot are variations of the gradient scale lengths from -30% to +30%. Colors show the frequencies in c_s/L_{ref} . Normalizations are different from panel to panel. Left: $k_y = 0.2/\rho_i$, right: $k_y = 10.0/\rho_i$. Top: ω_{Ti} vs ω_{Te} , Middle: ω_{Ti} vs ω_n , Bottom: ω_{Te} vs ω_n

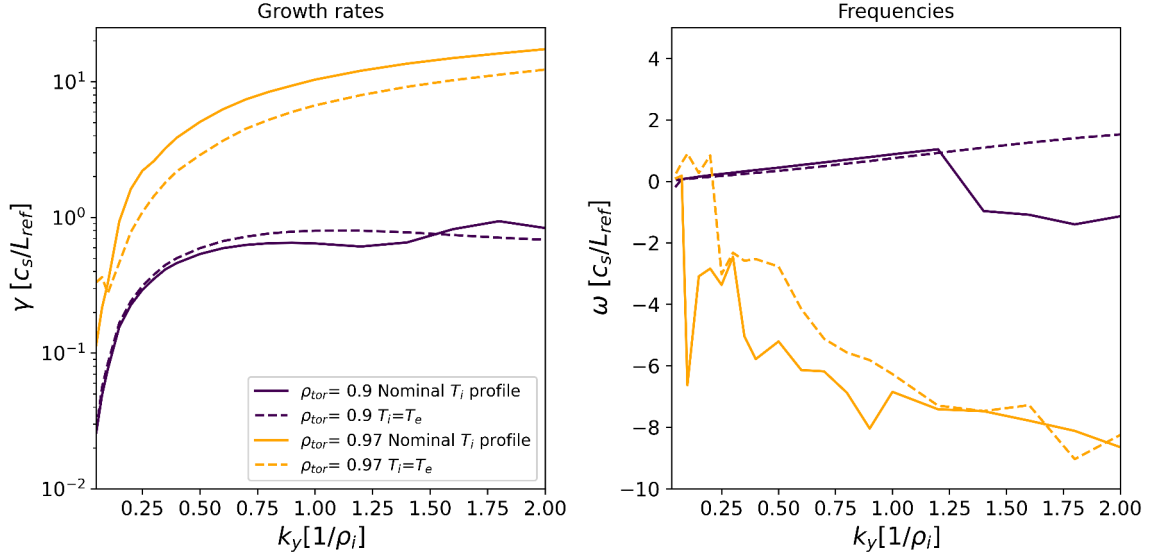


Fig. 6.16.: Influence of $T_i = T_e$ (dashed) on growth rates and frequencies of the dominant mode on ion-scales at pedestal top (purple) and center (yellow).

two middle plots offer an interesting comparison. The magnitude of the frequency at $k_y = 10/\rho_i$ (right column) increases with decreasing density gradient corresponding to the destabilization of the ETG mode. This trend is much less pronounced for the ion scale mode (left column), which, as discussed, is likely a TEM/ETG mode.

Fig. 6.16 investigates the impact of absolute ion temperature uncertainties on the instability spectrum. Growth rates and frequencies obtained with the best fit T_i profile and with $T_i = T_e$ are compared at the pedestal top (purple) and center (yellow). At the pedestal, the top growth rates are slightly increased, and the frequencies show that the transition from ITG to ETG is shifted to higher k_y compared to the best fit T_i profile. At the pedestal center, growth rates are reduced.

6.2.3. Convergence tests

These scans investigate the influence of the parallel resolution and $\bar{B}_{1\parallel}$ fluctuations on the growth rates.

Fig. 6.17 tests convergence for the parallel resolution. On ETG scales, high parallel resolutions are necessary to reach convergence in the growth rate of the fastest-growing mode. Even between $nz0=288$ and $nz0=360$ parallel grid points, small differences are visible. Only $nz0=360$ and $nz0=432$ show overlapping growth rates. High parallel resolution demands for JET pedestal ETG modes have also been observed in [104, 133].

6. JET pedestal simulations

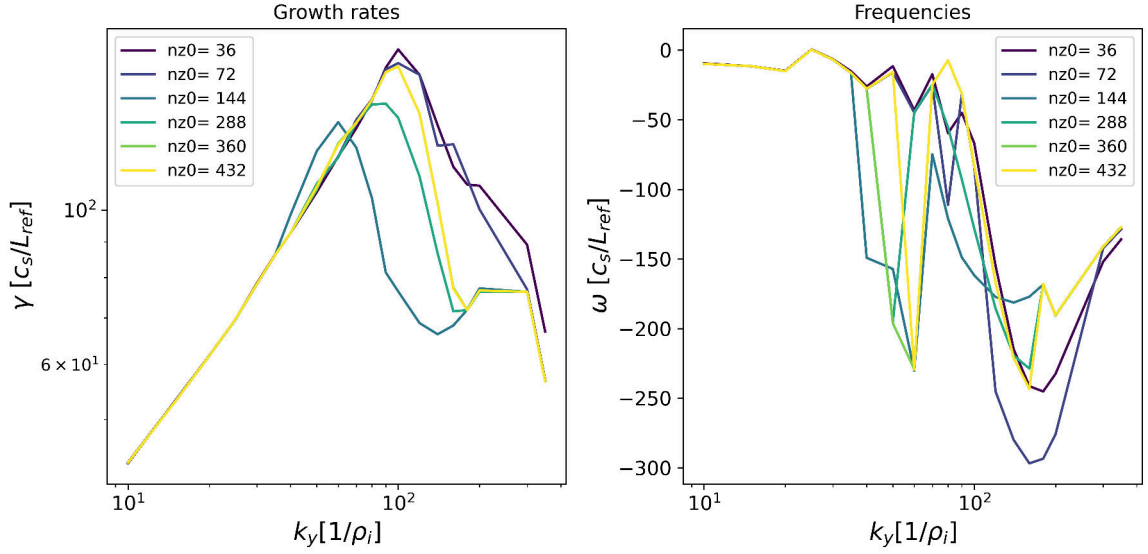


Fig. 6.17.: Convergence test: high- k_y growth rate spectra for different parallel resolutions at fixed box size and increasing number of parallel grid points $nz0$.

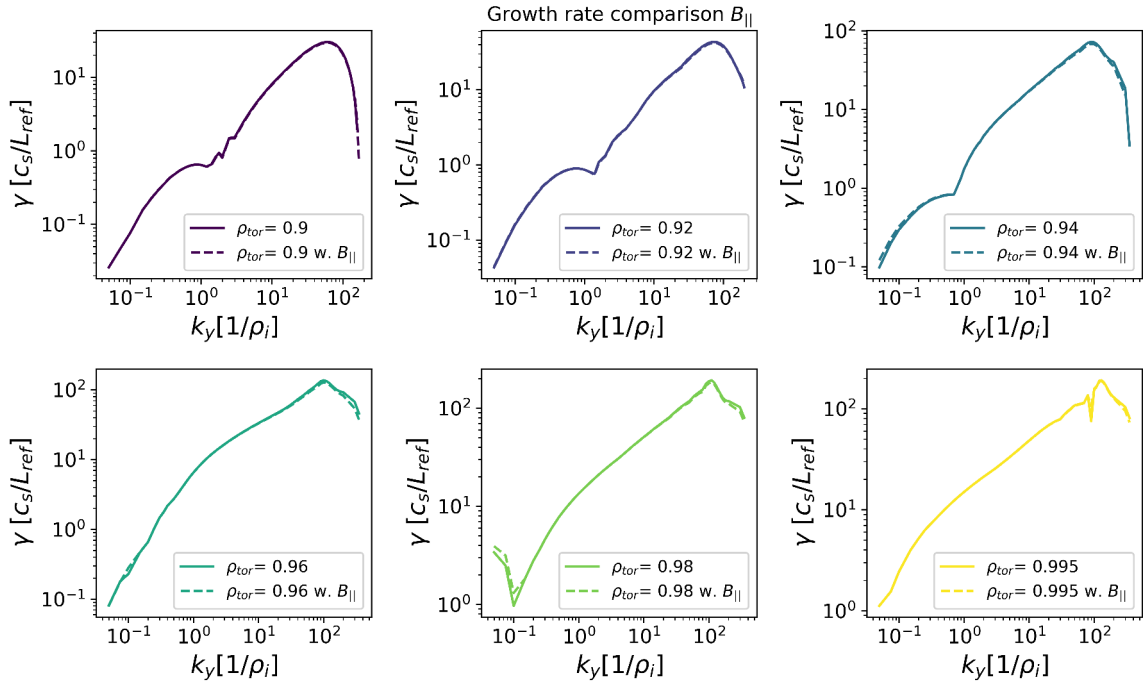


Fig. 6.18.: Growth rate spectra at different radial positions (different panels) with and without $B_{||}$ fluctuations.

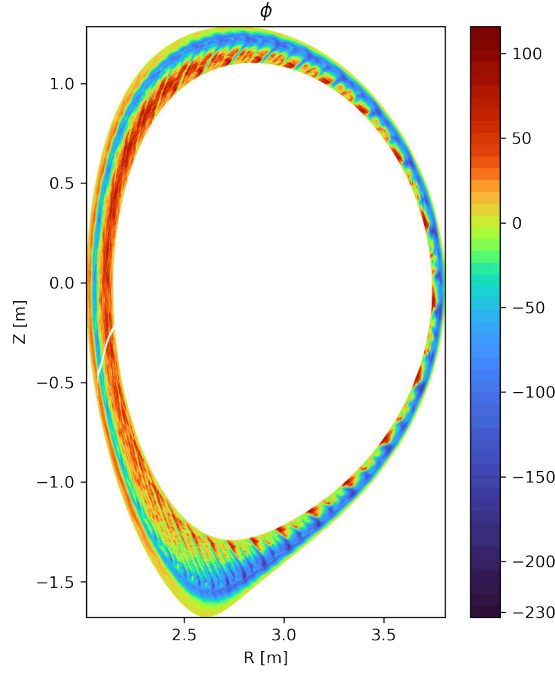


Fig. 6.19.: Snapshot of electric potential fluctuations from the nonlinear phase of a global JET simulation without $E_r \times B$ shear. ϕ in units of $(T_{\text{ref}}/e)\rho_{\text{ref}}^* \approx 1.85$ V.

Fig. 6.18 investigates the influence of $\bar{B}_{1\parallel}$ fluctuations on the linear growth rates. At the time of this analysis, global GENE simulations could not include $\bar{B}_{1\parallel}$ fluctuations. Therefore, sensitivity is tested in these local scans. The comparison of the spectra obtained without $\bar{B}_{1\parallel}$ fluctuations but with drift correction and the spectra with $\bar{B}_{1\parallel}$ fluctuations shows very small differences at all radial positions for this case. This suggests that $\bar{B}_{1\parallel}$ fluctuations in this case do not influence the instabilities strongly and/or that the drift approximation is widely applicable. This is encouraging for global simulations.

6.3. Nonlinear, global simulations

This section presents results from nonlinear, global, ion-scale simulations. The same simulation setup as for the nonlinear, global, ion-scale AUG simulations was used. Fig. 6.19 shows a snapshot of electric potential fluctuations. It illustrates the radial extent of the simulation domain. Furthermore, it shows the ballooned structure of ion-scale turbulence in this scenario with clear eddies on the outboard side. The figure is a projection of the actual simulation domain, which follows magnetic field lines and winds around the torus, to a poloidal plane.

6. JET pedestal simulations

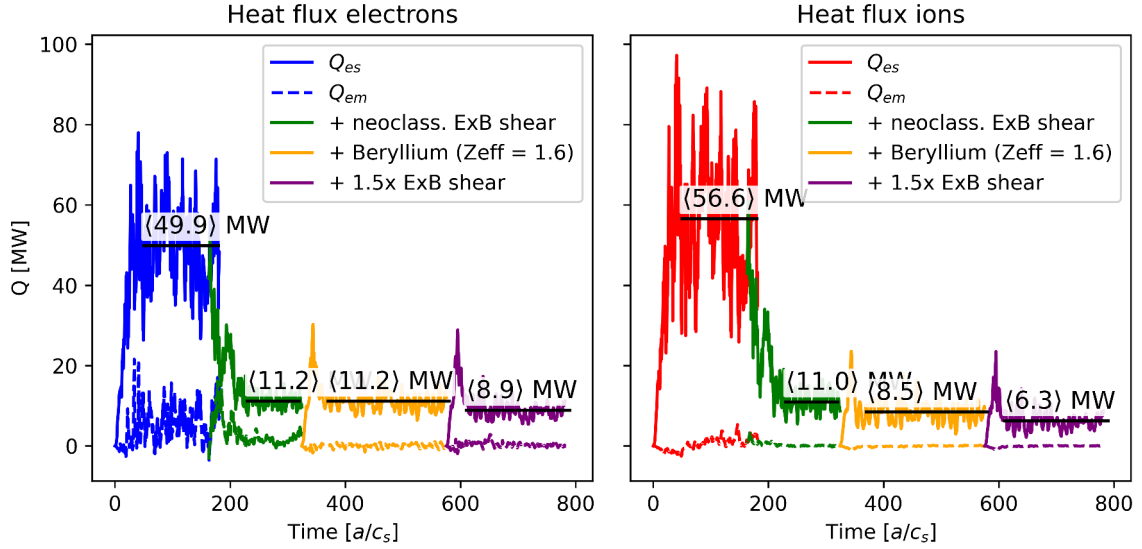


Fig. 6.20.: Turbulent heat flux from global nonlinear simulations as a function of time. Averaged over $\rho_{tor} = 0.92 - 0.99$ and flux surface.

Fig. 6.20 shows heat flux (averaged over flux surface and radius $\rho_{tor} = 0.92 - 0.99$) of electrons (left) and ions (right) as a function of time. The simulations are started with two species (electrons, deuterium) and no $E \times B$ shear (blue and red). Then neoclassic $E \times B$ shear is included (green), which strongly reduces both the electron and ion heat flux channel. Next, a three-species simulation (electrons, Deuterium, Beryllium) tests the influence of an impurity species on the heat flux (yellow). The electron channel is unaffected, but the main ion heat flux is reduced. Finally, the sensitivity to the $E \times B$ shear amplitude is tested by increasing $E \times B$ shear by a factor of 1.5 (purple). Both channels are slightly reduced. This underlines the importance of $E \times B$ shear on the total heat flux level and of impurities on the main-ion-to-electron heat flux ratio. A detailed comparison to experimental power balance has not yet been performed, but a first comparison to the heating power of the discharge is possible. The shot had a total heating power of 33 MW and radiation losses of about 12 MW [Hobirk et al., private communication, 2023]. Hence, 21 MW should be transported on average by turbulent and neoclassic heat flux channels. The turbulent fluxes in the analyzed radial domain reach comparable magnitudes but only if $E \times B$ shear is included in the simulations. It is, however, important to note that the turbulent fluxes show strong radial variations, as discussed in Fig. 6.25. For the pedestal top, the total heat flux remains a factor five too high even with $E \times B$ shear.

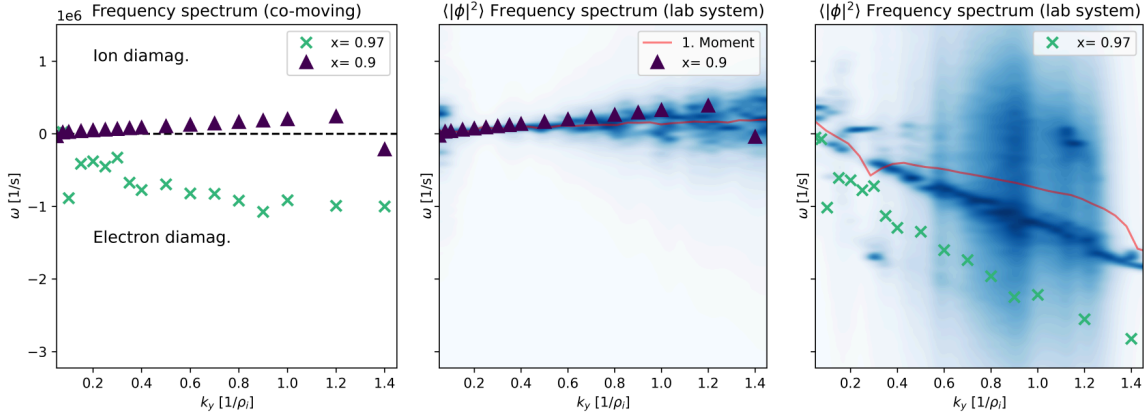


Fig. 6.21.: Linear-nonlinear frequency comparison. Left: Linear results in the co-moving frame for two positions. Middle: Comparison of linear (purple triangles) and nonlinear frequencies (blue distribution, analyzed in $\rho_{\text{tor}}=[0.89,0.91]$) at pedestal top. Right: Comparison of linear (green crosses) and nonlinear frequencies (blue distribution, analyzed in $\rho_{\text{tor}}=[0.96,0.98]$) at pedestal center. The red line indicates the mean of the nonlinear frequency distribution. Analyzed was the nonlinear simulation with three species and $E \times B$ shear (see orange line in 6.20) in the time interval 50-194, corresponding to the black average on top of the orange line.

6.3.1. Comparison to linear frequencies and cross phases

As explained in the analysis of the AUG scenario, nonlinear modes, and linear instabilities should be compared to gain confidence that the linear instabilities remain relevant in the turbulent state. Fig. 6.21 compares linear and nonlinear frequencies. The left-most plot is in the co-moving frame and allows one to distinguish between ion and electron diamagnetic drift directions. The other plots show the nonlinear frequency distribution as a blue background at two selected positions (pedestal top and center) overlaid by frequencies from the linear scan. For the comparison, the linear frequencies are shifted to the lab frame, taking into account the additional $E \times B$ drift due to the radial electric field, which shifts the apparent frequencies. At the pedestal top, linear and nonlinear frequencies coincide very well - the nonlinear phase retains linear characteristics. In the pedestal center, the match is worse, but some linear properties seem to survive as well. However, the nonlinear frequency distribution at the pedestal center has a greater variance than the pedestal top distribution.

The two cross-phase plots Fig. 6.22 and Fig. 6.23 compare linear and nonlinear cross-phases. In particular, at the pedestal top, a good agreement can be observed. But also at the pedestal center $\phi \times T_{\perp}$ seems to retain linear structures in the nonlinear state. The crossphases of $\phi \times n$ give insight into the particle transport. At the pedestal top, the dominant mode has a finite $\phi \times n$ at $k_y \rho_i = 0.3$, which indicates transport of particles (transport is maximal at a phase difference of $\pi/2$). This coincides with the peak of

6. JET pedestal simulations

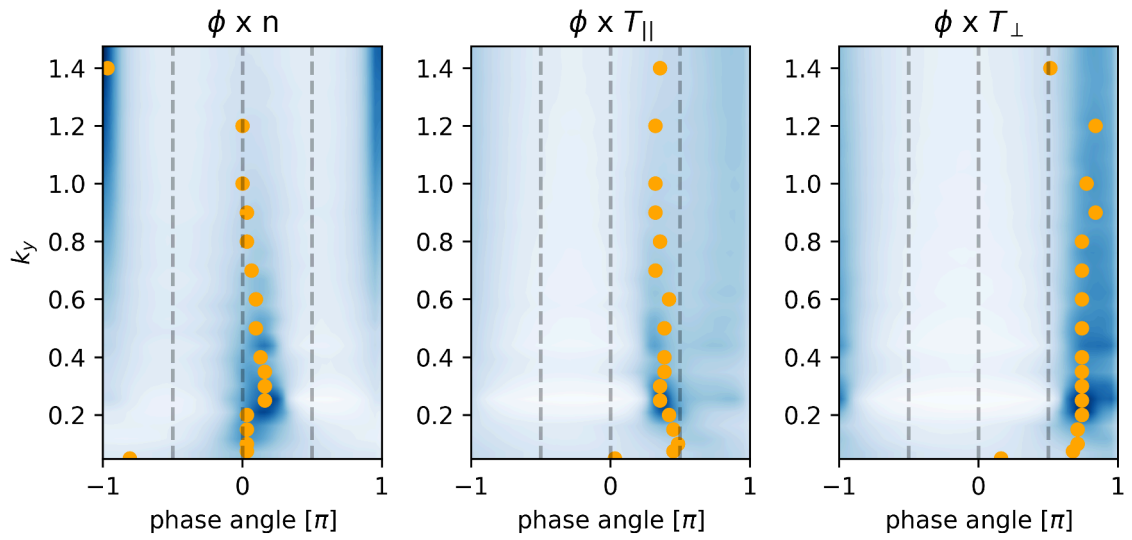


Fig. 6.22.: Cross-phases of density and parallel and perpendicular temperature with electric potential at the pedestal top $\rho_{\text{tor}} = 0.89$. The blue background shows the nonlinear distribution, and linear results are shown as orange circles. The nonlinear simulation with three species and $E \times B$ shear was analyzed (see orange line in 6.20) in the time interval 50-194, corresponding to the black average on top of the orange line.

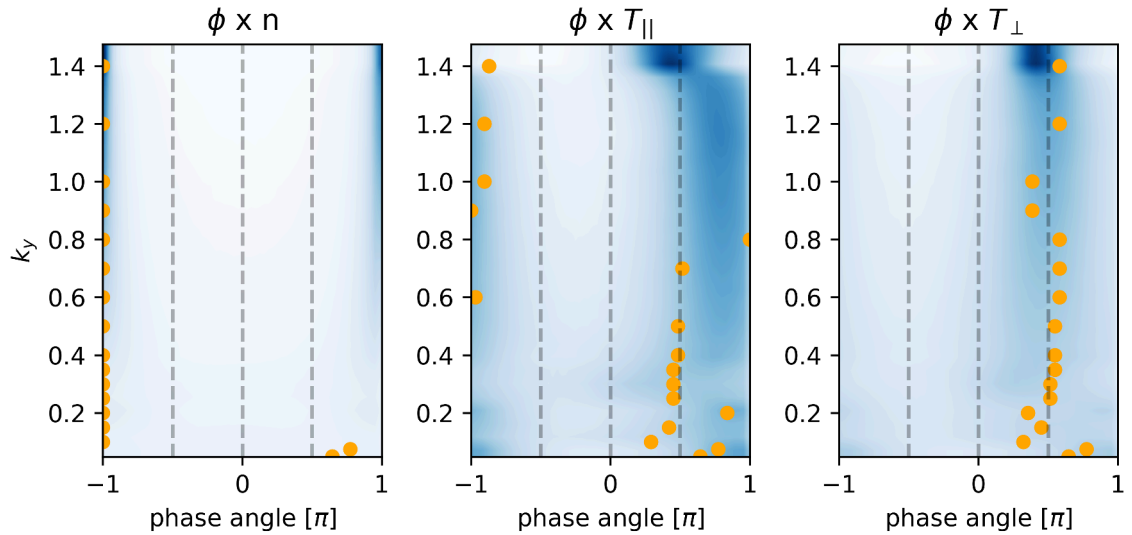


Fig. 6.23.: Cross-phases of density and parallel and perpendicular temperature with electric potential at the pedestal center $\rho_{\text{tor}} = 0.97$. The blue background shows the nonlinear distribution, and linear results are shown as orange circles. The nonlinear simulation with three species and $E \times B$ shear was analyzed (see orange line in 6.20) in the time interval 50-194, corresponding to the black average on top of the orange line.

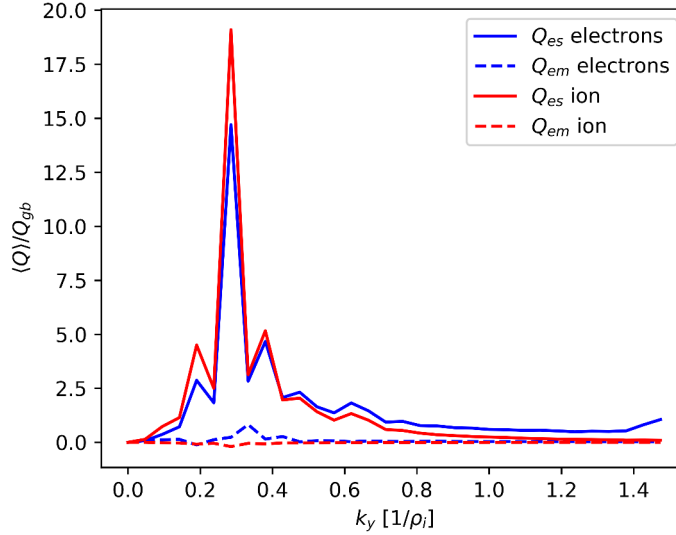


Fig. 6.24.: Heat flux spectrum of the global, nonlinear simulation with three species and increased $E \times B$ shear. Averaged over $\rho_{tor} = 0.85 - 0.99$, flux surfaces and time.

the heat flux spectrum at $k_y \rho_i = 0.3$ (cf. Fig. 6.24), corroborating the dominance of ITG transport at the pedestal top derived from the linear analysis. In the pedestal center, however, the $\phi \times n$ cross phases indicate vanishing particle transport. This is in agreement with the transport driver being ETG.

6.3.2. Heat flux analysis

This subsection analyses the turbulent ion-scale heat flux in more detail. The binormal spectrum and radial distribution of the heat flux from the simulation with three species and increased $E \times B$ shear (purple line Fig. 6.20) is analyzed.

Fig. 6.24 shows the radial heat flux spectrum of main ions (red) and electrons (blue) of the nonlinear phase of the three species simulation with increased $E \times B$ shear. A strong peak at $k_y \approx 0.3$ is present, which is driven by the pedestal top ITG. A slight increase in the electron channel at the high- k_y end of the distribution indicates the relevance of ETGs. They are not fully resolved in this simulation, and only their low- k_y tail extends into the range of scale included in the simulation.

Fig. 6.25 shows the heat flux profile for the global nonlinear three species simulation with increased $E \times B$ shear. Even though this is the simulation with the lowest heat fluxes (strong $E \times B$ shear, inclusion of impurities), the peak heat fluxes that are reached in the pedestal top/ outer core region ($\rho_{tor} \approx 0.9$) are unreasonably high with $Q_{tot} \approx 100$ MW. This is most likely due to too steep temperature profiles in this region. The structure of the heat flux is also interesting in comparison to the

6. JET pedestal simulations

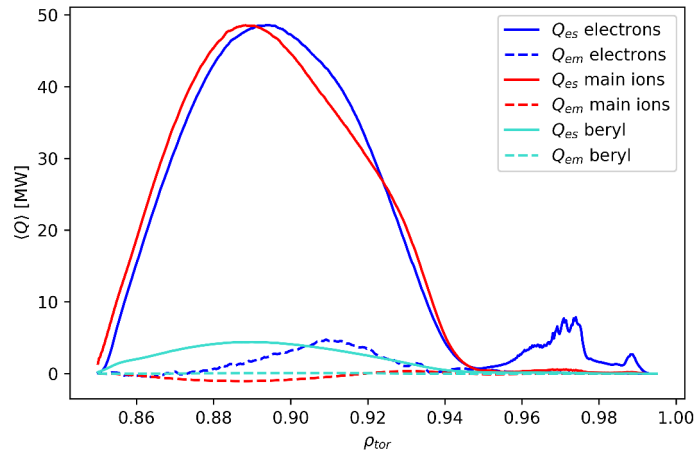


Fig. 6.25.: Heat flux profile of the global, nonlinear simulation with three species and increased $E \times B$ shear. Averaged over flux surfaces and time.

AUG case. As previously seen, turbulent ion transport is suppressed in the steep gradient region, beginning from around $\rho_{\text{tor}} = 0.95$, meaning the total ion transport is predominantly neoclassic. In contrast to AUG, an electron transport peak is present at $\rho_{\text{tor}} = 0.97$ in the steepest gradient region. This indicates that in the JET scenario, an effective electron transport mechanism in the pedestal center remains. Our linear analysis suggests that these are low- k_y tails of ETG modes, which extend due to the strong drive in the pedestal down to ion scales. Dedicated electron-scale simulations have not yet been completed.

6.3.3. Sensitivity scan

Fig. 6.26 shows the sensitivity of the calculated heat fluxes to gradients. The ion temperature profile is notoriously difficult to measure; hence, the best-fit profiles (green) and the assumption $T_i = T_e$ (yellow) are tested. This change corresponds to almost a factor two in the calculated heat fluxes, underlining the sensitivity and limitations on the absolute heat flux values calculated here.

6.4. Summary

In this chapter, instabilities and ion-scale turbulent transport in a pre-ELM JET pedestal of a hybrid H-mode shot have been characterized. The successful application of global, nonlinear simulations to the JET hybrid scenario pedestal confirms the capabilities of the new code upgrade. The dominant contribution to ion-scale transport on the pedestal top is identified to be ITG-driven turbulence. Towards the pedestal

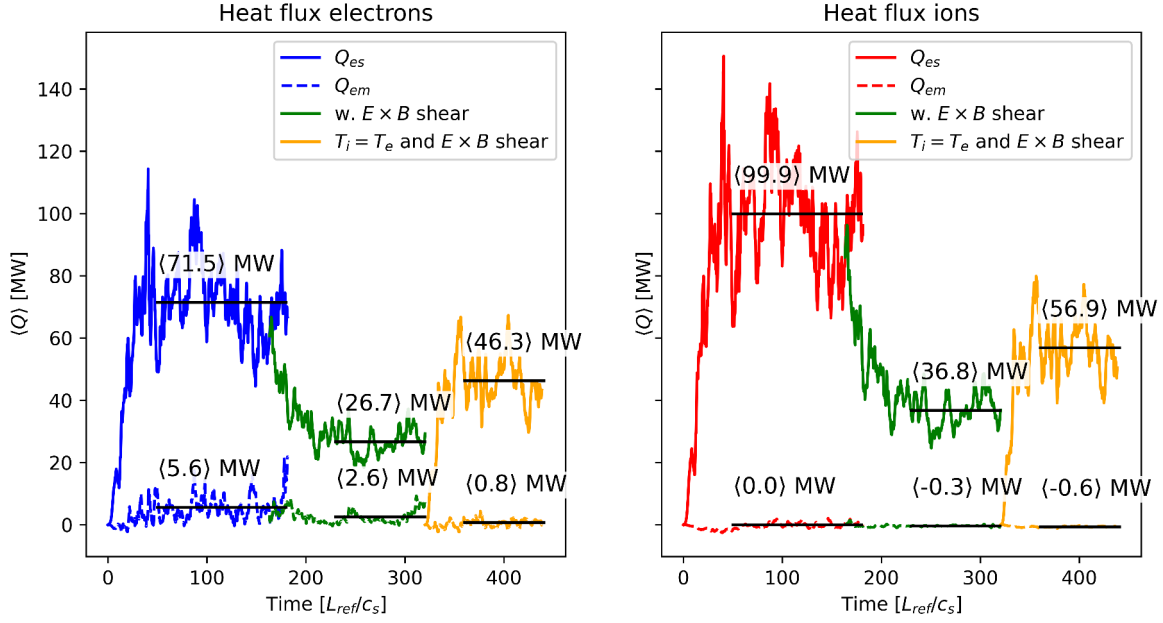


Fig. 6.26.: Sensitivity study: $T_i=T_e$. Heat flux from global nonlinear simulations as a function of time. Averaged over $\rho_{tor} = 0.85 - 0.99$ and flux surfaces. Blue/red: Without $E_r \times B$ shear. Green: With $E_r \times B$ shear. Yellow: With $E_r \times B$ shear and $T_i=T_e$.

foot, ETG modes become more prevalent, extending down to ion-scales. As for the AUG pedestal, $E \times B$ shear has been shown to be a crucial component in setting the turbulent heat flux level. Additionally, impurities have been shown to lower the main ion heat transport. In contrast to AUG, ETG-driven electron transport on ion scales is found in the pedestal center. Nonlinear electron-scale simulations have been started to complete the turbulent transport characterization - their results are left for future work.

Linear and nonlinear sensitivity scans show a robust presence of ITG turbulence at the pedestal top and sensitive dependence of the heat flux on the ion temperature profile. ITG modes in the JET-ILW pedestal have been reported before [133] but extended to the steep gradient region in this study. In the simulations of our scenario, low- k_y tails of ETG modes drive most of the transport in the pedestal center, and ITG is restricted to the pedestal top. The linear analysis of ETG modes has revealed a complex mode structure and high parallel resolution demands as described recently in [104, 105]. Similar to the AUG pedestal, a very good agreement between nonlinear and linear mode properties at the pedestal top has been observed, and there is still good agreement in the pedestal center. This is a further encouraging finding for the development of quasilinear pedestal models.

7. Conclusions & Outlook

This thesis has addressed an important challenge of fusion research: The simulation of turbulent transport in the H-mode pedestal. Since tokamak core profiles are typically stiff against increases in the heating power, the H-mode pedestal is particularly relevant for the overall confinement of energy and particles in tokamak experiments. Gyrokinetic turbulence is one of the key ingredients shaping the pedestal. The simulation of pedestal turbulence, however, is a great scientific and numerical challenge, as outlined in Chapter 4. Many physical effects have to be taken into account due to the steep profiles and strong changes in the H-mode pedestal. These include global effects, electromagnetic fluctuations, the presence of ion-scale as well as electron-scale instabilities, and shear flows.

To address these challenges, the capabilities of the GENE code have been extended, and gyrokinetic turbulence in two experimental H-mode pedestals has been investigated. This thesis has thereby pushed the frontiers of gyrokinetic analysis of H-mode pedestals and has improved the understanding of pedestal turbulence. The main achievements of this thesis are:

- An upgrade of the global, electromagnetic GENE code capabilities. The new implementation of the f-version enables global, nonlinear, electromagnetic simulations of pedestals at experimental β values. After ruling out that the omission of analytical higher-order terms was causing the code instability, more substantial code changes based on the proof-of-principle in [56] have been implemented. The main distribution function of GENE has been adapted, changes to the Vlasov equation and field equations have been implemented, and the changes have been made compatible with block-structured velocity grids. Details can be found in Sec. 3.3.
- The first global, nonlinear, electromagnetic turbulence simulation of an ASDEX Upgrade pedestal. Using the new code upgrade, one of the first global, nonlinear, electromagnetic gyrokinetic pedestal simulations has been performed. Supported by linear, local scans and nonlinear, local ETG simulations, the global simulations reveal a complex radial structure of turbulence in the pedestal. A linear stability mechanism related to the magnetic shear and the pressure gradient is found to be active. Furthermore, the crucial role of $E_r \times B$ shear in suppressing pedestal turbulence is confirmed in these high-fidelity simulations. Overall, ion-scale turbulence in the pedestal center is found to be suppressed, and a transition

7. Conclusions & Outlook

of electron transport from ion-scales at the pedestal top to electron-scales in the pedestal center has been found. Details can be found in Sec. 5.3.

- Global, nonlinear turbulence simulation of a JET hybrid scenario pedestal. The code upgrade could also be successfully applied to an ELMy H-mode pedestal from a JET hybrid scenario. The global simulations reveal a similar heat flux structure as in the AUG pedestal, with a substantial reduction of heat flux in the pedestal center. However, low- k_y tails of ETG modes prevail in the JET case and drive electron transport on ion-scales. Impurities are shown to reduce the turbulent transport of the main ions and the importance of $E_r \times B$ shear in setting the turbulent heat flux has been confirmed. Details can be found in Sec. 6.3.
- Well-resolved characterization of turbulence across two pedestals. Scans involving several thousand local, linear gyrokinetic simulations were performed to develop a radially resolved understanding of the microinstabilities present in the AUG and JET pedestals. These include scans in the binormal wave number k_y and radial wavenumber $k_{x,\text{center}}$ at nominal parameters, sensitivity scans in gradients, plasma β , or collisionality and convergence tests. In AUG at the pedestal top, TEMs and MTMs have been identified as relevant instabilities. In the pedestal center, ETGs have been found to be prevalent. In JET at the pedestal top, ITG has been found to be dominant. In the pedestal center, again, ETGs have been found to be the most relevant. Furthermore, both pedestals have been found to be close to a linear KBM threshold at pedestal center and foot. Details can be found in Sec. 5.2 and Sec. 6.2.
- Complex structure of pedestal-ETG modes. In both pedestals, ETG modes with toroidal and slab character have been identified that can require high parallel resolutions. In AUG, the slab-ETG modes are linearly subdominant but are relevant in the nonlinear simulations. In JET, linear convergence studies suggest that slab-ETG modes are the fastest-growing modes at high- k_y . The modes are found to have an intricate dependence on the ballooning angle. Details can be found in Sec. 5.3.2 and Sec. 6.2.
- Quasilinear nature of ion-scale pedestal turbulence. Frequencies and cross-phases of linear, local and nonlinear, global simulations have been compared for the AUG and JET pedestal. In both pedestals, a very good agreement between mode signatures at the pedestal top has been found, and still a good agreement in the pedestal center. This suggest that the linearly fastest-growing modes remain relevant in the saturated turbulent state. Hence, these findings are encouraging

for the development of quasilinear pedestal turbulence models. Details can be found in Sec. 5.3.1 and Sec. 6.3.1.

These results extend and refine the current understanding of pedestal turbulence. In agreement with interpretative modeling [152, 157], the turbulent ion heat flux in the pedestal center is found to strongly reduce, such that the total ion heat flux approaches neoclassic levels. Consistent with the fingerprint analysis of Ref. [103], we do not find significant contributions of ITGs or TEMs to the heat flux in the pedestal center. Their suppression by $E \times B$ shear has been confirmed by our high-fidelity global simulations. Additionally, we identify a linear stabilization mechanism linked to the magnetic shear and pressure gradient to locally suppress turbulent transport, even without $E \times B$ shear. In contrast to other gyrokinetic studies on JET [133, 134] and DIII-D [131, 132], we do not find significant electromagnetic transport due to MTMs in the pedestal center. In AUG, MTMs are present linearly and in the global simulations on the pedestal top but not the pedestal center. Hence, turbulent transport in the pedestal center is dominated by ETG transport in our analysis. Overall, our results highlight the importance of distinguishing between the different radial domains of the pedestal and demonstrate that the total turbulent pedestal transport is multi-channel and multi-scale.

7.1. Discussion and Outlook

The current GENE model and the implemented upgrade allow insightful studies of pedestal physics, as presented in this thesis. Several simulations of this thesis are among the highest-fidelity and most realistic pedestal turbulence simulations performed to date. In particular, they include global effects, electromagnetic fluctuations, and collisions (Landau operator). They use real experimental profiles, experimental magnetic equilibria (g-eqdk), and the true electron-to-ion mass ratio. Nonetheless, to identify possible extensions, it is worthwhile to recall the limitations of the employed simulation framework.

Some limitations apply to the fluctuations that can be simulated. In particular, the relative fluctuation amplitudes are limited due to GENE's δf ansatz for the distribution function. Very close to the separatrix, the ability to include larger fluctuation amplitudes would be desirable. Furthermore, not all types of magnetic fluctuations were included in the simulations. While the code upgrade enables stable simulations with perpendicular magnetic fluctuations $\bar{A}_{1\perp}$, compressional, parallel magnetic fluctuations are not included. Linear tests performed in this thesis for the JET case suggest that the currently employed drift correction works well. Nonetheless, B_{\parallel} fluctuations could

7. Conclusions & Outlook

further increase the fidelity of global simulations. The implementation of B_{\parallel} fluctuations for global GENE simulations is currently being pursued. Additionally, the current implementation of $E \times B$ flows in GENE limits them to be in the toroidal direction. In contrast, the dominant direction of $E_r \times B$ flows at a high safety factor in the pedestal is the poloidal direction. While the current implementation yields convincing results, it would be desirable to test if the flow direction has an impact on the resulting turbulence suppression.

Furthermore, to reduce the computational cost of simulations, electron scales and ion scales were not simulated in a single multi-scale simulation but in separate simulations. The separation of ion and electron scale simulations prohibits any mutual scale interaction and excludes a range of wavenumbers in our setup. Several effects have been observed in simulations that include cross-scale interactions: In JET pedestal conditions ion scale ETGs were found to decrease ETG transport [125] and in DIII-D pedestal top-like conditions an increase of ion-scale and decrease of electron-scale transport was reported [168]. In core conditions, a suppression of MTMs by ETG turbulence [169], a suppression of electron-scale turbulence by ion-scale turbulence, and an enhancement of ITGs by electron-scale transport have been found [127]. Furthermore, an overall increase of turbulent heat fluxes in multi-scale simulations was reported [128, 129]. Overall, these studies suggest that cross-scale interactions may decrease the ETG heat flux we observe by a few 10%.

Other limitations apply to the temperature and density profiles in the simulations. While real experimental profiles and equilibria have been used, the gradient-driven approach does not include the effect of the simulated turbulent fluxes on the background profiles. Instead, they are kept constant on average. A flux-driven approach would include the profile changes self-consistently. The proof-of-principle of the GENE-Tango approach in the pedestal has, however, highlighted the challenges of flux-driven pedestal simulations. Both, ion-scale and electron-scale fluctuations contribute to the turbulent fluxes in the different regions of the pedestal and would need to be included in some form in a flux-driven pedestal simulation.

A further limitation is the use of field-aligned coordinates, which strictly restricts our simulation domain to the region of closed flux surfaces. In combination with the Dirichlet boundary conditions of global simulations, this excludes any influence of scrape-off layer physics on the pedestal simulations. Approaches that can cross the separatrix would be well suited to expand the study of pedestal foot turbulence.

More generally, while present-day models successfully capture several important aspects of pedestal turbulence, the complexity of the pedestal suggests that one code alone can

hardly capture all relevant physics effects in a full pedestal. The strong differences in plasma conditions between pedestal top and foot and the wide range of scales involved in pedestal dynamics are large challenges to all computationally affordable models. Joint efforts of multiple codes applied to the same scenario with a flexible coupling, therefore, offer a path to a further improved understanding of pedestal physics.

A. Appendix

A.1. Derivation of additional terms

This section documents additional details for the derivation of the f-version and higher-order terms discussed in Chapter 3.

A.1.1. Γ_i terms in Vlasov equation

Here, the additional terms in the Vlasov equation arising from retaining all terms of Γ_i in the g-version are documented. This provides additional details to the discussion in Sec. 3.3.2. I start with the normalized GENE Vlasov equation (cf. Eq. 3.13) and plug in Γ_i and $\frac{\partial F_0}{\partial v_{\parallel}} = -\frac{mv_{\parallel}}{T_0(x)}F_0$. The terms containing Γ_i are listed.

1st term containing Γ_x :

$$-\frac{B_0}{B_{0\parallel}^*} \frac{T_0(x_0)}{q} \frac{\mu B_0 + 2v_{\parallel}^2}{B_0} K_x \times \left(\partial_x g_1 + \frac{q}{T_0} F_0 \partial_x \chi_1 + \frac{\rho_{\text{ref}}}{L_{\text{ref}}} v_T(x_0) q v_{\parallel} \bar{A}_{1\parallel} \frac{1}{T_0(x)} (-\partial_x F_0 + \frac{\partial_x T_0(x)}{T_0(x)} F_0) \right) \quad (\text{A.1})$$

2nd term containing Γ_y :

$$-\frac{B_0}{B_{0\parallel}^*} \left[\frac{T_0(x_0)}{q} \frac{\mu B_0 + 2v_{\parallel}^2}{B_0} K_y - \frac{T_0(x_0)}{q B_0} \frac{v_{\parallel}^2}{C} \beta_{\text{ref}} \frac{p_0}{B_0} \omega_p \right] \times \left(\partial_y g_1 + \frac{q}{T_0} F_0 \partial_y \chi_1 + \frac{\rho_{\text{ref}}}{L_{\text{ref}}} v_T(x_0) q v_{\parallel} \bar{A}_{1\parallel} \frac{1}{T_0(x)} (-\partial_y F_0) \right) \quad (\text{A.2})$$

3rd term containing Γ_y (Note that a $\frac{q}{T_0} F_0 \partial_y \chi_1$ part does not occur since it cancels with parts of the 4th term):

$$-\frac{B_0}{B_{0\parallel}^*} \frac{1}{C} \partial_x \chi_1 \left(\partial_y g_1 + \frac{\rho_{\text{ref}}}{L_{\text{ref}}} v_T(x_0) q v_{\parallel} \bar{A}_{1\parallel} \frac{1}{T_0(x)} (-\partial_y F_0) \right) \quad (\text{A.3})$$

4th term containing Γ_x (Note that a $\frac{q}{T_0} F_0 \partial_x \chi_1$ part does not occur since it cancels with parts of the 3rd term):

$$-\frac{B_0}{B_{0\parallel}^*} \frac{1}{C} (-\partial_y \chi_1) \left(\partial_x g_1 + \frac{\rho_{\text{ref}}}{L_{\text{ref}}} v_T(x_0) q v_{\parallel} \bar{A}_{1\parallel} \frac{1}{T_0(x)} (-\partial_x F_0 + \frac{\partial_x T_0(x)}{T_0(x)} F_0) \right) \quad (\text{A.4})$$

A. Appendix

5th term containing Γ_z :

$$-v_T(x_0) \frac{C}{JB_0} v_{\parallel} \left(\partial_z g_1 + \frac{q}{T_0} F_0 \partial_z \chi_1 + \frac{\rho_{\text{ref}}}{L_{\text{ref}}} v_T(x_0) q v_{\parallel} \bar{A}_{1\parallel} \frac{1}{T_0(x)} (-\partial_z F_0) \right) \quad (\text{A.5})$$

Not all of these terms are implemented in GENE (cf. Eq. (A.1) in Ref. [48]): All terms with the partial derivatives $\partial_x F_0$ and $\partial_y F_0$ are missing. The 5th term is fully implemented. To proceed, we assume a specific form of the background distribution (Maxwellian in velocity space, normalized):

$$F_0(\mathbf{x}, v_{\parallel}, \mu) = \frac{n_p(x)}{(\pi T_p(x))^{3/2}} e^{-\frac{v_{\parallel}^2 + \mu B_0(\mathbf{x})}{T_p(x)}} \quad (\text{A.6})$$

with $n_p(x) = \frac{n_0(x)}{n_0(x_0)}$, $T_p(x) = \frac{T_0(x)}{T_0(x_0)}$. The normalized spatial derivatives are:

$$\partial_x F_0 = F_0 \left[-\omega_n - \omega_T \left(\frac{v_{\parallel}^2 + \mu B_0}{T_0(x)/T_0(x_0)} - \frac{3}{2} \right) - \frac{\partial_x B_0}{B_0} \frac{\mu B_0 T_0(x_0)}{T_0(x)} \right] \quad (\text{A.7})$$

with $\omega_n = -\frac{L_{\text{ref}} \partial_x n_0(x)}{n_0(x)}$, $\omega_T = -\frac{L_{\text{ref}} \partial_x T_0(x)}{T_0(x)}$. The derivatives with respect to y and z , which lie on flux-surfaces on which the background temperature and density are constant, simplify to:

$$\partial_y F_0 = F_0 \left[-\frac{\partial_y B_0}{B_0} \frac{\mu B_0 T_0(x_0)}{T_0(x)} \right] \quad (\text{A.8})$$

Implementation in GENE The additional terms have been implemented. They are calculated in the subroutine `set_new_Apar_terms` in the module `dgdxxy_terms`. They are then added to `dgdxxy` in the x-global versions of `add_dgdxxy` (`add_dgdxxy_df1`, `add_dgdxxy_df2`, `add_dgdxxy_df3`) and in the global version of the nonlinearity before the Fourier transformation to real space. Translated to GENE variables, the new terms have the form:

$$\frac{\rho_{\text{ref}}}{L_{\text{ref}}} v_T(x_0) q v_{\parallel} \bar{A}_{1\parallel} \frac{1}{T_0(x)} (-\partial_x F_0) = \text{eps} \cdot \text{qvTvpar} \cdot \text{bar_Apar} \cdot \text{dF0dvdi} \quad (\text{A.9})$$

with (cf. Appendix of Ref. [48])

$$\frac{\rho_{\text{ref}}}{L_{\text{ref}}} = \text{eps} = \text{rhostar} \cdot \text{minor_r} \quad (\text{A.10})$$

$$\text{qvTvpar} = q v_T(x_0) v_{\parallel} = q \sqrt{\frac{2T_0(x_0)}{m}} v_{\parallel} \quad (\text{A.11})$$

$$\begin{aligned}
dF_0 dv_{di} &= -\frac{1}{mv_{\parallel}} \frac{\partial}{\partial x} \left(\frac{\partial F_0}{\partial v_{\parallel}} \right) = -\partial_x F_0 \frac{1}{T_0(x)} + \frac{\partial_x T_0(x)}{T_0^2(x)} F_0 \\
&= \frac{F_0}{T_0(x)} \left[\omega_n + \omega_T \left(\frac{v_{\parallel}^2 + \mu B_0}{T_0(x)/T_0(x_0)} - \frac{5}{2} \right) + \frac{\partial_x B_0}{B_0} \frac{\mu B_0 T_0(x_0)}{T_0(x)} \right]
\end{aligned} \tag{A.12}$$

$$dF_0 dv_{dj} = -\frac{1}{mv_{\parallel}} \frac{\partial}{\partial y} \left(\frac{\partial F_0}{\partial v_{\parallel}} \right) = -\partial_y F_0 \frac{1}{T_0(x)} = \frac{F_0}{T_0} \left[\frac{\partial_y B_0}{B_0} \frac{\mu B_0 T_0(x_0)}{T_0(x)} \right] \tag{A.13}$$

$$\bar{A}_{1\parallel} = \bar{A}_{1\parallel} \tag{A.14}$$

Adaptation of the numerical scheme for the nonlinearity In GENE, the nonlinearity is discretized using the Arakawa scheme [76], which ensures conservation of energy (cf. Ref. [50], p. 43). The nonlinear term is formulated in terms of a Poisson bracket

$$\begin{aligned}
NL &= -\frac{B_0}{B_{0\parallel}^*} \frac{1}{C} (\partial_x \chi_1 \Gamma_y - \partial_y \chi_1 \Gamma_x) \\
&= -\frac{B_0}{B_{0\parallel}^*} \frac{1}{C} (\partial_x \chi_1 \partial_y g_1 - \partial_y \chi_1 \partial_x g_1) \\
&= \frac{B_0}{B_{0\parallel}^*} \frac{1}{C} \{g_1, \chi_1\}_{x,y}
\end{aligned} \tag{A.15}$$

which is implemented as

$$NL = \frac{B_0}{B_{0\parallel}^*} \frac{1}{C} \frac{1}{3} [(\partial_y \chi_1 \partial_x g_1 - \partial_x \chi_1 \partial_y g_1) + \partial_y (\chi_1 \partial_x g_1 - g_1 \partial_x \chi_1) + \partial_x (g_1 \partial_y \chi_1 - \chi_1 \partial_y g_1)], \tag{A.16}$$

cf. Ref. [50]. Numerically, the derivatives are calculated in Fourier space, and the products in real space. As we want to retain the full Γ_i term, this changes as follows:

$$\begin{aligned}
NL &= -\frac{B_0}{B_{0\parallel}^*} \frac{1}{C} (\partial_x \chi_1 \Gamma_y - \partial_y \chi_1 \Gamma_x) \\
&= -\frac{B_0}{B_{0\parallel}^*} \frac{1}{C} \left[\partial_x \chi_1 \left(\partial_y g_1 + \frac{\rho_{\text{ref}}}{L_{\text{ref}}} v_T(x_0) q v_{\parallel} \bar{A}_{1\parallel} \frac{1}{T_0(x)} (-\partial_y F_0) \right) \right. \\
&\quad \left. - \partial_y \chi_1 \left(\partial_x g_1 + \frac{\rho_{\text{ref}}}{L_{\text{ref}}} v_T(x_0) q v_{\parallel} \bar{A}_{1\parallel} \frac{1}{T_0(x)} (-\partial_x F_0 + \frac{\partial_x T_0(x)}{T_0(x)} F_0) \right) \right] \\
&= \frac{B_0}{B_{0\parallel}^*} \frac{1}{C} \left[\{g_1, \chi_1\}_{x,y} - \frac{\rho_{\text{ref}}}{L_{\text{ref}}} v_T(x_0) q v_{\parallel} \bar{A}_{1\parallel} \left\{ \frac{F_0}{T_0}, \chi_1 \right\}_{x,y} \right]
\end{aligned} \tag{A.17}$$

Note that $\bar{A}_{1\parallel}$ is a function of x and y , which prevents us from drawing out the derivative and writing the nonlinearity in terms of only one Poisson bracket. This translates to

A. Appendix

the following terms in the Arakawa scheme:

$$\begin{aligned}
\text{NL} = \frac{B_0}{B_{0\parallel}^*} \frac{1}{C} & \left[\frac{1}{3} \left((\partial_y \chi_1 \partial_x g_1 - \partial_x \chi_1 \partial_y g_1) + \partial_y (\chi_1 \partial_x g_1 - g_1 \partial_x \chi_1) + \partial_x (g_1 \partial_y \chi_1 - \chi_1 \partial_y g_1) \right) \right. \\
& - \frac{\rho_{\text{ref}}}{L_{\text{ref}}} v_T(x_0) q v_{\parallel} \bar{A}_{1\parallel} \frac{1}{3} \left((\partial_y \chi_1 \partial_x (F_0/T_0) - \partial_x \chi_1 \partial_y (F_0/T_0)) + \right. \\
& \quad \left. + \partial_y (\chi_1 \partial_x (F_0/T_0) - F_0/T_0 \partial_x \chi_1) \right. \\
& \quad \left. \left. + \partial_x (F_0/T_0 \partial_y \chi_1 - \chi_1 \partial_y (F_0/T_0)) \right) \right] \tag{A.18}
\end{aligned}$$

A.1.2. The nonlinearity expressed by distribution functions f , g or h

This subsection documents the different forms the nonlinear term in GENE's Vlasov equation can have depending on which distribution function is used.

The nonlinearity has the following general form (omitting the prefactor $-\frac{B_0}{B_{0\parallel}^*} \frac{1}{C}$):

$$\text{NL} = \partial_x \bar{\chi}_1 \Gamma_y - \partial_y \bar{\chi}_1 \Gamma_x, \tag{A.19}$$

It is desirable for numerical reasons to express the nonlinearity as a Poisson bracket $\{A, B\}_{x,y} = \partial_x A \partial_y B - \partial_y A \partial_x B$. By expressing Γ_i through the different distribution functions f_1 , g_1 , or h_1 , the nonlinearity can be cast in different forms.

When using f_1 one obtains:

$$\text{NL}_{f_1} = \{\bar{\chi}_1, f_1\}_{x,y} + q \frac{F_0}{T_0} \{\bar{\chi}_1, \bar{\phi}_1 + \frac{\mu}{q} \bar{B}_{1\parallel}\}_{x,y} \tag{A.20}$$

This version (without the $\bar{B}_{1\parallel}$ term) has been implemented for the f-version within this thesis. Note that F_0 and T_0 are functions of x (the radial coordinate) in global simulations. Hence, the two Poisson brackets cannot be combined into one single nonlinear term.

When using $g_1 = f_1 - \frac{q}{mc} \bar{A}_{1\parallel} \frac{\partial F_0}{\partial v_{\parallel}} = f_1 + \frac{qv_{\parallel}}{c} \bar{A}_{1\parallel} \frac{F_0}{T_0}$ one obtains:

$$\Gamma_i = \frac{\partial g_1}{\partial x_i} - \frac{q}{mv_{\parallel}} \frac{\partial F_0}{\partial v_{\parallel}} \frac{\partial \bar{\chi}_1}{\partial x_i} + \frac{q}{mc} \bar{A}_{1\parallel} \frac{\partial}{\partial x_i} \left(\frac{\partial F_0}{\partial v_{\parallel}} \right) = \frac{\partial g_1}{\partial x_i} + q \frac{F_0}{T_0} \frac{\partial \bar{\chi}_1}{\partial x_i} - \frac{qv_{\parallel}}{c} \bar{A}_{1\parallel} \frac{\partial}{\partial x_i} \left(\frac{F_0}{T_0} \right) \tag{A.21}$$

and hence:

$$\begin{aligned} \text{NL}_{g_1} &= \{\bar{\chi}_1, g_1\}_{x,y} + q \frac{F_0}{T_0} \{\bar{\chi}_1, \bar{\chi}_1\}_{x,y} - \frac{qv_{\parallel}}{c} \bar{A}_{1\parallel} \{\bar{\chi}_1, \frac{F_0}{T_0}\}_{x,y} \\ &= \{\bar{\chi}_1, g_1\}_{x,y} - \frac{qv_{\parallel}}{c} \bar{A}_{1\parallel} \{\bar{\chi}_1, \frac{F_0}{T_0}\}_{x,y} \end{aligned} \quad (\text{A.22})$$

The GENE standard g-version approximates this to: $\text{NL}_{g_1} = \{\bar{\chi}_1, g_1\}_{x,y}$. An advantage of this approach is that it uses only one Poisson bracket. However, the standard version using this variant tends to be unstable in global, electromagnetic simulations. The inclusion of the omitted term $\frac{F_0}{T_0}$ was tested in this thesis. The g-version remained unstable.

When using $h_1 = f_1 + q \frac{F_0}{T_0} (\bar{\phi}_1 + \frac{\mu}{q} \bar{B}_{1\parallel})$ one obtains:

$$\Gamma_i = \frac{\partial h_1}{\partial x_i} - q \frac{\partial}{\partial x_i} \left(\frac{F_0}{T_0} \right) (\bar{\phi}_1 + \frac{\mu}{q} \bar{B}_{1\parallel}), \quad (\text{A.23})$$

and hence:

$$\text{NL}_{h_1} = \{\bar{\chi}_1, h_1\} - (q\bar{\phi}_1 + \mu\bar{B}_{1\parallel}) \{\bar{\chi}_1, \frac{F_0}{T_0}\}. \quad (\text{A.24})$$

Based on the same argument as in the g-version, the $\frac{F_0}{T_0}$ term could be neglected. The h-version has not been comprehensively explored in this thesis.

A.2. AUG simulation settings

Linear, local simulations

- 2 species, experimental β , realistic electron to ion mass ratio $m_e/m_D = 1/3670$, Landau collision operator, arakawa_zv=F, tracer_efit geometry interface.
- $E \times B$ shear was not used to avoid Floquet modes.
- Resolution: $n_x = 18$, $n_{ky} = 1$, $n_z = 36$, $n_v = 32$, $n_w = 16$.
- Box size: lv=3.1, lw=11.
- hyp_z=-1
- Convergence tests with increased parallel resolutions and increased velocity space resolution ($n_v = 128$, $n_w = 32$) were performed.
- Performed in double-precision floating-point format.

A. Appendix

- Simulations were performed with GENE code version
GIT_MASTER = 9a09515c6e9b8b5dd1bfda383bcae1a330c7ce9.

Nonlinear, local ETG simulations

- 1 kinetic species (electrons), adiabatic ions, experimental β , Landau collision operator, arakawa_zv=T, tracer_efit geometry interface.
- No $E \times B$ shear.
- Resolution: $n_x = 512$, $n_{ky} = 64$, $n_z = 288$, $n_v = 32$, $n_w = 16$.
- Box size: lv=3, lw=9, lx=3.5.
- Convergence tests for radial resolution, radial box size and parallel resolution (up to nz=576) were performed for the position $\rho_{\text{tor}} = 0.97$.
- GyroLES=T, hyp_z settings are discussed in the main text.
- Performed in single-precision floating-point format. Double-precision convergence tests were performed.
- Simulations were performed with GENE code version
GIT_MASTER = 59331b56545cdd88b3bb55bceb0bfa46a721bcea.

Nonlinear, global, ion scale simulations

- 2 species, experimental β , realistic electron to ion mass ratio $m_e/m_D = 1/3670$, Landau collision operator, arakawa_zv=F, tracer_efit geometry interface.
- With $E \times B$ shear when indicated.
- Resolution: $n_x = 512$, $n_{ky} = 32$, $n_z = 48$, $n_v = 32$, $n_w = 16$.
- Box size: lv=3.45, lw=14.23, lx=72.
- Boundary conditions: Dirichlet with radial buffer zones (5% of domain at both boundaries), in which the distribution function is damped by fourth-order Krook operators.
- hyp_x=1, hyp_z=-1.
- Performed with block-structured velocity grids [71] with 4 blocks.
- Performed in single-precision floating-point format. Double-precision convergence tests were performed.

- Simulations were performed with GENE code version
GIT_MASTER = 59331b56545cdd88b3bb55bceb0bfa46a721bcea.

Definitions

- lv is the extension of the simulation box in the v_{\parallel} direction, in units of the thermal velocity $v_T = (2T_0/m)^{1/2}$.
- lw is the extension of the simulation box in the μ direction, in units of T_0/B_{ref} .
- lx is the extension of the simulation box in the radial direction in units of the ion gyroradius at the reference position. In global simulations, the reference position is the center of the simulation domain. In most cases shown here, this is at $\rho_{tor} = 0.9225$.

A.3. JET simulation settings

A.3.1. Simulation parameters

Linear, local simulations

- 2 species, experimental β , realistic electron to ion mass ratio $m_e/m_D = 1/3670$, Landau collision operator. tracer_efit geometry interface.
- $E \times B$ shear was not used to avoid Floquet modes.
- Resolution: $n_x = 18$, $n_{ky} = 1$, $n_z = 36$, $n_v = 32$, $n_w = 16$.
- Box size: lv=3.1, lw=11.
- Convergence tests in the parallel resolution are discussed in the main text. Tests with $\bar{B}_{1\parallel}$ were performed and are discussed in the main text.
- Performed in double-precision floating-point format.
- Simulations were performed with GENE code version
GIT_MASTER = 9a09515c6e9b8b5dd1bfda383bcae1a330c7ce9.

Nonlinear, global, ion scale simulations

- 2 species, experimental β , realistic electron to ion mass ratio $m_e/m_D = 1/3670$, Landau collision operator. With $E \times B$ shear when indicated.
- Resolution: $n_x = 512$, $n_{ky} = 32$, $n_z = 48$, $n_v = 32$, $n_w = 16$.

A. Appendix

- Box size: $lv=3.39$, $lw=13.74$, $lx=106.18$.
- Boundary conditions: Dirichlet with radial buffer zones (5% of domain at both boundaries), in which the distribution function is damped by fourth-order Krook operators.
- $hyp_x=1$, $hyp_z=-1$.
- Performed with block-structured velocity grids [71] with 4 blocks.
- Performed in single-precision floating-point format.
- Simulations were performed with GENE code version
`GIT_MASTER = 59331b56545cdd88b3bb55bceb0bfa46a721bcea`.

Definitions

- lv is the extension of the simulation box in the $v_{||}$ direction, in units of the thermal velocity $v_T = (2T_0/m)^{1/2}$.
- lw is the extension of the simulation box in the μ direction, in units of T_0/B_{ref} .
- lx is the extension of the simulation box in the radial direction in units of the ion gyroradius at the reference position. In global simulations, the reference position is the center of the simulation domain. In most cases shown here, this is at $\rho_{tor} = 0.9225$.

A.4. ASDEX Upgrade (AUG) tokamak

ASDEX Upgrade (see Fig. A.1) is a tokamak operated since 1991 at the Max Planck Institute for Plasma Physics. ASDEX stands for Axially Symmetric Divertor Experiment. It features a major plasma radius of 1.65 m, a minor plasma radius of 0.5 - 0.8 m, and a plasma volume of 14 m³. It is part of the EUROfusion Medium-Sized Tokamak program and is strongly involved in the preparation of future tokamak reactors. More info at: <https://www.ipp.mpg.de/16195/asdex>

A.5. Joint European Torus (JET) tokamak

JET, the Joint European Torus (see Fig. A.2), is, as of writing, the world's largest tokamak in operation. It started operation in 1983. It has played a crucial role in the progress of fusion research as it was one of only two experiments with the capability to

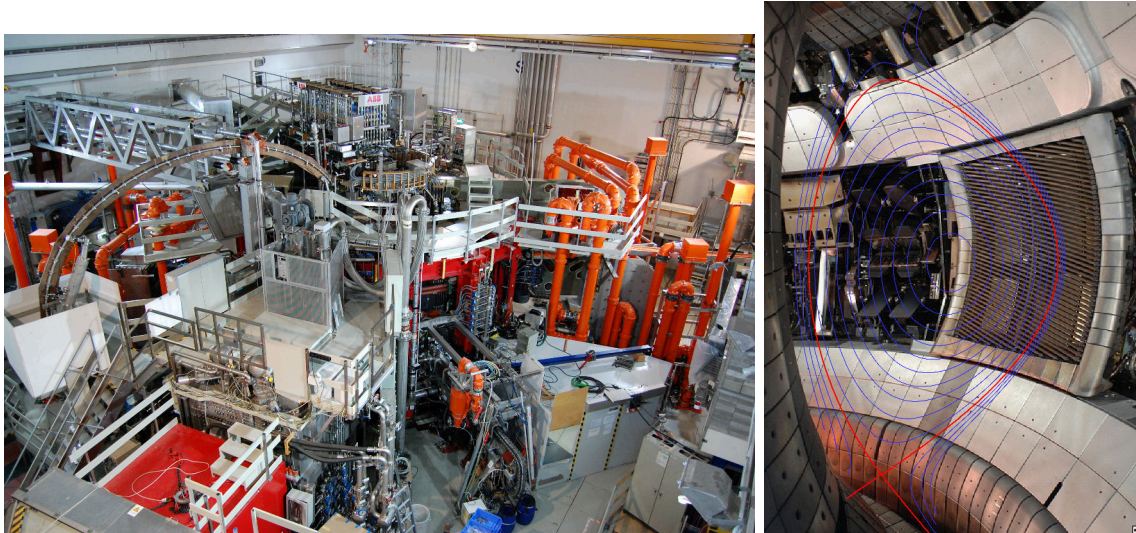


Fig. A.1.: Left: Photograph of the ASDEX Upgrade torus hall. Right: Photograph of the inner vessel with superimposed magnetic flux surfaces. Source: IPP Garching.

use Tritium in the experiments. JET holds the world record for the highest sustained fusion energy produced in a discharge. It features a major plasma radius of 2.96 m, a minor plasma radius of 1.25 - 2.1 m, and a plasma volume of 80 m³. More info at: <https://ccfe.ukaea.uk/programmes/joint-european-torus/> and <https://www.ipp.mpg.de/16701/jet>

A.6. High-performance computing systems

A.6.1. Cobra at MPCDF

Parts of the simulations for this thesis were performed on the Cobra Supercomputer of the Max Planck Computing and Data Facility of the Max Planck Society.

A.6.2. Raven at MPCDF

Parts of the simulations for this thesis were performed on the Raven Supercomputer of the Max Planck Computing and Data Facility of the Max Planck Society. Raven provides in total 1592 CPU compute nodes with 72 cores (Intel Xeon IceLake-SP 8360Y) and 256 GB of RAM per node as well as 192 GPU-accelerated nodes. For typical simulations 64 - 192 Nodes were used in parallel. For more information, see: <https://www.mpcdf.mpg.de/services/supercomputing/raven>

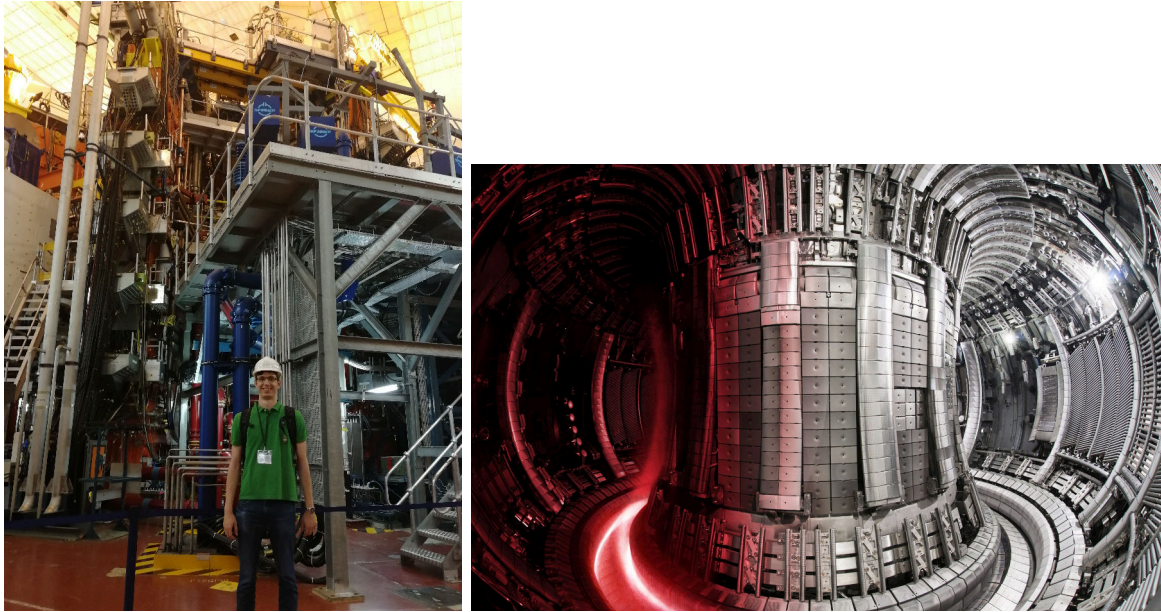


Fig. A.2.: Photograph of the JET torus hall (left) and the inner vessel with a superimposed plasma discharge (right, reproduced with permission from UKAEA).

A.6.3. JFRS at IFERC

Parts of the simulations for this thesis were performed on the Japanese supercomputer JFRS at the IFERC Centre. Compute time was made available via a proposal within the Broader Approach framework.

A.6.4. Marconi at CINECA

Most of the simulations for this thesis were performed on the EUROfusion A3 partition of the Marconi supercomputer at the Italian supercomputing center CINECA. Marconi-A3 provides 2912 nodes with 48 cores (2 x 24-cores Intel Xeon 8160 CPU (Skylake)) and 192 GB per node. For a typical simulation, 128 Nodes were used in parallel. Some simulations were performed on the GPU-accelerated partition MARCONI100. Compute time was made available via the EUROfusion TSVV1 project. For more information, see:

<https://wiki.u-gov.it/confluence/display/SCAIUS/UG3.1%3A+MARCONI+UserGuide>

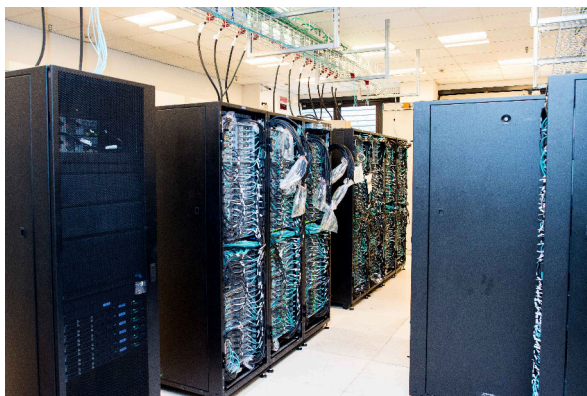


Fig. A.3.: Photograph of racks of the Marconi supercomputer during installation. Taken from Marconi @Cineca (ph. MMLibouri) [170].

Nomenclature

Notation

Vectors are denoted by bold letters, e.g. \mathbf{B} , with components B_i and magnitude $B = \|\mathbf{B}\| = \sqrt{\mathbf{B} \cdot \mathbf{B}}$. Unit vectors are lower-case, bold letters with a hat, e.g. $\hat{\mathbf{b}}$.

Scalars are denoted by roman or greek letters, e.g. q , ρ .

Averages are denoted by $\langle \cdot \rangle$.

Overbars $\bar{\cdot}$ denote gyroaveraged quantities.

Symbols

Not all symbols are used uniquely in this thesis, e.g. q is used in earlier Chapters to denote a charge and, in later chapters, the safety factor. Similarly, χ denotes the modified potential in the Vlasov equation but is occasionally used to denote the heat diffusivity. This approach has the advantage of adhering to conventions in the respective contexts.

Symbol	Meaning
β	plasma beta. Ratio between plasma pressure and magnetic pressure. $\beta = p/(B^2/2\mu_0)$, with $p = k_B n T$ the plasma pressure, B the magnetic field, μ_0 the magnetic permeability.
β_N	normalized plasma beta. $\beta_N = \beta/(I/aB_\phi)$ with I the plasma current, a the tokamak minor radius, B_ϕ the toroidal magnetic field. Derived for the Troyon beta limit.
H_{98}	H-factor. $H_{98} = \tau_E/\tau_{IPB98(y,2)}$ Measure for energy confinement quality of a shot by normalization to an empirical scaling factor.
v_{\parallel}	$= \mathbf{v} \cdot \hat{\mathbf{b}}$ parallel velocity (w.r.t. to the magnetic field)
v_{\perp}	$= \mathbf{v} - v_{\parallel} \hat{\mathbf{b}} $ perpendicular velocity (w.r.t. to the magnetic field)

A. Appendix

Symbol	Meaning
ω_c	$= qB/m$ gyrofrequency, with charge q , magnetic field strength B , mass m .
ρ_i	mv_{\perp}/qB ion gyroradius.
χ	modified potential or heat diffusivity
τ	$= Z_{\text{eff}}T_e/T_i$.
Z_{eff}	effective ion charge $Z_{\text{eff}} = \sum_i n_i Z_i^2 / n_e$ with n_i the ion density of species i , Z_i the charge state of species i and n_e the electron density
ρ_{tor}	normalized toroidal magnetic flux. The default radial coordinate in GENE for tracer_efit interface.
ρ_{pol}	normalized poloidal magnetic flux.
ρ^*	$= \rho_i/a$, ratio of (ion) gyroradius to minor radius
τ_E	energy confinement time
η_e	$= L_n/L_T = n_e \nabla T_e / T_e \nabla n_e$
ω_{T_e}	$= 1/L_{T_e} = -\nabla T_e / T_e$ inverse gradient scale length
\hat{s}	magnetic shear $\hat{s} = \frac{r}{q} \frac{dq}{dr}$
q	Either a charge, of the safety factor, i.e. pitch of magnetic field lines. Approximately the number of toroidal turns per poloidal turn of a magnetic field line or
Q_{gB}	gyro-Bohm heat flux
k_y	binormal wavenumber
$k_{x,\text{center}}$	Radial wavenumber at the outboard midplane. Related to the ballooning angle $\theta_0 = k_{x,\text{center}} / (\hat{s}k_y)$.

Abbreviations

Abbreviation	Meaning
H-mode	High-confinement mode
AUG	ASDEX Upgrade
ASDEX	Axi-symmetric Divertor Experiment
GENE	Gyrokinetic Electromagnetic Numerical Experiment
JET	Joint European Torus

Abbreviation	Meaning
ILW	ITER-like wall. Plasma facing wall of JET after upgrade from carbon wall. Beryllium wall material and Tungsten divertor.
ELM	Edge Localized Mode
IPB98	ITER Physics Base
ITER	International Thermonuclear Experimental Reactor
MHD	Magnetohydrodynamics
HPC	High Performance Computing
SOL	Scrape-off layer
LCFS	Last-closed flux surface
FLR	Finite Larmor Radius (finite meaning "not zero")
ITG	Ion Temperature Gradient mode
ETG	Electron Temperature Gradient mode
TEM	Trapped Electron Mode
KBM	Kinetic Ballooning Mode
RBM	Resistive Ballooning Mode
MTM	Micro Tearing Mode

List of Figures

1.1.	Illustration of the global energy challenge. Left: CO ₂ emissions of countries as a function of GDP (both per capita). Modified from [5]. Right: Global primary energy consumption by source as a function of time. Modified from [4].	2
1.2.	Rendering of ITER plant. Plasma physics is a crucial but only one part contributing to realizing fusion energy. Credit: ITER Organization, https://www.iter.org/	3
1.3.	Left: Fusion of Deuterium D= ² H and Tritium T= ³ H. Taken from wikipedia.org/wiki/Nuclear_fusion . Right: Fusion reactivity for different fusion reactions. Taken from [16].	4
1.4.	Top: Tokamak magnet structure. Credit: EUROfusion. Left: Magnetic field strength on a flux-surface in a tokamak. Example from DIII-D experiment. Reprinted from [19], with the permission of AIP publishing. Right: Poloidal cross-section showing nested flux surfaces in the confined region, separatrix, scrape-off layer, and divertor. Taken from [20] with the permission from P. Manz.	7
1.5.	3D rendering of a GENE turbulence simulation of a tokamak. Taken from genecode.org	11
1.6.	Left: Illustration of the H-mode pedestal. Reprinted from [35], with the permission of AIP Publishing. Right: Comparison of typical L-mode with H-mode pressure profiles. Reproduced from [36] with permission from IAEA.	11
1.7.	Lawson parameter achieved in different experiments. Illustrating progress, variety of approaches, and strong impact of tokamak experiments (red dots). Taken from [16].	14
2.1.	Illustration of the magnetic field structure and particle orbits in a tokamak. Taken from [43]. Reproduced with permission from Springer Nature.	18
2.2.	Illustration of guiding center and drifts in gyrokinetic theory. The full particle motion consists of a gyromotion around the guiding center trajectory. The guiding center trajectory follows the perturbed magnetic field line (solid, labeled B) in contrast to the equilibrium magnetic field (dashed, labeled B_0) and is subject to drifts, e.g. due to electric fields. Reproduced from [44] with permission from G.Howes and AAS.	18

LIST OF FIGURES

2.3.	Illustration of the gradient scale length using a fitted electron temperature profile from a real AUG shot (#31529). Gradient scale lengths at two positions are shown.	25
2.4.	Ratio of ion gyroradius and temperature/density scale lengths in the pedestal of an ASDEX Upgrade shot (#31529).	33
3.1.	One poloidal turn of a field line (coordinate line of z) in orange and the corresponding contour of a poloidal cross-section ($x = \text{const.}$) in the edge of an ASDEX Upgrade H-mode shot.	38
3.2.	Illustration of block-structured velocity grids. Reprinted from [71] with permission from Elsevier.	39
3.3.	Electrostatic heat flux of a global, nonlinear, electromagnetic simulations with unmodified GENE compared to a saturating heat flux as it would be expected in a stable simulation.	45
3.4.	Growth rate (left) and frequency (right) comparison between unmodified global GENE and the new f-version in a scan over plasma β . Standard GENE data from Ref. [77].	53
3.5.	Electrostatic heat fluxes as a proxy for the stability of the simulations. Unmodified GENE and the version with the additional $\bar{A}_{1\parallel}$ term in Γ_i are both unstable. The new f-version is stable for the same parameters. Left: NSTX-derived scenario. Right: ASDEX Upgrade pedestal of shot #31529.	54
3.6.	Growth rate spectrum of (Kinetic) Ballooning modes for different ρ^* calculated with ORB5, MISHKA, and global GENE. ORB5 and MISHKA data from Collar et al., PPCF, 2020 [90].	57
3.7.	Growth rate (left) and frequency (right) spectra of (Kinetic) Ballooning modes for global GENE compared to local results. ORB5 and MISHKA data from Collar et al., PPCF, 2020 [90].	58
3.8.	Fluctuation amplitudes of multiple quantities as a function of the parallel coordinate. From a nonlinear, local, electron-scale simulation with <code>hyp_z=0</code> and Arakawa scheme for the parallel derivative. Demonstrates grid scale oscillations in the absence of parallel hyperdiffusion.	60
3.9.	Demonstration of the influence of the mass normalization on hyperdiffusion. From a nonlinear, local, electron scale pedestal simulation.	61

3.10. Left: Sketch of `hyp_z` amplitude with and without v_{\parallel} dependence through prefactor. For a distribution peaking at $v_{\parallel} = 0$, the hyperdiffusion is effectively lowered. Right: Heat fluxes for different `hyp_z` settings with and without prefactor. With prefactor, the damping is reduced and the heat flux is increased. The simulations are based on the AUG scenario discussed in Chapter 5 61

4.1. Temperature and density pedestal profiles from an AUG H-mode. . . . 63

4.2. Left: Contour plots of a nonlinear, local, ion-scale simulation in the steep gradient region of an ASDEX Upgrade pedestal. Top: Electric potential, middle: parallel magnetic potential, bottom: density. Eddies short-circuit around the periodic radial boundary condition (horizontal axis) even with a width of $256\rho_i$. Right: Radial profile of electrostatic heat fluxes of a nonlinear, global pedestal simulation (AUG) with (orange) and without (blue) electromagnetic fluctuations for electrons (solid) and ions (dashed). 66

4.3. Illustration of drift wave instability. Taken from [20] with permission from P. Manz, based on [41]. 69

4.4. Illustration of interchange instability. Taken from [20] with permission from P. Manz, based on [41]. 71

4.5. Illustration of a magnetic island chain by a Poincaré plot of field lines. Reprinted from [107], with the permission of AIP Publishing. 72

4.6. Example of a growth rate and frequency spectrum of the most unstable mode. The scenario is an ASDEX Upgrade H-mode at $\rho_{tor} = 0.86$ (detailed discussion in Chapter 5). 74

4.7. Example of a ballooning (top) and tearing (bottom) parity. The scenario is an ASDEX Upgrade H-mode at $\rho_{tor} = 0.86$ (detailed discussion in Chapter 5). 76

4.8. Illustration of an untilted (left) and tilted (right) mode at the outboard midplane. The tilted mode has a finite radial wave number at the outboard midplane. 77

4.9. Illustration of the relation between ballooning angle θ_0 and radial wavenumber $k_{x,center}$ at the outboard midplane as a function of the binormal wavenumber k_y . Left: Lines of constant θ_0 in a $k_{x,center}$ - k_y plot. Right: Lines of constant $k_{x,center}$ in a θ_0 - k_y plot. 77

4.10. Example of a velocity space structure. Absolute value of the distribution (left) and heat flux (right). The scenario is a TEM in an ASDEX Upgrade H-mode at $\rho_{tor} = 0.86$ (detailed discussion in Chapter 5). . . . 78

LIST OF FIGURES

4.11. Example of cross phases. Left: Electric potential ϕ and density n . Middle: Electric potential and parallel temperature. Right: Electric potential and perpendicular temperature. Blue background: Nonlinear simulation. Orange circles: Linear simulations. The scenario is an ASDEX Upgrade H-mode at $\rho_{tor} = 0.86$ (detailed discussion in Chapter 5).	79
5.1. Poloidal shape of several flux surfaces in the pedestal region of AUG #31529. Generated from the experimental magnetic equilibria.	88
5.2. Profiles and gradient scale length $1/L_X = -X^{-1}\partial X/\partial\rho_{tor}$ of ion temperature (orange), electron temperature (blue) and density (green) of AUG #31529 6ms after the ELM crash. It is assumed that $n_e = n_i$. Data points show experimental measurements (see main text for details), solid lines show the best mtanh fit, and dashed lines illustrate alternative mtanh fits within the statistical uncertainty of fit parameters. Grey vertical lines indicate positions where instabilities have been characterized in detail (see Sec. 5.2).	88
5.3. Fits to complete temperature and density profiles from core to edge of AUG #31529. Left from $\rho_{tor} = 0$, right from half-radius $\rho_{tor} = 0.5$. The upper coordinate axis shows the radial position in units of ρ_{pol} . Vertical dashed lines mark the same positions as in Fig. 5.2.	90
5.4. Profiles of further relevant quantities influencing microinstabilities and edge turbulence: Plasma β (top left), collisionality (top right), ρ^* (bottom left) and safety factor q combined with magnetic shear \hat{s} (bottom right).	90
5.5. $E \times B$ velocity $v_{E_r \times B} = E_r \times B/B^2$ (left) and corresponding shear (right) caused by the edge radial electric field E_r	91
5.6. Relative strength of instability drive: η_i , η_e and L_{T_e}/L_{T_i}	91
5.7. Growth rate spectra of the dominant mode for four radial positions maximized over ballooning angle. $c_s = \sqrt{T_e/m_i}$ and ρ_i are local normalisations evaluated at each radial position. $L_{ref} = 0.65$ m. Shaded regions indicate the wavenumber ranges used in nonlinear heat flux simulations.	92
5.8. Growth rate (top) and frequency spectrum (bottom) at $\rho_{tor}=0.97$ in a 3D surface visualization with k_y and $k_{x,center}$ as axes. The color bar corresponds to growth rate and frequency, respectively.	94
5.9. Growth rates and frequencies as a function of $k_{x,center}$ in the pedestal center $\rho_{tor} = 0.97$ at an intermediate ETG wavenumber $k_y\rho_i = 50$ (top) and a high ETG wavenumber $k_y\rho_i = 140$	95

5.10. Growth rates as a function of plasma β at different radial positions. The vertical orange lines indicate the nominal plasma β value at the respective position. 96

5.11. Growth rates as a function of collisionality at pedestal top ($\rho_{\text{tor}} = 0.86$, top) and center ($\rho_{\text{tor}} = 0.97$, bottom) and two ion scale wavenumbers $k_y \rho_i = 0.5$ (left) and $k_y \rho_i = 0.8$ (right). Nominal collisionality in orange. The collisionality as defined in Eq. (6.87) of [154] is $\nu_e^* = \sqrt{2}aB_0/(B_{p0}v_{T,e}\epsilon^{3/2}\tau_e)$, with the minor radius a , thermal velocity $v_{T,e} = \sqrt{2T_e/m_e}$, inverse aspect ratio $\epsilon = a/R$ and the electron collision time τ_e 97

5.12. Growth rate and frequency spectrum at $\rho_{\text{tor}} = 0.97$ for different parallel resolutions nz0 97

5.13. Linear, local growth rates as a function of the toroidal mode number N_{tor} for three magnetic shear (\hat{s}) values at two different radial positions. Left: pedestal shoulder $\rho_{\text{tor}} = 0.86$. Right: low shear region $\rho_{\text{tor}} = 0.94$. Black crosses are nominal growth rates. 98

5.14. Volume-averaged heat fluxes (electrostatic Q_{es} and electromagnetic Q_{em}) for electrons (blue, left) and ions (red, right) as a function of time in MW. The green continuations include an external background velocity shear corresponding to experimentally measured $E \times B$ shear. 99

5.15. Heat flux spectra (electrostatic Q_{es} (solid) and electromagnetic Q_{em} (dashed)) of electrons (blue) and ions (red) for the global nonlinear simulation with $E \times B$ shear. 100

5.16. Comparison of frequencies of global ion scale simulations with linear simulations at two radial positions. Left: Frequency spectra at three radial positions from the linear simulations in a co-moving frame with the plasma. Right: Superposition of the frequency distribution from two positions of the global simulation (blue). Overlaid are the linear frequencies shifted to the lab frame. See main text for details. 101

5.17. Cross-phases of electric potential ϕ and electron density fluctuations n from nonlinear simulations (blue background) and linear simulations (orange circles). 102

5.18. Heat flux due to ETGs at $\rho_{\text{tor}} = 0.97$ as a function of time. $L_{ref} = 0.65$ m, $v_{T,e} = \sqrt{2T_e/m_e}$. Left axis in units of modified electron gyroBohm units $Q_{gB,e,mod} = Q_{gB,e} \times 1/L_{Te}^2$ following [104], right axis in units of MW. $Q_{gB,e,mod}$ is evaluated at $\rho_{\text{tor}} = 0.97$ for the tuned profiles. 103

LIST OF FIGURES

5.19. Heat flux spectra of the nonlinear ETG simulation with and without magnetic drifts. 104

5.20. Cross-phases of electric potential ϕ and electron density fluctuations n (left), parallel temperature component (middle), and perpendicular temperature component (right) from nonlinear simulations (blue background) and linear simulations (orange circles). 104

5.21. Dependence of heat flux on parallel hyperdiffusion and resolution. 105

5.22. Tuned electron temperature and density profiles (dashed) used to test the sensitivity of ETG heat flux in comparison to nominal profiles (solid). 106

5.23. Turbulent heat flux profile in an ASDEX Upgrade pedestal from pedestal top to foot. Top left: Gyro-Bohm heat flux profile. Top right: Components of the ion scale heat flux profile without $E \times B$ shear. Bottom left: Total heat flux ($Q_{es} + Q_{em}$) due to ion scale turbulence with and without $E \times B$ shear. Bottom right: Total heat flux due to ion scale turbulence from global simulations (red and blue solid line) as well as ETG heat fluxes from local simulations at nominal values (light blue stars) and increased electron temperature gradient (dark blue stars) compared with power balance calculations (broad lines). Region of increased measurement uncertainty in grey. 107

5.24. Convergence test: Double precision. 109

5.25. Convergence test: Parallel resolution 110

5.26. Convergence test: Radial resolution. 110

5.27. Convergence test: Radial hyperdiffusion hyp_x 111

5.28. Convergence test: Initial condition. 111

5.29. Convergence test: Heat flux profile without sources and a different initial condition. 112

5.30. Profile and gradient comparison for other time points in ELM cycle. From top to bottom: +2ms, +4ms, +6ms. The case +6ms has been investigated in detail in the previous sections. 113

5.31. Growth rate spectra comparison. From left to right: +2ms, +4ms, +6ms. The case +6ms has been investigated in detail in the previous sections. 114

5.32. Heat flux comparisons (radially averaged), without $E \times B$ shear. From top to bottom: +2ms, +4ms, +6ms. The case +6ms has been investigated in detail in the previous sections. 116

5.33. Heat flux profiles without $E \times B$ shear corresponding to the time traces shown in Fig. 5.32. From top to bottom: +2ms, +4ms, +6ms. The case +6ms has been investigated in detail in the previous sections. 117

5.34. Profiles of ion temperature (left), electron temperature (center), and density (right) in the simulation domain. Initial experimental profile (dashed), Tango results for five iterations, and the final profiles used in GENE. 118

5.35. Evolution of the ion heat flux (left), electron heat flux (middle), and particle flux (right) with the updated profiles in comparison to the power balance model (dashed). 119

6.1. Left: Temperature and density profiles of the JET #97781 pedestal. Right: The corresponding gradient scale lengths. 124

6.2. Radial profiles of plasma β , collisionality, ρ^* , safety factor q and magnetic shear \hat{s} 125

6.3. $E \times B$ velocity $v_{E_r \times B} = E_r \times B / B^2$ (left) and corresponding shear (right) due to a neoclassic radial electric field E_r . For comparison, the $E \times B$ velocity increased by 50% in orange. 126

6.4. Density profiles for different assumed effective ion charges Z_{eff} and assumed main impurities. 126

6.5. Left: The ratio of electron to ion temperature, assumed effective ion charge $Z_{\text{eff}} = 1.6$, and resulting τ . Right: Ratios of density and temperature gradients. 127

6.6. Top: Growth rate and frequency spectra of the dominant mode at different radial positions from pedestal top to pedestal bottom in a local flux-surface normalization c_s / L_{ref} . Bottom: The same data in SI units $1/s$ 128

6.7. Top: Growth rate and frequency spectra of the dominant mode at different radial positions in a lin-lin plot. Bottom: Zoom to the ion-scale range in a log-log plot. 130

6.8. Growth rate (top) and frequency (bottom) surface of the dominant mode in a k_y - $k_{x,\text{center}}$ plane at $\rho_{\text{tor}} = 0.97$ 131

6.9. Growth rates and frequencies of the dominant mode at $\rho_{\text{tor}} = 0.97$ for two k_y s as a function of $k_{x,\text{center}}$ 132

6.10. Parallel structure of the $k_y \rho_i = 20$ mode in the pedestal center. Top: $k_{x,\text{center}} \rho_i = 0$, bottom: $k_{x,\text{center}} \rho_i = 20$ 133

LIST OF FIGURES

6.11. Linear, local plasma β scan at $k_y\rho_i = 0.075$: Growth rates at different radial positions (left to right: pedestal top, center, foot) as a function of β . The orange bar indicates the nominal β value at the respective position and acts as a yardstick across the plots, always ranging from 0 to 1. 134

6.12. Growth rate and frequency spectra at pedestal top and center with changing impurity content. 135

6.13. Growth rates (left) and frequencies (right) scanned over the driving inverse gradient scale lengths ω_{Ti} , ω_{Te} , ω_n at the pedestal top at $k_y\rho_i = 0.7$. Axes of each subplot are variations of the gradient scale lengths from -30% to +30%. Colors show the growth rate/frequency in c_s/L_{ref} . Normalizations are different from panel to panel. Top: ω_{Ti} vs ω_{Te} , Middle: ω_{Ti} vs ω_n , Bottom: ω_{Te} vs ω_n 136

6.14. Growth rates scanned over the driving gradient scale lengths ω_{Ti} , ω_{Te} , ω_n at the pedestal center. Axes of each subplot are variations of the gradient scale lengths from -30% to +30%. Colors show the growth rate in c_s/L_{ref} . Normalizations are different from panel to panel. Left: $k_y = 0.2/\rho_i$, right: $k_y = 10.0/\rho_i$. Top: ω_{Ti} vs ω_{Te} , Middle: ω_{Ti} vs ω_n , Bottom: ω_{Te} vs ω_n 137

6.15. Frequencies in the gradient scan at the pedestal center corresponding to Fig. 6.14. Axes of each subplot are variations of the gradient scale lengths from -30% to +30%. Colors show the frequencies in c_s/L_{ref} . Normalizations are different from panel to panel. Left: $k_y = 0.2/\rho_i$, right: $k_y = 10.0/\rho_i$. Top: ω_{Ti} vs ω_{Te} , Middle: ω_{Ti} vs ω_n , Bottom: ω_{Te} vs ω_n 138

6.16. Influence of $T_i = T_e$ (dashed) on growth rates and frequencies of the dominant mode on ion-scales at pedestal top (purple) and center (yellow). 139

6.17. Convergence test: high- k_y growth rate spectra for different parallel resolutions at fixed box size and increasing number of parallel grid points $nz0$ 140

6.18. Growth rate spectra at different radial positions (different panels) with and without $B_{||}$ fluctuations. 140

6.19. Snapshot of electric potential fluctuations from the nonlinear phase of a global JET simulation without $E_r \times B$ shear. ϕ in units of $(T_{ref}/e)\rho_{ref}^* \approx 1.85$ V. 141

6.20. Turbulent heat flux from global nonlinear simulations as a function of time. Averaged over $\rho_{tor} = 0.92 - 0.99$ and flux surface. 142

6.21. Linear-nonlinear frequency comparison. Left: Linear results in the co-moving frame for two positions. Middle: Comparison of linear (purple triangles) and nonlinear frequencies (blue distribution, analyzed in $\rho_{\text{tor}}=[0.89,0.91]$) at pedestal top. Right: Comparison of linear (green crosses) and nonlinear frequencies (blue distribution, analyzed in $\rho_{\text{tor}}=[0.96,0.98]$) at pedestal center. The red line indicates the mean of the nonlinear frequency distribution. Analyzed was the nonlinear simulation with three species and $E \times B$ shear (see orange line in 6.20) in the time interval 50-194, corresponding to the black average on top of the orange line. 143

6.22. Cross-phases of density and parallel and perpendicular temperature with electric potential at the pedestal top $\rho_{\text{tor}} = 0.89$. The blue background shows the nonlinear distribution, and linear results are shown as orange circles. The nonlinear simulation with three species and $E \times B$ shear was analyzed (see orange line in 6.20) in the time interval 50-194, corresponding to the black average on top of the orange line. 144

6.23. Cross-phases of density and parallel and perpendicular temperature with electric potential at the pedestal center $\rho_{\text{tor}} = 0.97$. The blue background shows the nonlinear distribution, and linear results are shown as orange circles. The nonlinear simulation with three species and $E \times B$ shear was analyzed (see orange line in 6.20) in the time interval 50-194, corresponding to the black average on top of the orange line. 144

6.24. Heat flux spectrum of the global, nonlinear simulation with three species and increased $E \times B$ shear. Averaged over $\rho_{\text{tor}} = 0.85-0.99$, flux surfaces and time. 145

6.25. Heat flux profile of the global, nonlinear simulation with three species and increased $E \times B$ shear. Averaged over flux surfaces and time. . . . 146

6.26. Sensitivity study: $T_i=T_e$. Heat flux from global nonlinear simulations as a function of time. Averaged over $\rho_{\text{tor}} = 0.85-0.99$ and flux surfaces. Blue/red: Without $E_r \times B$ shear. Green: With $E_r \times B$ shear. Yellow: With $E_r \times B$ shear and $T_i=T_e$ 147

A.1. Left: Photograph of the ASDEX Upgrade torus hall. Right: Photograph of the inner vessel with superimposed magnetic flux surfaces. Source: IPP Garching. 163

A.2. Photograph of the JET torus hall (left) and the inner vessel with a superimposed plasma discharge (right, reproduced with permission from UKAEA). 164

LIST OF FIGURES

A.3. Photograph of racks of the Marconi supercomputer during installation.
Taken from Marconi @Cineca (ph. MMLibouri) [170]. 165

Bibliography

1. Leppin, L. *et al.* Complex Structure of Turbulence across the ASDEX Upgrade Pedestal. *Journal of Plasma Physics* **89**, 905890605. doi:10.1017/S0022377823001101 (2023).
2. Leppin, L. *et al.* The JET Hybrid H-mode Scenario from a Pedestal Turbulence Perspective. *Nuclear Fusion* **Submitted** (2024).
3. Calvin, K. *et al.* *IPCC, 2023: Climate Change 2023: Synthesis Report. Contribution of Working Groups I, II and III to the Sixth Assessment Report of the Intergovernmental Panel on Climate Change [Core Writing Team, H. Lee and J. Romero (Eds.)]. IPCC, Geneva, Switzerland.* (Intergovernmental Panel on Climate Change (IPCC), 2023). doi:10.59327/IPCC/AR6-9789291691647.
4. Ritchie, H. *How Have the World's Energy Sources Changed over the Last Two Centuries?* Our World in Data. <https://ourworldindata.org/global-energy-200-years> (2023).
5. Roser, M. *The World's Energy Problem* Our World in Data. <https://ourworldindata.org/worlds-energy-problem> (2023).
6. *European Researchers Achieve Fusion Energy Record* EUROfusion. <https://euro-fusion.org/eurofusion-news/european-researchers-achieve-fusion-energy-record/> (2023).
7. Song, Y. *et al.* Realization of Thousand-Second Improved Confinement Plasma with Super I-mode in Tokamak EAST. *Science Advances* **9**, eabq5273. doi:10.1126/sciadv.abq5273 (2023).
8. *Wendelstein 7-X Reaches Milestone: Power Plasma with Gigajoule Energy Turnover Generated for Eight Minutes* Max Planck Institute for Plasma Physics. https://www.ipp.mpg.de/5322229/01_23 (2023).
9. Bishop, B. *Lawrence Livermore National Laboratory Achieves Fusion Ignition* Lawrence Livermore National Laboratory. <https://www.llnl.gov/archive/news/lawrence-livermore-national-laboratory-achieves-fusion-ignition> (2023).
10. *Positionspapier Fusionsforschung* Bundesministerium für Bildung und Forschung. https://www.bmbf.de/SharedDocs/Publikationen/de/bmbf/7/775804_Positionspapier_Fusionsforschung.html (2023).

Bibliography

11. *Eine Milliarde Euro Für Die Fusionsforschung Bis 2028* Bundesministerium für Bildung und Forschung. https://www.bmbf.de/bmbf/shareddocs/kurzmeldungen/de/2023/09/230905_fusion-PK.html (2023).
12. *STEP* UK Atomic Energy Authority. <https://ccfe.ukaea.uk/programmes/step/> (2023).
13. *Fact Sheet: Developing a Bold Vision for Commercial Fusion Energy* The White House. <https://www.whitehouse.gov/ostp/news-updates/2022/03/15/fact-sheet-developing-a-bold-vision-for-commercial-fusion-energy/> (2023).
14. *The Global Fusion Industry in 2023* Fusion Industry Association. <https://www.fusionindustryassociation.org/fusion-industry-reports/>.
15. Creely, A. J. *et al.* Overview of the SPARC Tokamak. *Journal of Plasma Physics* **86**, 865860502. doi:10.1017/S0022377820001257 (2020).
16. Wurzel, S. E. & Hsu, S. C. Progress toward Fusion Energy Breakeven and Gain as Measured against the Lawson Criterion. *Physics of Plasmas* **29**, 062103. doi:10.1063/5.0083990 (2022).
17. Hathaway, D. H. *The Solar Interior* National Aeronautics and Space Administration (NASA). <https://solarscience.msfc.nasa.gov/interior.shtml>.
18. Betti, R. & Hurricane, O. A. Inertial-Confinement Fusion with Lasers. *Nature Physics* **12**, 435–448. doi:10.1038/nphys3736 (2016).
19. Proll, J. H. E., Xanthopoulos, P. & Helander, P. Collisionless Microinstabilities in Stellarators. II. Numerical Simulations. *Physics of Plasmas* **20**, 122506. doi:10.1063/1.4846835 (2013).
20. Manz, P. *The Microscopic Picture of Plasma Edge Turbulence* Habilitation (Technische Universität München, 2018).
21. Zohm, H. *Magnetohydrodynamic Stability of Tokamaks* (Wiley-VCH, Weinheim, 2015).
22. Greenwald, M. *et al.* A New Look at Density Limits in Tokamaks. *Nuclear Fusion* **28**, 2199–2207. doi:10.1088/0029-5515/28/12/009 (1988).
23. Wagner, F. & Wobig, H. in *Plasma Physics: Confinement, Transport and Collective Effects* (eds Dinklage, A., Klinger, T., Marx, G. & Schweikhard, L.) red. by Beig, R. *et al.* (Springer Berlin Heidelberg, Berlin, Heidelberg, 2005). doi:10.1007/b103882.

24. Dawson, J. On Landau Damping. *The Physics of Fluids* **4**, 869–874. doi:10.1063/1.1706419 (1961).
25. Richardson, L. *Weather Prediction by Numerical Process* (Cambridge University Press, 1922).
26. Kolmogorov, A. N. A Refinement of Previous Hypotheses Concerning the Local Structure of Turbulence in a Viscous Incompressible Fluid at High Reynolds Number. *Journal of Fluid Mechanics* **13**, 82–85. doi:10.1017/S0022112062000518 (1962).
27. Davidson, P. A. *Turbulence: An Introduction for Scientists and Engineers* (Oxford University Press, Oxford; New York, 2004).
28. Kim, E.-j. & Diamond, P. H. Zonal Flows and Transient Dynamics of the L- H Transition. *Physical Review Letters* **90**, 185006. doi:10.1103/PhysRevLett.90.185006 (2003).
29. Hoelzl, M. *et al.* The JOREK Non-Linear Extended MHD Code and Applications to Large-Scale Instabilities and Their Control in Magnetically Confined Fusion Plasmas. *Nuclear Fusion* **61**, 065001. doi:10.1088/1741-4326/abf99f (2021).
30. Stegmeir, A. *et al.* GRILLIX: A 3D Turbulence Code Based on the Flux-Coordinate Independent Approach. *Plasma Physics and Controlled Fusion* **60**, 035005. doi:10.1088/1361-6587/aaa373 (2018).
31. Staebler, G. M., Kinsey, J. E. & Waltz, R. E. A Theory-Based Transport Model with Comprehensive Physics. *Physics of Plasmas* **14**, 055909. doi:10.1063/1.2436852 (2007).
32. Staebler, G. *et al.* Verification of a Quasi-Linear Model for Gyrokinetic Turbulent Transport. *Nuclear Fusion* **61**, 116007. doi:10.1088/1741-4326/ac243a (2021).
33. Bourdelle, C. *et al.* Core Turbulent Transport in Tokamak Plasmas: Bridging Theory and Experiment with QuaLiKiz. *Plasma Physics and Controlled Fusion* **58**, 014036. doi:10.1088/0741-3335/58/1/014036 (2016).
34. Citrin, J. *et al.* Tractable Flux-Driven Temperature, Density, and Rotation Profile Evolution with the Quasilinear Gyrokinetic Transport Model QuaLiKiz. *Plasma Physics and Controlled Fusion* **59**, 124005. doi:10.1088/1361-6587/aa8aeb (2017).
35. Connor, J. W., Kirk, A., Wilson, H. R. & Benkadda, S. *Edge Localised Modes (ELMs): Experiments and Theory* in *AIP Conference Proceedings* Turbulent Transport in Fusion Plasmas: First ITER International Summer School. **1013** (AIP, Aix en Provence (France), 2008), 174–190. doi:10.1063/1.2939030.

Bibliography

36. Lang, P. *et al.* ELM Control Strategies and Tools: Status and Potential for ITER. *Nuclear Fusion* **53**, 043004. doi:10.1088/0029-5515/53/4/043004 (2013).
37. Transport, I. P. E. G. O. C. a. Chapter 2: Plasma Confinement and Transport. *Nuclear Fusion* **39**, 2175–2249. doi:10.1088/0029-5515/39/12/302 (1999).
38. Wagner, F. *et al.* Regime of Improved Confinement and High Beta in Neutral-Beam-Heated Divertor Discharges of the ASDEX Tokamak. *Physical Review Letters* **49**, 1408–1412. doi:10.1103/PhysRevLett.49.1408 (1982).
39. Wagner, F. A Quarter-Century of H-mode Studies. *Plasma Physics and Controlled Fusion* **49**, B1–B33. doi:10.1088/0741-3335/49/12B/S01 (12B 2007).
40. Cathey, A. *et al.* Non-Linear Extended MHD Simulations of Type-I Edge Localised Mode Cycles in ASDEX Upgrade and Their Underlying Triggering Mechanism. *Nuclear Fusion* **60**, 124007. doi:10.1088/1741-4326/abbc87 (2020).
41. Stroth, U. *Plasmaphysik: Phänomene, Grundlagen und Anwendungen* 2. Auflage (Springer Spektrum, Berlin, 2018).
42. Stacey, W. M. *Fusion Plasma Physics* (Wiley-VCH ; John Wiley [distributor], Weinheim : Chichester, 2005).
43. Fasoli, A. *et al.* Computational Challenges in Magnetic-Confinement Fusion Physics. *Nature Physics* **12**, 411–423. doi:10.1038/nphys3744 (2016).
44. Howes, G. G. *et al.* Astrophysical Gyrokinetics: Basic Equations and Linear Theory. *The Astrophysical Journal* **651**, 590–614. doi:10.1086/506172 (2006).
45. Hammett, G. *Computational Plasma Physics: Powerful New Tools of Scientific Discovery* PPPL. 2012.
46. Brizard, A. J. & Hahm, T. S. Foundations of Nonlinear Gyrokinetic Theory. *Reviews of Modern Physics* **79**, 421–468. doi:10.1103/RevModPhys.79.421 (2007).
47. Stone, M. & Goldbart, P. *Mathematics for Physics: A Guided Tour for Graduate Students* doi:10.1017/CB09780511627040 (Cambridge University Press, Cambridge, 2009).
48. Goerler, T. *Multiscale Effects in Plasma Microturbulence* (Universität Ulm, Ulm, 2009).
49. Candy, J., Waltz, R. E., Parker, S. E. & Chen, Y. Relevance of the Parallel Nonlinearity in Gyrokinetic Simulations of Tokamak Plasmas. *Physics of Plasmas* **13**, 074501. doi:10.1063/1.2220536 (2006).

50. Told, D. *Gyrokinetic Microturbulence in Transport Barriers* PhD thesis (Universität Ulm, Ulm, 2012).
51. Wootton, A. J. *et al.* Fluctuations and Anomalous Transport in Tokamaks. *Physics of Fluids B: Plasma Physics* **2**, 2879–2903. doi:10.1063/1.859358 (1990).
52. Nold, B. *et al.* Generation of Blobs and Holes in the Edge of the ASDEX Upgrade Tokamak. *Plasma Physics and Controlled Fusion* **52**, 065005. doi:10.1088/0741-3335/52/6/065005 (2010).
53. Xu, G. *et al.* Blob/Hole Formation and Zonal-Flow Generation in the Edge Plasma of the JET Tokamak. *Nuclear Fusion* **49**, 092002. doi:10.1088/0029-5515/49/9/092002 (2009).
54. Raeth, M. & Hallatschek, K. *High Frequency Non-Gyrokinetic Turbulence at Tokamak Edge Parameter* arXiv: 2310.15981 [physics]. <http://arxiv.org/abs/2310.15981> (2023). preprint.
55. Krommes, J. A. The Gyrokinetic Description of Microturbulence in Magnetized Plasmas. *Annual Review of Fluid Mechanics* **44**, 175–201. doi:10.1146/annurev-fluid-120710-101223 (2012).
56. Crandall, P. C. *Collisional and Electromagnetic Physics in Gyrokinetic Models* (University of California Los Angeles, 2019).
57. Jenko, F., Dorland, W., Kotschenreuther, M. & Rogers, B. N. Electron Temperature Gradient Driven Turbulence. *Phys. Plasmas* **7**, 8 (2000).
58. Germaschewski, K. *et al.* Toward Exascale Whole-Device Modeling of Fusion Devices: Porting the GENE Gyrokinetic Microturbulence Code to GPU. *Physics of Plasmas* **28**, 062501. doi:10.1063/5.0046327 (2021).
59. Maurer, M. *et al.* GENE-3D: A Global Gyrokinetic Turbulence Code for Stellarators. *Journal of Computational Physics* **420**, 109694. doi:10.1016/j.jcp.2020.109694 (2020).
60. Wilms, F. *et al.* Global Electromagnetic Turbulence Simulations of W7-X-like Plasmas with GENE-3D. *Journal of Plasma Physics* **87**, 905870604. doi:10.1017/S0022377821001082 (2021).
61. Michels, D., Stegmeir, A., Ulbl, P., Jarema, D. & Jenko, F. GENE-X: A Full-f Gyrokinetic Turbulence Code Based on the Flux-Coordinate Independent Approach. *Computer Physics Communications* **264**, 107986. doi:10.1016/j.cpc.2021.107986 (2021).

Bibliography

62. Ulbl, P., Michels, D. & Jenko, F. Implementation and Verification of a Conservative, Multi-species, Gyro-averaged, Full- f , Lenard-Bernstein/ Dougherty Collision Operator in the Gyrokinetic Code GENE-X. *Contributions to Plasma Physics* **62**, e202100180. doi:10.1002/ctpp.202100180 (2022).
63. Di Siena, A. *Implementation and Investigation of the Impact of Different Background Distributions in Gyrokinetic Plasma Turbulence Studies* PhD thesis (Universität Ulm, 2019).
64. Görler, T. *et al.* The Global Version of the Gyrokinetic Turbulence Code GENE. *Journal of Computational Physics* **230**, 7053–7071. doi:10.1016/j.jcp.2011.05.034 (2011).
65. Pan, Q., Ernst, D. R. & Crandall, P. First Implementation of Gyrokinetic Exact Linearized Landau Collision Operator and Comparison with Models. *Physics of Plasmas* **27**, 042307. doi:10.1063/1.5143374 (2020).
66. Hariri, F. & Ottaviani, M. A Flux-Coordinate Independent Field-Aligned Approach to Plasma Turbulence Simulations. *Computer Physics Communications* **184**, 2419–2429. doi:10.1016/j.cpc.2013.06.005 (2013).
67. Ottaviani, M. An Alternative Approach to Field-Aligned Coordinates for Plasma Turbulence Simulations. *Physics Letters A* **375**, 1677–1685. doi:10.1016/j.physleta.2011.02.069 (2011).
68. Sauter, O. & Medvedev, S. Yu. Tokamak Coordinate Conventions: *Computer Physics Communications* **184**, 293–302. doi:10.1016/j.cpc.2012.09.010 (2013).
69. D’haeseleer, W. D., Hitchon, W. N. G., Callen, J. D. & Shohet, J. L. *Flux Coordinates and Magnetic Field Structure: A Guide to a Fundamental Tool of Plasma Theory* (Springer Berlin Heidelberg, Berlin, Heidelberg, 1991).
70. Jarema, D. *Efficient Eulerian Gyrokinetic Simulations with Block-Structured Grids* PhD thesis (Technische Universität München, München, 2016).
71. Jarema, D. *et al.* Block-Structured Grids in Full Velocity Space for Eulerian Gyrokinetic Simulations. *Computer Physics Communications* **215**, 49–62. doi:10.1016/j.cpc.2017.02.005 (2017).
72. Oberparleiter, M. *Interaction between the Neoclassical Equilibrium and Microturbulence in Gyrokinetic Simulations* PhD thesis (Universität Ulm, Ulm, 2015).

73. Oberparleiter, M., Jenko, F., Told, D., Doerk, H. & Görler, T. Interaction between Neoclassical Effects and Ion Temperature Gradient Turbulence in Gradient- and Flux-Driven Gyrokinetic Simulations. *Physics of Plasmas* **23**, 042509. doi:10.1063/1.4947200 (2016).
74. McMillan, B. F., Ball, J. & Brunner, S. Simulating Background Shear Flow in Local Gyrokinetic Simulations. *Plasma Physics and Controlled Fusion* **61**, 055006. doi:10.1088/1361-6587/ab06a4 (2019).
75. Merz, F. *Gyrokinetic Simulation of Multimode Plasma Turbulence* PhD thesis (Westfälische Wilhelms-Universität Münster, Münster, 2008).
76. Arakawa, A. Computational Design for Long-Term Numerical Integration of the Equations of Fluid Motion: Two-Dimensional Incompressible Flow. Part I. *Journal of Computational Physics* **135**, 12 (1997).
77. Görler, T. *et al.* Intercode Comparison of Gyrokinetic Global Electromagnetic Modes. *Physics of Plasmas* **23**, 072503. doi:10.1063/1.4954915 (2016).
78. Hassan, E., Hatch, D. R., Guttenfelder, W., Chen, Y. & Parker, S. Gyrokinetic Benchmark of the Electron Temperature-Gradient Instability in the Pedestal Region. *Physics of Plasmas* **28**, 062505. doi:10.1063/5.0043006 (2021).
79. Höfler, K. *Turbulence Measurements at the ASDEX Upgrade Tokamak for a Comprehensive Validation of the Gyrokinetic Turbulence Code GENE* PhD thesis (Technische Universität München, München, 2022).
80. Di Siena, A. *et al.* Global Gyrokinetic Simulations of ASDEX Upgrade up to the Transport Timescale with GENE–Tango. *Nuclear Fusion* **62**, 106025. doi:10.1088/1741-4326/ac8941 (2022).
81. Reynders, J. V. W. *Gyrokinetic Simulation of Finite-Beta Plasmas on Parallel Architectures* PhD thesis (Princeton University, 1993).
82. Leppin, L. *et al.* Complex Structure of Turbulence across the ASDEX Upgrade Pedestal. *Journal of Plasma Physics* **Accepted** (2023).
83. Mishchenko, A. *et al.* Mitigation of the Cancellation Problem in the Gyrokinetic Particle-in-Cell Simulations of Global Electromagnetic Modes. *Physics of Plasmas* **24**, 081206. doi:10.1063/1.4997540 (2017).
84. Pan, Q., Told, D., Shi, E. L., Hammett, G. W. & Jenko, F. Full- f Version of GENE for Turbulence in Open-Field-Line Systems. *Physics of Plasmas* **25**, 062303. doi:10.1063/1.5008895 (2018).

Bibliography

85. D'Ippolito, D. A., Myra, J. R. & Krasheninnikov, S. I. Cross-Field Blob Transport in Tokamak Scrape-off-Layer Plasmas. *Physics of Plasmas* **9**, 222–233. doi:10.1063/1.1426394 (2002).
86. Shi, E. L., Hammett, G. W., Stoltzfus-Dueck, T. & Hakim, A. Full-f Gyrokinetic Simulation of Turbulence in a Helical Open-Field-Line Plasma. *Physics of Plasmas* **26**, 012307. doi:10.1063/1.5074179 (2019).
87. Parker, J. B. *et al.* Bringing Global Gyrokinetic Turbulence Simulations to the Transport Timescale Using a Multiscale Approach. *Nuclear Fusion* **58**, 054004. doi:10.1088/1741-4326/aab5c8 (2018).
88. Snyder, P. B., Groebner, R. J., Leonard, A. W., Osborne, T. H. & Wilson, H. R. Development and Validation of a Predictive Model for the Pedestal Height. *Physics of Plasmas* **16**, 056118. doi:10.1063/1.3122146 (2009).
89. Snyder, P. *et al.* A First-Principles Predictive Model of the Pedestal Height and Width: Development, Testing and ITER Optimization with the EPED Model. *Nuclear Fusion* **51**, 103016. doi:10.1088/0029-5515/51/10/103016 (2011).
90. Martin Collar, J. P., McMillan, B. F., Saarelma, S. & Bottino, A. Comparing Electromagnetic Instabilities in Global Gyrokinetic Simulations with Local and MHD Models. *Plasma Physics and Controlled Fusion* **62**, 095005. doi:10.1088/1361-6587/ab81db (2020).
91. Collar, J. P. M. *Global Gyrokinetic Simulations of Kinetic Ballooning Modes* PhD thesis (University of Warwick, 2018).
92. Dudkovskaia, A. V., Wilson, H. R., Connor, J. W., Dickinson, D. & Parra, F. I. Nonlinear Second Order Electromagnetic Gyrokinetic Theory for a Tokamak Plasma. *Plasma Physics and Controlled Fusion* **65**, 045010. doi:10.1088/1361-6587/acb173 (2023).
93. McMillan, B. Relationship between Drift Kinetics, Gyrokinetics and Magneto-hydrodynamics in the Long-Wavelength Limit. *Journal of Plasma Physics* **89**, 905890115. doi:10.1017/S0022377823000089 (2023).
94. Pueschel, M., Dannert, T. & Jenko, F. On the Role of Numerical Dissipation in Gyrokinetic Vlasov Simulations of Plasma Microturbulence. *Computer Physics Communications* **181**, 1428–1437. doi:10.1016/j.cpc.2010.04.010 (2010).
95. Groebner, R. *et al.* Progress in Quantifying the Edge Physics of the H Mode Regime in DIII-D. *Nuclear Fusion* **41**, 1789–1802. doi:10.1088/0029-5515/41/12/306 (2001).

96. Terry, P. W. Suppression of Turbulence and Transport by Sheared Flow. *Reviews of Modern Physics* **72**, 109–165. doi:10.1103/RevModPhys.72.109 (2000).
97. Schirmer, J., Conway, G., Zohm, H., Suttrop, W. & Team, t. A. U. The Radial Electric Field and Its Associated Shear in the ASDEX Upgrade Tokamak. *Nuclear Fusion* **46**, S780–S791. doi:10.1088/0029-5515/46/9/S13 (2006).
98. Plank, U. *et al.* Overview of L- to H-mode Transition Experiments at ASDEX Upgrade. *Plasma Physics and Controlled Fusion* **65**, 014001. doi:10.1088/1361-6587/aca35b (2023).
99. Kammerer, M., Merz, F. & Jenko, F. Exceptional Points in Linear Gyrokinetics. *Physics of Plasmas* **15**, 052102. doi:10.1063/1.2909618 (2008).
100. Pueschel, M. J. *Electromagnetic Effects in Gyrokinetic Simulations of Plasma Turbulence* (Westfälische Wilhelms-Universität Münster, 2009).
101. Pueschel, M. J., Kammerer, M. & Jenko, F. Gyrokinetic Turbulence Simulations at High Plasma Beta. *Physics of Plasmas* **15**, 102310. doi:10.1063/1.3005380 (2008).
102. Terry, P. *et al.* Overview of Gyrokinetic Studies of Finite- Beta Microturbulence. *Nuclear Fusion* **55**, 104011. doi:10.1088/0029-5515/55/10/104011 (2015).
103. Kotschenreuther, M. *et al.* Gyrokinetic Analysis and Simulation of Pedestals to Identify the Culprits for Energy Losses Using ‘Fingerprints’. *Nuclear Fusion* **59**, 096001. doi:10.1088/1741-4326/ab1fa2 (2019).
104. Chapman-Oplopoiou, B. *et al.* The Role of ETG Modes in JET–ILW Pedestals with Varying Levels of Power and Fuelling. *Nuclear Fusion* **62**, 086028. doi:10.1088/1741-4326/ac7476 (2022).
105. Parisi, J. F. *et al.* Toroidal and Slab ETG Instability Dominance in the Linear Spectrum of JET-ILW Pedestals. *Nuclear Fusion* **60**, 126045. doi:10.1088/1741-4326/abb891 (2020).
106. Varennes, R. *Flow Drive in Tokamak Plasmas: Competition and Synergies between Turbulence and Neoclassical Effects* PhD thesis (Aix-Marseille Universite, Aix-Marseille, 2022).
107. Yu, Q. Numerical Modeling of Diffusive Heat Transport across Magnetic Islands and Local Stochastic Field. *Physics of Plasmas* **13**, 062310. doi:10.1063/1.2206788 (2006).
108. Citrin, J. *et al.* Fast Transport Simulations with Higher-Fidelity Surrogate Models for ITER. *Physics of Plasmas* **30**, 062501. doi:10.1063/5.0136752 (2023).

Bibliography

109. Guttenfelder, W. *et al.* Testing Predictions of Electron Scale Turbulent Pedestal Transport in Two DIII-D ELMy H-modes. *Nuclear Fusion* **61**, 056005. doi:10.1088/1741-4326/abec7 (2021).
110. Dannert, T. & Jenko, F. Gyrokinetic Simulation of Collisionless Trapped-Electron Mode Turbulence. *Physics of Plasmas* **12**, 072309. doi:10.1063/1.1947447 (2005).
111. Jenko, F., Dannert, T. & Angioni, C. Heat and Particle Transport in a Tokamak: Advances in Nonlinear Gyrokinetics. *Plasma Physics and Controlled Fusion* **47**, B195–B206. doi:10.1088/0741-3335/47/12B/S15 (12B 2005).
112. Patel, B., Dickinson, D., Roach, C. & Wilson, H. Linear Gyrokinetic Stability of a High Beta Non-Inductive Spherical Tokamak. *Nuclear Fusion* **62**, 016009. doi:10.1088/1741-4326/ac359c (2022).
113. Beer, M. A., Cowley, S. C. & Hammett, G. W. Field-aligned Coordinates for Nonlinear Simulations of Tokamak Turbulence. *Physics of Plasmas* **2**, 15 (1995).
114. Jenko, F., Dorland, W. & Hammett, G. W. Critical Gradient Formula for Toroidal Electron Temperature Gradient Modes. *Physics of Plasmas* **8**, 4096–4104. doi:10.1063/1.1391261 (2001).
115. Romanelli, F. Ion Temperature-Gradient-Driven Modes and Anomalous Ion Transport in Tokamaks. *Physics of Fluids B: Plasma Physics* **1**, 1018–1025. doi:10.1063/1.859023 (1989).
116. Roberg-Clark, G., Plunk, G. & Xanthopoulos, P. Calculating the Linear Critical Gradient for the Ion-Temperature-Gradient Mode in Magnetically Confined Plasmas. *Journal of Plasma Physics* **87**, 905870306. doi:10.1017/S0022377821000507 (2021).
117. Dimits, A. M. *et al.* Comparisons and Physics Basis of Tokamak Transport Models and Turbulence Simulations. *Physics of Plasmas* **7**, 969–983. doi:10.1063/1.873896 (2000).
118. Mikkelsen, D. R. & Dorland, W. Dimits Shift in Realistic Gyrokinetic Plasma-Turbulence Simulations. *Physical Review Letters* **101**, 135003. doi:10.1103/PhysRevLett.101.135003 (2008).
119. Stallard, B. W. *et al.* Electron Heat Transport in Improved Confinement Discharges in DIII-D. *Physics of Plasmas* **6**, 1978–1984. doi:10.1063/1.873494 (1999).

120. Ryter, F. *et al.* Experimental Characterization of the Electron Heat Transport in Low-Density ASDEX Upgrade Plasmas. *Physical Review Letters* **86**, 5498–5501. doi:10.1103/PhysRevLett.86.5498 (2001).
121. Jenko, F. & Dorland, W. Prediction of Significant Tokamak Turbulence at Electron Gyroradius Scales. *Physical Review Letters* **89**, 225001. doi:10.1103/PhysRevLett.89.225001 (2002).
122. Walker, J. & Hatch, D. R. ETG Turbulence in a Tokamak Pedestal. *Physics of Plasmas* **30**, 082307. doi:10.1063/5.0146968 (2023).
123. Field, A. R. *et al.* Comparing Pedestal Structure in JET-ILW H-mode Plasmas with a Model for Stiff ETG Turbulent Heat Transport. *Philosophical Transactions of the Royal Society A: Mathematical, Physical and Engineering Sciences* **381**, 20210228. doi:10.1098/rsta.2021.0228 (2023).
124. Told, D. *et al.* Gyrokinetic Microinstabilities in ASDEX Upgrade Edge Plasmas. *Physics of Plasmas* **15**, 102306. doi:10.1063/1.3000132 (2008).
125. Parisi, J. *et al.* Three-Dimensional Inhomogeneity of Electron-Temperature-Gradient Turbulence in the Edge of Tokamak Plasmas. *Nuclear Fusion* **62**, 086045. doi:10.1088/1741-4326/ac786b (2022).
126. Hatch, D. R. *et al.* Reduced Models for ETG Transport in the Tokamak Pedestal. *Physics of Plasmas* **29**, 062501. doi:10.1063/5.0087403 (2022).
127. Maeyama, S. *et al.* Cross-Scale Interactions between Electron and Ion Scale Turbulence in a Tokamak Plasma. *Physical Review Letters* **114**, 255002. doi:10.1103/PhysRevLett.114.255002 (2015).
128. Howard, N., Holland, C., White, A., Greenwald, M. & Candy, J. Multi-Scale Gyrokinetic Simulation of Tokamak Plasmas: Enhanced Heat Loss Due to Cross-Scale Coupling of Plasma Turbulence. *Nuclear Fusion* **56**, 014004. doi:10.1088/0029-5515/56/1/014004 (2016).
129. Howard, N. T. *et al.* Multi-Scale Gyrokinetic Simulations of an Alcator C-Mod, ELM-y H-mode Plasma. *Plasma Physics and Controlled Fusion* **60**, 014034. doi:10.1088/1361-6587/aa9148 (2018).
130. Mazzucato, E. *et al.* Short-Scale Turbulent Fluctuations Driven by the Electron-Temperature Gradient in the National Spherical Torus Experiment. *Physical Review Letters* **101**, 075001. doi:10.1103/PhysRevLett.101.075001 (2008).
131. Halfmoon, M. R. *et al.* Gyrokinetic Analysis of Inter-Edge Localized Mode Transport Mechanisms in a DIII-D Pedestal. *Physics of Plasmas* **29**, 112505. doi:10.1063/5.0102152 (2022).

Bibliography

132. Hassan, E. *et al.* Identifying the Microtearing Modes in the Pedestal of DIII-D H-modes Using Gyrokinetic Simulations. *Nuclear Fusion* **62**, 026008. doi:10.1088/1741-4326/ac3be5 (2022).
133. Hatch, D. *et al.* Direct Gyrokinetic Comparison of Pedestal Transport in JET with Carbon and ITER-like Walls. *Nuclear Fusion* **59**, 086056. doi:10.1088/1741-4326/ab25bd (2019).
134. Hatch, D. *et al.* Microtearing Turbulence Limiting the JET-ILW Pedestal. *Nuclear Fusion* **56**, 104003. doi:10.1088/0029-5515/56/10/104003 (2016).
135. Doerk, H. *Gyrokinetic Simulation of Microtearing Turbulence* PhD thesis (Universität Ulm, Ulm, 2012).
136. Ishizawa, A., Imadera, K., Nakamura, Y. & Kishimoto, Y. Global Gyrokinetic Simulation of Turbulence Driven by Kinetic Ballooning Mode. *Physics of Plasmas* **26**, 082301. doi:10.1063/1.5100308 (2019).
137. Wan, W. *et al.* Global Gyrokinetic Simulations of the H-mode Tokamak Edge Pedestal. *Phys. Plasmas* **20**, 9. doi:10.1063/1.4803890 (2013).
138. Rogers, B. N., Drake, J. F. & Zeiler, A. Phase Space of Tokamak Edge Turbulence, the L - H Transition, and the Formation of the Edge Pedestal. *Physical Review Letters* **81**, 4396–4399. doi:10.1103/PhysRevLett.81.4396 (1998).
139. Eich, T., Manz, P. & the ASDEX Upgrade team. The Separatrix Operational Space of ASDEX Upgrade Due to Interchange-Drift-Alfvén Turbulence. *Nuclear Fusion* **61**, 086017. doi:10.1088/1741-4326/ac0412 (2021).
140. De Dominicis, G. *et al.* Quasilinear Nature of L-mode Edge Turbulent Transport in Fluid Nonlinear Simulations. *Nuclear Fusion* **59**, 126019. doi:10.1088/1741-4326/ab3ec6 (2019).
141. Bourdelle, C., Garbet, X., Singh, R. & Schmitz, L. New Glance at Resistive Ballooning Modes at the Edge of Tokamak Plasmas. *Plasma Physics and Controlled Fusion* **54**, 115003. doi:10.1088/0741-3335/54/11/115003 (2012).
142. Shen, Y. *et al.* Properties of Ubiquitous Modes in Tokamak Plasmas. *Nuclear Fusion* **59**, 106011. doi:10.1088/1741-4326/ab2e95 (2019).
143. Coppi, B. & Pegoraro, F. Theory of the Ubiquitous Mode. *Nuclear Fusion* **17**, 969–993. doi:10.1088/0029-5515/17/5/009 (1977).
144. Rogers, B. N., Dorland, W. & Kotschenreuther, M. Generation and Stability of Zonal Flows in Ion-Temperature-Gradient Mode Turbulence. *Physical Review Letters* **85**, 5336–5339. doi:10.1103/PhysRevLett.85.5336 (2000).

145. Diamond, P. H., Itoh, S.-I., Itoh, K. & Hahm, T. S. Zonal Flows in Plasma - a Review. *Plasma Physics and Controlled Fusion* **47**, R35–R161. doi:10.1088/0741-3335/47/5/R01 (2005).
146. Horton, W. Drift Waves and Transport. *Reviews of Modern Physics* **71**, 735–778. doi:10.1103/RevModPhys.71.735 (1999).
147. Hatch, D. *et al.* Gyrokinetic Study of ASDEX Upgrade Inter-ELM Pedestal Profile Evolution. *Nuclear Fusion* **55**, 063028. doi:10.1088/0029-5515/55/6/063028 (2015).
148. Hatch, D., Kotschenreuther, M., Mahajan, S., Valanju, P. & Liu, X. A Gyrokinetic Perspective on the JET-ILW Pedestal. *Nuclear Fusion* **57**, 036020. doi:10.1088/1741-4326/aa51e1 (2017).
149. Predebon, I. *et al.* Isotope Mass Dependence of Pedestal Transport in JET H-mode Plasmas. *Nuclear Fusion* **63**, 036010. doi:10.1088/1741-4326/acb44f (2023).
150. Farcaş, I.-G., Merlo, G. & Jenko, F. A General Framework for Quantifying Uncertainty at Scale. *Communications Engineering* **1**, 43. doi:10.1038/s44172-022-00045-0 (2022).
151. Cavedon, M. *et al.* Pedestal and Er Profile Evolution during an Edge Localized Mode Cycle at ASDEX Upgrade. *Plasma Physics and Controlled Fusion* **59**, 105007. doi:10.1088/1361-6587/aa7ad0 (2017).
152. Viezzer, E. *et al.* Dynamics of the Pedestal Transport during Edge Localized Mode Cycles at ASDEX Upgrade. *Plasma Physics and Controlled Fusion* **62**, 024009. doi:10.1088/1361-6587/ab5b1d (2020).
153. Fischer, R. *et al.* Integrated Data Analysis of Profile Diagnostics at ASDEX Upgrade. *Fusion Science and Technology* **58**, 675–684. doi:10.13182/FST10-110 (2010).
154. Hinton, F. L. & Hazeltine, R. D. Theory of Plasma Transport in Toroidal Confinement Systems. *Reviews of Modern Physics* **48**, 239–308. doi:10.1103/RevModPhys.48.239 (1976).
155. Bourdelle, C. *et al.* Impact of the Alpha Parameter on the Microstability of Internal Transport Barriers. *Nuclear Fusion* **45**, 110–130. doi:10.1088/0029-5515/45/2/005 (2005).
156. Connor, J. *et al.* A Review of Internal Transport Barrier Physics for Steady-State Operation of Tokamaks. *Nuclear Fusion* **44**, R1–R49. doi:10.1088/0029-5515/44/4/R01 (2004).

Bibliography

157. Viezzer, E. *et al.* Investigation of Inter-ELM Ion Heat Transport in the H-mode Pedestal of ASDEX Upgrade Plasmas. *Nuclear Fusion* **57**, 022020. doi:10.1088/0029-5515/57/2/022020 (2017).
158. Maslov, M. *et al.* JET D-T Scenario with Optimized Non-Thermal Fusion. *Nuclear Fusion* **63**, 112002. doi:10.1088/1741-4326/ace2d8 (2023).
159. Hobirk, J. *et al.* The JET Hybrid Scenario in Deuterium, Tritium and Deuterium-Tritium. *Nuclear Fusion* **63**, 112001. doi:10.1088/1741-4326/acde8d (2023).
160. Challis, C. *et al.* Improved Confinement in JET High Beta Plasmas with an ITER-like Wall. *Nuclear Fusion* **55**, 053031. doi:10.1088/0029-5515/55/5/053031 (2015).
161. Joffrin, E. *et al.* The ‘Hybrid’ Scenario in JET: Towards Its Validation for ITER. *Nuclear Fusion* **45**, 626–634. doi:10.1088/0029-5515/45/7/010 (2005).
162. Hobirk, J. *et al.* Improved Confinement in JET Hybrid Discharges. *Plasma Physics and Controlled Fusion* **54**, 095001. doi:10.1088/0741-3335/54/9/095001 (2012).
163. Garcia, J. *et al.* Key Impact of Finite-Beta and Fast Ions in Core and Edge Tokamak Regions for the Transition to Advanced Scenarios. *Nuclear Fusion* **55**, 053007. doi:10.1088/0029-5515/55/5/053007 (2015).
164. Citrin, J. *et al.* Integrated Modelling and Multiscale Gyrokinetic Validation Study of ETG Turbulence in a JET Hybrid H-mode Scenario. *Nuclear Fusion* **62**, 086025. doi:10.1088/1741-4326/ac7535 (2022).
165. Doerk, H. *et al.* Gyrokinetic Study of Turbulence Suppression in a JET-ILW Power Scan. *Plasma Physics and Controlled Fusion* **58**, 115005. doi:10.1088/0741-3335/58/11/115005 (2016).
166. Landreman, M. & Ernst, D. R. Local and Global Fokker–Planck Neoclassical Calculations Showing Flow and Bootstrap Current Modification in a Pedestal. *Plasma Physics and Controlled Fusion* **54**, 115006. doi:10.1088/0741-3335/54/11/115006 (2012).
167. Sertoli, M., Carvalho, P. J., Giroud, C., Menmuir, S. & JET Contributors. Measuring the Plasma Composition in Tokamaks with Metallic Plasma-Facing Components. *Journal of Plasma Physics* **85**, 905850504. doi:10.1017/S0022377819000618 (2019).
168. Belli, E. A., Candy, J. & Sfligoi, I. Spectral Transition of Multiscale Turbulence in the Tokamak Pedestal. *Plasma Physics and Controlled Fusion* **65**, 024001. doi:10.1088/1361-6587/aca9fa (2023).

169. Maeyama, S., Watanabe, T.-H. & Ishizawa, A. Suppression of Ion-Scale Microtearing Modes by Electron-Scale Turbulence via Cross-Scale Nonlinear Interactions in Tokamak Plasmas. *Physical Review Letters* **119**, 195002. doi:10.1103/PhysRevLett.119.195002 (2017).
170. https://wiki.u-gov.it/confluence/display/SCAIUS/Marconi%3A+gallery?preview=/75497859/76153888/DSC_23011ig.jpg (2023).
171. Di Siena, A. *et al.* Impact of Supra-Thermal Particles on Plasma Performance at ASDEX Upgrade with GENE-Tango Simulations. *Nuclear Fusion*. doi:10.1088/1741-4326/ad4168 (2024).
172. Leppin, L. A. & Wilczek, M. Capturing Velocity Gradients and Particle Rotation Rates in Turbulence. *Physical Review Letters* **125**, 224501. doi:10.1103/PhysRevLett.125.224501 (2020).
173. Leppin, L. *et al.* *Pedestal Turbulence in AUG and JET from a Global Gyrokinetic Perspective* Talk. 27th Joint EU-US Transport Task Force Meeting (TTF), Nancy, France. 2023.
174. Leppin, L. *et al.* *Gyrokinetic Turbulence Simulations in the Pedestal* Talk. DPG SMuK, Dresden, Germany. 2023.
175. Leppin, L. *et al.* *Tackling Turbulence from Pedestal Top to Foot with Global and Local GENE Simulations* Poster and preview Talk. 18th International Workshop on H-mode Physics and Transport Barriers (H-mode Workshop), Princeton, NJ, USA. 2022.
176. Leppin, L. *et al.* *Tackling Turbulence in the Plasma Edge Pedestal with a Revised Version of the GENE Code* Poster. DPG (Virtual). 2022.
177. Leppin, L. *et al.* *Tackling Turbulence in the Plasma Edge Pedestal with a Revised Version of the GENE Code* Poster. DPG SMuK (Virtual). 2021.

Acknowledgements

This thesis and research would not have been possible without the direct and indirect help from many colleagues. As part of a big science endeavor, this project has been enabled by the teams of people running the experiments AUG and JET, the high-performance computers at MPCDF, IFERC, and CINECA, and the current and former members of the GENE development team. The access to experimental data, as well as the compute time, is greatly acknowledged. This thesis has greatly profited from the vibrant research atmosphere in the TOK department, at IPP, and large parts of the fusion community. I want to thank all colleagues at IPP and within the EUROfusion TSVV 1 project for their support and many fruitful discussions.

I would particularly like to thank Tobias Görler, my daily supervisor, for providing help and guidance from start to finish of this thesis and for sharing his extensive knowledge of gyrokinetics and the GENE code. I am very grateful to Frank Jenko, my academic supervisor, for the opportunity to work on this exciting research project and present my work at various conferences and workshops. I also want to thank Elisabeth Wolfrum, my scientific counsel, for very helpful suggestions and discussions at various stages of the thesis.

I am very grateful to Marco Cavedon and Mike Dunne for providing experimental input data for the AUG simulations of Chapter 5 and their help in working with these data. I am also very grateful to Lorenzo Frassinetti, Samuli Saarelma, Jörg Hobirk, and the JET team for providing experimental input data for the JET simulations of 6 and their support. I want to thank Alessandro di Siena for his help in setting up and analyzing the GENE-Tango simulations of Section 5.5.

Finally, I would like to thank Facundo Sheffield, Michael Bergmann, and Tobias Görler for many helpful suggestions and comments on earlier versions of this thesis.

List of Publications

Publications

1. Leppin, L., Görler, T., Frassinetti, L., Saarelma, S., Hobirk, J., Jenko, F. & JET Contributors. The JET Hybrid H-mode Scenario from a Pedestal Turbulence Perspective. *Nuclear Fusion* **Submitted** (2024)
2. Leppin, L., Görler, T., Cavedon, M., Dunne, M., Wolfrum, E., Jenko, F. & the ASDEX Upgrade Team. Complex Structure of Turbulence across the ASDEX Upgrade Pedestal. *Journal of Plasma Physics* **89**, 905890605. doi:10.1017/S0022377823001101 (2023)
3. Di Siena, A., Bilato, R., Banon Navarro, A., Bergmann, M. G., Leppin, L., Görler, T., Poli, E., Weiland, M., Tardini, G. & Jenko, F. Impact of Supra-Thermal Particles on Plasma Performance at ASDEX Upgrade with GENE-Tango Simulations. *Nuclear Fusion*. doi:10.1088/1741-4326/ad4168 (2024)
4. Di Siena, A., Bañón Navarro, A., Luda, T., Merlo, G., Bergmann, M., Leppin, L., Görler, T., Parker, J., LoDestro, L., Dannert, T., Germaschewski, K., Allen, B., Hittinger, J., Dorland, B., Hammett, G. & Jenko, F. Global Gyrokinetic Simulations of ASDEX Upgrade up to the Transport Timescale with GENE-Tango. *Nuclear Fusion* **62**, 106025. doi:10.1088/1741-4326/ac8941 (2022)
5. Wilms, F., Navarro, A. B., Merlo, G., Leppin, L., Görler, T., Dannert, T., Hindenlang, F. & Jenko, F. Global Electromagnetic Turbulence Simulations of W7-X-like Plasmas with GENE-3D. *Journal of Plasma Physics* **87**, 905870604. doi:10.1017/S0022377821001082 (2021)
6. Leppin, L. A. & Wilczek, M. Capturing Velocity Gradients and Particle Rotation Rates in Turbulence. *Physical Review Letters* **125**, 224501. doi:10.1103/PhysRevLett.125.224501 (2020) (on results of Master's thesis)

Conference presentations

1. Leppin, L., Görler, T., Cavedon, M., Dunne, M., Wolfrum, E., Frassinetti, L., Saarelma, S., Hobirk, J., Jenko, F., ASDEX Upgrade Team & JET Contributors. *Pedestal Turbulence in AUG and JET from a Global Gyrokinetic Perspective* Talk.

Bibliography

- 27th Joint EU-US Transport Task Force Meeting (TTF), Nancy, France. 2023
2. Leppin, L., Görler, T., Cavedon, M., Dunne, M., Wolfrum, E., Jenko, F. & ASDEX Upgrade Team. *Gyrokinetic Turbulence Simulations in the Pedestal* Talk. DPG SMuK, Dresden, Germany. 2023
 3. Leppin, L., Görler, T., Cavedon, M., Dunne, M., Wolfrum, E., Jenko, F. & ASDEX Upgrade Team. *Tackling Turbulence from Pedestal Top to Foot with Global and Local GENE Simulations* Poster and preview Talk. 18th International Workshop on H-mode Physics and Transport Barriers (H-mode Workshop), Princeton, NJ, USA. 2022
 4. Leppin, L., Görler, T., Jenko, F., Cavedon, M., Dunne, M. & ASDEX Upgrade Team. *Tackling Turbulence in the Plasma Edge Pedestal with a Revised Version of the GENE Code* Poster. DPG (Virtual). 2022
 5. Leppin, L., Crandall, P., Görler, T., Jenko, F., Cavedon, M., Dunne, M. & ASDEX Upgrade Team. *Tackling Turbulence in the Plasma Edge Pedestal with a Revised Version of the GENE Code* Poster. DPG SMuK (Virtual). 2021